OPPOSING FREE AND FORCED CONVECTIVE HEAT TRANSFER IN A VERTICAL PIPE

OPPOSING FREE AND FORCED CONVECTIVE HEAT TRANSFER TO TURBULENT AIR FLOW IN A VERTICAL PIPE

by

Jagjit Kumar Khosla, B.Sc.Ch.E, M.Eng.

A Thesis

Submitted to the Faculty of Graduate Studies

in Partial Fulfilment of the Requirements

for the degree

Doctor of Philosophy

McMaster University

November 1973

Doctor of Philosophy (1973)
(Chemical Engineering)

McMaster University
Hamilton, Ontario.

TITLE: Opposing Free and Forced Convective Heat Transfer to Turbulent Air Flow in a Vertical Pipe

AUTHOR: Jagjit Kumar Khosla, B.Sc. Chem. Eng. (Panjab), M.Eng. (McGill)

SUPERVISOR: Dr. T. W. Hoffman

SCOPE AND CONTENTS

The interaction between the opposing free and forced convection has been studied, by first defining the limits of the onset of flow reversal, through flow visualisation experiments involving the cooling of upward flowing hot water. From dynamic similarity considerations, these experiments were used to define the operating conditions, for experiments involving the heating of downward flowing air, to ensure unidirectional flow. Radial measurements of the temperature and velocity were made, in a 24 in. long, 8.054 in. diameter test section, with fully developed turbulent air flow entering its inlet. The inlet Reynolds numbers ranged from 7500 to 37500, the test section wall temperature was maintained constant for any run; the temperature range covered was 122°F to 890°F. Some temperature profiles exhibited unusual behaviour and this indirectly indicated flow reversal in situations where it was expected from the dynamic similarity considerations.

The partial differential equations for the conservation of mass, momentum and energy were solved numerically by an implicit finite difference formulation. Good agreement between the predictions and the observations was obtained for negligible buoyancy force; while deviations increased with an increase in the relative magnitude of the buoyancy force. During the various attempts to resolve this discrepancy, it was felt that a change in the turbulence structure might have occurred. The effective conductivity profiles, calculated from the measured temperature profiles indicated an increase in the turbulent activity with increasing free-forced convection interaction. Heat transfer rates were found to be 215% higher than those obtained from pure forced convection considerations, for $Gr/Re^2 \sim 0.90$.

ACKNOWLEDGEMENTS

The author wishes to express his sincere thanks and appreciation to all those who have contributed their time and talents during the course of this investigation. In particular he is indebted to:

His research supervisor, Dr. T. W. Hoffman, for his guidance and encouragement throughout the ups and downs of this investigation.

R. W. Dunn and J. J. Newton, for help in the fabrication of the experimental equipment.

His many friends, especially Mark Wainwright for fellowship and concern.

His wife, Amrit, for her love, patience, understanding and encouragement when it seemed to be the end of the world.

TABLE OF CONTENTS

LIST OF FIGURES

LIST OF TABLES

CHAPTER I

INTRODUCTION

1.1 General

The interaction of free and forced convection in heat transfer systems has attracted renewed interest with the advent of gas cooled nuclear reactors. The high heat fluxes involved in such systems create large density differences in the gaseous flow field and hence large body forces which are responsible for free convection. In such a reactor, if present in a spinning spaceship, gas flow will experience large body forces due to the centrifugal forces acting on the flow field. Flow of a coolant through the internal passages of a turbine blade is another example where large body forces are encountered due to centrifugal forces. However, it is the relative magnitude of the free and forced convection which determines the extent of this interaction. That is, when the body forces and the inertia forces are of comparable magnitude, the interaction between the two convections becomes significant.

The motivation for the present study originally came from a practical application in the pulp and paper industry. The atomised suspension technique is a process for destroying waste liquors from the pulp mills by spraying them into the top of a vertical cylindrical column, the walls of

which are maintained at a high temperature (~ 1600°F). The vapours generated by the evaporation process transport the spray and/or particles downward through the column. The vapours are maintained at a low temperature by the evaporation process although the walls are maintained at nearly 1600°F [H10]. The throughput of this process is limited by the rate of heat transfer and in turn the required residence time of the liquor droplets in the furnace. Thus large body forces due to the high wall temperature and low gas flow rates (for a practical height of the furnace) generate free and forced convections of comparable magnitude.

When the two convections are of comparable magnitude their interaction can no longer be ignored and this gives rise to the 'mixed convection' regime. In this case, it has been found that the net effect is not given by the simple algebraic sum of the effects of the two convections, if they had been present alone. The relative direction of the free and forced convection and the turbulence level of the flow have been found to have a great effect on the interaction phenomena. That is to say, laminar or turbulent flow, aiding or opposing directions of the two convections affect the mechanism of heat and momentum transport in different ways.

Thus due to the importance of free and forced convections interaction in practical applications, and the complexity of the transport mechanism involved, a detailed study of the mixed convection phenomena is required.

1.2 Objectives of the Present Investigation

To study the opposing free and forced convection interaction in turbulent flow, the original spray drying problem has been simplified to a simple downward flow of a gas in a heated vertical pipe. Thus the complexities due to the distribution and motion of the liquid droplets in the flow field, and those due to their absorption of heat and the resulting evaporation are eliminated. However, other complications of significant importance remain. Firstly, the large temperature differences introduce considerable physical property variations with axial and radial locations; secondly, because the gas is the hottest near the wall and since gas viscosity increases substantially with temperature, there is a tendency towards laminarisation in the wall region; and thirdly, the body force due to density difference may be large enough to create flow reversal adjacent to the wall. All these phenomena have a great influence on the heat transfer rates.

In the opposing mixed convection phenomena, the flow reversal creates drastic changes in the flow pattern and the turbulent structure of the flow. Even without flow reversal, the buoyancy force causes substantial changes in the flow field and the heat transfer rates.

In the present investigation the effects of opposing buoyancy force, relaminarisation and physical property variations were simultaneously considered and investigated theoretically as well as experimentally. Analysis of the flow

field of a turbulent air stream, flowing downward and being heated in an 8 in. diameter pipe was carried out. The mass, momentum and energy conservation equations, together with appropriate boundary conditions, were solved simultaneously by a finite difference formulation. Only those situations where the flow was unidirectional were considered. To ensure that the proposed experimental program, which was used to check the validity of the numerical solution, conforms to the condition of unidirectional flow, flow visualisation experiments were performed. These experiments involved the cooling of hot water in vertical upward flow. Flow visualisation was obtained by producing a dark blue dye streak in the wall region by electrochemical technique. Conditions representing the initiation of flow reversal were determined. The experimental conditions at which to expect flow reversal in the air flow field were obtained from the dynamic similarity considerations.

Radial temperature and velocity profiles were measured at three axial locations within a 8.054 in. diameter, 24 in. long test section, the walls of which were maintained at some given temperature. These profiles were compared with the predicted ones from the theoretical solution. The assumptions of the theoretical analysis had to be modified to allow a direct match of the experimental observations and predicted results.

CHAPTER 2

LITERATURE REVIEW

2.1 Introduction

Turbulent flow heat transfer has been the subject of numerous investigations over the last six decades due to its importance in the chemical and power industries. Experimental work during the initial stages of development of knowledge was focussed mainly on obtaining empirical correlations applicable to the widest possible range of operating conditions. However, the limitations of such an approach were soon recognised and predictions of heat transfer rates based on the laws of conservation of heat and momentum transport were attempted using various levels of simplifications. With the possibilities of new practical applications, more complex aspects of pipe flow heat transfer, e.g., effects of low Reynolds number, variable physical properties, entrance region, relaminarisation and interacting free convection, have been studied. In any system, the relative importance of each of these effects must be evaluated and taken into consideration.

In the present investigation of the interaction of opposing free and forced convection in the entrance region, high wall-to-fluid temperature differences are involved and these create appreciable buoyancy forces. In the past, a large number of heat transfer studies with high temperature differences

have been carried out both experimentally as well as theoretically. Most of them have concentrated on only one aspect either by design of experiments or simply by ignoring the interaction of other effects. A review of the current state of knowledge of the various aspects of heat transfer phenomena relevant to the present problem is presented in the following sections.

Although a very good review of various aspects of turbulent flow heat transfer has recently been published by Petukhov [P8], some of the highly relevant papers reviewed in [P8] will also be discussed here for the sake of completeness.

2.2 Fully Developed Turbulent Flow

Far removed from the entrance region when the heat transfer coefficient is independent of the length of the pipe ($L/D \geq 60$) an empirical relation recommended by Dittus and Boelter [D4] correlated the Nusselt number with Reynolds number and Prandtl number.

$$Nu = \frac{hD}{k} = 0.023 \left(\frac{DG}{\mu}\right)^{.8} \left(\frac{C_p \mu}{k}\right)^{.4} \tag{2.1}$$

The physical properties were evaluated at the bulk temperature. The correlation is valid for moderate temperature differences for viscosity of the fluid less than 2 cp and for $10000 < Re < 120000$.

Evaluating properties at a film temperature, an average between wall and bulk temperatures, Colburn [C2] recommended a slightly different form of the above equation in

the form of the Stanton number, St.

$$St = Nu/(Re\ Pr) = .023\ Re^{-.2}\ (Pr)^{-.67} \qquad (2.2)$$

To account for the viscosity change at the wall due to heating, the Stanton number was multiplied by $(\mu_w/\mu_b)^{.14}$ and the physical properties were evaluated at the bulk temperature.

If it is assumed that the mechanisms for transport of heat and momentum are analogous, then the heat flux and the shear stress can be shown to vary linearly with radial distance for fully developed flow both from energy and force balance considerations. For Pr = 1, which is approximately the case for most gases, the analogy between momentum and heat transport called Reynolds' analogy, leads to a correlation between St and friction factor

$$St = f/2 \qquad (2.3)$$

An empirical correlation for friction factor, f, for $10000 < Re < 120000$ is given by

$$f = 0.046\ Re^{-.2} \qquad (2.4)$$

Using Reynolds' analogy this leads to the classical heat transfer correlations given by [C2] for Pr = 1. For Pr other than 1

$$St\ (Pr)^{.67} = f/2 = j_H \qquad (2.5)$$

The implication of this simple analysis is that friction factor data can be used to predict heat transfer rates and the advantage lies in the fact that the former can be obtained more easily and more cheaply than the latter.

Increasing the surface roughness, however, increases heat transfer rates very little in comparison to the friction factor.

With Pr = 1, the dimensionless temperature and velocity profiles are identical, but for Pr greater than 1, the dimensionless temperature profile is steeper at the wall than the velocity profile, while the reverse is true for small values of Prandtl number. Martinelli [M4] assuming equality of eddy viscosity and eddy conductivity and a linear heat flux distribution, derived equations for predicting heat transfer under a variety of conditions. Nikuradse's [N1] universal velocity profile was used to calculate eddy viscosity and the flow field was subdivided into the following three zones:

(i) Laminar sublayer, where turbulent transport is negligible,

$$u^+ = y^+ \qquad y^+ < 5 \qquad (2.6)$$

(ii) Buffer zone, where molecular and turbulent transport are of comparable magnitude,

$$u^+ = -3.05 + 5.0 \ln y^+ \qquad 5 < y^+ < 30 \qquad (2.7)$$

(iii) Turbulent core, where turbulent mixing is the major contributor to the transport phenomena

$$u^+ = 5.5 + 2.5 \ln y^+ \qquad y^+ > 30 \qquad (2.8)$$

Even though these subdivisions are artificial, it is instructive to note that for Pr = 100, 95 percent of temperature drop occurs in the laminar sublayer while only 5 percent for liquid metals, Pr = .01. It indicates the relative importance of molecular and turbulent thermal diffusivities.

Seban and Shimazaki [S19] derived equations for temperature profiles for constant wall temperature which were found to be in good agreement with measured profiles for air flowing in a tube at Re = 10400. Deviations between the observed results and the predictions calculated by [M4] were attributed to the different wall condition used, i.e., constant wall temperature in [S19] and constant wall heat flux in [M4].

Deissler [D1] presented theoretical predictions for heat transfer rates assuming shear stress and heat flux density to be constant across the cross-section. However, these restrictions were later relaxed to linear variation in shear stress and heat flux density.

The effect of this change for Pr = 1, was shown to be small. Von Karman's similarity hypothesis was used to evaluate the eddy diffusivity and the wall region value was modified to account for the viscous effects [D8].

It was proposed that the eddy diffusivity in the wall region is not directly proportional to the distance from the wall as suggested by Von Karman but experiences an exponential decay.

The presence of the wall dampens the motion of turbulent eddies by viscous effects such that in the laminar sublayer region the major contribution to the transport process is by molecular diffusion.

The modified wall region eddy diffusivity is given by

$$\epsilon_m = n^2 uy \left(1 - \exp\left(-n^2 uy/\nu\right)\right) \qquad 0 < y^+ < 26 \qquad (2.9)$$

For $y^+ > 26$, the Von Karman relation gives

$$\epsilon_m = k^2 \, (du/dy)^3/(du^2/dy^2)^2 \qquad (2.10)$$

where n = 0.124 and k = .36

The significant deviations of the experimental data of [D3] from the predictions of [V2] and [S10] for high Pr and Sh were removed by the modification of wall region eddy diffusivity.

Deissler's assumptions [D1] regarding heat flux density and shear stress distribution across the cross-section of the pipe were somewhat arbitrary and were made for ease in obtaining an analytical solution. A linear heat flux density for uniform wall heat flux condition requires a flat velocity profile while a linear shear stress represents a fully developed velocity field. Owing to this incompatibility the results from the analysis of Deissler would be seriously affected for low Re or for high heat flux where the velocity profile is substantially changed by the heat transport.

Churchill and Balzhiser [C6] studied the heat flux distribution across the cross-section of the pipe for a number of cases of constant wall temperature and uniform wall heat flux. The heat flux density (BTU/hr-ft^2) was found to go through a maximum near the wall due to the competing effects of convective and diffusive heat transport. However, the heat flux (BTU/hr) decreases monotonically from the value at the wall to zero at the centre line. The heat flux distribution

has been found to be a better indicator of the development of the thermal-boundary layer than normally assumed constant Nusselt number criterion; the latter criterion gives shorter development lengths.

2.3 Physical Property Variation

The density, viscosity and the thermal conductivity of a gas change substantially with a change of temperature. For a perfect gas, the density is inversely proportional to the absolute temperature while viscosity and thermal conductivities increase proportionally to approximately the 0.7 power of the absolute temperature. For small temperature differences resulting in small heat fluxes, the variation in properties may be neglected.

At moderately high or high heat flux at the wall where the wall-to-bulk temperature ratio is considerably different from 1, systematic deviations from the constant property solution have been observed even at high Re [Fig. 5 of P10] indicating the effect of physical property variation across the cross-section of the pipe. If the physical properties are evaluated at a film temperature, that is, some average between the wall and bulk temperatures, the effect of variable properties can be partially eliminated.

Deissler [D3, D6, D8] modified his analysis by introducing the physical properties as power functions of absolute temperature. He found that if the properties in Nu and Re were evaluated at $T_{.4} = T_b + 0.4\ (T_w - T_b)$ then the

experimental results were in fair agreement with those from the theoretical analysis for Re > 15000 and $(T_w/T_b) < 1.9$. For lower Reynolds numbers, partial transition from turbulent to laminar flow and the breakdown of Reynolds analogy were suggested to be the reasons for the disagreement between theoretical and experimental results. Even for $T_w/T_b \sim 1.2$, the observed temperature profiles deviated substantially from the predicted ones while the velocity profiles were in fair agreement. This was cited as an indication of the inequality between eddy diffusivity for heat and momentum transfer. At higher (T_w/T_b) ratios, however, predicted velocity profiles deviated as much as 30% from the experimental values [D7]. The analysis was extended to supercritical water flow and it was found that the film temperature had to be a function of both T_w and (T_w/T_b) to eliminate the effect of physical property variation.

Zellnik and Churchill [Z1] in their experimental investigation of cooling of hot gases in a short tube observed that if physical properties were evaluated at bulk temperatures, then the heat transfer results could be correlated by a Dittus-Boeltor type equation. This is in contrast to the Deissler's suggestion that properties should be evaluated at a film temperature. It was pointed out that Deissler assumed the thermal conductivity of air to be proportional to $(T)^{0.68}$, while actually $(T)^{.85}$ is a better representation. Recalculating on the basis of $(T)^{.68}$, Zellnik and Churchill found their results to be in agreement with the predictions of Deissler.

This points out how correlations and conclusions are affected by the estimates of the physical properties.

For the constants in the eddy diffusivity expression obtained from isothermal data, to be used for variable property situation, it becomes important that the flow similarity hypothesis used to obtain eddy diffusivity expression should be as near the actual mechanism as possible. Deissler in his analysis non-dimensionalised the radial distance $y^+ = \frac{\sqrt{\tau_w/\rho_w}}{\nu_w} y$ by evaluating the physical properties at the wall temperature. He also assumed that turbulent transport is a universal function of this dimensionless distance from the wall. Goldmann [G6] questioned the use of the non-dimensionalised velocity and distance based on wall temperature. He proposed that the local turbulence characteristics of the flow depend upon physical properties at that point and not on some point in the near vicinity as Deissler assumed. If the dimensionless radial distance and velocity are defined as:

$$y^+ = \int_0^y \sqrt{\tau_w \rho} / \nu \; dy$$

$$u^+ = \int_0^u 1/\sqrt{\tau_w \rho} \; du \qquad (2.11)$$

the experimental results for air and for water at 5000 psi were predicted with a higher accuracy than those obtained by using Deissler's method.

Petukhov and Popov [P9] improved upon Deissler's analysis by using the velocity profile calculated from the

solution of the momentum equation. Thus variations in shear stress and heat flux were governed by the transport equations rather than by arbitrarily chosen functions. For fully developed flow and uniform wall heat flux it was assumed that the axial gradients of fluid enthalpy and sum of pressure and kinetic energy were not functions of radial position. Using Reichardt's [R2] expressions for eddy viscosity and Goldmann's non-dimensionalising velocity and distance, integral solutions for constant as well as variable properties were given; these indicated less than 3% error from the experimental results for Re > 25000 for air and hydrogen. This analysis showed a considerable improvement over that by Deissler.

For high wall heat fluxes the ratio of variable property and constant property Nusselt numbers was expressed as a function of the ratio of wall to bulk temperatures.

$$Nu/Nu_{c.p.} = (T_w/T_b)^n \qquad (2.12)$$

The value of the exponent n was found from experimental measurements to be -0.5 by Petukhov and Popov [P9] and McEligot et al. [M5], -0.4 by Magee [M6] and -0.7 by Perkins and Warsoe-Schmidt [P3]. Petukhov [P4] expressed n by a logarithmic function of (T_w/T_b). Kutateladze and Leontiev [K5] proposed the following correlation from theoretical considerations

$$\frac{Nu}{Nu_{c.p.}} = \left(\frac{2}{1+\sqrt{T_w/T_b}}\right)^2 \qquad (2.13)$$

All this indicates that there does not seem to be a single value of n which will allow predictions of heat transfer rates over a wide range of heat flux or wall-to-bulk temperature differences. Indeed, the phenomena seems to be much too complex to yield this simple representation.

All the previous analyses [D3, B8, J3, M6, P9] assumed some shear stress and/or heat flux density distributions across the cross-section of the pipe. However, high heat fluxes create severe velocity gradients near the wall and thus make the flow continually developing. McEligot et al. [M7] reviewing the current state of knowledge, decided to solve the momentum and energy conservation equations for developing thermal boundary layer and assessed the fully developed behaviour by considering the results at large downstream distances. These partial differential equations were solved numerically by finite-difference approximation. Turbulent transport models of four different types (Reichardt, Van Driest, modified Deissler and Kendall) were tried. The dimensionless distance y^+ was evaluated either at the conditions at the wall or at the local temperatures. At large downstream distances asymptotic behaviour of Nusselt number with axial distance was observed from the numerical calculations. At low heat flux the point of start of the asymptotic curve, was found to be a function of heat flux but independent of entering Reynolds number while at high heat flux it is a function of both. A value of 40 diameters seemed enough in some cases while as much as 80 to 120 dia. were necessary in others. Agreement with

the data of Perkins and Worsoe-Schmidt [P3], Taylor [T4] and Kutateladze [K5] was shown to be fair, though a temperature ratio power law could not be given.

Though Kutateladze's Equation (2.13) gives a reasonable representation of the heat transfer rates, yet complete solution of conservation equation using local properties seems to be the ideal approach.

2.4 Entrance Region

When a fluid flowing past a solid boundary suddenly experiences a change in wall temperature, a thermal boundary layer starts developing. The thickness of this thermal boundary layer increases with downstream distance and the heat transfer rates decrease as the temperature gradients become less and less steep. At low heating rates the momentum boundary layer is not affected by the development of this thermal boundary layer but at high heating rates both boundary layers try to adjust themselves to an equilibrium state. Axial momentum and enthalpy gradient terms in the conservation equations change with both axial and radial distances and hence the continuity equation must be satisfied simultaneously.

Berry [B9] analytically determined the entry length, i.e., downstream distance required to attain a fully developed thermal boundary layer, for a turbulent flow heat transfer in a pipe. Only the energy equation was solved by the separation of variables technique and converting it into a Sturm-Liouville problem. A series solution was given and conditions were

examined for the Nusselt number to reach 99% of its asymptotic value. Assuming Von Karman's hypothesis for eddy diffusivity, a fully developed velocity profile and uniform wall temperature, the entry length was given in terms of friction factor, f.

$$x/D = 2.262/\sqrt{f} \qquad (2.14A)$$

Deissler [D8] provided an integral solution for the development of the thermal boundary layer in the entrance region. He assumed that all the resistance to heat transfer lies in the boundary layer thickness, δh, and the fully developed temperature profiles exist in this region. Assuming a linear variation in shear stress and heat flux across the boundary layer, thermal boundary layer growth as a function of axial distance was calculated by considering heat balance over an elemental volume and integrating. An entry length of less than 10 diameters was calculated and verified by experimental data for low heat fluxes (constant property situation). It was observed that in the laminar flow, the boundary layer thickness determined the rate of heat transfer while the flattening of the temperature profiles in the turbulent flow was the controlling factor. In turbulent flow the ratio of the local Nusselt number to that under fully developed conditions was found to be higher for lower Reynolds number.

Wolf [W3] extended Deissler's analysis of entry length taking into account physical property variations. His results agree more closely with the observed values for air

and CO_2. Heating and cooling experiments with large gas-to-wall temperature differences were carried out for 17000 < Re < 218000. Temperature differences of the order of 1200°R between wall and gas were attained. At these high heat fluxes (high temperature differences) the experimental values of the Nusselt number were higher than those predicted by the theory for heating, while smaller for cooling. The explanation offered is that the eddy diffusivity expression and Reynolds analogy between momentum and heat transfer is invalid under these conditions. The development length predictions were found to be lower than the experimentally observed values. This was probably due to the fictitious boundary layer thickness and the arbitrary radial distributions of shear stress and heat flux which were assumed in the analytical solution.

Wolf expressed concern over the criterion of thermally fully developed flow. He recommended the constancy of heat transfer coefficient instead of the Nusselt number as a measure of development length. The former choice seems more logical as the heat transfer coefficient is wall heat flux per unit driving force. It is this factor which determines the universality of the dimensionless temperature profiles. It is only at high heat fluxes, accompanied by appreciable physical property changes, that the constancy of heat transfer coefficient gives a more accurate description of the thermal development of the flow. Another indicator is the radial heat flux distribution. At large distances from the entrance, the radial heat flux (BTU/hr) made dimensionless with respect to

the wall heat flux, becomes independent of the axial distance. This occurs when there is an equilibrium between the diffusional and convective heat transfer processes. Churchill [C6] indicated that the radial heat flux distribution is more sensitive to the development of the thermal boundary layer than the Nusselt number. However, this criterion, though more accurate, is difficult to use for design purposes as compared to the heat transfer coefficient or the Nusselt number.

Sparrow et al. [S1] solved the energy equation in the entrance region using the principle of superposition according to which the radial temperature distribution is the sum of fully developed temperature profile and the correction for the entrance region. Fluid properties and the dimensionless velocity profile were assumed not to be changed by heat transfer. Deissler's eddy viscosity expression (modified for viscous effects) Equation (2.9) was used for the wall region while away from the wall eddy viscosity was obtained from linear shear stress and logarithmic velocity distribution across the pipe cross-section. Fully developed temperature profile was obtained by direct integration of the energy equation. The correction for the entrance region was obtained by forming an eigenvalue problem of Sturm-Liouville type. Higher Nusselt numbers were predicted as compared to the experimental data of Wolf and Lehman, while predictions from Deissler's analysis [D1] were lower than the experimental data. Sparrow questioned Deissler's assumption of fully developed temperature

profiles in the thermal boundary layer and the use of linear heat flux distribution across the radius of the tube. Siegel and Sparrow [S11] concluded that the turbulent flow heat transfer mechanism is quite insensitive to the thermal condition of the pipe wall, since they found essentially the same results for both uniform wall heat flux and uniform wall temperature.

Magee, using the same assumptions as Sparrow but taking variation in physical properties into account, carried out a finite-difference solution of the energy equation. The theoretical solution and the experimental data indicated that for Reynolds number of the order of 10^5 and T_w/T_b about 2, the heat transfer results could be correlated by

$$Nu = 0.0205\ Re^{.8}\ Pr^{.4}\ (T_w/T_b)^{-.4}[1+.6(D/x)(T_w/T_b)^{.4}] \tag{2.14}$$

Perkins and Worsoe-Schmidt [P3] correlated their experimental data for $10^4 < Re_b < 10^5$, $T_w/T_b < 2.46$ and $x/D > 1.2$ by:

$$Nu = 0.024\ Re^{.8}\ Pr^{.4}\ (T_w/T_b)^{-.7}[1+(x/D)^{-.7}(T_w/T_b)^{.7}] \tag{2.15}$$

with properties evaluated at bulk temperature. When properties where evaluated at wall temperature, the correlation reduces to

$$Nu = 0.023\ Re^{.8}\ Pr^{.4}\ [1+(x/D)^{-.7}(T_w/T_b)^{.7}] \tag{2.16}$$

Bankston and McEligot [B10] solved the momentum and energy conservation equations along with the continuity equation by a finite difference approximation. Flow situations in laminar and turbulent flow with a uniform or a fully developed entering velocity profile, and low to high wall heat flux were studied. Of the various turbulent transport models tried, Van Driest's mixing length model with properties evaluated at the wall temperature was found to be the best of all those tried.

$$\epsilon_m = k^2 y^2 [1-\exp(-y/A)]^2 \left|\frac{du}{dy}\right| \tag{2.17}$$

where $k = 0.4$ and $A = 26\nu/u^*$.

For a constant property solution, a generalised correlation agreeing with numerical predictions within 2% for $x/D > 0.1$ was proposed.

$$Nu_\infty = 0.259\ Re^{.785}\ Pr^{0.4} \tag{2.18}$$

$$Nu/Nu_\infty = 1 + 2.2\ Re^{-.144}\ (x/D)^{-.807}\ Re^{-.516} \exp\left[1 - 1.42\ Re^{-.2}\ (x/D)\right] \tag{2.19}$$

The fully developed Nusselt number values were slightly higher than those given by the eigenvalue solution of Sparrow [S1] and the Dittus-Boelter Equation (2.1). Good agreement was also obtained with the predictions of Sparrow for entry region $x/D > 3$. However, for smaller axial distances it seems that more eigenvalue terms in the series

solution of Sparrow need to be included.

In contrast to the Deissler type analysis [D8, W3], the analyses of [S1, M6, B10] did not use any arbitrarily assumed heat flux distribution across the pipe cross-section, but solved the conservation equations numerically. The assumptions of Deissler's analysis break down at high heat fluxes and low Reynolds numbers and this was suggested as the reason why Wolf [W3] measured higher development lengths than given by his analysis. However, the solution of only energy equation [S1, M6] though more realistic than Deissler type analysis, assumes the velocity profile is not affected by heat transfer. The analysis of Bankston [B10] relaxes this assumption by solving simultaneously the momentum and energy equations. Even this analysis has its limitations because of some basic changes occurring in the mechanism of turbulent heat transport at high heat flux and low Reynolds numbers.

At low wall heat fluxes, Perkins and Worsoe-Schmidt [P3] observed that the wall temperature after an initial sudden rise, increased almost linearly with axial distance. But at high heat fluxes, a peak in the wall temperature was observed around 20 diameters from the entry followed by a gradual rise along the length. This kind of peak was not observed in the bulk temperature measurements, indicating that it is a wall phenomena.

Bankston and McEligot [B10] studied this behaviour in detail by means of their numerical solution of the governing conservation equations. A minima was observed in Nusselt number at approximately the place of wall temperature peak

experimentally observed. The calculated minima moved towards the entrance and the peak became more abrupt with increased heat flux. The minima became lower and moved towards the entrance as the Reynolds number was increased.

The predicted velocity profiles indicated that the viscous sublayer became thicker with heating. The criterion for sublayer thickness was proposed to be the radial location at which the contribution of turbulent transport is equal to that by molecular diffusion. The calculation of viscous sublayer thickness along axial distance showed a peak, and this was used to explain the decrease in Nusselt number and hence the observed rise in the wall temperature. A comparison of the predictions with the experimental data of [P3, M5, P4] showed overprediction of wall temperature in the entry region and underprediction in the downstream region. It was suggested that the turbulence models, based on fully developed isothermal flow measurements, may fail to account for the phenomena occurring under strongly nonisothermal conditions.

The velocity profile in the transition region deviates substantially from the universal velocity profile for high Reynolds number turbulent flow [P7, R3]. Reichardt's two equation eddy diffusivity expression [R2] was modified by Reynolds et al. [R3] into a single equation and the viscous effect damping factor, y_ℓ^+ was found to be a function of Reynolds number.

$$\varepsilon_m/\nu = \frac{k}{6}\,[y^+ - y_\ell^+ \tanh y^+/y_\ell^+][1-r/R][1+2(r/R)^2] \qquad (2.20)$$

where $k = .423$ and $y_\ell^+ = 11 + 9 \exp(-.0003Re)$

Reynolds et al. [R4] analysed the constant property entrance region heat transfer problem at low Reynolds number. A seven term eigenvalue solution of the Sturm-Liouville form of energy equation was obtained assuming fully developed entering velocity profile for $3000 < Re < 50000$. Calculated normalised Nu increased with a decrease in Re and could be correlated by

$$Nu/Nu_\infty = 1 + .8\,(1 + 70000\,Re^{-3/2})(x/D)^{-1} \qquad (2.21)$$

Experimental data for He and air were compared with their numerical predictions and those of [M8] for $3800 < Re < 10250$. The agreement was good except for $x/D < 2$ where experimental error due to axial conduction was responsible for lower observed heat transfer rates. This analysis is likely to give inaccurate results for strong heating rates because the property variations have not been taken into account.

2.5 Relaminarisation

When a turbulently flowing gas is heated in a pipe with high wall heat flux, its viscosity in the wall region increases due to high temperatures. Since turbulence is generated in the wall region, the increased viscosity in the wall region is expected to dampen the generation of turbulence.

Thus under suitable conditions, a turbulently flowing gas may revert to laminar flow, which is indicated by decreased heat transfer rates. Similarly it has been observed that under suitable conditions, adiabatic turbulent flows change to laminar regime in turbine nozzle cascades, supersonic nozzles and wind tunnel contractions. Favourable pressure gradients arising in strongly accelerating flows and the resulting large shear stress gradients bring about this transition. These relaminarisations due to severe heating or due to favourable pressure gradients are analogous situations. It has been pointed out that the transition from laminar to turbulent and from turbulent to laminar are two quite distinct phenomena. The former depends upon the conditions present in the system which amplify any disturbance that may be present, while the latter will depend upon the severity of the heating rate or that of the favourable pressure gradient. It also depends upon the characteristics of the inlet turbulent flow. In a fully turbulent flow there exists a local equilibrium between the production, dissipation and diffusion of turbulent energy. The initiation of reverse transition represents a break down of this equilibrium.

Measurements of Patel and Head [P11] indicate that initiation of laminarisation, in a favourable pressure gradient situation, is indicated by the dimensionless velocity profile being higher than the universal profile, as is the case for transition Reynolds number flows.

Since the wall shear stress gradient, α, is a characteristic of the turbulent flow and the breakdown of turbulent flow is initiated in the wall region, a critical value of the shear stress gradient parameter $\Delta\tau = \frac{\nu\alpha}{\rho u^{*3}} = -.009$ has been proposed, below which a turbulent flow cannot maintain itself. The use of the shear stress gradient rather than the pressure gradient has been stressed because the shear stress gradient can also be created by means other than pressure gradient and cause laminarisation.

Bankston [B11] tried to use the knowledge of laminarisation by shear stress gradient in external flows, to explain the reverse transition by high heat flux in pipes. Increased viscosity of a gas due to heating results in increased viscous damping of the turbulent eddies and if heating is continued over a sufficient length the turbulent flow will revert to laminar as the bulk Reynolds number approaches about 3000. As with accelerating flows, strongly heated flows experience distortions in velocity profile by flattening with respect to the law of the wall and an apparent thickening of the viscous sublayer. Heat transfer experiments for hydrogen and helium were done by Bankston [B11] using a constant wall heat flux in a 3/16" nickel-chromium alloy tube with Reynolds numbers based on inlet conditions from 2350 to 12500 and with heat flux parameters $q^+ (= \dot{q}_w''/GC_pT_o)$ from .0021 to .0061. At low heat fluxes the experimentally observed Stanton number, after the entry length, followed the well accepted constant

property heat transfer equation and as the heating proceeded the transition to the laminar regime was obtained. At high heat fluxes, even though the entering Reynolds number was as high as 12000, the observed heat transfer rate did not agree with that predicted by the turbulent flow correlations, but instead exhibited a trend characteristic of the transition regime. When the bulk Reynolds number reached 4000, heat transfer rates were those given by laminar flow correlation. It was termed premature laminarisation. The abnormal transition was also indicated in the entrance region by a steeper approach to the fully developed laminar flow correlation than would have been obtained if the entering flow had been laminar. Perkins and Worsoe-Schmidt [P3] also noted the tendency of strongly heated flows ($T_w/T_b > 2.5$) to depart from the turbulent behaviour even though the bulk Reynolds number was of the order of 10000 to 15000.

Similar to the acceleration parameter $k = \frac{\nu}{u_\infty^2}\frac{du_\infty}{dx}$ for external boundary layer flows, a parameter $k' = \frac{\nu_b}{u_b^2}\frac{du_b}{dx}$ for heating in pipe flows was defined to define conditions of reverse transition. It was found that a critical range of these parameters exist; $8 \times 10^{-7} < k' < 1.14 \times 10^{6}$ and $2 \times 10^{-6} < k < 1.5 \times 10^{-6}$. For values of these parameters higher than the given range, the turbulent flow cannot maintain itself. A critical value of k' defined in terms of wall heat flux,

$$= \frac{4\,\mu_b\,\dot{q}_w''}{G^2 D\,T_b\,Cp_b} = 1.5 \times 10^{-6}$$ was suggested by Coon and

Perkins [C3] from heat transfer experiments with air and helium with wall-to-bulk temperature ratio of the order of 4.4. An empirical expression giving the downstream distance at which the flow will be completely laminar was suggested,

$$x/D = 2 \times 10^{-8} (Re_0)^2 T_0 (T_b/T_w)_{max} \qquad (2.22)$$

This correlation predicted values which agreed within ± 20% of the experimentally observed values.

A pressure gradient parameter related to Patel and Head's shear stress gradient parameter [P11] was also suggested by Hankston [H11]

$$\Lambda_p = -2 \Lambda_1 = \frac{4\mu_w}{\bar{\rho}} \frac{1}{\sqrt{\rho_w \tau_w}} = 0.018 \qquad (2.23)$$

but heat transfer results indicated a range of $0.014 < \Lambda_p < 0.023$.

It can thus be concluded that relaminarisation by heating and by flow acceleration are analogous situations, though the proposed parameter characterisation may not be exact.

McEligot et al. [M8] studied theoretically as well as experimentally in a 1/8 in. diameter vertical tube, fully developed heat transfer rates for air, N_2, He for $1450 < Re < 45000$ and wall-to-gas temperature ratios up to 4.8. Using the isothermal data of Senecal [S12], the limit of the laminar sublayer, y_ℓ, was defined as the point where the eddy viscosity became essentially zero. At Reynolds numbers less than 5000, considerable departure was observed from the high Reynolds number value of $y_\ell^+ = 5$. It was represented by the expression

$$y_\ell/R = \frac{5}{Re\sqrt{(f/8)}}\,[1 + 3.65\exp(-5.25.10^{-4}\,Re)] \qquad (2.24)$$

For regions beyond the laminar sublayer, the mixing length, expressed as a series function of distance from the wall, was modified to account for low Reynolds number effect using the experimental data of Senecal. The velocity profile was obtained from linear shear stress distribution and the energy equation was solved for uniform wall heat flux.

At low heat fluxes good agreement between predictions and experiment was obtained for Re > 3000. For moderate heating the general behaviour indicated a wall-to-gas temperature ratio exponent of -0.5 for Nusselt number normalised with respect to the constant property value, with 15-20% scatter. For large heat fluxes, because of large changes in physical properties, many fold reduction in bulk Reynolds number occurred and the initially turbulent flow was observed to be laminar at a large downstream distance [M9]. A modified wall $Re_{w,m}$ was defined as $Re_{w,m} = \frac{DG}{\mu_w}\frac{T_b}{T_w}$ and flow regime classification was done as functions of $Re_{w,m}$ and T_w/T_b. The turbulent region started around $Re_{w,m}$ = 4000 for T_w/T_b between 1 and 2 and for higher T_w/T_b, $Re_{w,m}$ could be of the order of 6000.

McEligot and Bankston [M10] relaxed the assumption of linear shear stress used in [M8] and tried to predict the laminarisation due to heating in a pipe by simultaneously solving momentum, energy and continuity equations. Van Driest's eddy diffusivity expression, Equation (2.17), along with the Reynolds analogy assumption was used. The damping constant A^+

in the Van Driest mixing length hypothesis was defined with respect to properties at wall temperature. It was recognised that the value of $A^+ = 26$ obtained from high Reynolds number flows ($Re \sim 5 * 10^5$) was not valid in the transition regime. Tabulated values of A^+ increasing with decrease in Reynolds number to account for increased viscous effects were given. Comparison of predicted and experimental Stanton number showed that the use of a modified wall Reynolds number $Re_{w,m} = \frac{DU_b}{\nu_w}$ to evaluate A^+ gave less deviation than the use of $Re_w = \frac{DG}{\mu_w}$, even though the former is not very satisfactory either. It appears that a rapid increase in the thickness of the viscous sublayer to almost the centreline of the pipe may perhaps be necessary to obtain at least partial agreement between numerical predictions and the experimental data, for those cases where premature laminarisation occurs. It was noted that the use of the mixing length hypothesis assumes flow similarity in order for the eddy viscosity to be a function of Reynolds number and radial location only. It implies that there exists a local equilibrium between production, dissipation and diffusion of turbulent energy. Laminarisation results in decay of turbulence and hence departure from the equilibrium. On the basis of the work of Goldberg [G8], Nash and MacDonald [N2] and McDonald [M14], it was proposed that the variation of mixing length with axial distance should be considered to account for the transition from turbulent to laminar flow occurring along the pipe length. It was suggested to be proportional to its

departure from the equilibrium value as given by

$$\frac{\partial \ell}{\partial x} = C \frac{\sqrt{\tau(y)/\rho(y)}}{\nu(y)} (\ell_{fd} - \ell) \tag{2.25}$$

where ℓ_{fd} is the equilibrium mixing length assuming fully developed flow and C is a constant whose value is to be found from experimental data. Comparison with the data of [P3, B11, C4, M11] shows that even though in general the axial variation in the mixing model is better than the equilibrium model, it still is not satisfactory in predicting premature laminarisation.

It is of interest to note that in the relaminarisation studies of [B11, C3, M5, M7, M8] small diameter tubes 1/8 to 1/4 in. have been used. With small tube diameter and the accompanying high velocities for a certain Reynolds number, the relative magnitude of the buoyancy force as compared to the inertia force was very small. But for a larger diameter pipe, the interaction of free and forced convection will be significant.

2.6 Combined Free and Forced Convection

In most of the forced convective heat transfer situations, free convection is invariably present as it is caused by a change in the density of the fluid due to the transfer of heat. When free convection becomes significant due to either a large temperature difference or a large acceleration (cooling of a turbine blade with accompanying high centrifugal force), the interaction of the two convections can not be ignored.

It is the ratio of buoyancy and inertia forces which determines the relative magnitude of the two convections for a turbulent flow system. At a fixed Reynolds number, an increase in buoyancy force (for example, by a temperature difference) increases the relative magnitude of free convection. A similar situation arises when the flow (Reynolds number) is decreased with a fixed temperature difference. A transition from the complete dominance of forced convection to dominance by pure free convection can thus be accomplished in either of the two ways, though most conveniently by decreasing the Reynolds number. The interaction of the two convections, when they are of comparable magnitude, is a complex phenomenon and very little work has been done on it. Entirely different effects arise when the free and forced convection aid or oppose each other or the flow regime is laminar or turbulent.

2.6.1 Aiding Mixed Convection

In laminar flow, with free convection aiding, heat transfer rates are observed to be higher than those with only forced flow. These rates are increased by virtue of the increased velocity gradient at the wall [J2, H2, M3, M12]. On the other hand for turbulent flow and the convections aiding each other, a deterioration in heat transfer rate has been observed over the first 20 to 30 diameters of length; after this length improvement in the heat transfer rate was observed [H7]. The explanation offered is that the aiding buoyancy force reduces the shear stress in the region where turbulence

is generated, thus decreasing the turbulent diffusivity. With a further increase in the buoyancy force, it exerts a pulling action on the main flow and consequently restores the production of turbulence. Relaminarisation of flow due to decreased turbulence activity caused by the aiding buoyancy force has also been observed by Steiner [S18].

2.6.2 Opposing Mixed Convection

A. Laminar Flow

In laminar flow, with free convection opposing the forced convection, a decrease in heat transfer rates was observed by Guerrieri and Hanna [G3] due to the deceleration of velocity near the wall. Increased buoyancy created a stagnation point in the velocity profile near the wall following which flow reversal and semi-turbulent conditions increased heat transfer rates. Acrivos [A4] tried to predict the flow separation point as a function of Pr for flow on a vertical flat plate by the momentum integral method. Rosen's [R1] predictions of the separation point for opposing convections, laminar flow gave lower values of Gr/Re than those from the flow visualisation observations of Scheele et al [S16].

Scheele [S16] in his study of opposing free and forced convection found a sudden transition from laminar to turbulent flow rather than a gradual growth of small disturbances which usually characterise the transition regime. This sudden transition was similar to that characterising the separated boundary layer flow along a flat plate. Asymmetry and instability

of the laminar flow were associated with this transition for a constant heat flow situation. Hallman [H2] also observed asymmetry in the wall temperature, but this asymmetry was not observed when the two convections were aiding each other.

Biggs [B5] found that the heat transfer rates for opposing convections could be predicted by the constant property laminar flow solution by Kays [K3] in the entrance region. Further downstream, the heat transfer rates deviated from the predictions; he ascribed this to flow reversal and asymmetric flow. With increasing buoyancy force, transition to turbulence occurred beyond the usual entry region but its effect was observed in the whole tube. In this case, heat transfer coefficients in the entry region were reduced by 20% probably because of deceleration of velocity near the wall as observed by Guerrieri [G3].

B Turbulent Flow

Opposing free and forced convection in turbulent flow follow a different transport mechanism altogether. In spite of the deceleration of the velocity in the wall region by virtue of the buoyancy force, Altman and Staub [A5] observed an increase in the heat transfer rates by as much as 100% than those by forced convection considerations ($1100 < Re < 7600$).

Eckert and Diaguila [E1] measured heat transfer rates for short tubes ($L/D = 5$) for air at 14.7 to 125 psia pressure to obtain a wide range of flow conditions ($40000 < Re < 362000$, $10^8 < GrPr < 3 \times 10^{12}$). For large Grashof numbers the heat

transfer rates were found to be independent of Reynolds number indicating that the free convection is controlling the transport process.

To define the boundary between pure free or forced convection and the mixed convection zones it was postulated that if the heat transfer rates differ by more than 10% than those for the appropriate pure convection regime, then the flow was in the so-called mixed convection regime. The lower limit of Re_x for which mixed convection prevails was given by

$$Re_x = 18.15\ (Gr_x Pr)^{.33} \tag{2.26}$$

where x is the distance from the downstream end of the tube and properties were evaluated at the film temperature. With increasing Reynolds number, the heat transfer rates were observed to be independent of (GrPr), thus indicating the dominance of forced convection. It was found that whereas, for a constant Re_x, heat transfer data converged to pure free convection results as the buoyancy force was increased, this certainly did not happen in the case of constant Grashof number and increasing Reynolds number. In this mixed convection regime, when heat transfer rates became independent of Grashof-Prandtl number product, higher heat transfer rates were still obtained than those expected from pure forced convection. It was concluded that the mixed-flow regime approaches pure forced flow conditions gradually. The high heat transfer rates were attributed to the increased turbulence which seems to be generated

by the opposing convective forces.

Metais and Eckert [M1] mapped the regions of free, mixed and forced convections from the experimental data available in the literature. The three convection regions were presented on a plot of Re_f vs. $(Gr_f Pr_f D/L)$, with Grashof number based on the difference between wall and bulk temperatures and physical properties at the mean of the two temperatures. It is important to recognise that the boundaries between the convection regimes are not sharp delineations but the regions over which the change from one regime to the other takes place. The observation of Eckert [E1] indicated that there is a very gradual change from the mixed convection to the pure forced convection for opposing free and forced convections. Thus the boundary between the mixed and forced convection is a wide band.

Brown and Gauvin [B3] studied the rates of heat transfer to air entering, with a flat velocity profile, at the top of a heated vertical pipe (23 diameters long) at $378 < Re < 6900$ and $77 < T_w < 1022^{\circ}F$. The rates of heat transfer were found to be independent of Reynolds number indicating perhaps free convection was the dominating mechanism. It was suggested that perhaps this lack of dependence on Reynolds number was only the result of the way the Nusselt and Grashof numbers were calculated, since wall-to-centreline rather than wall-to-bulk temperature differences were used in calculating these dimensionless numbers. It was argued that this calculation scheme does not account for the effect of velocity profile. But this is only true for immediate entrance region (5 to 10 diameters)

where the centreline is essentially at the inlet fluid temperature. Two types of heat transfer behaviour were observed for $Gr < 3 \times 10^5$ the observed heat transfer rate was less than that predicted for pure free convection. This was attributed to deceleration of the fluid in the wall region though laminarisation may have contributed to this result as well. The rates of heat transfer did increase to 45% above the pure free convection results for $Gr > 10^6$. They suggested that the turbulence characteristics of the flow may have been changed in this system. In the entrance region, the Nusselt number was observed to increase with axial distance and then after a peak, levelled off. The initial rise was thought to be due to the flow reversal that might have occurred and the consequent mixing in the flow field.

Brown and Gauvin [B3A] observed some very high temperature fluctuations in the entrance region, which could have been caused by unstable flow due to flow reversal. For large downstream distances (5 to 13 diameters), temperature fluctuations for opposing free and forced convections were consistently higher than when the convections were aiding each other, for $390 < Re < 2200$. At $Re = 5000$, $T_w = 932^oF$, $(Gr/Re^2)_f \sim 0.2$, the difference between the two cases was quite small, suggesting the domination of the forced convection. This $(Gr/Re^2)_f$ ratio seems rather high to deduce such a conclusion as Eckert [E1] suggested a gradual transition from mixed convection to pure forced convection. Moreover, Herbert and Sterns [H6] observed

54% increase in heat transfer rate over the pure forced convection predictions for $(Gr/Re^2)_f = 0.1$.

Herbert and Sterns [H6] studied heat transfer rates for the heating of downward flow of water. Evaluating physical properties at the film temperature the data were correlated as:

$$Nu = 0.56\ Re^{.46}\ Pr^{.4} \tag{2.26A}$$

for $4500 < Re < 15000$, while for $Re < 18000$ the values of the Nusselt number given by the Dittus-Boelter equation were approached. For low Reynolds number range, a higher coefficient and a lower exponent of the Reynolds number in Equation (2.26A) than those for the Dittus-Boelter Equation (2.1) indicate higher heat transfer rates. At $Re = 15000$, the observed Nusselt number was as much as 54% higher than the value given by the modification to the Dittus-Boelter equation suggested by Everett [E2] for the transition regime. The increased heat transfer rate was attributed to the increased disturbance in the flow due to the opposing free and forced convections.

Hall and Price [H5] studied the opposing mixed convection phenomena on a vertical plate forming one side of a rectangular duct. Increased heat transfer rates than those calculated for pure free or forced convection were observed. Measurements of transverse temperature profiles for mean downward air velocities of 0.39 m/sec and 0.64 m/sec at 0.15 m and 0.75 m from the start of the heating plate indicated flow reversal at lower velocities. Its occurrence can best be appreciated by superimposing Figures 113.5 and 113.7 of [H5]

and studying the behaviour of temperature profiles at the two axial locations. The temperature profile for a velocity of 0.39 m/sec at 0.15 m was higher than at 0.75 m. This can only happen if some of the hot-fluid from downstream recirculates back up the wall and thus increasing the temperature at the upstream location. The occurrence of flow reversal concluded from temperature profile measurements was confirmed by flow visualisation with smoke. At 0.64 m/sec the forced flow was high enough to suppress any recirculation and the temperature profile increased with axial distance. However, the interaction between the free and forced convections resulted in a rapid lateral growth of the thermal boundary layer. Temperature fluctuation measurements substantiate the theory of increased turbulence activity due to the opposing free and forced convection interaction.

Pollock [P1] measured the radial temperature profiles in the entrance region of an 8 in. diameter pipe with downward air flow, for $10000 < Re < 21000$ and a uniform pipe wall temperature in the range of 140 to 1400°F. Analysis of the thermal flow field was carried out using the eddy diffusivity profile used by Sparrow [S1]. Velocity profile not affected by the temperature field and constant physical properties at the inlet temperature were assumed. For $T_w < 600°F$, good agreement was found between the observed and predicted temperature profiles, while for higher wall temperatures, the predictions were higher. The agreement of the observations and

predictions is surprising as at 600°F and Reynolds number at 21000 and 10000, Gr/Re^2 is 0.467 and 2.06 respectively. Such high values of Gr/Re^2 suggest strong interaction between the opposing free and forced convections and flow reversal might have occurred in some cases. No account of such a high buoyancy force was taken in the analysis and under such conditions the assumptions of constant properties and velocity profile not being affected by heat transfer are highly questionable. The only explanation that can be offered is that fortuitous agreement between the predictions and the observations might have been obtained due to not so good an averaging device used for a highly fluctuating temperature field.

2.7 Turbulent Prandtl Number

Analogous to the Reynolds stresses, $\overline{u'v'}$, for momentum transfer; turbulent transport of heat is given by the time average product of the transverse velocity and temperature fluctuations, $\overline{v'T'}$. Prandtl's mixing length concept has been extended to heat transfer. The eddies retain the mean velocity and temperature of the original layer during their flight through a distance equal to the mixing length, ℓ, and dissipate themselves into the second layer when they arrive there. Instinctively, it can be seen that this assumption is going to be far from true, at least for the case of molten metals. Because of their large thermal conductivity, the adiabatic flight of eddies will not be possible and significant leakage of heat can result during the eddy travel. For lack of information

because of the difficulty in obtaining measurements of $\overline{v'T'}$, the eddy diffusivities for heat and momentum are taken to be equal. For gases with Pr = 1 this may be true to some extent for large Reynolds numbers and low heat fluxes.

The turbulent component of heat flux, defined in a manner similar to momentum flux, is given by:

$$\dot{q}''_t = \rho\ C_p\ \overline{v'T'} = \rho\ C_p\ \varepsilon_h \frac{\partial T}{\partial y} \qquad (2.27)$$

The total heat flux is the sum of molecular and turbulent transport of heat and can be written as

$$\dot{q}'' = \dot{q}''_m + \dot{q}''_t = (k + \rho C_p\ \varepsilon_h) \frac{\partial T}{\partial y} = k\ (1 + \frac{Pr}{Pr_t} \frac{\varepsilon_m}{\nu}) \frac{\partial T}{\partial y} \qquad (2.28)$$

where the turbulent Prandtl number, Pr_t, is equal to the ratio of eddy diffusivities of momentum and heat transfer, $\varepsilon_m/\varepsilon_h$. For the concept of turbulent Prandtl number to be of any use, it is important that momentum eddy diffusivity be known with sufficient accuracy. This point is brought into focus by considering high Pr flows. Near the wall $\varepsilon_m/\nu \ll 1$ and any inaccuracy in ε_m will not affect the velocity profile very much while the turbulent heat flux will be greatly affected because it involves the product of Pr and ε_m/ν. Thus it is possible to prove that $Pr_t = 1$ while it is not, if there is an error in the value of the momentum eddy diffusivity. Deissler's [D6] results are a good example of this kind of trap because later investigators cast doubt on his value of ε_m and the fact that there is a discontinuity in ε_m expression at $y^+ = 26$. The invalidity of $Pr_t = 1$ becomes apparent in free convection studies

where the velocity profile shows a maxima while the temperature profile decreases monotonically. At the maxima, ε_m vanishes while ε_h is finite. Values of Pr_t as low as .18 have been found in such cases.

The turbulent Prandtl number based on the somewhat shaky concept of momentum eddy diffusivity and its mixing length representation becomes limited in its usefulness. However, for air flow in pipes its value is not far from unity. Seban and Shimazaki [S13] found for their measurements of air flow in a pipe, $Pr_t = .825$ for $90 < y^+ < 300$ and unity for $y^+ < 300$. Page et al. [P12] reported velocity and temperature measurements in a rectangular channel for $9000 < Re < 53000$. Consistent variation of Pr_t with Reynolds number and distance from the channel wall was observed. Pr_t increased towards the centre and also with increasing Reynolds number. It appears that the value might reach unity at the centre for high Reynolds numbers. The momentum eddy diffusivity, ε_m, certainly did not appear to reach zero at the centre as suggested by the assumption of universal velocity profile. Sleicher [S14] observed Pr_t behaviour similar to the observation of Page [P12] for fully developed flow of air in a pipe. Near the wall ($y^+ = 20$) a constant value of $Pr_t = 0.71$ appears to exist.

Experimental measurements of Pr_t for a developing thermal boundary layer on a flat plate were performed by Blom [B13]. Measurement of turbulent quantities $\overline{u'v'}$ and $\overline{v'T'}$ along with other mean quantities were obtained. For only $y^+ < 30$ a universal Pr_t profile was observed, with Pr_t increasing

with y^+. At $y^+ > 30$ the slope of the Pr_t vs. radial distance curve decreased with an increase in boundary layer thickness.

Developing thermal boundary layers for air flow in a pipe were studied by Abbrecht and Churchill [A3] and Johnk and Hanratty [J5]. For a fully developed entering velocity profile at Reynolds numbers of 15000 and 65000, Abbrecht and Churchill observed that the thermal eddy diffusivity profile is almost independent of the axial location. A plot of $(\frac{\varepsilon_h \rho C_p}{k} + 1)/(r/R_o)$ vs. y^+ gave a universal profile independent of Reynolds number and axial distance, for $(1-r/R_o) < 0.33$. A similar plot for momentum eddy diffusivity was obtained. The eddy diffusivity ratio $\varepsilon_h/\varepsilon_m = Pr_t^{-1}$ was found to increase rapidly near the wall and the scatter was attributed to errors in graphical evaluation of the gradients.

Johnk and Hanratty [J5] observed that ε_h is independent of axial distance only for $(1-r/R_o) < .15$. A fully developed ε_h profile was obtained after about 12 diameters. Near the centre of the pipe, ε_h values were found to be lower in the entry region as compared to fully developed region. It was claimed that inserting a measuring probe for measurement at various axial locations is likely to give more accurate results than the method of changing the length of heated section used by Abbrecht and Churchill. Deissler's assumption of fully developed temperature profiles in the thermal boundary layer was challenged. It was shown that near the wall at $y^+ < 30$, temperature profiles become fully developed within 3 diameters.

Beyond $y^+ = 30$ there is not a uniform temperature core as assumed by Deissler [D3]. There is a transition region between the wall region and the uniform temperature region. The region where the ε_h profile is fully developed, is thicker than the region of fully developed temperature profiles. This could be fortuitous because towards the centre, radial temperature gradients decrease and the point temperature becomes less sensitive to the value of ε_h.

Lawn [L3] tried to resolve the discrepancy between the lower experimentally observed heat transfer rates and the theoretical predictions of [D3, S11, M8, B12] in transitional Reynolds number by suggesting a break down of Reynolds analogy. At low Reynolds numbers the peak in the heat flux density profile near the wall, due to the competing effects of convective and diffusive heat transport [C6], in contrast to the linear shear stress profile indicates that the mechanisms of turbulent momentum and heat transport are not the same. Using Corcoran's [C7] measured velocity profiles and Ludwieg's recommendation [L12] (of $Pr_t = .9$ in the wall region and 0.7 in the fluid core) the energy equation was solved and some improvement in the agreement between the theory and the experiments was obtained. It was suggested that turbulent Prandtl number greater than unity is required for Reynolds number less than 10000 and $Pr_t = 0.8$ for higher Reynolds numbers. However, measurements of Corcoran [C7] for Re = 9190 show no indication of turbulent Prandtl number becoming greater than unity.

Azer and Chao [A2] modified the Prandtl mixing length theory by proposing that an eddy when travelling from one layer to another may exchange momentum and heat with the surrounding fluid. Thus an eddy generated at layer 1 with velocity u_1 and temperature t_1 acquires at the end of travel velocity u_1' and temperature t_1' and disintegrates into layer 2 having u_2 and t_2 as velocity and temperature. The turbulent Prandtl number should thus be written as

$$Pr_t = \frac{\varepsilon_m}{\varepsilon_h} = \frac{(u_2-u_1')(t_2-t_1)}{(u_2-u_1)(t_2-t_1')} \tag{2.29}$$

Assuming an eddy to be a rigid sphere and considering friction and heat transfer during its travel, two equations, one for moderate Pr and the other for low Pr can be written (Equations 29, 29a, 29b, 29c of [A2]). These equations have Re, Pr and distance from the wall as parameters and that is why they exhibit a variation of Pr_t similar to those observed by experimental observations [S14, P12, V3].

Quarmby and Quirk [Q1] measured radial and tangential eddy diffusivities for heat and mass in a fully developed turbulently flowing air in a pipe. The studies covered a Reynolds number range of 10000 to 160000 for heat and 6000 to 170000 for mass diffusivities. A ring source (of heat or mass) at the wall was used for radial diffusivities and a wall patch source for tangential diffusivities. Injection of nitrous oxide from the appropriate porous section allowed mass diffusion studies while electrical heating was used for heat diffusion. The heat eddy diffusivity, ε_h, was calculated by the integration

of the energy conservation equation. This was done by numerically calculating the radial temperature gradients from the observed temperature profile. The velocity profile was calculated by assuming linear shear stress distribution and the following expressions for momentum eddy diffusivity, ε_m:

For $0 < y^+ < y^+_\ell$

$$\varepsilon_m/\nu = n^2 u^+ y^+ [1 - \exp(-n^2 u^+ y^+)] \tag{2.30}$$

for $y^+_\ell < y^+ < y^+_i$

$$\varepsilon_m/\nu = \frac{k^2 (du^+/dy^+)^3}{(d^2u^+/dy^{+2})^2} \tag{2.31}$$

and for $y^+_i < y^+ < y^+_t$.

$$\varepsilon_m/\nu = R^+_o \sum_{j=0}^{4} b_j (r/R_o)^j \tag{2.32}$$

where $b_j = \sum_{i=0}^{4} a_{ij} (Re/10^5)^j$

and the coefficients a_{ij} are tabulated in [Q1]. The ratio of heat to momentum diffusivity could be correlated by a simple expression, independent of Reynolds number, viz.:

$$Pr_t = \varepsilon_m/\varepsilon_h = [1 + (400)^{(r/R_o - 1)}]^{-1} \tag{2.33}$$

A similar but much steeper curve was obtained for tangential diffusivity ratios with the wall value of the order of 10. This result suggests that radial and tangential eddy diffusivities

should not be assumed equal as has been done by previous workers. This method of eddy diffusivity measurement using a point source has the advantage that the flow field remains essentially isothermal and thus no change in velocity profile occurs. Consequently, the difficulties of measurement of velocity profile in a non-isothermal flow are circumvented.

Comparison of the Pr_t distribution obtained by various investigators shows that the experimental results of Sleicher [S14], Corcoran [C7] and Page [12], and the solid sphere eddy model of Azer and Chao [A2] indicate variation of Pr_t with radial position as well as Reynolds number. A value of $Pr_t = 0.66$ at the wall was indicated by Sleicher while towards the centre-line it varied from 0.77 to .87 depending upon Reynolds number. It appeared that at high Reynolds number ($> 10^5$) the turbulent Prandtl number may approach unity. Quarmby's measurements, however, indicate $Pr_t = 0.5$ at the wall and asymptotically approaches unity towards the centreline. Although a scatter of $\pm$ 15% was observed around the proposed equation, its lack of Reynolds number dependence was indicated by the wide range of Reynolds number (10^4 to 1.6×10^5) covered. It should, however, be recognised that the Pr_t values cannot be obtained with high accuracy as it involves the ratio of two eddy diffusivities, ε_m and ε_h, which are determined from the gradients of velocity and temperature profiles respectively. Large errors occur in the calculation of gradient from a set of discrete data.

Landis while discussing the paper by Sleicher [S14] remarked that $\varepsilon_h > \varepsilon_m$ could be explained by Jenkins' theory [J4].

According to this theory, the buffer layer in the flow can be alternately turbulent and laminar, and that turbulent friction occurs due to momentary dislocation of stream lines and vortex formation. But mixing length theories could not be applied to eddy diffusivities which are a function of both the spatial turbulence distribution and the nature of flow instability between laminar and turbulent regions. Thus ϵ_m and ϵ_h become nothing but operational values to satisfy the postulated differential equations. Moreover, since mixing length and eddy viscosity are only parameters in a theory and can only be estimated indirectly, their usefulness is limited to interpolation. Extrapolation to other flow geometries may introduce significant errors, for example, $Pr_t = .5$ for jet mixing and wakes. Similar kinds of objections were raised by Levy in the discussion of Sleicher's paper [S14] regarding the use of the fully developed eddy diffusivity values in the entrance region or for a fluid which has an internal heat source, in which case the temperature and velocity profiles are changing along the flow.

Thus very little is known about the turbulent Prandtl number and one has to be very careful in its application to the situation for which information in the literature is not available.

2.8 Structure of Wall Turbulence

To understand the behaviour of turbulent flow, it is very important to study the forces involved in maintaining it. The velocity of the fluid at any point can be resolved into its components in the direction of the coordinate axes.

Each velocity component is assumed to be the sum of two parts, (i) the mean velocity, $\bar{u}$ and (ii) the fluctuating velocity, u'. In systems of the kind under consideration, the fluctuating velocity component is small as compared to the mean velocity and its mean is zero. The kinetic energy of turbulence is the energy associated with these fluctuating components of the velocity vector. Shear in the flow causes the production of turbulent kinetic energy and this energy is dissipated by the presence of the wall and also where the velocity gradients are small. In addition, there is turbulent diffusion of kinetic energy towards the centre and diffusion of pressure energy towards the wall participating in the energy exchange process. Production and diffusion of pressure energy is balanced by its dissipation and the diffusion of kinetic energy (see Hinze [H4]). Laufer [L1] conducted extensive experiments to study these energy exchange processes in turbulent pipe flow. In the wall region at $y^+ = 12$ the production of turbulence energy is maximum. Most of it is dissipated on the spot but part is transferred to the wall and to the more wall-remote regions. Three divisions of the flow field have been suggested, (i) wall proximity region ($0 < y^+ < 30$) where turbulent energy production, diffusion and viscous action are equally important; (ii) central region ($r/R_o > .1$) with negligible production; the energy gain by diffusion is predominant and is equal to the dissipation; (iii) intermediate region ($y^+ > 30$ to $r/R < .1$) the rate of energy diffusion is much smaller than that of production or dissipation, i.e., energy produced is locally dissipated. It is in this

intermediate region, where mixing length theories, approximates somewhat to the observed behaviour of the structure of turbulence. Townsend [T3] and Hinze [H4] explained this energy transport by means of small and large eddies. Near the wall, small eddies with high intensity are produced. Some of them move towards the wall and get dissipated, these are called attached eddies; others, called detached eddies, diffuse by turbulence towards the inner regions of the pipe, thus transporting their kinetic energy. At the same time, however, they decay and dissipate their energy. The core region of the pipe contains large elongated eddies. These eddies have small ones superimposed on them. The large eddies are responsible for the transport and diffusion of small high energy eddies from the wall region to the centre. To take their place, low energy fluid lumps are transported towards the wall where they are broken into smaller high energy eddies by the shearing process.

Kline et al. [K1] did an extensive study of the transport of eddies, in channel flow of water, from wall region to the outer layer by the hydrogen bubble visualisation technique and by hot-wire anemometry. The laminar sublayer was observed to be in unsteady three-dimensional motion in contrast to the two-dimensional flow usually assumed. While the motion was dominated by viscosity, eddy effects were observed throughout the entire wall region. The mechanism of production of turbulent kinetic energy is the violent ejection of low speed fluid from very near the wall to the outer regions. This was studied with motion pictures and using dye injection at the solid

boundary. The dye streak pattern appeared to be moving downstream as a whole with slow drift outward. At $y^+ \approx 8$ to 12, it began to oscillate. These oscillations were amplified with outward motion and terminated as an abrupt breakup in the region $10 < y^+ < 30$. After breakup the streak became contorted and stretched and a portion of it migrated to the outer layers. This whole process was randomly intermittant. The violent bursting process plays the dominant role in turbulence energy production. The study with favourable pressure gradient in the flow (i.e., accelerated flow) showed a reduced bursting rate and ultimate relaminarisation. But with an adverse pressure gradient (i.e., decelerating flow) the bursting became more violent and frequent. This observation is very important to the present study because the interaction of opposing free and forced convection is a phenomenon very similar to the adverse pressure gradient flows, as both lead to flow separation at the wall if the conditions are severe enough.

A study by Grass [G5] of the structural features of turbulent flow gave a similar picture of turbulence structure. With the ejection of eddies from the wall region and the inrush of fluid lumps towards the wall to fill the void, there was associated oscillations of the longitudinal velocity profile about some mean. Ejection decreased the fluid velocity near the wall while inrush increased it. The calculation of these instantaneous velocity profiles from flow visualisation studies via the hydrogen bubble technique confirmed the proposed mechanism of transport.

2.9 Conclusions

The present problem of opposing free and forced convection interaction involves varied heat transfer phenomena like entry region effects, physical property variation ~~and~~ the consequent relaminarisation due to high heating rates and the breakdown of equality between the turbulent momentum and heat diffusivities. In the entrance region the heat transfer rates decrease with the axial distance as the driving force decreases and asymptotically approach the fully developed conditions. With high wall heat fluxes the increased viscosity of the flow medium (air) dampens the turbulent eddies near the wall and thus causes premature laminarisation. The assumption that the turbulent transport mechanism of heat and mass transfer are similar has been found to be incorrect especially at low Reynolds numbers. The presence of the buoyancy term in opposing direction to the forced flow has been found to increase heat transfer rates and create flow reversal when it becomes of larger magnitude than the inertia force due to the forced flow. Owing to such a large number of interacting heat transfer phenomena, the present problem requires a very rigorous analytical treatment and an extensive experimental study.

CHAPTER 3

THEORETICAL ANALYSIS

3.1 Introduction

In this chapter, the fundamental equations governing the transport of heat and momentum in a fluid flowing in a cylindrical conduit will be developed from elemental volume considerations. The formulated partial differential equations with appropriate boundary conditions will be approximated by finite-difference approximation methods to sets of algebraic equations which can be solved by standard techniques of matrix inversion. The conservation equations of mass, momentum and energy are highly non-linear and coupled to each other. The finite-difference approximation has the advantage of locally linearising and uncoupling the partial differential equations. The penalty for this simplification is that an iterative solution is required. A computer program has been written in Fortran IV for the numerical solution, on CDC 6400 digital computer of the algebraic equations resulting from this finite difference approximation; the details are indicated in Appendices D and Z. The output is in the form of temperatures and velocities at the chosen mesh points, and the local Nusselt number and/or heat flux at the wall. The test of the solution technique and computer programming has been done by comparing the results of this numerical solution with known solutions from the literature.

3.2 Conservation of Property

A two-dimensional flow field shown in Figure 3.1 is considered. x is the axial distance in the direction of the flow from the start of the test section and r is the radial distance from the centreline. u and v are the axial and radial components respectively of the velocity in the flow field. The velocities are taken positive along the positive directions of the axes. The conservation of mass, momentum and energy is considered over an elemental ring volume of thickness δr and length δx.

3.2.1 Assumptions

1. Two-dimensional steady-state flow prevails, that is, the mean velocity and temperature distributions are functions of only space co-ordinates and are independent of time. Negative axial velocities are absent.
2. The flow is axi-symmetric and the magnitude of the radial pressure gradient is very small so that only the axial momentum conservation equation needs to be considered.
3. Time averaged values of the fluctuating components of axial and radial velocity components and of temperature are zero so that the conservation equations are fully described by the time averaged values of the velocities and the temperatures.
4. Axial diffusions of momentum and energy can be neglected in comparison with radial diffusions, that is, a thin boundary layer is assumed.

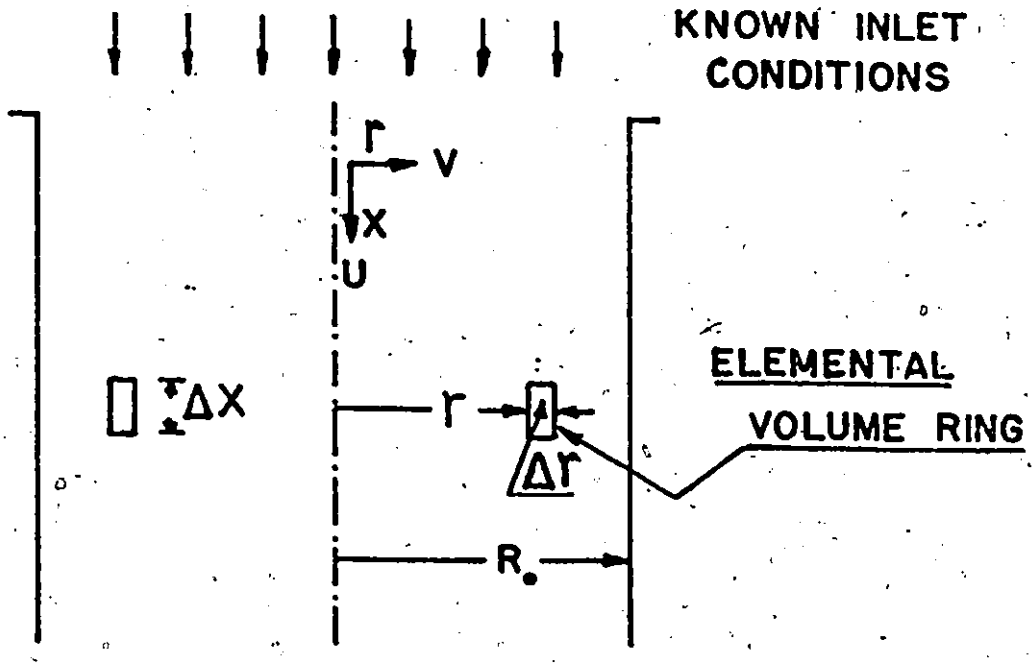

Figure 3-1. Representation of the Flow Field.

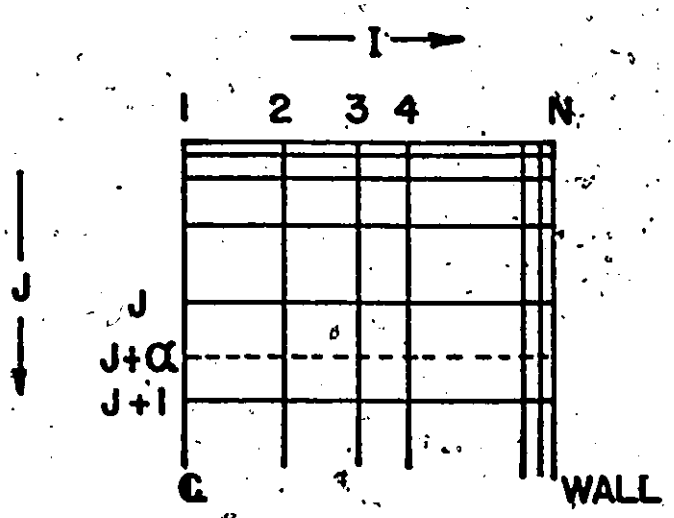

Figure 3-2. Non-uniform Step Size Mesh in the Flow Field.

5. Viscous dissipation is negligible and the flow is incompressible.

6. Effective momentum and thermal diffusivities are sums of molecular and turbulent diffusivities, that is, the molecular and turbulent transport processes are additive.

7. Equilibrium between the generation, dissipation, advection and diffusion of turbulent kinetic energy is assumed such that flow similarity conditions prevail and the turbulent eddy diffusivity is a function of radial position only.

8. Eddy diffusivity is given by the empirical equations available in the literature for isothermal turbulent flow.

9. The flow field does not contain any heat source, such as that arising from viscous dissipation, and the transfer is only through convection and diffusion.

3.2.2 Conservation Equations

Considering mass balance over the elemental fluid volume $2\pi r\ \delta r\ \delta x$ and taking limits as the intervals δx and δr approach zero, the resulting continuity equation can be written as

$$\frac{\partial}{\partial x}(\rho u) + \frac{1}{r}\frac{\partial}{\partial r}(\rho v r) = 0 \qquad (3.1)$$

The balance of forces, acting on the elemental volume, arising from the convective and diffusive transport of momentum, the normal pressure force and the body force

yields the momentum conservation equation

$$\rho u \frac{\partial u}{\partial x} + \rho v \frac{\partial u}{\partial r} = - g_c \frac{dp}{dx} - \frac{g_c}{r} \frac{\partial}{\partial r} (r \tau_{rx}) + g(\rho - \rho_a) \qquad (3.2)$$

The two terms on the left hand side of Equation (3.2) are the axial and radial convective transport of the axial component of the momentum. The first term on the right hand side is the normal pressure gradient in the axial direction; the second represents momentum transport by diffusion; and the third is the body force due to the gravitational acceleration of the mass of the fluid.

The shear stress, τ_{rx}, whose radial gradient represents transport of momentum by diffusion, can be represented by a sum of molecular and turbulent shear stress.

$$\tau_{rx} = \tau_m + \tau_t$$

The turbulent shear stress, $g_c \tau_t = \rho \overline{u'v'}$, can be assumed to be represented by a velocity gradient with a suitable coefficient known as the eddy viscosity, $(\varepsilon_m \rho)$.

$$g_c \tau_{rx} = - \mu \frac{\partial u}{\partial r} - (\varepsilon_m \rho) \frac{\partial u}{\partial r} = - (\mu + \varepsilon_m \rho) \frac{\partial u}{\partial r} \qquad (3.3)$$

Since the system is open (i.e., exhausted to the atmosphere), the magnitude of the body force term is proportional to the density difference between the fluid in the flow field and the ambient fluid. The reason for the choice of ambient density can be appreciated by considering the 'chimney effect' that will occur if the flow in the system is suddenly shut off.

Substituting Equation (3.3) in (3.2)

$$\rho u \frac{\partial u}{\partial x} + \rho v \frac{\partial u}{\partial r} = - g_c \frac{dp}{dx} + \frac{1}{r} \frac{\partial}{\partial r} (r(\mu+\epsilon_m\rho) \frac{\partial u}{\partial r}) + g(\rho-\rho_a) \qquad (3.4)$$

Considering the conservation of energy by mean of convective and diffusive transport over the elemental volume, the energy conservation equation can be written as

$$\rho u \frac{\partial T}{\partial x} + \rho v \frac{\partial T}{\partial r} = - \frac{1}{r} \frac{\partial}{\partial r} (r \dot{q}''/C_p) \qquad (3.5)$$

The two terms on the left hand side of Equation (3.4) are the axial and radial convective transport of energy and the term on the right hand side is the diffusive transport. The heat flux density, $\dot{q}''$ (BTU/ft^2-sec) can be considered as the sum of molecular and turbulent diffusive heat transport, viz:

$$\dot{q}'' = \dot{q}''_m + \dot{q}''_t = -k \frac{\partial T}{\partial r} + \rho C_p \overline{v'T'}$$

The turbulent diffusive heat flux density can be represented by the product of the radial temperature gradient and the thermal eddy conductivity:

$$\dot{q}''_t = \rho C_p \overline{v'T'} = - \rho C_p \epsilon_h \frac{\partial T}{\partial r}$$

$$\dot{q}''/C_p = - \frac{k}{C_p} \frac{\partial T}{\partial r} - \rho \epsilon_h \frac{\partial T}{\partial r} = - (\frac{k}{C_p} + \epsilon_h\rho) \frac{\partial T}{\partial r} \qquad (3.6)$$

Substituting Equation (3.6) into (3.5)

$$\rho u \frac{\partial T}{\partial x} + \rho v \frac{\partial T}{\partial r} = \frac{1}{r} \frac{\partial}{\partial r} (r(\frac{k}{C_p} + \epsilon_h\rho) \frac{\partial T}{\partial t}) \qquad (3.7)$$

The wall of the test section is assumed impermeable so that the total mass flow at any cross-section in the pipe remains the same. This condition yields the integral mass conservation equation.

$$2\pi \int_{o}^{R_o} \rho u \; r \, dr = \text{Total mass flow rate} \tag{3.8}$$

Assuming the flow medium obeys the perfect gas law, the equation of state is

$$PM = \rho \; RT \tag{3.9}$$

where R is gas constant ft-$lb_f/(lb_m\text{-}^oF)$ and M is the molecular weight

Introducing the non-dimensionalising variables

$$X = x/R_o \qquad R = r/R_o \qquad RO = \rho/\rho_o$$

$$U = u/\bar{u}_o \qquad V = v/\bar{u}_o \qquad P = \frac{p\,gc}{\rho_o \bar{u}_o^2}$$

$$Re_o = \frac{R_o\,\bar{u}_o\,\rho_o}{\mu_o} \qquad \theta = \frac{T-T_o}{T_w-T_o} \tag{3.10}$$

$$Gm = (\mu+\varepsilon_m\rho)/\mu_o \qquad Gh = ((k/C_p) + \varepsilon_h\rho)/\mu_o$$

where R_o is the radius of the pipe and the subscript o indicates inlet conditions.

Substituting Equations (3.10) in Equations (3.1), (3.4), (3.7) and (3.8), dimensionless forms of continuity and momentum, energy and integral mass conservation equations

(3.11 to 3.14) are obtained.

$$\frac{\partial}{\partial X}((RO)U) + \frac{1}{R}\frac{\partial}{\partial R}((RO)RV) = 0 \tag{3.11}$$

$$(RO)U\frac{\partial U}{\partial X} + (RO)V\frac{\partial U}{\partial R} = -\frac{dP}{dX} + \frac{1}{Re_o}\frac{1}{R}\frac{\partial}{\partial R}\left(R\,Gm\frac{\partial U}{\partial R}\right) + \frac{R_o g}{\rho_o u_o^2}(\rho-\rho_a) \tag{3.12}$$

$$(RO)U\frac{\partial \theta}{\partial X} + (RO)V\frac{\partial \theta}{\partial R} = \frac{1}{Re_o}\frac{1}{R}\frac{\partial}{\partial R}\left(R\,Gh\frac{\partial \theta}{\partial R}\right) \tag{3.13}$$

$$\int_0^1 (RO)\,U\,R\,dR = 1/2 \tag{3.14}$$

3.2.3 Boundary Conditions

The following boundary conditions are imposed on the system.

1.	Fully developed (or known) inlet velocity profile	$U(O,R) = U(R)$	
2.	Uniform inlet temperature profile	$\theta(O,R) = 0$	(3.15)
3.	Uniform (or known) wall temperature distribution	$\theta(X,1) = 1$	
4.	No slip, suction or blowing at the wall	$U(X,1) = V(x,1) = 0$	
5.	Axi-symmetric velocity profile	$\left.\frac{\partial U}{\partial R}\right\|_{R=0} = 0$	
6.	Axi-symmetric temperature profile	$\left.\frac{\partial \theta}{\partial R}\right\|_{R=0} = 0$	

The diffusive transport of momentum term in Equation (3.12) can be written as

$$\frac{1}{R}\frac{\partial}{\partial R}\left(R\, Gm \frac{\partial U}{\partial R}\right) = Gm \frac{\partial^2 U}{\partial R^2} + \frac{Gm}{R}\frac{\partial U}{\partial R} + \frac{\partial Gm}{\partial R}\frac{\partial U}{\partial R}$$

At the centreline $R = 0$, $\frac{\partial U}{\partial R} = 0$ $\therefore$ $\frac{\partial U/\partial R}{R}$ = indeterminate.

Using L'Hopital's rule

$$\left.\frac{\partial U/\partial R}{R}\right|_{R=0} = \frac{\partial/\partial R(\partial U/\partial R)}{\partial/\partial R(R)} = \frac{\partial^2 U}{\partial R^2}$$

Therefore the diffusive transport of momentum term at the centreline takes the form

$$\left.\frac{1}{R}\frac{\partial}{\partial R}\left(R\, Gm \frac{\partial U}{\partial R}\right)\right|_{R=0} = 2\, Gm \frac{\partial^2 U}{\partial R^2} \qquad (3.16)$$

Similarly the diffusive transport of heat term at the centreline can be written as

$$\left.\frac{1}{R}\frac{\partial}{\partial R}\left(R\, Gh \frac{\partial \theta}{\partial R}\right)\right|_{R=0} = 2\, Gh \frac{\partial^2 \theta}{\partial R^2} \qquad (3.17)$$

Thus the partial differential equation representing the continuity, and momentum, energy and integral mass conservation equations in the dimensionless form (Equations 3.11 to 3.14) along with the boundary conditions (Equations 3.15 to 3.17), can be solved numerically. The solution will give the radial velocity and temperature profiles as functions of axial location.

The numerical solution in contrast to the analytical solution gives discrete values of the dependent variable in terms of the independent variables. The capability of the numerical solution to solve complex problems for which analytical solutions either do not exist or are very difficult, offsets its disadvantages, viz: high computing cost, various kinds of errors, instability and non-convergence problems and the necessity of numerical differentiation to obtain derivatives of the calculated profiles.

3.3 Numerical Solution

3.3.1 Selection of the Method

A good review of the solution of turbulent boundary layers is given by Spalding [S20]. He rejected the explicit integral method of solution involving converting the partial differential equations to ordinary differential equations by defining integral quantities like momentum thickness, enthalpy deficit thickness. The basis of rejection was the wide variety of empirical information for different flow situations that must be provided. This information is not normally available and has to be obtained experimentally. For the present case of free and forced convection interaction where data on turbulent flow is non-existent, it has been considered preferable not to use the explicit integral method in spite of the ease of solution of ordinary differential equations as compared to partial differential equations.

On the other hand, the various hypotheses of eddy diffusivity, which although requiring empirical constants, have a far greater generality. The methods using eddy diffusivity concept are the parametric integral method, the cross-stream integration and the finite-difference method. The parametric integral method is approximate as the dependent variables, velocity and temperature, are assumed to be functions (e.g., polynomials) of the independent variables. The coefficients of the polynomial are evaluated by substituting them in the conservation equations. The accuracy of the solution depends upon how well the polynomials describe the dependent variable profiles. Although it can be increased by increasing the degree of the polynomials, high computing costs result. In the cross-stream integration procedure, the flow field is assumed to be represented by a series of ordinary differential equations valid over a succession of small regions. Since the boundary conditions for each of these equations are determined by the equations for the surrounding region, an iterative integration procedure is required. Consequently this method also suffers from the disadvantage of high computing cost.

In the finite-difference method, the partial differential equations are converted into a set of algebraic equations by approximating the partial differentials by finite-differences. The flow field is divided into a grid and its properties are calculated at the grid nodes by solving the set of algebraic equations using matrix inversion. This method has become the

most acceptable one for its generality and low cost especially when a changing grid size has been introduced to increase accuracy and decrease the computing time.

3.3.2 Finite-Difference Formulation

The conservation equations of momentum and energy are parabolic partial differential equations and hence a marching type of solution can be effected. This situation results when the axial diffusion term is neglected, since with it the partial differential equations are elliptic and then the whole flow field has to be solved simultaneously. In the marching solution (in the axial direction for this case) predictions for the next state can be made entirely from the knowledge of the present state, and for the next cycle the predicted state forms the present one. Thus the solution moves in steps and hence the name marching solution.

The differentials in the conservation equations can be approximated to finite-differences through Taylor series expansion. If a function $\phi(h)$ is known at $h = h_o$, its value at $h = h_o + \Delta h$ can be written in terms of various orders of derivatives of ϕ with respect to h at $h = h_o$. Taylor series, being an infinite series has to be limited to a convenient number of terms for practical purposes. The error thus introduced is called truncation error and is a function of step size Δh. It can be decreased by making Δh infinitesimally small. Expanding $\phi(h)$ at more than one of the neighbourhood points about h_o, e.g., $h_o + \Delta h$, $h_o - \Delta h$, it is possible to approximate the first and second order differentials in terms of values

of the function ϕ at h_o, $h_o + \Delta h$, $h_o - \Delta h$. The details of these formulations are given in Appendix D. The truncation error of the series can be reduced if more neighbourhood points, e.g., $h_o + 2\Delta h$, $h_o - 2\Delta h$ are used. This will, however, increase the complexity of the algebraic equations to be solved at the later stage.

3.3.3 Variable Step Size

For the present case of a developing thermal boundary layer, the gradients near the wall and at the start of the heating section are likely to be very large. Under such conditions, in order that finite differencing may approximate the differential to a reasonable accuracy, it is important that the grid size be small. This implies that for a uniform mesh over the flow field, calculations will have to be done at a very large number of nodes, thus resulting in a large computer memory and time requirement. To circumvent this problem, the grid size may be allowed to vary over the flow field. That is, a finer mesh may be used where the gradients are large while a coarse mesh may be used where gradients are not so large. A slightly different version of the function used by Pollock [P1], to define grid spacing has been adopted for the present problem.

$$\Delta_k = \frac{H^k - 1}{\sum_{k=1}^{N-1} (H^k - 1)} \qquad k = 1,2,3\ldots N-1 \qquad (3.18)$$

where N is the number of nodes along any of the axes and H is a constant greater than 1.

Let i represent the location of a node in the radial direction and j in the axial direction. At the centreline

$i=1 \quad R_i = 0$

For $i \geq 2 \quad R_i = R_{i-1} + \Delta_{N-i+1}$ (3.19)

This will ensure a very small step size near the wall which will progressively increase towards the centre.

For the axial direction, at the start of the heating section

$j = 1, \; X_j = 0$

For $j \geq 2, \; X_j = X_{j-1} + L \cdot \Delta_j$ (3.20)

where L is the maximum number of radii to be travelled in the axial direction. Δ_j is given by Equation (3.18) where j varies from 1 to NN-1, NN being the number of axial step sizes over L radii. The step size is small for the entrance region and becomes progressively large with axial distance. This formulation is especially useful when calculations are to be done for large axial distances, e.g., to obtain fully developed flow. For a fixed number of axial steps, large distances can be covered while maintaining reasonably fine step size at the entrance. Equation (3.18) has a great flexibility in step size variation by various combinations of the judicious choices of H and N or NN.

For the present case 50 nodes in the radial direction, N=50, and 100 in the axial direction, NN = 100, were chosen. Increasing the number of axial nodes increases the number of

steps to be calculated for a given length. But increasing the number of radial nodes increases the size of the matrix to be inverted with every calculation. An increase in the size of the matrix increases the computing time per matrix inversion at a rapid rate. Thus a compromise between the accuracy and the computing time involved has to be reached.

The value of H for use in Equation (3.18) has been chosen to be 1.05 for both radial and axial directions. The value of H determines the fineness of the mesh at low subscript values of Δ. The fineness of the mesh increases with the value of H. Since for a fixed N, the increase in the fineness of the mesh near the wall is accompanied by the increased coarseness near the centre, the value of H can not be increased without bound lest the finite-difference approximation of the differentials at the centre may become a large source of truncation error. Similar comments can be made for axial direction.

Small adjustments in the axial step size at strategic locations were required so that the predictions are made at exactly the same axial location at which the experiments are planned.

Figure 3.2 shows the variable step-size grid in the flow field. If ϕ represents the axial velocity or temperature in the flow field then its derivatives can be written as

$$\left.\frac{\partial \phi_i}{\partial X}\right|_j = \frac{\phi_{i,j+1} - \phi_{i,j}}{\partial x} + \underline{0}\ (\Delta x) \qquad (3.21)$$

The radial gradients can be represented as

$$\left.\frac{\partial\phi_i}{\partial r}\right|_j = \frac{1}{h_1+h_2}\left[\frac{h_2}{h_1}\phi_{i+1,j} - \frac{h_2}{h_1}\phi_{i-1,j} + \frac{h_1^2-h_2^2}{h_1h_2}\phi_{i,j}\right]+\underline{0}(\Delta X^2)+\underline{0}(h^2) \tag{3.22}$$

$$\left.\frac{\partial 2\phi_i}{\partial r^2}\right|_j = \frac{2\phi_{i+1,j}}{h_1(h_1+h_2)} - \frac{2\phi_{i,j}}{h_1h_2} + \frac{2\phi_{i-1,j}}{h_2(h_1+h_2)} + \underline{0}(\Delta X^2)+\underline{0}(h^2) \tag{3.23}$$

where h_1 and h_2 are the two consecutive step sizes in the neighbourhood of ϕ_i. A weighting factor $0 \leq \alpha \leq 1$ is chosen so that the radial gradients can be represented as the weighted average of the present axial location j and the location to be predicted j+1.

$$\therefore \quad \left.\frac{\partial\phi_i}{\partial r}\right|_{j+\alpha} = \alpha\frac{\partial\phi_{i,j+1}}{\partial r} + (1-\alpha)\frac{\partial\phi_{i,j}}{\partial r} \tag{3.24}$$

$$\left.\frac{\partial 2\phi_i}{\partial r}\right|_{j+\alpha} = \alpha\frac{\partial 2\phi_{i,j+1}}{\partial r^2} + (1-\alpha)\frac{\partial 2\phi_{i,j}}{\partial r^2} \tag{3.25}$$

In Appendix D, the details of transformation of partial differential Equations (3.11) to (3.14) into the algebraic equations by means of finite-difference approximation are given.

3.3.4 Solution Scheme

The continuity, integral mass conservation and the momentum conservation equations are coupled to each other through axial and radial velocity terms and these in turn are coupled to the energy equation through the density term. Moreover, these equations are highly non-linear. Finite-difference

methods have the capability of handling non-linear coupled equations by linearising and locally uncoupling them. The penalty for this is that iterations at each step are required.

In an iterative solution, uncoupling of the equations can be done by assuming the coupling parameters as an initial guess, or using the presently known value from a previous calculation step or some estimate from it. For the first iteration, at the first axial step, an initial guess is provided

$$U_{i,j+1} = U_{i,j},\ V_{i,j+\alpha} = 0,\ RO_{i,j+1} = RO_{i,j},\ \left.\frac{dP}{dX}\right|_{j+\alpha} = \text{friction factor}$$

where $X = X \equiv j$ $\quad X = X + \Delta X \equiv j+1$ and $X = X + \alpha\Delta X \equiv j+\alpha$

For the first iterations at any axial step, the estimates at j+1 are obtained from the gradients of temperature and velocity calculated in the previous step, at j.

$$U_{i,j+1} = U_{i,j} + \left.\frac{\Delta U}{\Delta X}\right|_j \Delta X;\ U_{i,j+\alpha} = U_{i,j} + \left.\frac{\Delta U}{\Delta X}\right|_j \Delta X.\alpha$$

$$V_{i,j+\alpha} = V_{i,j-\beta} \text{ (from previous step)},\ (dP/dX)_{j+\alpha} = (dP/dX)_{j-\beta} \qquad (3.2$$

$$RO_{i,j+1} = RO_{i,j} + \left.\frac{\Delta RO}{\Delta X}\right|_j \Delta X;\quad RO_{i,j+\alpha} = RO_{i,j} + \left.\frac{\Delta RO}{\Delta X}\right|_j \Delta X\ \alpha$$

For any other iterations, estimates from a previous iteration are used. The steps for each iteration cycle are as follows:

1. The new estimates of $\theta_{i,j+1}$ and $RO_{i,j+1}$ are provided by the solution of the energy Equation (3.13).

2. Substitute the algebraic expression for $U_{i,j+1}$ from the finite-difference version of momentum Equation (3.12) in the integral mass conservation Equation (3.14) and integrate to obtain $(dP/dX)_{j+\alpha}$. This step is not done for the first iteration.
3. Solve the continuity Equation (3.11) to obtain $V_{i,j+\alpha}$ from the estimates of $U_{i,j+1}$ and $RO_{i,j+\alpha}$.
4. Solve the momentum conservation Equation (3.12) for $U_{i,j+1}$ from the estimates of $V_{i,j+\alpha}$, $RO_{i,j+1}$, $(dP/dX)_{j+\alpha}$.
5. Solve the continuity Equation (3.11) to obtain new estimates of $V_{i,j+\alpha}$.
6. Check if $T_{i,j+1}$ and $U_{i,j+1}$ for two consecutive iterations have differences less than a preset tolerance (.01%). If yes, return to step (1) to start the calculations for the next axial location by transferring the j+1 th values to j th location. If the tolerance is not met return to step (1) for the next iteration.

The maximum number of iterations was set at 100 so that unnecessary computer time is not wasted if convergence is not likely.

The solution of the set of algebraic equations obtained from the finite-difference approximation of the momentum and energy conservation equations can be done by matrix inversion. Tridiagonal matrices were obtained for each of the two conservation equations and were solved by a standard library subroutine. The integration of Equation (3.14) was carried out by the trapezoidal rule. The variable step size allowed high accuracy of the trapezoidal rule and the results were as

good as those obtained by using Gaussian Quadrature. Radial integrations were also carried out to check the total mass flow at any cross-section and to obtain the bulk (mixed mean) temperature and the average axial velocity. Shear stress profiles were calculated by integrating the finite-difference version of Equation (3.2).

Linearisation of the axial convective terms in the momentum and energy equations was found to be necessary. The evaluation of their coefficient (RO)U for use in this finite difference representation should be at j+1 th location. But instabilities resulted from its use. Evaluation at j+α th location did alleviate the problem to some extent but not entirely. Consequently the coefficients were evaluated as $(RO)_{i,j}\ U_{i,j}$. This kind of instability mostly resulted when the starting velocity profile was flat. However, when the instability did not occur it was found that nearly identical (within 0.1%) results were obtained for all the three evaluations of the term (RO)U.

3.3.5 Stability and Convergence

For $\alpha = 0$ in Equations (3.2) and (3.25), the finite difference scheme is explicit, that is no knowledge of ϕ at the j+1 location is needed. However, in the explicit solution scheme there is a limit on the axial step size and consequently a large number of axial steps have to be calculated for a given axial distance. To economise on this, an implicit method, $\alpha > 0$, which is much stabler and allows a larger axial step size is used. For linear parabolic partial differential equations,

it has been found that this two-level scheme is unconditionally stable for $\alpha \geq 0.5$. It can be shown that for the Crank-Nicholson method ($\alpha = 0.5$) the order of magnitude for all the approximations of differentials is $\underline{0}(\Delta X^2) + \underline{0}(h^2)$, while for $\alpha \neq .5$ the order of magnitude of errors is $\underline{0}(\Delta X) + \underline{0}(h^2)$. It has been found by Worsoe-Schmidt and Leppert [W5] and others that the Crank-Nicholson method is not stable for non-linear equations, at least of the Navier-Stokes' type. This instability has also been observed in the present investigation. The cause of the instability is considered to be the alternate propogation of errors by the momentum and continuity equations and that the amplification of errors occurs through the solution of the latter. Considerations of the stability requirement and the requirement of small truncation error of α to be close to 0.5 has led to a compromise value of $\alpha = 0.75$.

In the solution of partial differential equations three types of solutions should be considered:

i) Exact solution of the partial differential equations

ii) Exact solution of the partial difference equations obtained by approximating differentials by finite-differences.

iii) Numerical solution of the difference equations.

The difference between (i) and (ii) is the truncation error caused by termination of the Taylor series expansion after a certain number of terms. The difference between (ii) and (iii) is called round-off error caused by the computer which carries results only up to a certain number of significant digits. This round-off error is perpetuated from one step to

another. It is interesting to note that the effect of step size is different for the two kinds of errors. Decreasing the step size decreases the truncation error as it is a function of some power (>1) of the step size. On the other hand, a decrease in step size means a large number of steps to be calculated and consequently the round-off error increases. Thus a compromise between the two has to be made in the selection of the step size.

If the numerical solution approaches the exact solution of the difference equations then it is stable, and if it also approaches the exact solution of partial differential equations then it is convergent. It is obvious from these definitions that the stability does not necessarily imply convergence. Restrictive conditions have been given for convergence of linear parabolic partial differential equations by Lax and Richtmeyer [L9] and Barakat and Clark [B15]. But it is difficult to give such conditions for non-linear equations.

The stability of the solution can be increased by suitably weighting the results of two consecutive iterations. Let $\phi^{n}_{i,j+1}$ and $\phi^{n+1}_{i,j+1}$ represent the predictions of velocity or the temperature at the axial location j+1 after n th and n+1 th iteration. A weighting factor $0 \leq \gamma \leq 1$ is introduced such that the n+1 th prediction is modified.

$$\phi^{n+1}_{i,j+1} = \gamma\phi^{n+1}_{i,j+1} + (1-\gamma)\,\phi^{n}_{i,j+1} \tag{3.27}$$

Thus γ acts as a damping factor if the errors tend to be amplified

with each successive iteration. The optimum value of γ for the present case has been found to be 0.75. If there is no danger of instability, $\gamma > 1$ can be used to accelerate the convergence.

3.4 Empirical Equations

3.4.1 Physical Properties

The physical properties of air such as density, viscosity, thermal conductivity and heat capacity are required during the solution of the flow field. Instead of assuming density as inversely proportional to the absolute temperature and the latter three as proportional to a certain fractional power of the temperature, higher accuracy is obtained by the use of tabulated values from National Bureau of Standards circular 564. These tabulated values have been expressed as polynomial functions of temperature using a linear least square analysis by Pollock [P1]. These polynomials and the values of their coefficients are listed in Appendix A. In the numerical solution program these polynomials are used as arithmetic function statements.

3.4.2 Eddy Viscosity

The contribution of the turbulence to the transport of momentum has been expressed as the product of a suitable coefficient (eddy viscosity) and the velocity gradient. Prandtl's mixing length concept, which describes the eddy viscosity as a property of the flow field, has been widely

accepted. It is assumed that the flow field behaves as fully developed flow implying local equilibrium between the production, dissipation, convection and diffusion of turbulent kinetic energy. Consequently, the eddy viscosity is not a function of axial direction but only of the dimensionless radial distance. According to Prandtl's mixing length hypothesis, fluid particles coalesce into lumps and these lumps move bodily from one place to another in the flow field without losing their identity for a certain length ℓ. After the travel of length ℓ, the lumps completely lose their identity and mix with the local fluid, thus causing a transfer of momentum by bulk motion. Prandtl correlated the turbulent shear stress and eddy viscosity with the mixing length assuming the the mixing length is proportional to the distance from the wall.

$$\tau_t \, g_c = \overline{\rho u' v'} = \rho \epsilon_m \frac{du}{dy} = \rho \ell^2 \left|\frac{du}{dy}\right| \frac{du}{dy} = \rho k^2 y^2 \left|\frac{du}{dy}\right| \frac{du}{dy}$$

Since it is assumed that at the wall there are no eddies, Van Driest [V1] argued that near the pipe wall, the presence of a solid surface has a damping effect on the turbulent eddies. He showed that the damping effect of the pipe wall can be given by an exponential decay of the mixing length and so modified the mixing length to give

$$\ell = ky \, [1-\exp(-y/A)] \tag{3.28}$$

where k and A are constants.

The validity of the modified mixing length was given to be $y^+ = 60$ beyond which eddy viscosity was calculated from the definition on the assumption that the velocity distribution is given by universal velocity profile. Thus the eddy diffusivity expression takes the form

$$\frac{\varepsilon_m}{\nu} = \rho k^2 y^{+2} \left[1-\exp(-y^+/A^+)\right]^2 \left|\frac{du^+}{dy^+}\right| \quad 0 < y^+ < 60 \tag{3.29}$$

$$= k\, y^+ [1-y^+/R_o^+] - 1 \qquad 60 < y^+ < y_\ell^+ \tag{3.30}$$

The constants k and A^+ have found to be 0.4 and 26, respectively, from experimental measurements under isothermal conditions.

Among the host of eddy viscosity empirical equations that are available, (see for example McEligot [M13]) the one given by Reichardt and modified by Travis [T1] has been shown to represent Laufer's [L1] data of isothermal velocity distribution better than Van Driest's expression. At the centre of the pipe, a non-zero eddy viscosity is given by the modified Reichardt's expression which is more realistic than the zero value predicted by the universal velocity profile. A detailed discussion of this will be presented later in this chapter. The modified Reichardt expression is given by:

$$\frac{\varepsilon_m}{\nu} = k[y^+ - A \tanh (y^+/A)] \qquad 0 < y^+ < y_\ell^+ \tag{3.31}$$

$$= \frac{k}{6} \frac{R_o u^*}{\nu} [1-(FR)^2][\tfrac{2}{3} + 2(FR)^2] \qquad y_\ell^+ < y^+ < y_\ell^+ \tag{3.32}$$

The constants k, F, y_ℓ^+, A are given as functions of Reynolds number in the form

$$\phi = \sum_{j=0}^{3} a_j \, (\log Re - \alpha)^j \tag{3.33}$$

The values of a_j and α for all the constants are tabulated in [T1].

The constants in the eddy diffusivity expression have been obtained from measurements of isothermal flows. Application of these expressions to the non-isothermal flow situation raises the question at what temperature the physical properties should be evaluated. The logical choices are the temperature of (i) bulk of fluid (mixed mean), (ii) at the wall (iii) some average of wall and bulk, (iv) local temperatures in the flow field. The last choice seems the most logical one and is recommended by McEligot [M13]. It is therefore used here.

The value of shear stress at the wall is also required in the eddy diffusivity expression. Wall shear stress, for fully developed flow, is related to the pressure drop by a force balance and the friction factor through Fannings equation, viz:

$$\pi D \tau_w = \frac{\pi}{4} D^2 \frac{\Delta P}{\Delta L} = \frac{2 f \bar{\rho} \bar{u}^2}{D g_c} \cdot \frac{\pi D^2}{4}$$

The bulk density, the average velocity and an expression for the friction factor, f, have been used to evaluate τ_w. For non-isothermal flows, Taylor [T2] recommended the following friction factor correlation.

For $Re_w > 3000$

$$f = \left(.0014 + \frac{.125}{Re_w^{.32}}\right) \left(\frac{T_b}{T_w}\right)^{.5} \tag{3.34}$$

For $Re_w < 3000$

$$f = 16/Re_w \tag{3.35}$$

where $Re_w = \frac{GD}{\mu_w} \frac{T_b}{T_w}$, T_b and T_w are bulk and wall temperatures respectively.

3.4.3 Eddy Conductivity

Eddy conductivity is normally given as proportional to eddy viscosity and the proportionality factor is termed the turbulent Prandtl number, Pr_t.

$$\epsilon_h = \epsilon_m/Pr_t \tag{3.36}$$

Considerable controversy exists in the literature as to the value of the Pr_t. The so-called Reynolds analogy suggests $\epsilon_m = \epsilon_h$, that is, $Pr_t = 1$. On the other hand, Quarmby [Q1] from his experimental data recommended that

$$Pr_t = [1+(400)^{(R-1)}]^{-1} \tag{3.36A}$$

In the present analysis, initially $Pr_t = 1$ will be used. The effect of Quarmby's equation will be examined in section 5.4.3.

Both eddy viscosity and eddy conductivity are evaluated from conditions existing at the axial location $j+\alpha$ for the radial point in question.

3.5 Computer Program

To solve the sets of algebraic Equations (D-12), (D-14), (D-16) and (D-18) and the associated boundary conditions,

a sequence of execution of the arithmetical operations was written in Fortran IV and carried out on a CDC 6400 digital computer. The input required the empirical equations describing the physical properties of air as functions of temperature, friction factor, and the eddy diffusivity equations for heat and momentum transport. In addition, the inlet velocity and temperature distribution, the total flow rate and the ambient temperature were required. The output is in the form of temperature and velocity profiles at the grid nodes, heat flux at the wall and the Nusselt number. Provision is made for comparison with the given temperature and velocity profiles (experimentally obtained ~~or otherwise~~) and plotting the difference between the two. For the program to be flexible, a number of control parameters needs to be specified to guide the sequence of calculations according to the input specifications. A listing of the program is given in Appendix Z along with the subroutines and sample of the input data.

3.5.1 Time Requirement

The cost of obtaining a solution depends upon the computing time required. The major contributor to the time factor is the matrix inversion subroutine. It is evaluated twice in one iteration and hence the number of iterations required for convergence will effect the time required. The variable step size in the axial direction is particularly helpful since the number of iterations decreases with a decrease in step size and the decrease in the axial gradients in the flow

field. Near the entrance where gradients are large, a small step size stabilises the solution as well as reduces the number of iterations. At large distances from the entrance when the gradients are small, a large step size means a small number of axial steps for a given length.

Time requirement is also greatly affected by the size of the matrix, i.e., the choice of radial nodes. It is determined by a compromise between the accuracy and time requirement. For a fixed number of radial nodes, the mesh becomes finer near the wall but coarser near the centre. For the choice of $N = 50$, $H = 1.05$, tests were made to see if the step size at the centre was too large for the finite difference approximation. This was done by dividing the step-size at the centre into five subdivisions. No improvement in accuracy was found.

For short axial distances, e.g., the present case of heating of air where the heating section is only six radii long and the thermal boundary layer is still developing, some modifications are required in the scheme for determining the axial step-size. Use of $L = 6$ in Equation (3.20) will yield towards the end of the heating section, step sizes which are rather large for the developing thermal boundary layer. An increase in the number of axial step sizes is one way of circumventing this problem though at the expense of greatly increased computing time. A technique that has been found suitable is to use a large value of L say 100 and terminate the solution when the end of the heating section is reached. Thus a reasonably close axial spacing over the entire flow field

(6 radii long) is obtained in 48 steps (for L = 100, H = 1.05, NN = 100). It has all the advantages of progressively increasing step sizes. Two to three minutes on the CDC 6400 is the time requirement for a solution of 48 axial steps with all the complexities considered in the present investigation. Less than two minutes were required for the solution of simple situations, e.g., the development of an isothermal velocity profile from a uniform velocity distribution, for a pure laminar or turbulent forced convection solution.

3.6 Test of the Numerical Solution

Confidence in the numerical solution scheme can be established by comparing its predictions with those found for the same problem by other numerical techniques or analytical solutions. It is highly desirable that situations with known results are as close as possible to the problem at hand so that the comparison of results will highlight flaws in mathematical modelling and in the numerical solution scheme, as well as in computer programming.

Since in the present study simultaneous solution of the mass, momentum and energy conservation equations for flow of a gas in a pipe has been carried out, comparison under the following situations should give sufficient confidence in the proposed scheme:

(i) Solution of the mass and momentum conservation equations alone.

(ii) Solution of the energy conservation equation alone.

(iii) Solution of all the three conservation equations including

effects of natural convection.

3.6.1 Solutions of the Mass and Momentum Conservation Equations

At large distances from the entrance, isothermal flow in a pipe ceases to accelerate and the loss in pressure in the flow direction is only due to wall friction. Under this condition of fully developed flow, the velocity profile is a function of wall shear stress and radial distance. For laminar flow, the fully developed velocity profile is of parabolic shape, while for turbulent flow it is more flat near the centre line with sharper gradients near the wall.

For computational purposes it is assumed that at the entrance of the pipe the velocity profile is flat and the correlations for wall friction for fully developed flow are applicable. The solution of the momentum conservation Equation (3.12) gives the development of the velocity profile; the radial component of velocity is calculated from the continuity Equation (3.11). The unknown pressure drop term is calculated by substituting the momentum equation into the integral mass conservation Equation (3.14), since pressure is assumed to be uniform over the cross-section of the pipe. As all these equations are coupled, an iterative solution has been carried out till the difference between two successive iterations is below some predetermined small tolerance. A check on total mass flow by integration of the calculated velocity profile assured its constancy.

A. Laminar Flow:

In the laminar flow regime where momentum transport is by molecular motion only, the calculated velocity profile at about 500 diameters downstream from the entrance, is compared in Fig. 3.3 with the parabola calculated from the well-known analytical solution for a Newtonian fluid. The agreement between the two provides confidence in the computer program, numerical representation of the partial differential conservation equations and the scheme of calculating the pressure drop term from the integral mass conservation equation.

B. Turbulent Flow:

In the turbulent flow regime, however, the momentum transport is due to turbulent motion as well as to molecular motion. Of the various semi-theoretical equations describing the turbulent transport of momentum by eddy viscosity, the two most popular expressions, (i) Van Driest equations and (ii) the modified Reichardt equation have been employed to check the numerical solution scheme for the calculation of an isothermal fully developed turbulent velocity profile.

Shear stress in an isothermal turbulent flow varies linearly from the value at the wall to zero at the centre line and is equal to the product of eddy viscosity and velocity gradient.

$$\tau = \tau_w (1-y/R_o) = (\mu + \epsilon\rho_m) \frac{du}{dy} \qquad (3.36)$$

Substitution of the empirical expression of eddy viscosity into Equation (3.36) which upon integration will give a velocity

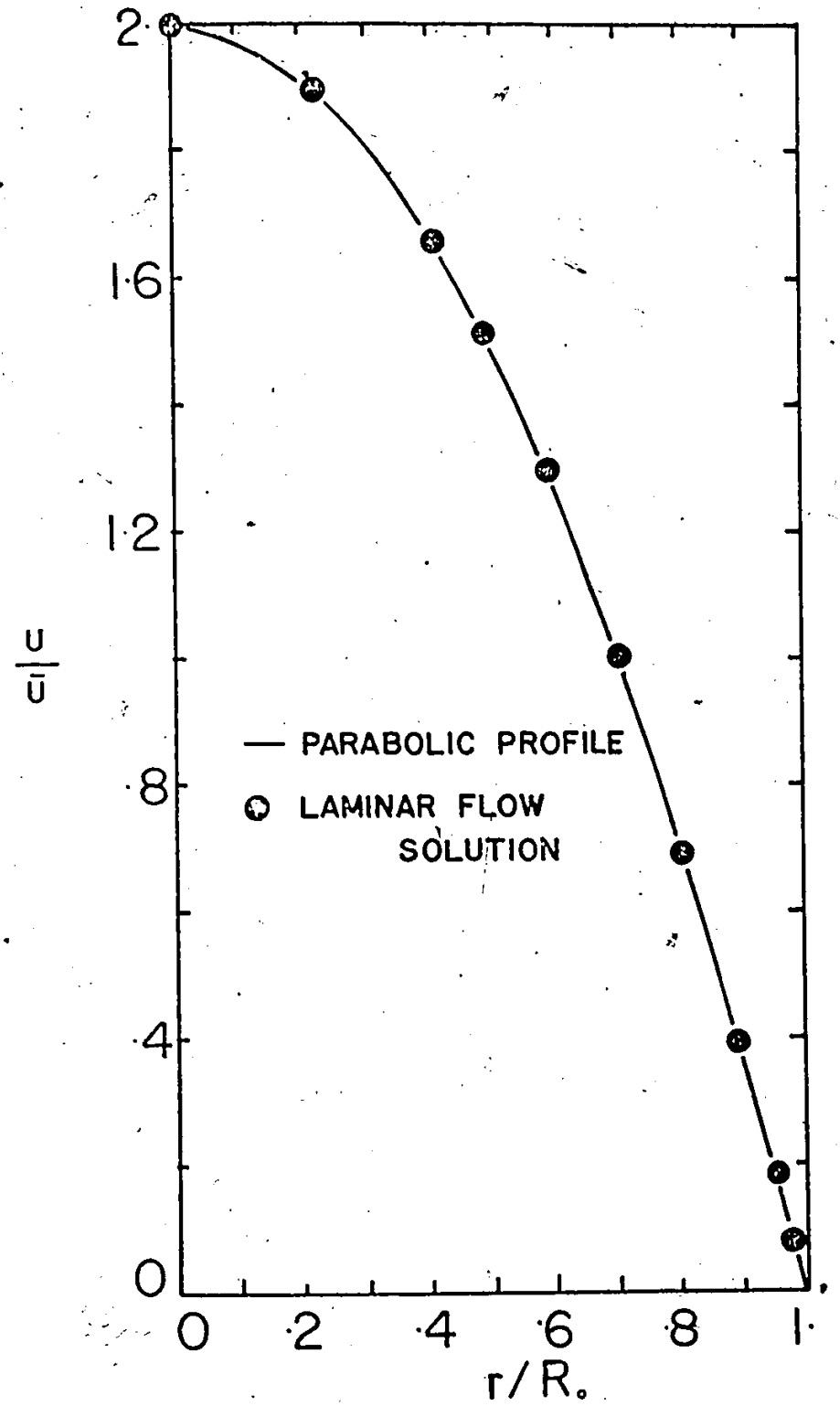

Figure 3-3. Test of the Numerical Solution; Development of Parabolic Velocity Profile for Isothermal Laminar Flow.

profile distribution in the dimensionless form

$$u^+ = \int_0^{y^+} \frac{(1-y/R_o)}{(1+\epsilon_m/\nu)} \, dy^+ \qquad (3.37)$$

(i) Van Driest's Equations

Van Driest's Equations (3.29) and (3.30) were substituted in Equation (3.37) and the resulting velocity profile was compared to the solution obtained from the conservation equations. It was found that the solution obtained from the conservation equations was lower at the centre and higher in the area where wall and core regions meet.

It was found during the integration of Equation (3.37) that the matching point between the eddy viscosity profiles for the wall region and the core region was somewhat different from $y_\ell^+ = 60$, the value Van Driest assumed. To avoid any mismatch and hence the resulting discontinuities, the boundary for the application of one or the other of these two equations was established by determining the point at which both the equations gave the same value of eddy viscosity. This boundary was found to be a function of Reynolds number and the following empirical expression was found to predict it.

$$y_\ell^+ = 35 + 0.247 \, y_{max}^+ \qquad (3.38)$$

Although the eddy viscosity values matched, a discontinuity occurred in the velocity profile. To circumvent this, the universal velocity profile was forced to pass through

u_ℓ^+ (corresponding to y_ℓ^+) by its following version.

$$u^+ = u_\ell^+ + 2.5 \ln (y^+/y_\ell^+) \tag{3.39}$$

Integrating the velocity profile, obtained in this way, gave rise to a total mass flow which was 2% less than the actual flow.

Upon further examination it was found that the eddy viscosity value at the centre of the pipe, i.e., at y^+_{max}, became negative. This arises because the universal velocity profile has a finite slope at the centreline and when substituted into

$$\varepsilon_m \rho = \frac{\tau_w (1-y/R_o)}{du/dy} - \mu \tag{3.40}$$

gives at $y = R_o$ $\varepsilon_m \rho = - \mu$. The axial symmetry of the flow in a pipe requires velocity to be a smooth function of radial location with continuous first and second derivatives. The velocity gradient at the centreline is zero in contrast to the finite value given by the universal profile. Substituting zero velocity gradient at the centreline in the eddy viscosity definition, Equation (3.40) renders it indeterminate.

It has been pointed out by Lynn [L7] that a change of the independent variable y to $\zeta = (1-y/R_o)^2$ in the eddy viscosity definition changes it to

$$\varepsilon_m \rho = - \frac{\tau_w R_o}{2 \frac{du}{d\zeta}} - \mu \tag{3.41}$$

where $\frac{du}{dy} = \frac{-2}{R_o}(1-\frac{y}{R_o})\frac{du}{d\zeta}$ and $\underset{y \to R_o}{\text{Limit}} \frac{d^2u}{dy^2} = \frac{2}{R_o^2}\frac{du}{d\zeta}$

For $(u+\varepsilon_m\rho)$ to be zero at the centreline as obtained by the use of universal velocity profile, the value of $\frac{du}{d\zeta}$ has to be quite large which in turn implies large values of $\frac{d^2u}{dy^2}$ and consequently a pointed profile at the centreline. This condition can not exist as it requires large shear stress at the centreline. Lynn examining the data of Nikuradse, Corcoran et al., and Senecal and Rothfus found that the value of eddy viscosity at the centreline is about 50% of the maximum value. This estimate was obtained from the plot of u vs ζ taking into account the zero slope of the velocity profile at the centreline.

It can thus be concluded that the failure of the solution of conservation equations to agree with that from Equation (3.37) is due to the inadequacies of the eddy viscosity expressions mentioned above.

(ii) Modified Reichardt Equations

Travis et al. [T1] modified Reichardt's two-region expression for eddy viscosity to make the predicted velocity profile agree with the experimental observations. In addition, constraints of axial symmetry, smooth velocity profile and continuity of its derivatives, matching eddy viscosity values and their derivatives at the boundary between the wall and core regions and constancy of total mass flow have been satisfied. The centreline eddy viscosity has been chosen to

be 75% of the maximum value over the cross-section.

Comparison of the velocity profile obtained by substituting the eddy viscosity Equations (3.31) and (3.32) in Equation (3.37) and that calculated from the solution of momentum and continuity equations is shown in Figure 3.4. The excellent agreement between the two confirms the capability of the numerical solution to develop a fully developed turbulent velocity profile from a given distribution (uniform in the present case). Other criteria for full development of a velocity profile such as: its being independent of axial distance, the calculated pressure drop being equal to that given by Fanning's equation and a straight line radial shear stress profile were also met.

3.6.2 Solution of the Energy Equation

The solution of the energy equation can be obtained independent of the solution of momentum and continuity equations, if the velocity profile and changes in this profile with temperature can be specified a priori. Sparrow et al. [S1, S11] and Pollock [P1] assumed that the dimensionless, fully developed, isothermal velocity profile was maintained even though the fluid was either heated or cooled, that is, dimensionless velocity is only a function of dimensionless radial distance for all heat flux levels. The physical properties of the flow medium were assumed constant and evaluated at the inlet temperature. The eddy conductivity was assumed equal to the eddy viscosity and was assumed to be given by the expression

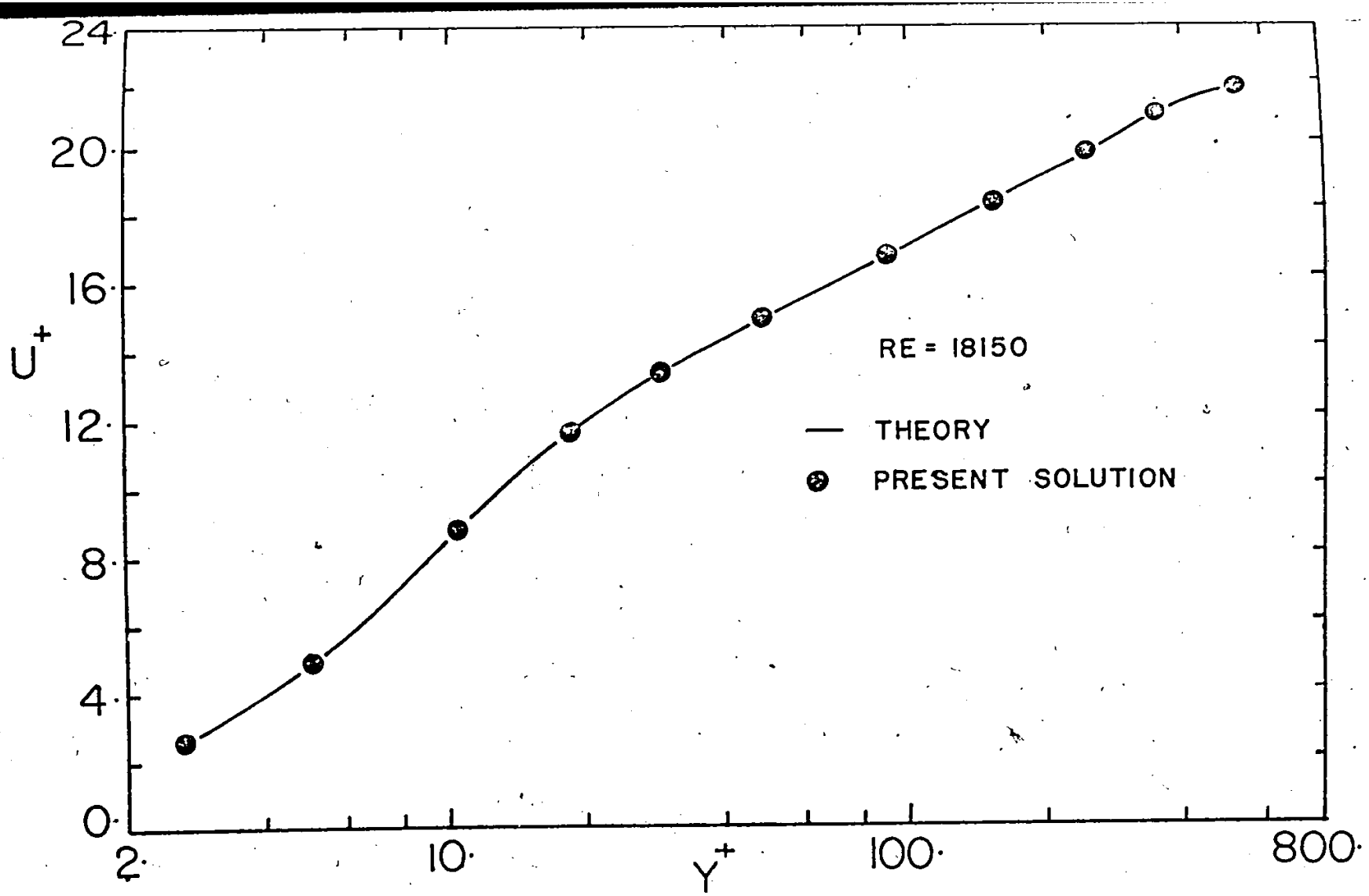

Figure 3-4. Test of the Numerical Solution; Development of Fully Developed Velocity Profile for Isothermal Turbulent Flow.

recommended by Deissler [D8] for the wall region; the universal velocity profile was assumed to hold in central region. The point of demarcation between the two regions was $y^+ = 26$. The entering velocity profile was calculated by integrating Equation (3.37) with Deissler's eddy viscosity expressions. Table 3.1 compares the values of Nusselt Numbers given by [S11], [P1] and the present solution under the above mentioned conditions. The agreement is excellent.

Table 3.1

Comparison of Nu/Nu_∞ Ratio in the Entrance Region (Constant Wall Temperature and Fully Developed Pipe Flow)

	Re=10000			Re=50000	
x/D	Sparrow	Pollock	This Work	Sparrow et al.	This Work
2	1.265	1.264	1.270	1.272	1.276
5	1.116	1.117	1.118	1.136	1.137
10	1.044	1.046	1.05	1.064	1.061
20	1.008	1.008	1.007	1.02	1.013
30	1.002	1.001	1.00	1.009	1.002

3.6.3 Simultaneous Solution of all Conservation Equations

Marner and McMillan [M12] have published a numerical solution for laminar convective flow in a pipe with a buoyancy force aiding the forced convection. Constant physical properties

evaluated at the inlet temperature, except in the body force term were used in the momentum equation. With an isothermal, fully developed, laminar velocity profile experiencing a step change in wall temperature, a solution is given for Gr/Re = 120 where the characteristic length is taken as the radius of the pipe. Velocity and temperature profiles are given for various dimensionless axial distances $\bar{Z} = Z/(R_0 \text{ Re} \cdot \text{Pr})$. Figure 3.5 compares these profiles with those obtained from the present solution under similar conditions for $\bar{Z} = 0.02$. The agreement between the two is excellent considering the inaccuracies involved in retrieving results from graphical representation.

Thus it has been shown that the present numerical solution scheme is capable of solving simultaneously as well as independently the mass, momentum and energy conservation equations. Comparison with known solutions for the three cases discussed above has generated full confidence in the solution scheme.

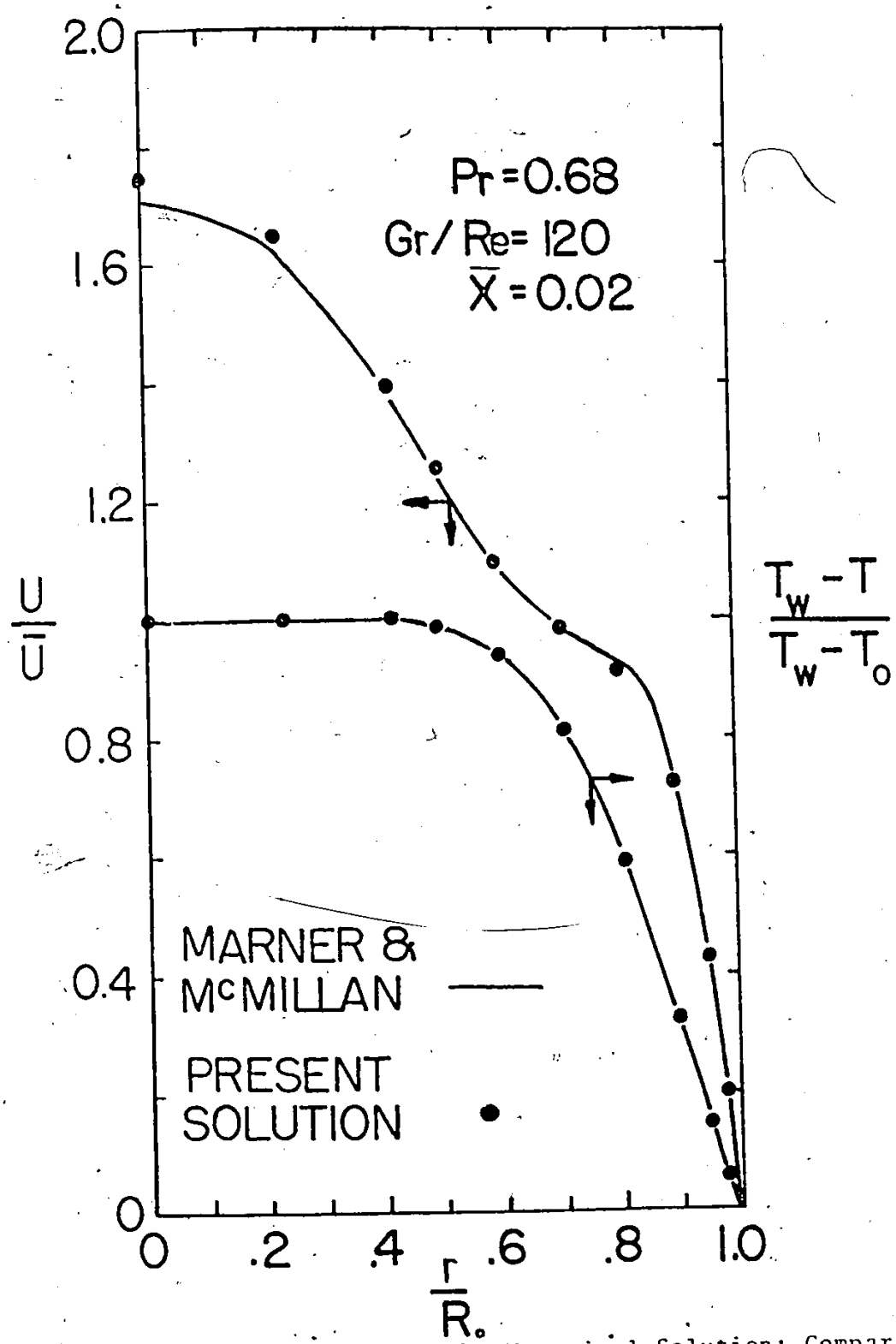

Figure 3-5. Test of the Numerical Solution; Comparison with the solution of Marner and McMillan for Aiding Free and Forced Convection Laminar Flow.

CHAPTER 4

EXPERIMENTAL PROGRAM

4.1 Introduction

In opposing free and forced convection interaction systems, increasing the magnitude of buoyancy forces relative to the inertia force, will ultimately result in free convection dominating the flow. Under these conditions the flow will change its direction to that of the buoyancy force. Since this flow reversal phenomenon is due to the unstable equilibrium between the two opposing forces, whose magnitudes vary over the flow field, a sudden change in flow direction is not expected. On the contrary, it is a gradual process first starting at the place where the local magnitude of the buoyancy force has become dominant.

In the proposed numerical scheme for the solution of conservation equations, only the unidirectional flow has been considered, that is, flow reversal does not occur. Thus it is important to define the limits of applicability of the numerical solution.

The experimental program for the present investigation is divided into two sections:

(i) Flow Visualisation - to determine the conditions defining the onset of flow reversal.

(ii) Measurements in a turbulently flowing air stream under conditions defined by (i), of the radial and axial tempera-

ture and velocity profiles so that a comparison with the numerical predictions can be made.

4.2 Observation of Flow Reversal by Flow Visualisation

4.2.1 Introduction

Determining the conditions at which unidirectional flow becomes unstable and flow reversal occurs in the region of high buoyancy force is best done through a flow visualization experiment. It must be recognized at the outset, that in an opposed free/forced convective system, the buoyancy forces are going to be the highest relative to the inertia forces in the region of the wall and hence the flow reversal will first occur in the immediate wall region. Furthermore, the axial and circumferential position at which flow reversal will first appear is difficult to determine a priori. This suggests, therefore, that the entire pipe should be transparent. Difficulties arise in designing a hot glass or plastic walled system and still maintain transparency. Therefore the wall should be cooled to achieve the buoyancy force and the flow of hot fluid upward to maintain opposed inertia and buoyancy forces. Dynamic similarity can be achieved however, with water, by proper design and operating conditions. That is, since free convection is characterized by the Grashof number, Gr, forced convection by the Reynolds number, Re, and physical properties by the Prandtl number, Pr; a suitable combination of these parameters can represent the flow field regardless of the flow medium. Indeed, because of the differences in physical properties between air

and water, the same buoyancy forces can be produced in water as in air with much lower wall-to-fluid temperature differences. This is fortunate since transparent plastic pipe has a relatively low upper temperature limit. Flow visualisation in water is much easier as well.

4.2.2 Selection of Flow Visualisation Technique

A large variety of flow visualisation techniques have been used by the investigators in the past for various flow situations. A dye or a small particle which is able to follow the streamlines exactly, without disturbing the flow to be studied, is suitable for flow visualisation. Dye injection or creation of a coloured liquid by photochemical reaction, production of minute hydrogen bubbles by electrolysis or suspension of small aluminum or other particles with essentially neutral buoyancy have been used successfully in some situations. The requirement in the present case is that the tracer producing technique must not disturb or affect in any way the flow forces and it must be observable in the immediate region of the wall. The first requirement means that the tracer must have neutral buoyancy at all points and must not require the insertion of probes (which could conduct heat). The electrochemical technique suggested by Baker [B1] meets these requirements. In this technique, water is made weakly electrically conducting by adding 0.1N NaOH and 0.1 N HCl in such amounts to make the solution slightly on the acidic side of the end point of an acid-base indicator. With thymol blue as indicator, the solution is pale yellow at pH = 8.0 and changes to deep blue

at pH = 9.6. Application of electric potential to the solution of pH = 8.0 causes an increase in the pH at the cathode due to the neutralisation of H^+ ions and thus producing a blue dye locally which is neutrally buoyant. Moreover, since the cathode can be made a part of the pipe wall, the dye can be produced in the region of interest. Thus this technique meets all the requirements of the present study.

4.2.3 Experimental Equipment

A water tunnel shown schematically in Figure 4-1, was used to observe the flow reversal phenomenon in opposing free and forced convection flow field. The opposite directions of the two convections were created by the upward flow of hot water through a water-cooled test section. The circulation loop consisted of a 25 gallon heating tank A, a centrifugal pump, a 25 gallon constant head tank B, a test section, and a flow control and measuring system. Water was heated in tank A by a steam jacket and at the same time cooled by a copper cooling coil. A thermocouple, an electro-pneumatic temperature control system and a mixer was used to maintain a desired uniform temperature of water. The simultaneous heating and cooling in the tank A was provided to achieve better control on the water temperature. Especially at low temperature levels having low steam requirements for heating, the steam control valve will be at the lower end of its operating range and thus very inefficient from control point of view. The cooling coil

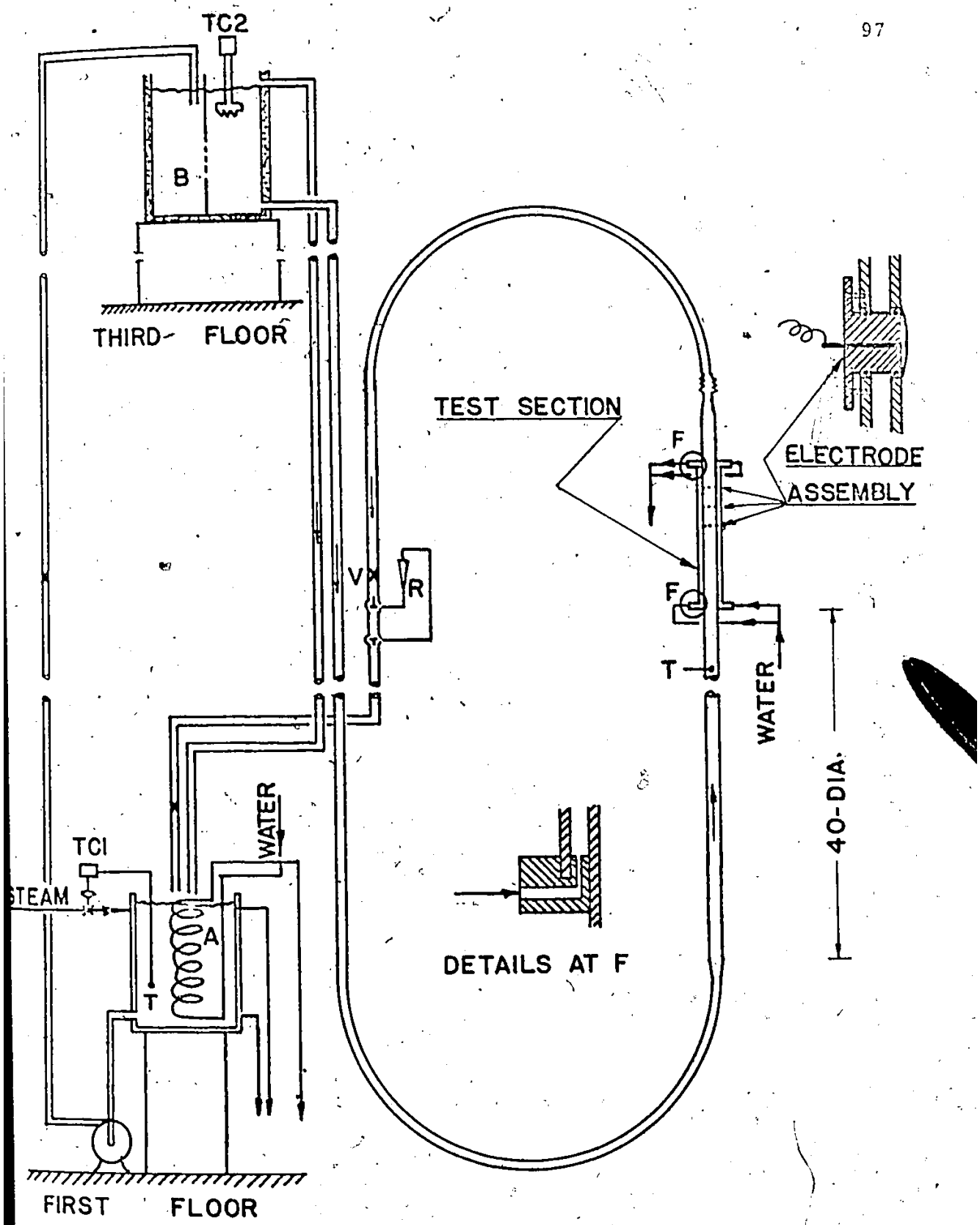

Fig. 4-1. Schematic Diagram of Water Circulation Loop for Flow Visualisation.

increases the steam requirements and consequently the effectiveness of the control system.

Water from tank A was pumped by a centrifugal pump of 96 gal./min capacity, to the constant-head tank B. The overflow from tank B returned to tank A. An additional temperature controller with 1000 Watt heater was provided in tank B to compensate for the heat losses. Hot water from tank B flowed downwards through a 2 in. copper tube, through a U-bend (radius 8 ft) into the bottom of a 10ft length of 3.0 in. I.D. acrylic pipe followed by the test section. Flow control was achieved by a valve V located in the return leg of the loop. The latter returned the water into tank A and thus completing the water circulation circuit. A rotameter R was used to measure the flow rate of water.

The transition from 2 in. copper tube to 3 in. acrylic pipe was achieved by two copper cones. A 9 in. length of 2 in. diameter stainless steel bellows joins the cone at the top of the test section to the return leg of the loop. This served to relieve the stresses caused by the difference in the thermal expansions of copper and the plastic pipes. Although the velocity measurements were not made, the flow was assumed to be fully developed after the better than 40 diameter section upstream of the test section.

All the piping (except the test section) was covered with 1 1/4 in. fiberglass insulation. To avoid any disturbance to the flow, a copper-constantan thermocouple was located at 20 diameters upstream from the test section to measure the hot

water temperature. It was estimated that this temperature was the same as that entering the test section.

4.2.4 Test Section

The test section was a 3 ft long, 3.0" I.D. and 3 1/4" O.D. plexiglass pipe surrounded by 3 1/2" I.D. plexiglass pipe making a cocurrent double pipe heat exchanger. Hot water flowing in the test section was cooled by the cold water in the annulus. The cold water entrance was designed to avoid localized cold spots. Water flowed into the plexiglass flange at the end from whence it flowed through fourteen 0.04 in. diameter holes, uniformly spaced around the periphery, into the annulus surrounding the inner pipe carrying the hot water. The outlet flange is of the same design. By having fairly high water flows and with this design, the heat transfer surface was maintained at essentially a uniform temperature as indicated at seven locations by chromel-alumel thermocouples imbedded in the pipe wall. With the high cold water flows, its temperature remained essentially unchanged through the test section.

The chromel-alumel thermocouples were mounted in pairs at 1 1/4, 7, 13, 19, 25, 31 and 34 3/4 in. from the inlet to the test section; they are equally distributed around the periphery of the test section. To minimize conduction errors, the thermocouple wires were mounted in slots milled into the outside of the inner plastic pipe. Each thermocouple was fixed in the slot bed at a known distance from the inner wall as shown in table 4.1. In this way, using the Fourier heat conduction equation, the

inner surface temperature can be estimated. Plexiglass cement with the same properties as the pipe material was used to permanently fix the thermocouples and wires into the pipe and fill in the slot spaces. Pipe wall thickness at each thermocouple location was measured at the holes which were drilled for the twelve plexiglass plugs to house the electrodes. One 1 1/2 in. long, 1/16 in. diameter platinum rod to serve as electrode was fixed in each plug by plexiglass cement. The plug with the rod mounted was machined to provide the same contour as the inner pipe, so that the entire pipe was hydrodynamically smooth throughout and the electrode flush with the wall. The electrodes were located at 21, 27 and 33 in. from the inlet of the test section. Each location has four electrodes located at 90° to one another; this allowed observation of any asymmetry of the flow or any preferentially unstable location.

4.2.5 Experimental Procedure

Tanks A and B and the circulation loop piping were filled with water from the water mains. A steady flow of the circulating water in the loop was obtained by establishing a constant head of water in tank B. Rotameter R was calibrated by temporarily diverting the flow of water in the return leg of the loop into a barrel and weighing it. The calibration curve is given in Appendix B.

The water in the circulation loop was heated to a predetermined temperature by supplying steam to the jacket of

Table 4-1

Thermocouple Locations in the Test Section Wall Thickness

Thermocouple No.	Distance from Upstream End in.	Wall Thickness in.	Thermocouple Distance from Inner Surface in.
1A	35.0	.130	.036
1B	35.0	.130	.086
2A	31.5	.131	.035
2B	31.5	.131	.072
3A	25.5	.128	.034
3B	25.5	.128	.059
4A	19.5	.125	.031
4B	19.5	.125	.088
5A	13.5	.125	.030
5B	13.5	.125	.091
6A	7.5	.125*	.030
6B	7.5	.125*	.093
7A	1.5	.125*	.030
7B	1.5	.125*	.091

* Estimated

Tank A and the cold water flow rate in the cooling coil was adjusted so that the temperature controller TC1 operated at maximum efficiency. A heater with temperature controller TC2 was used to compensate for the heat losses in Tank B. The temperature of the water in the loop was controlled to better than 0.5^{o}F as observed by the thermocouple upstream of the test section.

Twenty five grams of the indicator, thymol blue, was added to the 55 gallon capacity circulation loop to provide a concentration of about 0.01% by weight. A small quantity of the indicator was dissolved at a time in a very dilute NaOH solution and added to the system till all the indicator was completely dispersed. The pH of the system was adjusted by adding dilute HCl solution so that the water is of light yellow-orange colour and is just on the acidic side of the end point.

One of the twelve electrodes was chosen as the cathode and the other eleven formed a common anode. A 45-V battery was used as a power source and a potentiometer allowed the adjustment of voltage applied across the electrodes. As soon as the current was switched on, the H^+ ions in the solution moved towards the cathode and after being neutralised formed hydrogen bubbles. To prevent flow disturbance arising from the hydrogen bubbles their formation was kept to a minimum by adjusting the voltage across the electrodes. The loss of positive charge at the cathode created around it a region of low concentration of H^+ ions and thus higher pH. Since the

system was near its end point, a plume of blue dye was seen to originate from the cathode and follow the flow streamlines near the wall. This dye plume ultimately mixed with the main flow of low pH, and lost its colour.

At a fixed hot water temperature in the loop, flow reversal can be created by decreasing the mass flow rate of the water. Since the test section is made of plexiglass which starts distorting around 200°F, the upper limit for the experiment was set at 175°F. A lower temperature limit of 100°F was chosen so as to have a reasonably accurate wall-temperature estimation. At each of the selected temperature levels, the hot water flow rate was gradually reduced till the dye plume near the cathode indicated flow reversal.

4.2.6 Results

Since the onset of flow reversal is a transition phenomenon indicating a change in the domination of flow from forced to free convection, the demarcation is not very sharp. Any asymmetry or flow fluctuation can trigger the change. Indeed, the first sign of the onset of flow reversal is the unstable behaviour of the dye plume which shows intermittant and momentary flow reversal. Thus it was difficult to assert that the flow reversal had occurred at any of the electrode positions earlier than the others. Logically, one would expect the flow reversal to occur at the farthest downstream location, since the fluid there experiences the greatest buoyancy force and consequent flow retardation. No clear cut observation

of this nature could be made.

Since no sharp demarcation of the onset of flow reversal existed, two flow rates were used to define flow reversal.

(i) When flow reversal is no longer an occasional random event and occurs at most of the electrode locations.

(ii) When flow reversal is a definite event occurring at all the electrode locations.

Experimental observations indicated that with a decrease in flow rate, the upward moving plume occasionally also covered the area immediately below the cathode. The frequency and the area below the cathode covered by the dye increased with decreasing flow rate. When flow rate was substantially reduced, the plume was permanently covering the space 1/2 in. to 1 in. below the cathode. This was the condition where permanent flow reversal near the wall had occurred. Even under the conditions of flow reversal, the dye plume was seen to rise upward after it had reached a minimum position. This occurred because the fluid layer undergoing flow reversal was very thin and the blue dye thus diffused out of this layer into the upward flowing mainstream, both by the turbulent and molecular processes.

Unfortunately, it was not possible to take clear photographs of this behaviour although some attempts were made. Photographing the very fine line of the dye was difficult under the best of conditions, and the difficulty was greatly magnified by the distortion caused by curvatures of the plastic pipes

and the water in the annulus.

Metais and Eckert [M1] drew a map indicating free, mixed and forced convection regimes on a plot of Re_f vs. $(Gr_f\ Pr_f\ D/L)$. The classification of the convection regimes was based on the experimental data on combined free and forced convection available in the literature. If for a particular set of operating conditions, the heat transfer rate could not be predicted within $\pm$ 10% by the standard free or forced convection correlations, it was declared to be in the mixed convection region. Figure 4.2 shows the Metais plot and the flow reversal band from the present investigation. The Grashof number was based on the difference between the average inside surface temperature and the entering hot water temperature. The former was estimated from the paired thermocouples imbedded in the test section wall thickness. The physical properties were evaluated at the film temperature.

As expected the observed flow reversal band is in the mixed convection region. The former lies somewhere in the middle of the latter, which is logical, as the start of flow reversal is only an intermediate stage between the dominance of flow by either free or forced convection. In the area below the band, the reversal of flow is expected to occur, while above the band it is not. Buoyancy force is expected to influence the heat transfer rates in both regions, although with flow reversal the phenomenon is made much more complicated by the local change in direction of the flow.

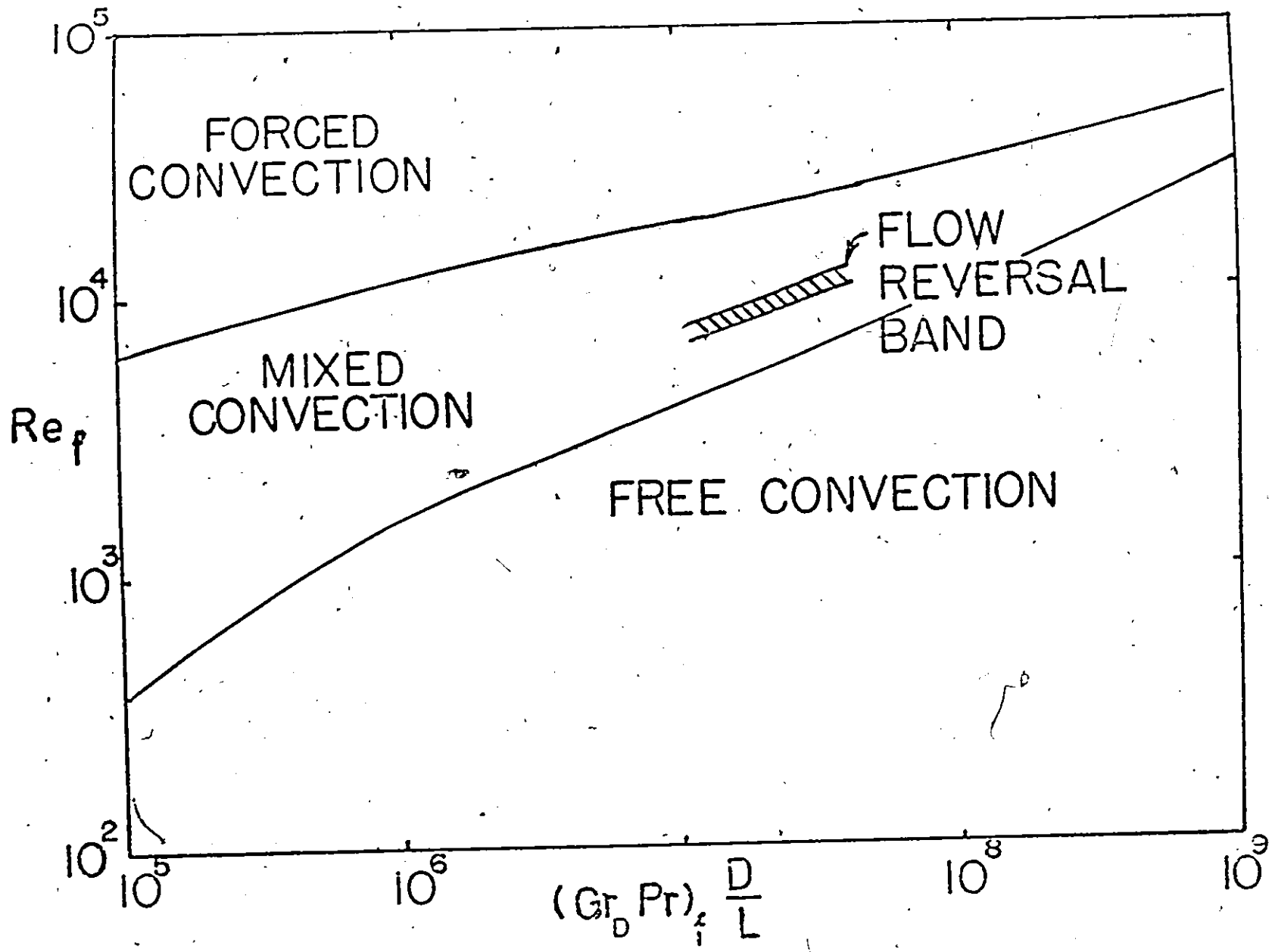

Fig. 4-2. The Band Representing the Initiation of Flow Reversal in Opposing Free and Forced Convection. Free, Mixed and Forced Convection Regime Map from [M1].

Thus using the conditions of dynamic similarity between cooling of upward flowing water and downflow heating of air, most experiments for the latter have been designed to avoid the flow reversal region since this research program relates only to unidirectional flow. Some experiments were designed at conditions below the critical band to indicate the effect.

4.3 Air Heating Experiments

4.3.1 Experimental Apparatus

In the present investigation of opposing free and forced convection interaction, it was proposed to study the heat transfer aspect of this phenomenon by a detailed examination of the temperature and velocity profiles in the flow field. Air was chosen as the flow medium because this project originated from a practical application, spray drying in flowing gases; and it was readily available in large volumes. A schematic diagram of the experimental apparatus is shown in Figure 4.3. Air at 100 p.s.i.g. was obtained from the compressed air supply to the building. A constant-flow rate was obtained by maintaining a constant air pressure upstream of a sonic orifice. Air then entered the entrance section of the 8.054" diameter column where a unidirectional flat velocity profile was created. In the following 40 diameters of the pipe length, a fully developed isothermal velocity profile was established before the heating section was reached. The vertical orientation of the test section and downward flow of air ensured opposing directions of free and forced

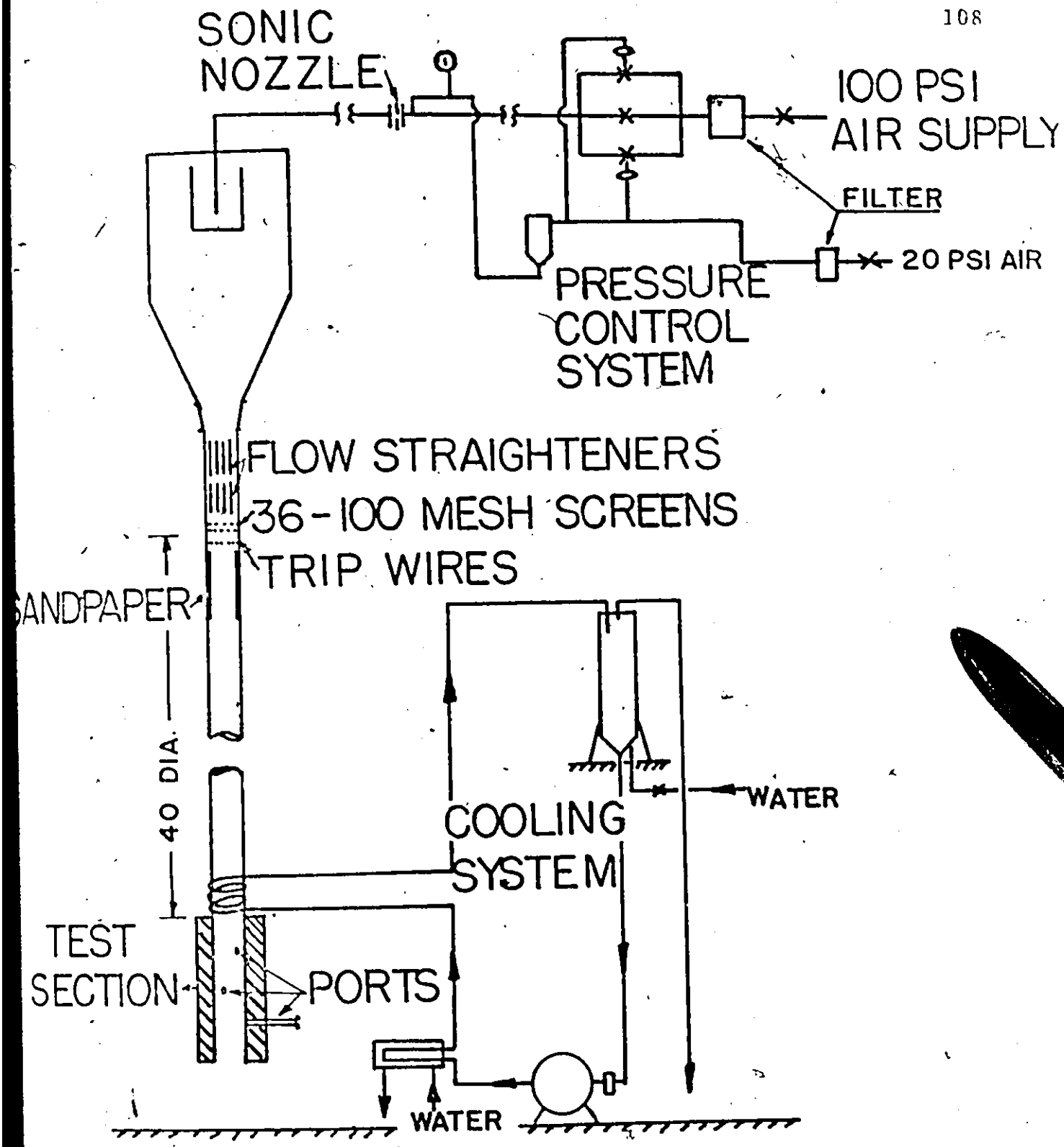

Figure 4-3. Schematic Diagram of Air Heating Experiment.

convection. Radial temperature and velocity profile measurements were made at the three port locations in the test section while its wall was maintained at a uniform temperature. A detailed design of the experimental set up is described below.

4.3.2 Test Section

The test section was made of a stainless steel pipe 8.5 in. O.D. and machined to an inside diameter of 8.054 in. Three ports for probe insertion were drilled with 6 in. axial and 60° circumferential separation from each other. The centreline of the top port was located at 6 in. from the start of the test section. Five inch lengths of 2 in. pipe were welded at each of the portholes. Additional pieces of 2 in. pipe, 13 3/8 in. long, were bolted to make 18 3/4 in. long port pipes. The thickness of the 8 in. diameter test section pipe was reduced to 1/32 in. for a distance of 7/8 in. at both ends, in order to reduce the heat loss by conduction to the adjoining pieces. The flanges on both ends were grooved to accommodate 0.44 in. diameter circular heating elements each of 1500 W capacity. They were used to compensate for the heat loss through the flanges. The final machining of the inside of the test section was delayed till all the flanges and the port pipes had been welded. This was done to correct any distortions in the inside diameter of the pipe that might have occurred during the welding process.

Twenty seven 1/8 in. Chromel-Alumel Ceramo thermocouples were used to monitor the pipe wall temperature at various

axial and circumferential positions. 1/8 in. x 1/8 in. grooves of appropriate lengths were milled into the outside surface of the test section. The stainless steel sheathed thermocouples were peened into these grooves and taken out near the top and the bottom flanges, so that the thermocouple lead wires do not experience any large temperature variations in the vicinity of the thermocouple junctions. This procedure minimised heat conduction errors. The thermocouple junctions, made by electric arc welding under oil, were placed in small holes at the end of the grooves and peened to make good thermal contact. Figure 4-4 shows the thermocouples peened to the test section wall. Table 4-2 indicates the axial and circumferential locations of the thermocouples. Hot and cold junctions of the thermocouples were connected by thermocouple extension wires to Honeywell multi-point millivolt recorders.

Heat was supplied to the test section by Kanthal A-1 (72% Fe, 22% Cr, 5.5% Al and .5% Co) heating strip wound on the test section covered with a 1/4" thick layer of Hiloset, a refractory cement to provide electrical insulation and good heat transfer. The mechanical strength of the .625" x .015" heating strip was enhanced at the right angle bends, required to make electrical connections to the power supply, by welding additional strips onto the main one. The lengths of the heating element and the spacing between the consecutive turns was varied so that more heat could be supplied towards the ends of the test section than in the middle. To compensate for conduction losses in the port pipes and to avoid cold spot

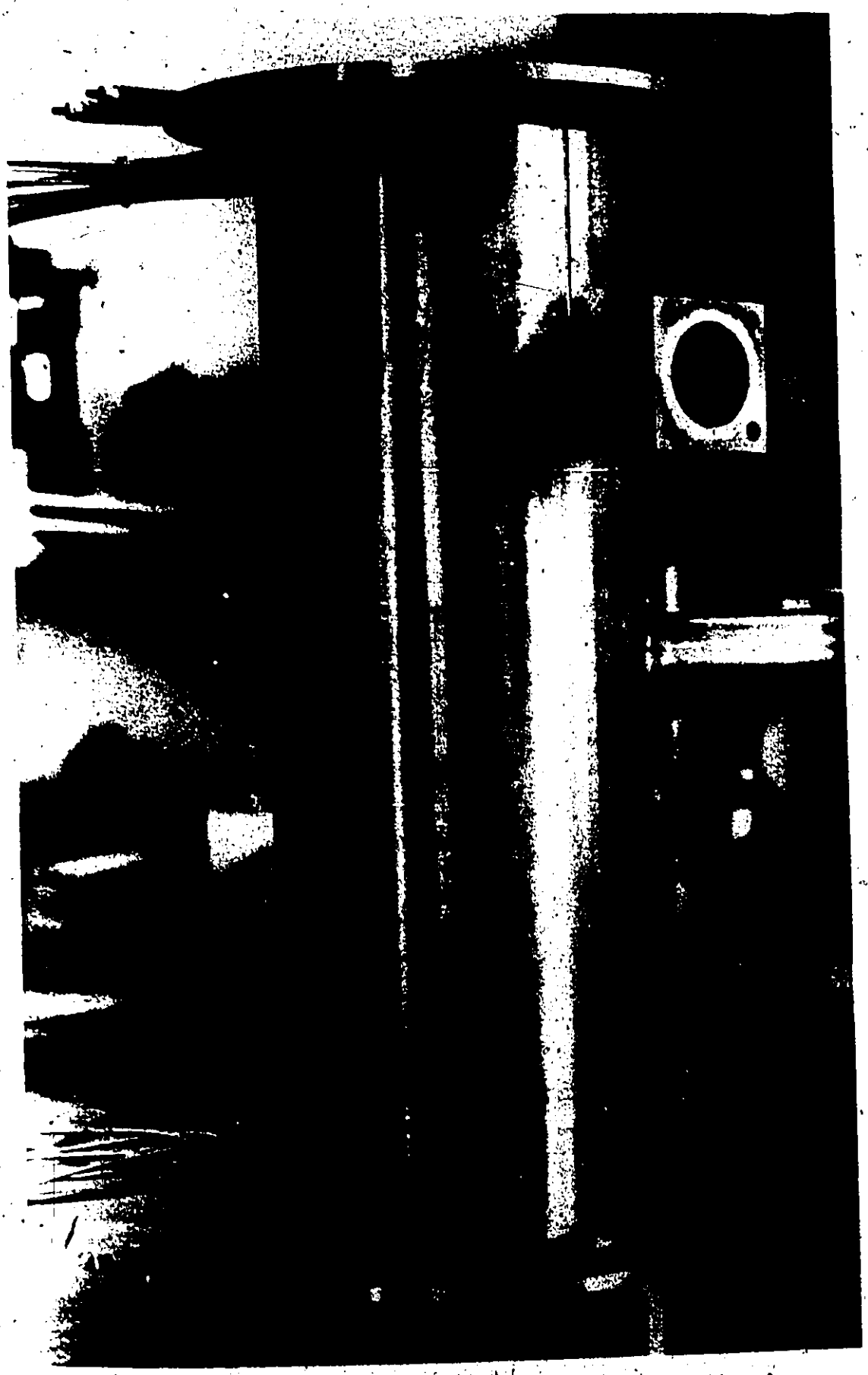

Figure 4-4. Photograph of the Test Section Showing Thermocouples Imbeded in the Pipe Wall.

Table 4-2

Thermocouple Location on the Test Section

Thermocouple Code*	Distance from Top Flange in.
L1T	1
L2T	2
L4T	4
L5T	5
L6T	6
C3T	3
C10T	10
C11T	11
C12T	12
R6T	6
R9T	9
R12T	12
L16B	8
L12B	12
L6B	18
C9B	15
C6B	18
C3B	21
COB	23.5
R8B	16
R7B	17
R4B	20
R2B	22
R1B	23
P1	Top Port
P2	Middle Port
P3	Bottom Port

* The thermocouples are located on the test sections along the axial lines diametrically opposite to the ports. The first letter of the code L, C and R refers to the Top, Middle and Bottom ports respectively.

formation in the test section near them, 0.064 in. diameter Kanthal heating wire was wound for a length of 4 in. on each port pipe. All the heating elements were covered with about 1/2 in. layer of Hiloset cement. The heater resistances are listed in Table 4-3.

Galvanized iron sheet with holes cut for the thermocouples, heating elements and port pipes was used to enclose 3" thick insulation of loose glass wool around the test section. To provide a step change in temperature at the entrance of the test section, the adjoining pipe was wound for a distance of about 10 in. with 1/2 in. copper tubing for cooling water circulation. Three copper constantan thermocouples were peened into the pipe wall at 1 1/2 in., 5 1/2 in., and 10 in. upstream of the test section to monitor the flow of heat. The copper tubing was set in place by Thermon heat transfer cement.

The power was supplied to the test section heaters from a 240-V, 3-phase A.C. mains from three different bus-bars. Step-down transformers (ratio 1:10) were used in each phase so that the input voltage to the heating elements is reduced to a maximum of 24-V. Auto-transformers were used to regulate this voltage and thus the current supplied to the individual heaters. Flange heaters were supplied by two of the three phases of 240-V A.C. mains and the heat input was controlled by auto-transformers. The power cables from the powerstats were well supported so that their weight did

Table 4-3

Resistance of Test Section Heating Elements

Heater No.	Resistance Ω
1	.42
2	.43
3	.77
4	.78
5	.81
6	.38
7	.38
8	.40
Each Port Heater	.68
Top Flange Heater	8.6
Bottom Flange Heater	9.42

not create excessive strain on the heater elements as the latter have very low mechanical strength at high temperatures.

4.3.3 Air Supply

Compressed air at 100 p.s.i.g. from the building supply line was used as the heat transfer medium. A high capacity (275 scfm at 100 p.s.i.g. inlet) air filter removed oil and dirt particles from the air. A sonic nozzle was used to supply a constant flow of air. Since sonic flow in a nozzle can be assured by keeping the ratio of the downstream-to-upstream absolute pressures below a critical value of .533, a constant flow of air can be obtained simply by controlling the upstream pressure. This air pressure control was achieved by using pneumatically operated control valves and a proportional pressure controller. The pressure just upstream of the sonic nozzle was fed to the Honeywell 5 to 15 p.s.i. range pressure controller. Two pneumatic control valves and a globe valve all connected in parallel constituted the air supply regulating system. By manually adjusting the by-pass valve, the pneumatic control valves could be operated in their most effective range and thus a large range of flow rates could be achieved. Thus the air pressure and hence the flow rate could be controlled within $\pm$ 1% of any given value.

4.3.4 Sonic Nozzle

The sonic nozzle was machined from 1/2 in. thick brass plate according to the design given in [F1]. The entrance

contour of the nozzle was carefully machined by a form tool and polished so that the discharge coefficient of the nozzle is quite close to 1 for all flow rates. To cover a large range of flow, sonic nozzles of three sizes 1/2 in. 5/16 in. and 3/16 in. were made. Since a large upstream area-to-orifice area ratio is desirable 2 in. mild steel, schedule 40 pipe was used to house the sonic nozzle. A straight length of 35 diameters upstream from the nozzle was provided to dampen the flow disturbances. The inside surface of the pipe downstream from the nozzle was lined with a cork sheet for a length of 12 in. to absorb the shock waves hitting the pipe walls. This greatly reduced the noise from sonic nozzle.

4.3.5 Entrance Section

The ratio of mean velocities in 2 in. pipe and in 8 in. column is approximately 16. Since these two pipes meet at 90°, care must be taken to ensure the uniform flow distribution in 8 in. column. High kinetic energy flow in the 2 in. pipe, coupled with a 90° elbow can cause serious maldistribution of flow in the column. To avoid this, an entrance section joined the 2 in. pipe to the 8 in. column. The entrance section is made of a 23 in. diameter 30 in. long steel drum; a 28 in. long cone joined the drum to an 8 in. diameter column. The air flow in the 2 in. pipe entered the drum and its flow direction was twice reversed by means of a cylindrical baffle inside it. The flow reversals and almost 130 fold reduction in the velocity from the 2 in. pipe to the drum and the flow acceleration in the following cone

are expected to redistribute the flow uniformly over the cross-section of the 8 in. pipe, at the entrance. The flow out of the cone is made unidirectional by the use of plastic straws (7/32 in. I.D. and .007 in. wall thickness) glued together to fill the cross-section of the column. Two such 8 in. long packs were used. The thin walled straws were particularly selected so that a very small percentage of the column cross-section is obstructed. Approximately 1000 small jets of air coming out of the straw pack impinged on a set of 36-100 mesh bronze screens. A set of five concentric rings made from 1/16 in. steel wire with ring diameters varying from 6.25 in. to 7.938 in. was placed normal to the flow and 4 in. downstream of the screens. The placement of the rings is based on the recommendation of Brighton [B14] and is shown in Figure 4-5. These rings act as trip wires for the development of the boundary layer and create a velocity defect in the wall region. The wakes from the wire rings merge with each other and with the boundary layer at the wall, as they move downstream, resulting in faster growth of the boundary layer. A 16 in. length of 40-grit floor sanding paper was glued to the pipe wall just downstream of the rings; this material provided a wall roughness which further helped the boundary layer to grow quickly. The following 24ft.6 in. length of the smooth straight 8.054 in. diameter pipe was provided so that the air flow reaching the test section was symmetric and had a fully developed turbulent velocity profile as shown in Figure E-2.

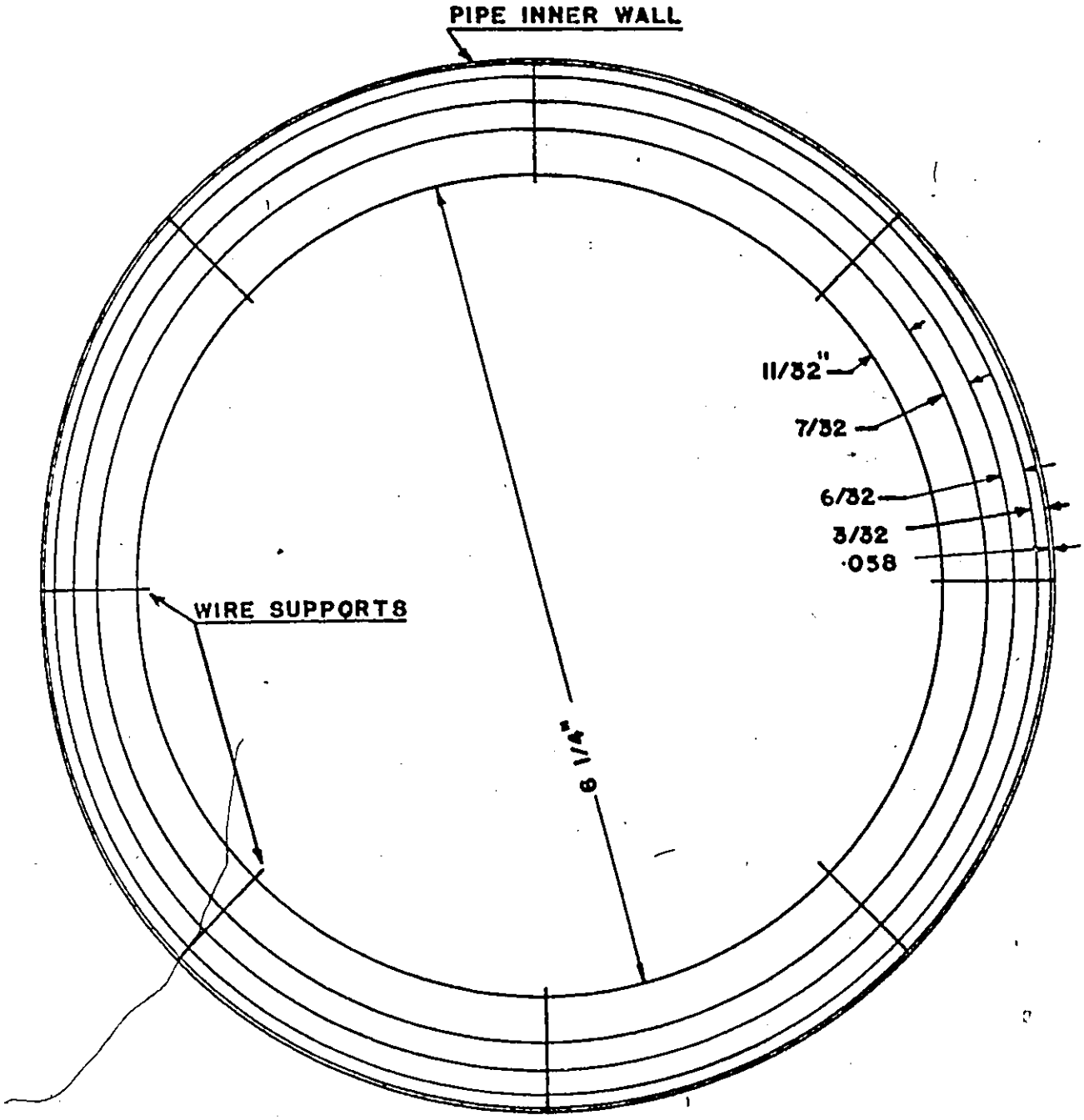

Figure 4-5. Design of Trip-Wire Rings used to Accelerate the Development of Turbulent Flow.

This design of the entrance section was the latest of the series of designs tried in an attempt to achieve symmetric and fully developed turbulent boundary layer in the test section. Some details of these designs are given in Appendix E. Since the symmetry in the flow was not achieved for Reynolds number $\geq$ 48000 (outside the range of present interest), it is recommended that the annulus between the expansion drum and the baffle be filled with the plastic straws and the cone following the drum be replaced by a well contoured nozzle.

4.3.6 Flow Development Section

The test section was preceded by 40 diameters of flow development length. It was made up of 4 pieces of mild steel pipe for ease in assembling. All the pipes were honed to the test section size with a tolerance of $\pm$ .005 in. diameter and 15 μ in. surface finish. A wooden plug 8.032 in. diameter and 10 in. long was used to align the various pieces of pipe. Two adjoining pieces of pipe were bolted together with the wooden plug inserted at the place of their junction. Two 1/4 in. holes, diametrically opposite to each other, were drilled in the flanges to accept brass tapered pegs at a later stage in assembling. The assembly was dismantled and this process was repeated for all the adjoining flanges. At the time of assembling the whole pipe structure, the brass tapered pegs were hammered into the holes, thus ensuring alignment of the pipes over the three floors of the building. The pipe structure was supported on the second and third floor levels.

4.3.7 Cooling Circuit

One half in. copper tubing was wrapped around the 8 in. pipe in a tight coil for about 11 in. length immediately upstream of the test section. By circulating cold water in this copper tubing, the pipe upstream of the test section was maintained very close to the incoming air temperature. Thus a step change in the wall temperature was obtained at the entrance of the test section. Cooling water was stored in a reservoir and a positive displacement gear pump circulated it through a shell and tube heat exchanger, the cooling coil and the reservoir. The heat exchanger was cooled by city water.

4.3.8 Radial Temperature Measurement Probe

To measure radial temperature profiles, a Pt-Pt+10% Rh thermocouple was used. The advantage in using this thermocouple over other materials is the ease in making thermocouples with very fine wire (.0005"). The high temperature range possible, the availability of high purity metals and corrosion resistance are the additional features in favour of this choice. High cost and low e.m.f./^{o}F are offset by the need to make thermocouple junctions (.001-.002" diameter bead) small enough to be used in a high temperature gradient environment. The thermocouple junction was supported by fusing the Pt. and Pt.+10% Rh. wires on the corresponding wires of 1/16 in. stainless steel sheathed ceramo. Another

thermocouple junction immersed in an ice-water mixture served as reference temperature.

The thermocouple in the probe holder assembly is shown in Figure 4.6. The probe holder assembly is long enough to fit in the port pipes. The flange on the probe holder has a circular shoulder to fit in the recess of the port pipe flange. The disc on the other end of the probe holder is machined to fit in the port hole in the test section and is contoured to be flush with the inside surface of the pipe. Careful machining and aligning was done to ensure that the probe holder fits in the port pipe and the in and out movement of the probe is smooth. A micrometer head was attached to the probe to assist in the precise location of the thermocouple junction by means of accurately machined 'Joe' blocks. A 1 1/4 in. long 1/16 in. diameter stainless steel needle was attached to the probe to act as a stopper so that the thermocouple junction does not hit the wall when inserted in the test section. It was observed by Pollock [P1] that the presence of any metal piece in the flow field would lower the temperature of the surroundings by acting as a heat sink. For this reason, the thermocouple junction was located 1 in. upstream from the stopper, a distance found to be sufficient after considerable testing of various designs.

4.3.9 Plate Thermocouple Probe

To measure the inside surface temperature of the test section a Pt-Pt+10% Rh 1/16 in. diameter Ceramo thermocouple

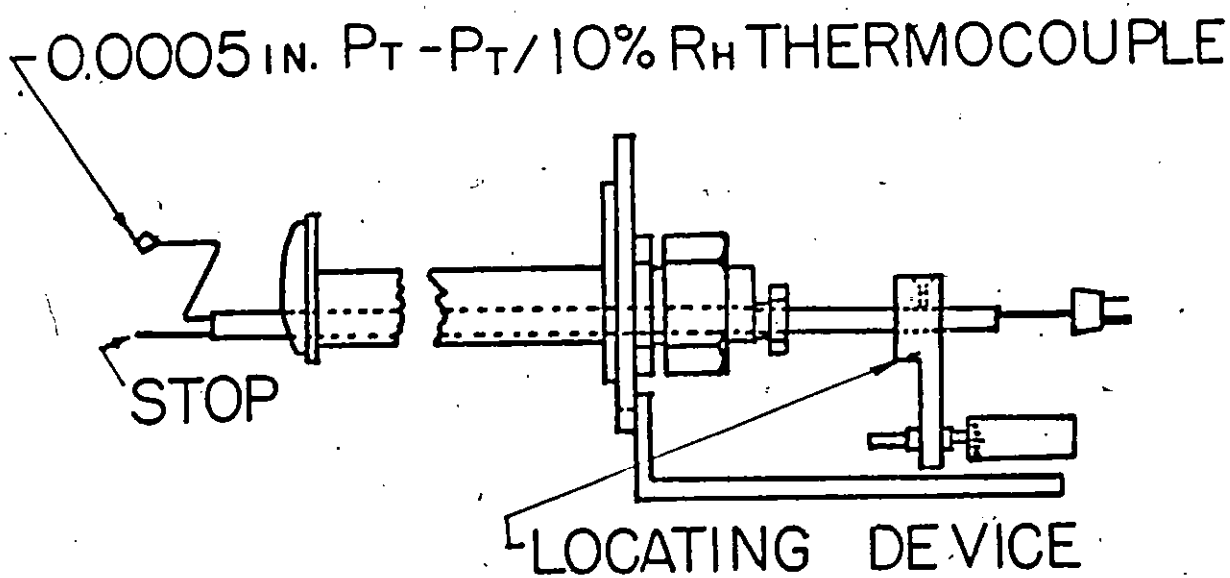

Figure 4-6. Thermocouple Probe Assembly.

was used. A 1/4 in. diameter 30 in. long stainless steel tube capable of in and out movement in the probe holder carried the Ceramo. A 1/16 in. diameter 1 in. long needle was brazed to one end of the 1/4 in. tube and a 1/4 in. diameter, 1 1/2 in. long ceramic tube was fastened on the needle. The free end of the ceramic tube was contoured to the same curvature as the test section inside surface. The thermocouple wires were butt silver soldered on a 0.2"x0.1"x.001" platinum foil. The platinum foil was supported on the contoured end of the ceramic tube and a groove cut on the latter accepted the thermocouple wires. Sauereisen cement was used to hold the platinum foil and the thermocouple wires in place. The ceramic material for the tube supporting the thermocouple was chosen to minimize the heat conduction along its length. By pressing the platinum foil against the test section inside surface, it was felt that this design ensured a true wall temperature measurement. This was indirectly tested by noting that all the radial temperature profiles extrapolated to the measured wall temperature within $5^{o}F$ in all the cases.

4.3.10 Velocity Measurement Probe

A constant temperature hot-wire anemometer (Flow Corporation 700 series) with built-in lineariser and temperature compensation circuit was used for the measurement of velocity profiles. The anemometer probe was a 36 in. long 1/4 in. diameter stainless steel tube. The probe was held in a probe holder

similar to the one used for the thermocouple probe with only minor modifications. The hot-wire sensors were a set of two .0005 in. diameter, .125 in. long platinum wires soldered across stainless steel prongs such that the wires were parallel to each other with 3/16 in. separation and in the same vertical plane.

Of the two sensors, one was for the measurement of velocity and the other was supplied with a very small current from the anemometer circuit and acted as a temperature sensor. This latter circuitry was to compensate for temperature changes in the flow and was called the cold wire. The cold wire was kept upstream of the hot wire because the former produced essentially no thermal wake; the separation between the two wires was enough to dampen any velocity wake. A stopper similar to the one used in the radial temperature measurement probe prevented the sensors from hitting the wall.

The calibrations of the temperature measurements probes and hot-wire anemometer are given in Appendix B.

4.4 Experimental Procedure

4.4.1 Isothermal Flow

A chosen flow rate of air was obtained by the proper selection of the sonic nozzle size and adjustment of its upstream pressure by means of the pneumatic control system. The barometric pressure and temperature of the flowing air were recorded for total mass flow calculations.

The sensors of the hot-wire anemometer and the thermocouple were located at a nominal distance of 0.010 in. from the

needle point end of the stopper. The actual distance was measured, by measuring with a 15X cathetometer, the distance of each point from a 0.004 in. diameter copper wire plumb-line, the weight of which was immersed in glycerine to minimize vibrations.

For the measurement of the velocity and temperature profiles, the location of the sensor relative to the wall was determined initially by locating the needle stopper against the wall, and by inserting accurately machined 'Joe' blocks (of known thickness) between the probe flange and a micrometer head attached to the probe stem externally. Each radial position was preselected and was essentially free of backlash or other such problems.

4.4.2 Non-Isothermal Flows

For the measurement of temperature and velocity profiles, a step change in wall temperature to a uniform wall temperature had to be approximated as closely as possible in the experimental test section. This was achieved by adjustment of the cooling water temperature and flow rate and the many powerstats controlling the local heat input. Because of interactions among the heaters on the test section, flanges and ports, this adjustment of powerstats was extremely tedious and time consuming (usually taking two to three days to achieve the desired result).

To ensure that no disturbance of flow is created, only one probe was inserted at a time.

The other ports had carefully contoured (to the inside diameter of the 8 in. pipe) plugs inserted when not in use.

The inside wall surface temperature was measured by holding the plate thermocouple probe hard against the wall for 15 minutes. Gas temperature at each preselected radial position was measured after the sensor was left at a given location for 15 minutes before a reading was taken. Since the temperature gradient was large near the wall, averaged temperature readings and r.m.s. temperature fluctuations were measured every 0.010 in. for the first five readings; thereafter the interval increased to 0.05, then 0.1 and finally 1.0 inches.

4.4.3 Signal Measurement

The output voltage signals from the hot-wire anemometer was 0-10 DCV while the thermocouple output was in millivolts. Due to the turbulent nature of the air flow, large fluctuations (~10%) were observed in the temperature and velocity signals. These voltage signals were fed to a voltage-to-frequency converter such that the output signal's frequency was proportional to the input voltage. The average value of the latter was obtained by counting and averaging the frequency of this signal over a time span of up to 100 seconds. A Hewlett Packard mode 2212B voltage-to-frequency converter and model 5321B digital frequency counter were used for this purpose. Since the range of the frequency converter is up to

1-DCV, a voltage divider with 10 MΩ impedence was used to reduce the input signal to less than 1-V.

For the measurement of the temperature fluctuations signal, a Flow Corporation model 12A1 Random Signal voltmeter with a time constant of 16 seconds was used. The millivolt signal from the thermocouple required amplification. A Bell and Howell 1-165 high gain D.C. amplifier was used for this purpose.

4.4.4 Non-Isothermal Velocity Profile Measurement

For lack of suitable calibration for the hot-wire anemometer under non-isothermal conditions, the velocity measurement was done by a 1/8 in. O.D. Pitot tube. The Pitot tube was used to calibrate the hot-wire anemometer under isothermal conditions. The large size of the Pitot tube was to ensure a coefficient of unity [A6]. Because of the difficulty of inserting the Pitot tube through the ports, the velocity measurements were made at 1 1/2 in. upstream of the exit. The size of the Pitot tube head prevented measurements any closer than 1/2 in. from the wall. The pressure differential across the Pitot tube was measured by a DISA model 9132H001 inclined micromanometer (inclination 1 in 10) and a cathetometer to view the alcohol meniscus. The velocity was calculated using the density of air corresponding to the existing temperature. The latter was obtained from extrapolation of measurements at the three ports.

4.5 Operating Conditions

Table 4-4 shows the operating conditions at which the air heating experiments were carried out.

Table 4-4

Air Heating Experiments - Operating Conditions

Run No.	T_o °F	Re_o	T_w °F
1	80	37535	175
2	79	24600	122
3	77	24600	420
4	77	24600	700
5	78.5	18150	126
6	79	18150	443
7	77.5	18150	745
8	85	9875	302
9	82.7	10000	744
10	68	7750	889

The maximum variation of temperature of the test section wall along the length was not more than 2% in any case. The interacting nature of the various heaters and the high thermal inertia of the test section made any finer adjustment very time consuming and tedious. At the test section inlet 97% of the mean wall temperature was reached within 1/2 inch

in the worst case. Adjustment of the water temperature in the cooling system maintained the section, immediately upstream of the test section, at the most $10^{o}F$ above the inlet air temperature. Thus the conditions of uniform wall temperature with a step change at the inlet were met.

4.5.1 Flow Regime Determination

These operating conditions were translated into the parameters of Metais' flow regime map [M1], and are shown in Figure 4.7. Also shown is the flow reversal band obtained from the flow visualisation study in section 4.2.6. It is observed that most of the experimental runs are in the mixed convection region. Since the boundaries between the various flow regimes are diffuse rather than sharp lines, the points close to the boundary are considered in mixed convections. Run No. 1 is definitely in the forced convection region. Run Nos. 9 and 10 are in the flow reversal region and it was expected that the flow reversal would take place. Since the proposed numerical solution of the conservation equations considers only unidirectional flow, it will be used to generate predictions of the temperature and velocity profiles for comparison with the results from the experimental runs 1 to 8.

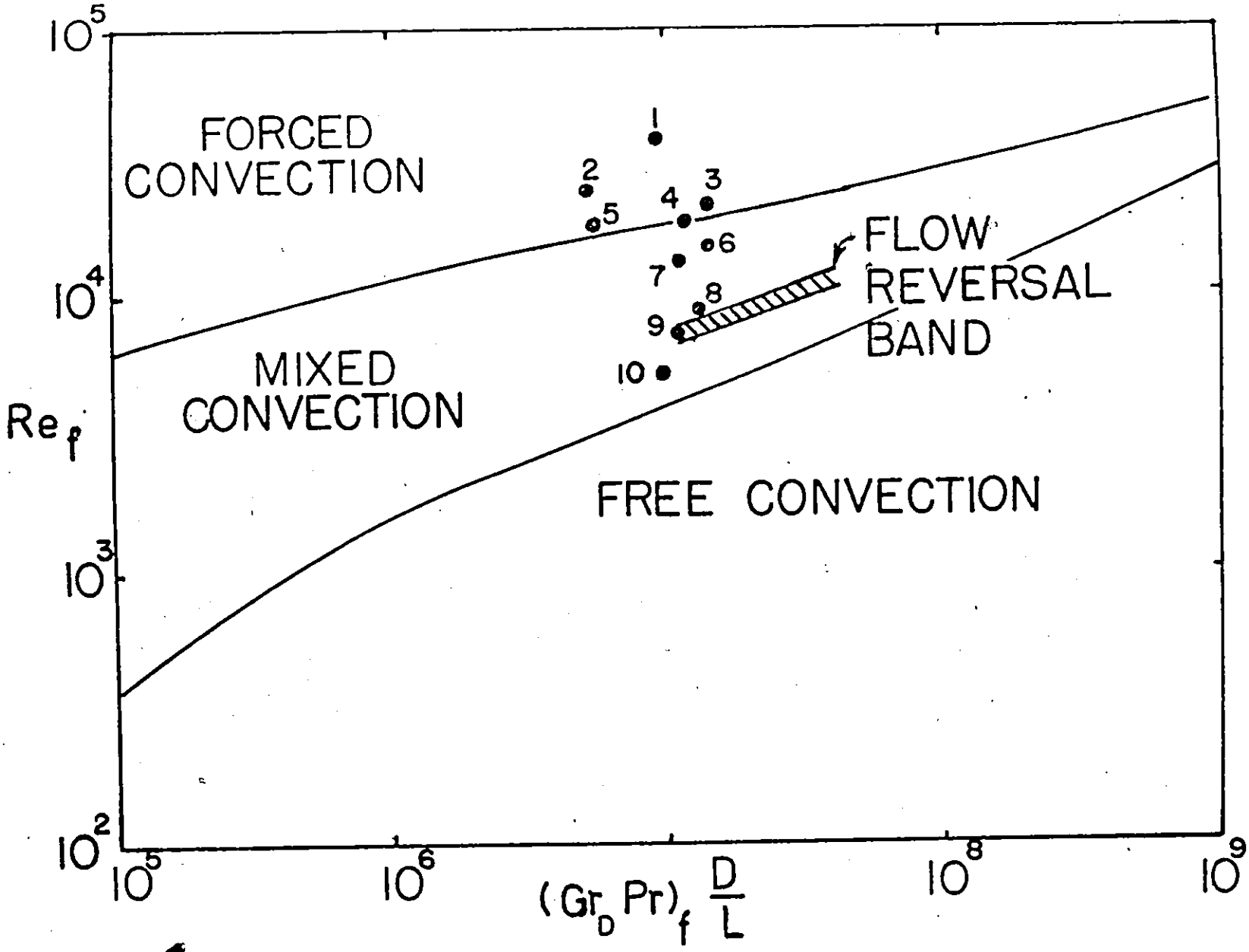

Figure 4-7. Air Heating Experiments and Flow Reversal Band in Convection Regime Map Assuming Dynamic Similarity.

CHAPTER 5

RESULTS AND DISCUSSION

The experimental apparatus was developed and measurements were obtained in a planned sequence. Since advancement to each stage in the sequence rested on the successful measurements and analysis of the previous stage, the same sequence has been adopted in reporting, analysing and discussion of the results. This sequence is as follows:

The ability of the apparatus to provide a fully developed, symmetric velocity profile at the entrance of the test section was tested; the temperature profiles under low wall-to-fluid temperature were measured and compared with those predicted to test the computation method; the temperature and velocity profiles were measured and analysed for higher temperature differences.

5.1 Isothermal Velocity Profile

As an initial boundary condition in the theoretical solution, the flow entering the test section has been assumed to be isothermal, symmetric and fully developed. These conditions have been chosen so that the laws of turbulent momentum transport, which were developed from fully developed flow, can be used. To ensure that the flow is fully developed, a great amount of effort has been directed towards the design of the flow development section upstream of the heater. 'Rule-of-thumb'

recommendation suggests that a flow development length of at least 40 diameters is required to obtain a fully developed velocity profile. Since the maximum height available in our laboratory was only slightly greater than 40 diameters, it became imperative to design an entrance section that would promote the early development of the flow field. Moreover, the design must ensure that the flow symmetry is obtained. After a large number of trials on various designs of the entrance section, a symmetric isothermal flow was obtained.

Appendix E lists the details of the series of design changes and their effect on the velocity profile.

Attempts made to measure the velocity profile, across the cross-section of the test section by the technique of cross-correlation of signals from two hot wire anemometers, are described in Appendix F. The failure of the technique to give reliable measurements near the wall is attributed to the break down of the assumption that turbulence travels with the mean local velocity in this region. This technique was attempted because it is independent of interference of the temperature field (in contrast to the conventional hot-wire anemometry).

Velocity profile measurements by a constant temperature hot-wire anemometer were made and the dimensionless velocity, u^+, plotted against dimensionless distance, y^+, is shown in Figure 5-1 for isothermal turbulent flow, approximately 40 diameters downstream from the entrance. The experimental observations at two Reynolds numbers are compared with the theoretical profiles obtained from the modified Reichardt eddy

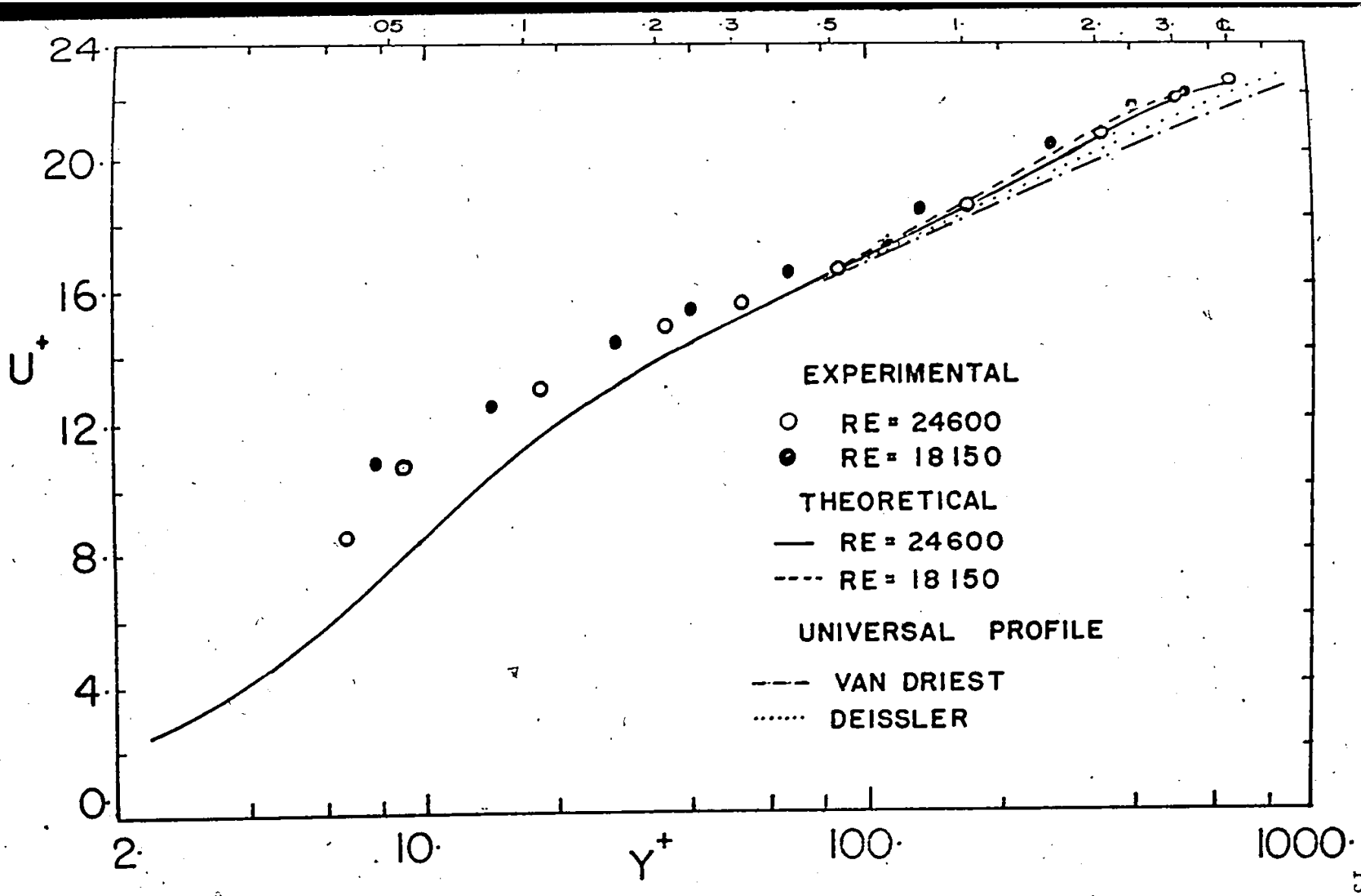

Figure 5-1. Comparison of the Theoretical and Experimental Isothermal Velocity Profiles.

viscosity expressions (Equations 3.31 to 3.33). Good agreement (< 3%) between the two is obtained at the centre of the pipe and for a major portion (up to 1/4" from the wall) of its cross section. The straight line relationship given by the universal profile is also shown for comparison. Deissler used slightly different constants than those used by Van Driest in the universal profile. The departure of experimental observations from universal profiles near the centre of the pipe is due to the fact that the latter gives a non-zero velocity gradient at the centre. The excellent agreement with modified Reichardt profile indicates that smooth and symmetrical velocity profile with zero gradient at the centre, characteristic of the pipe flow, has been obtained.

However, near the pipe wall, the experimental velocity profile begins to deviate from the theoretical one. The higher experimental values could be attribued to one or more of the following reasons.

(i) Wall Proximity

Near the wall, the presence of the wall changes the heat transfer phenomena occurring at the hot-wire sensor of the anemometer. In this region, heat is conducted from the wire, across the gap between the wire and the wall, to the wall which acts as a heat sink. Thus the heat transfer rate at the wire is higher than that which would occur in an infinite gas medium. Thus errors in the velocity measurement become progressively greater as the wall is approached unless an estimate of conduction heat loss is made and accounted for.

Richardson [R5], Wills [W4] and Repik and Ponomareva [R6] studied the effect of wall proximity on hot-wire anemometer response. On the basis of these investigations, the influence of the wall in the present case should only become significant at $y^+ < 3$. Thus the higher velocities observed for $y^+ < 30$ can not be attributed to the influence of wall proximity.

(ii) Developing Velocity Profile

The turbulent flow in the pipe has been developed from a flat velocity profile, at the entrance of the column, to a fully developed one at the test section. Even though symmetry of the velocity profile has been obtained for the Reynolds number region of interest, changes in velocity profile may still be taking place. If it is assumed that the velocity near the wall is higher than the predicted one then for a fixed mass flow rate, the measured velocity should be lower than that predicted near the centre. However, this criterion cannot be used to establish if the wall velocities are actually higher. Because the higher mass flow near the wall can be compensated for, by very slightly lower velocities (within experimental error) over the central cross section of the pipe. Sleicher's [S14] velocity profile measurements at 50 and 80 diameters show that at 50 diameters, the profile is still developing but it is the central core region of the cross section that is undergoing adjustments rather than the wall region. Hence it is unlikely that higher velocities in the wall region in

the present investigation are due to the fact that the flow is not fully developed.

(iii) Influence of Sound on Heat Transfer from the Wire

Considerable sound was generated by the turbulent phenomena associated with the gas expansion at the entrance of the system. The presence of sonic orifice in the system might have caused resonance in the flow near the wall (even though the pipe downstream from the sonic orifice was lined with cork and the entrance to the column had a large amount of obstruction to the flow). If it is true then the pressure changes near the wall resulting in density changes can give higher measured velocities.

(iv) Calibration

At the low velocities (0-10 ft/sec) encountered in this investigation, the calibration of the hot-wire anemometer posed a major problem. A DISA flow nozzle (model 55D 90) was used to calibrate the Hot-wire anemometer. It is claimed to provide a flat velocity profile over its cross section for velocities greater than 1.5 ft/sec. The total mass flow through the nozzle was held constant and measured by the use of a sonic orifice with controlled upstream pressure. The range of the flow could be increased by changing the size of the orifice. The calibration system was mounted such that the flow from the nozzle was downward and the wire was in the same orientation as used in the test section; thus natural

convection effects, if present, should be the same. It was found that with the calibration of the hot-wire anemometer thus obtained, it always measured low velocities (approximately 12%) as compared to the theoretical values at the centre of the test section. A thorough check of the calibration system and repeated measurements confirmed this observation.

It was then decided to calibrate the hot-wire anemometer in situ. At the centre of the 8" column, the anemometer and a Pitot tube were alternatly placed to measure the air velocity. By changing the total mass flow rate, a calibration curve for the anemometer, using the Pitot tube as a primary standard, was obtained. The Reynolds number based on the Pitot tube head was always greater than 100 so that the Pitot tube coefficient was taken equal to 1. It was found that the centre line velocity measured by the Pitot tube was in excellent agreement with the theoretical predictions. Around 3 ft/sec, however, the pressure differential generated in the Pitot tube was of the order of 0.05 mm H_2O. It becomes difficult to measure such low pressure differences even with an inclined micro-manometer (inclination 1 in 10) and a cathetometer (magnification 8) to view the manometer meniscus. Further increase in the inclination resulted in loss of reproducibility. Visual averaging of the meniscus movement was another factor in reducing the accuracy of the measurement. At such low

pressures, surface tension effects also become significant causing a further loss in accuracy. The details of the calibration procedure and the calibration curve is given in Appendix B-5.

Since the flow coming out of the DISA flow nozzle had a different turbulence structure (laminar) than the flow at the centre of the 8" column (turbulent), it may be hypothesised that the hot-wire anemometer readings are influenced by the turbulence level of the flow. Perhaps at these low velocities, natural convection effects are changed by the turbulence phenomena. In any event, these observations suggest that the calibration may not be the same near the wall where the intensity of turbulence goes through a peak and approaches zero in the laminar sub-layer. This experience was unexpected and in the absence of information on these phenomena and on the basis of the analysis presented, it was assumed that the velocity profile corresponded to the fully developed one.

5.1.1 Previous Work

Experimental data from the previous workers in Reynolds number region of interest (<30000) is scarce. Most of the investigators have used pipes less than 2" in diameter and for the same value of y^+, the local mean velocity is four to five times than that in the present study. Use of higher density flow medium [C5] alleviates the problem of the measurement of low differentials. Thus inaccuracies in velocity measurement are

greatly reduced.

The classical work of Laufer [L1] who used 9.7 in. diameter pipe reported 50000 as the lowest Reynolds number studied. Sleicher [S14] concluded that Laufer's data for $y^+ < 30$ and Re = 50000 is not representative of the pipe flow because of the anomalies in the mean velocity measurement in this range. Johnk and Hanratty reported velocity profile measurements for a 3" diameter pipe but only for $y^+ > 30$.

Reynolds et al. [R3] reported deviations (lower values) from the theoretical predictions for Re = 15000 for $y^+ \leq 20$ for his measurements in 1.61" diameter pipe. This was attributed to the presence of a slot, machined in the pipe wall to allow the entrance of the velocity probe, thus generating additional turbulence in the flow field. In the present investigation, however, great pains were taken to ensure, the probe holder fits flush with the port hole so that smooth and continuous pipe wall is obtained. However, the data of Pennell et al. [P7] for 1.4" diameter pipe wall did not show the deviation observed in [R3] perhaps because the measurements were done at the pipe exit.

In conclusion, it may be stated that the experimental velocity profiles agree with the predictions from modified Reichardt eddy viscosity expression over 80% of the cross section. Near the wall $y^+ < 30$, the observed higher velocities are due to difficulties in such low velocity measurements. In view of these facts and that the symmetric velocity profile was obtained from

asymmetric entrance flow distribution, it is reasonable to assume that the flow is fully developed. Hence for the purpose of providing initial boundary conditions to the solution of momentum, mass and energy conservation equations, the theoretical profile given by the modified Reichardt expression can be used.

5.2 Temperature Profiles

Radial temperature profiles in the flow field were measured at the three ports for the experimental runs listed in Table 4-3. When these gas temperature profiles were extrapolated to the wall, this temperature agreed with the wall temperature as measured by the surface temperature probe. In the worst case (at the highest wall temperature) the difference was about $5^{o}F$. Figure 5.2 shows a set of typical measured temperature profiles, in the dimensionless form, for the top, middle and the bottom ports for Run No. 3. The data for all the runs are listed in Appendix G. Starting with a value of 1.0 at the wall, the dimensionless temperature sharply decreases in the wall region and asymptotically approaches a constant value (depending upon its axial location) in the central region of the pipe. As the gas picks up heat along the length of the test section, the temperature at every radial point rises as it should if the flow is unidirectional at all the ports. It is also observed that the effect of heating has been felt only in the wall region and the core of the fluid remains at its inlet temperature. These observations are characteristics of a developing thermal boundary layer.

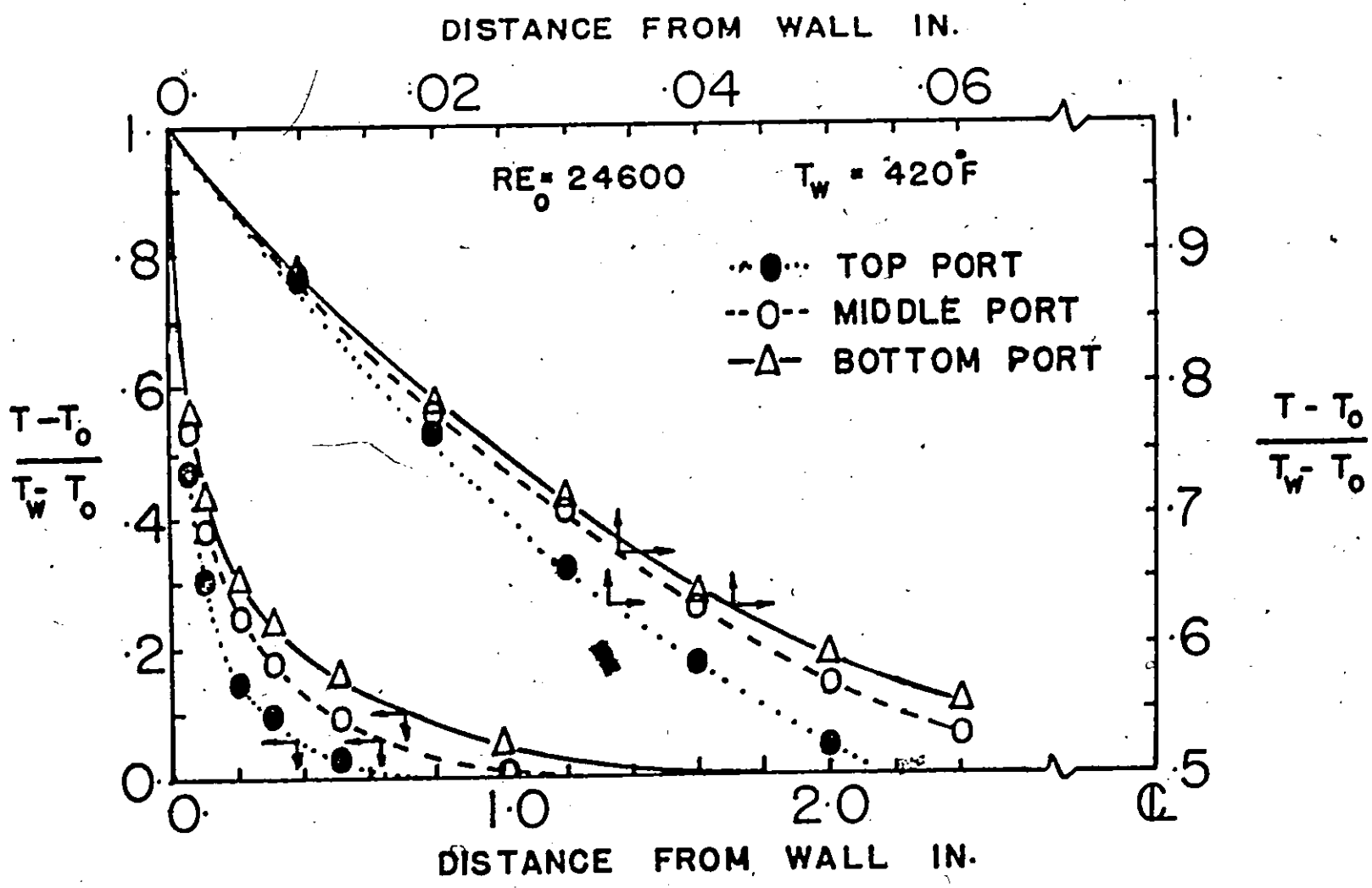

Figure 5-2. Measured Radial Temperature Profiles for Run No. 3.

The thickness of the thermal boundary layer increases with axial distance. It is observed that the temperature difference between the wall and the centre line, a measure of driving force for heat transfer, remains constant while the temperature gradient at the wall decreases with increase in axial distance. This phenomenon gives rise to a decreasing heat transfer coefficient in the entrance region. This characteristic behaviour for the measured temperature profiles was observed for all experimental runs except 9 and 10.

5.2.1 Flow Reversal

On the basis of flow visualisation experiments, it is expected that the experimental conditions used in Runs 9 and 10 should give rise to flow reversal because of the comparable magnitude of the opposing buoyancy and inertia forces. The measured temperature profiles for these runs are shown in Figures 5.3A and 5.3B and these depict a different behaviour than shown in Figure 5.2.

In the wall region, $(R-r) < 0.06$ in., the regular rise of the temperature profile from top to the bottom port is no longer observed. In Figure 5.3A, the bottom port profile is consistently highest but the top port profile is higher than that at the middle port with a crossover occurring at about .060 in. away from the wall. For greater distances away from the wall, the temperature profiles show the regular behaviour characteristic of the entrance region. At 0.03" away from the wall, the measurements of the average temperature showed a standard

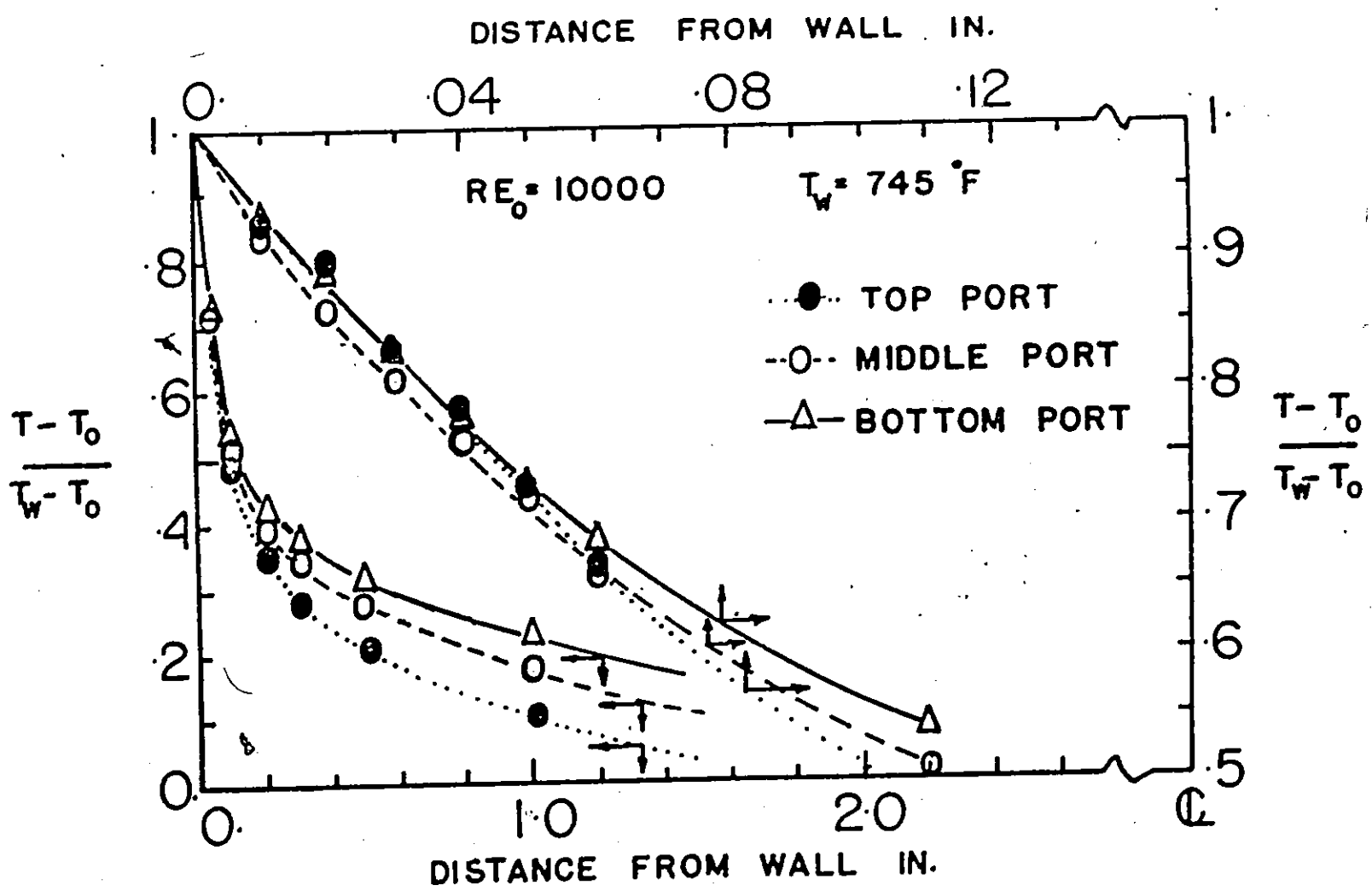

Figure 5-3A. Measured Radial Temperature Profiles for Run No. 9. Flow Reversal expected from Dynamic Similarity Considerations (Figure 4-7).

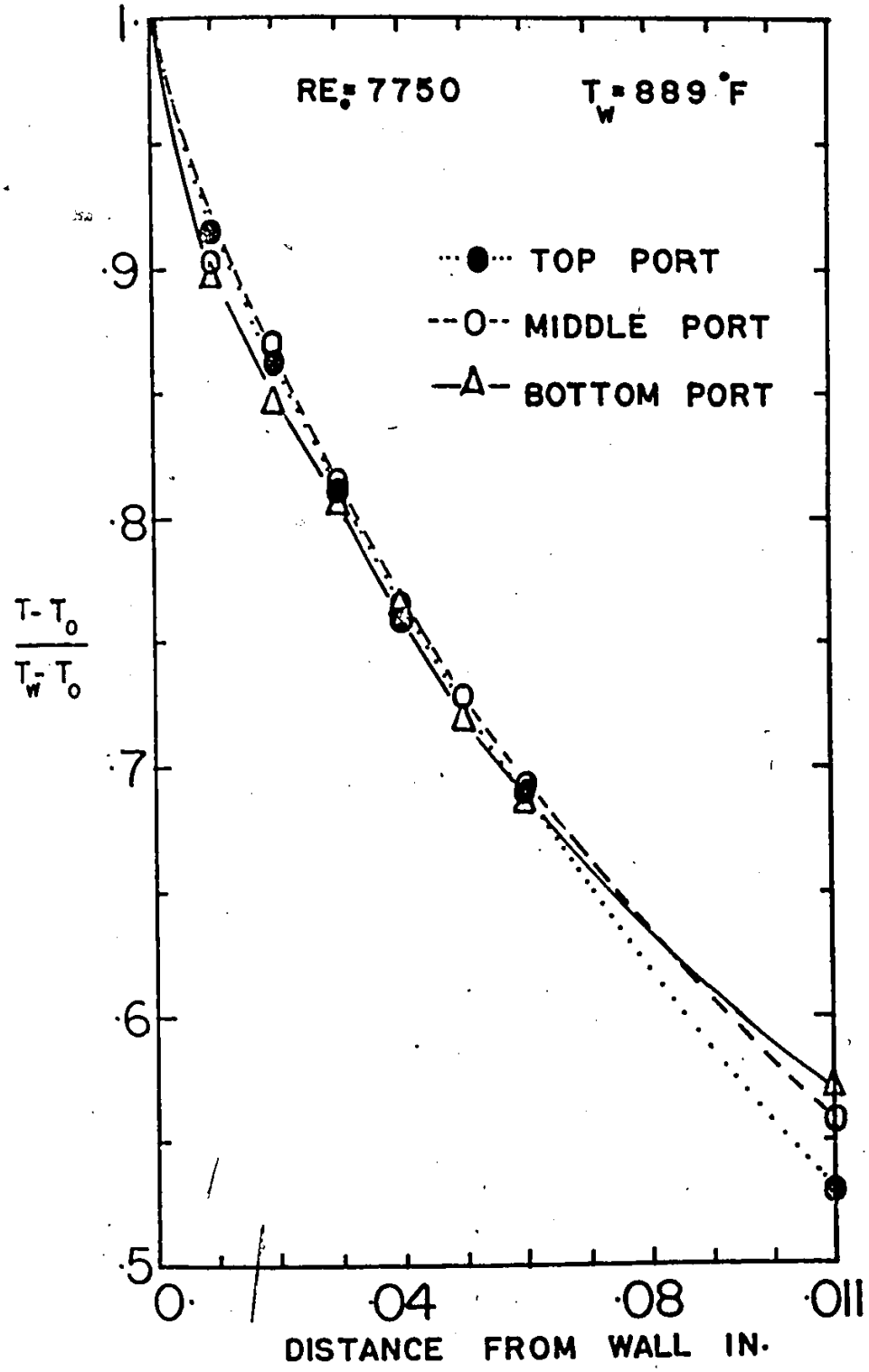

Figure 5-3B. Measured Radial Temperature Profiles for Run No. 10. Flow Reversal expected from Dynamic Similarity Considerations (Figure 4-7).

deviation of 4.87°F (where the root mean square temperature fluctuation was of the order of 35°F) for five replicates. Thus on statistical grounds, the 13°F difference between the top and the middle port can not be attributed to the inaccuracies in experimental measurements. In Figure 5.3B, a similar behaviour is shown except that now the bottom port profile is the lowest of all, though the separation between the profiles is not as great. At 0.01 in. away from the wall, the standard deviation (for five replicates) of the average temperature measurement is 3°F. Thus the 8°F difference between the top and middle port, and 6°F between the middle and the bottom port is significant. It has been shown by Pollock [P1] that the radiation and conduction errors in temperature measurement under flow conditions, similar to those in the present investigation are negligible.

The observations of Hall and Price [H5] for opposing turbulent free and forced convection from a vertical plate in a square duct, can be examined with reference to the unusual behaviour of the temperature profiles for runs 9 and 10. At a fixed plate temperature, the radial temperature profiles were observed for down flow average velocities of 0.64 and 0.39 m/sec. Figures I13.5 and 113.7 of [H5] can be combined to compare the temperature profiles, for the two flow rates, at 0.15 m and 0.75 m from the top of the heated plate. For the high flow rate, the radial temperatures increased with axial distance while for the low flow rate, higher temperatures were recorded at the upstream location than at the downstream location. This is only possible if, ~~at low~~ flow rate, the heated fluid is recirculated to absorb

more heat. That is, the pockets of fluid at some downstream location, which had been heated in their downward motion, started moving up in the wall region and absorbed more heat; they thus created higher temperatures at the upstream location. Flow visualisation in situ by smoke confirmed the occurrence of flow reversal at 0.39 m/sec. These observations of Hall and Price can not be compared with the flow reversal band obtained in the present investigation, as the boundary layer on a flat plate is quite different from that in a pipe.

Flow reversal phenomenon in a turbulent flow is, however, more complex than the simplified explanation given above. Flow reversal can occur with a small perturbation to the unstable equilibrium between the buoyancy and the inertia forces. Asymmetry in the flow field can also trigger it. The occurrence of flow reversal is thus a sudden phenomenon. The flow visualisation experiments of the present investigation where no clearcut pattern of initiation and propagation, with axial distance, of the circulating eddy could be observed, substantiates the above reasoning. The occurrence of flow reversal generates a zero velocity streamline away from the wall. Because of the unstable aspect of the turbulent flow, the radial location of this streamline fluctuates about some mean value. Moreover, the high intensity of the gas temperature fluctuations indicates that there is a much higher level of turbulence under these conditions, thus leading to higher heat transfer rates. In a flow situation with flow reversal, the temperature profiles will be determined by the net effect of the hot fluid coming from the

downstream locations and the high rate of turbulent exchange across the circulation eddy. The radial temperature profiles shown in Figures 5.3B for Run no. 10 indicate the combined effect of the two phenomena. The decrease in temperature with axial distance at 0.01 in. from the wall indicates the dominance of the rising hot fluid. As we move away from the wall, the turbulent exchange process, with its cooling effects, starts to take over. Intuitively, it may be said that the region between 0.03 to 0.06 in. away from the wall could possibly be the centre of the circulating eddy. It is observed that the operating conditions for Run no. 9 are such that it lies on the flow reversal band, separating the unidirectional and circulating flow regimes. It being the unstable region where flow pattern may be fluctuating between the two regimes intermittantly, irregular temperature profile behaviour is observed in Figure 5.3A.

It can be concluded that the different behaviour of the temperature profiles observed for Run nos. 9 and 10, from those observed in Run Nos 1 to 8, is due to the occurrence of flow reversal near the wall. The dynamic similarity consideration along with flow visualisation experiments confirm this conclusion. Since the numerical solution of the conservation equations is restricted to unidirectional flow, only runs from 1 to 8 will be considered for comparison with the numerical predictions.

5.3 Comparison of Non-Isothermal Experimental and Predicted Profiles

Since the experimental system and the operating conditions correspond very closely to those employed in the finite

difference solution of the conservation equations (Chapter 3), the experimentally observed temperature and velocity profiles can be compared directly with the predicted ones. In the numerical solution, the following constitutive equations were employed.

(i) The turbulent velocity profile at the heater inlet was obtained by substituting the modified Reichardt expressions for eddy viscosity, Equations (3.31 to 3.33), in Equation (3.37).

(ii) The modified Reichardt expressions were also used in the heated section to evaluate eddy properties. The shear stress at the wall was calculated from Taylor's modification for the friction factor, Equation (3.34), to account for the thermal effects in the flow field.

(iii) Physical properties were evaluated from the polynomials obtained by regressing the available tabulated data (Appendix A).

(iv) The eddy conductivity was assumed to be equal to the eddy viscosity obtained from Equations (3.31 to 3.32).

It is therefore important to note that the predicted results have accounted for the temperature varying physical properties and for the local buoyancy force. The marching solution requires that the flow be unidirectional. Since the equations are coupled, an iterative procedure was used and all the conservation equations were solved simultaneously for any particular location. The predicted temperature profiles at all the three port locations were interpolated and compared with the experimental

observations. The velocity profile was observed at 1.5 in. upstream of the exit of the heating section and comparison was made with the corresponding predictions.

A comparison between the observed and predicted temperature profiles is shown in Figure 5.4 for the bottom port ~~for~~ various runs. Since the thermal boundary layer extends only a short distance from the wall into the flow field, the predicted and the observed results in this region require close examination. The predicted results are in excellent agreement with the experimental ones for Run No. 1, where the buoyancy effects are small. The predicted results, however, do not compare well for the other runs, the deviations becoming greater as the wall temperature increases. Similar behaviour was observed at the other two port locations. For the experimental conditions of Runs 7 and 8, the numerical solution became unstable. In these cases, flow reversal was indicated since the flow velocity near the wall became zero as a result of the opposing buoyancy force. As will be shown later, this does not necessarily mean that flow reversal has actually occurred. Numerical solutions for Runs 9 and 10 were not attempted since flow reversal was indicated by dynamic similarity considerations and irregular behaviour of the temperature profiles was observed.

In the numerical solution of the conservation equations, it was assumed that the contribution of the axial diffusion term is negligible as compared to the radial diffusion. Pollock [P1] showed that this is true for Reynolds numbers of the order of 10000 or higher, even in the immediate entrance

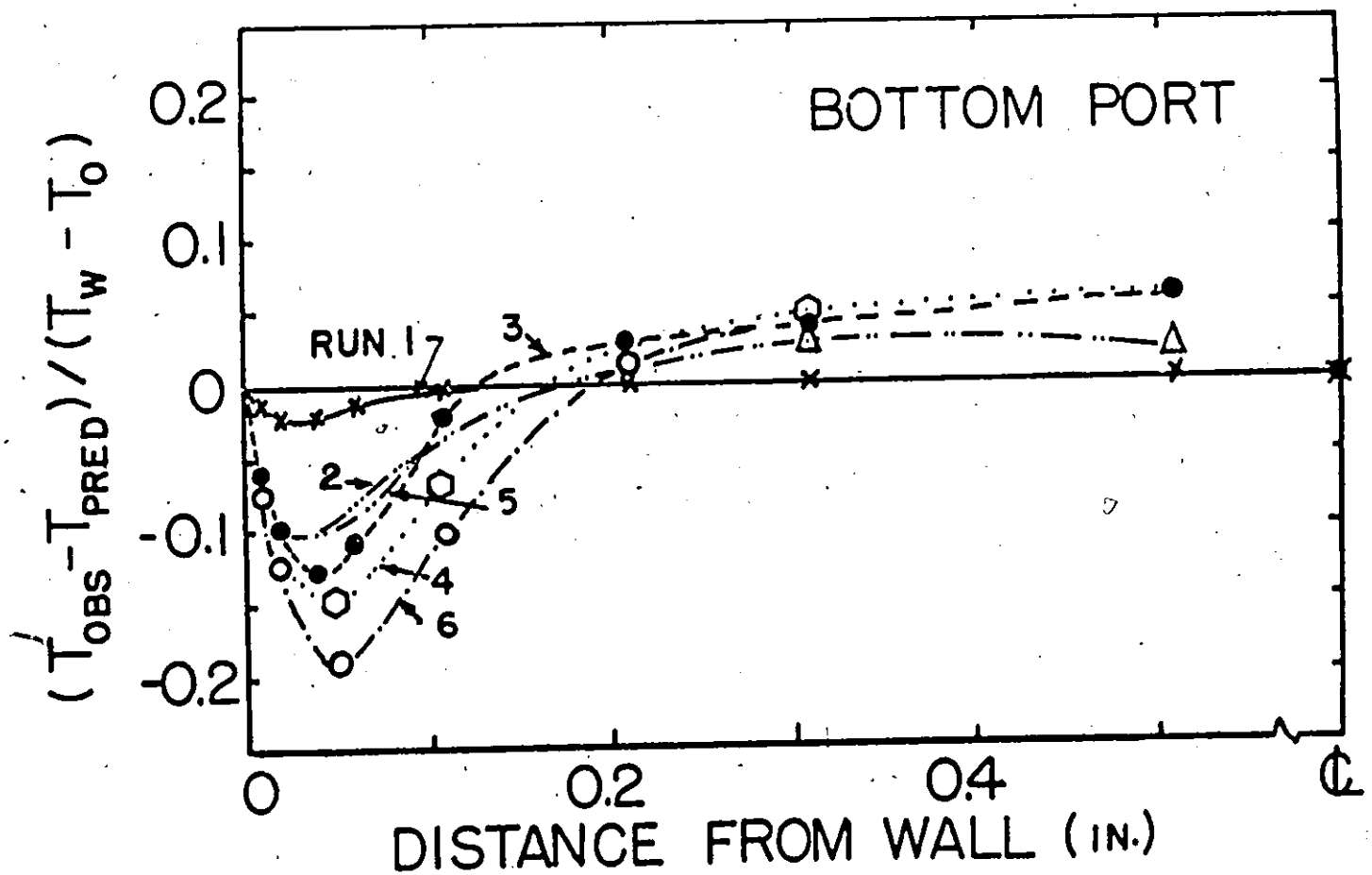

Figure 5-4. Comparison of the Observed and Predicted Temperature Profiles for Various Runs for the Bottom Part.

region. Its validity was also checked in the present investigation by accounting for axial diffusion in the energy equation using simplifications to preserve the parabolic nature of the partial differential equation.

It can thus be concluded that the progressively increasing discrepancy between the observed and predicted temperature profiles, with increasing relative magnitude of the buoyancy force suggests that the modelling procedure for turbulent flow is inadequate. A number of reasons for this inadequacy can be suggested, such as:

(i) The changing physical properties of the fluid affect the turbulent properties in the thermal boundary layer and these must be accounted for in the eddy diffusivity expressions.

(ii) The turbulent Prandtl number is not unity.

(iii) The shear stress distribution, assumed to be the same as for isothermal flow, is different when the buoyancy forces are present and consequently the turbulent properties are changed.

(iv) The turbulent phenomena is quite different from that occurring in isothermal flow and the empirical expressions developed from isothermal measurements are not valid. This is especially true for a developing thermal boundary layer.

Each of these effects will be discussed in turn.

5.3.1 Various Eddy Diffusivity Models

A comparison of the two most popular eddy viscosity models was made in section 3.6.1, and it was concluded that the modified Reichardt model is superior to that of Van Driest. The latter does not consider zero slope of the velocity profile at the centre line of the pipe and the velocity profile does not integrate to the total flow. The modified Reichardt's model is free from both these defects and this is the reason it was adopted in the present numerical solution. However, when this model was not found adequate, Van Driest's model was tried to see if it was any better. McEligot [M13] in his numerical solution study of the laminarization of forced convective flow in a pipe, suggested a modification to Van Driest's model. Instead of assuming Universal velocity profile in the core of the fluid, the exponential expression (Equation 3.29) of the wall region is assumed to be valid over the whole cross section. Figure 5.5 shows the comparison of the observed and predicted temperature profiles for Run No. 3, using two-equation and one-equation versions of the modified Reichardt and Van Driest models. Their complete expressions are listed in Table 5-1. It is observed that all the turbulent exchange models follow the same pattern and do not give very much different results. One equation version of Van Driest's model, VD10, seems to be the best of all of them. However, a comparison of the predicted and observed velocity profiles indicates that model VD10 gives lower velocities near the centre than those given by the other models and the observations by Pitot tube, Fig. 5.6. Moreover, for the case of the develop-

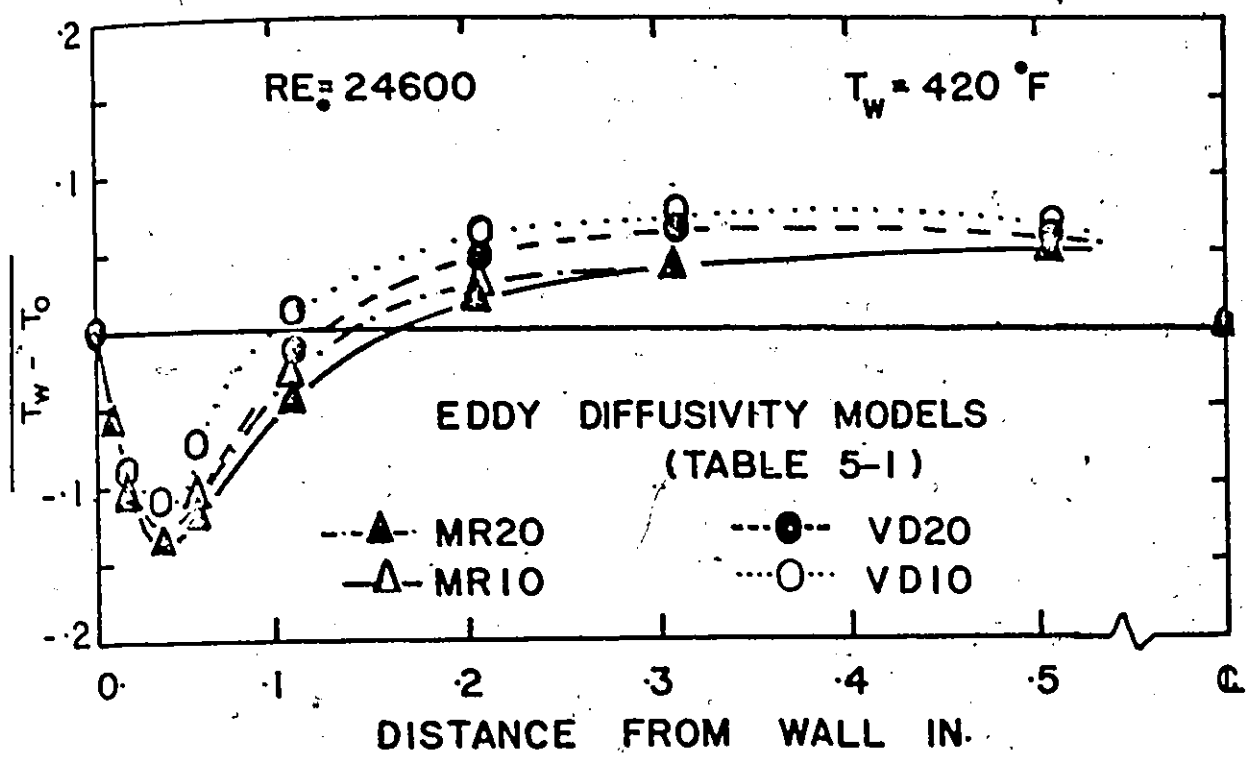

Figure 5-5. Comparison of the Observed and Predicted Temperature Profiles for the Bottom Port, Run No. 3, using Various Eddy Diffusivity Models.

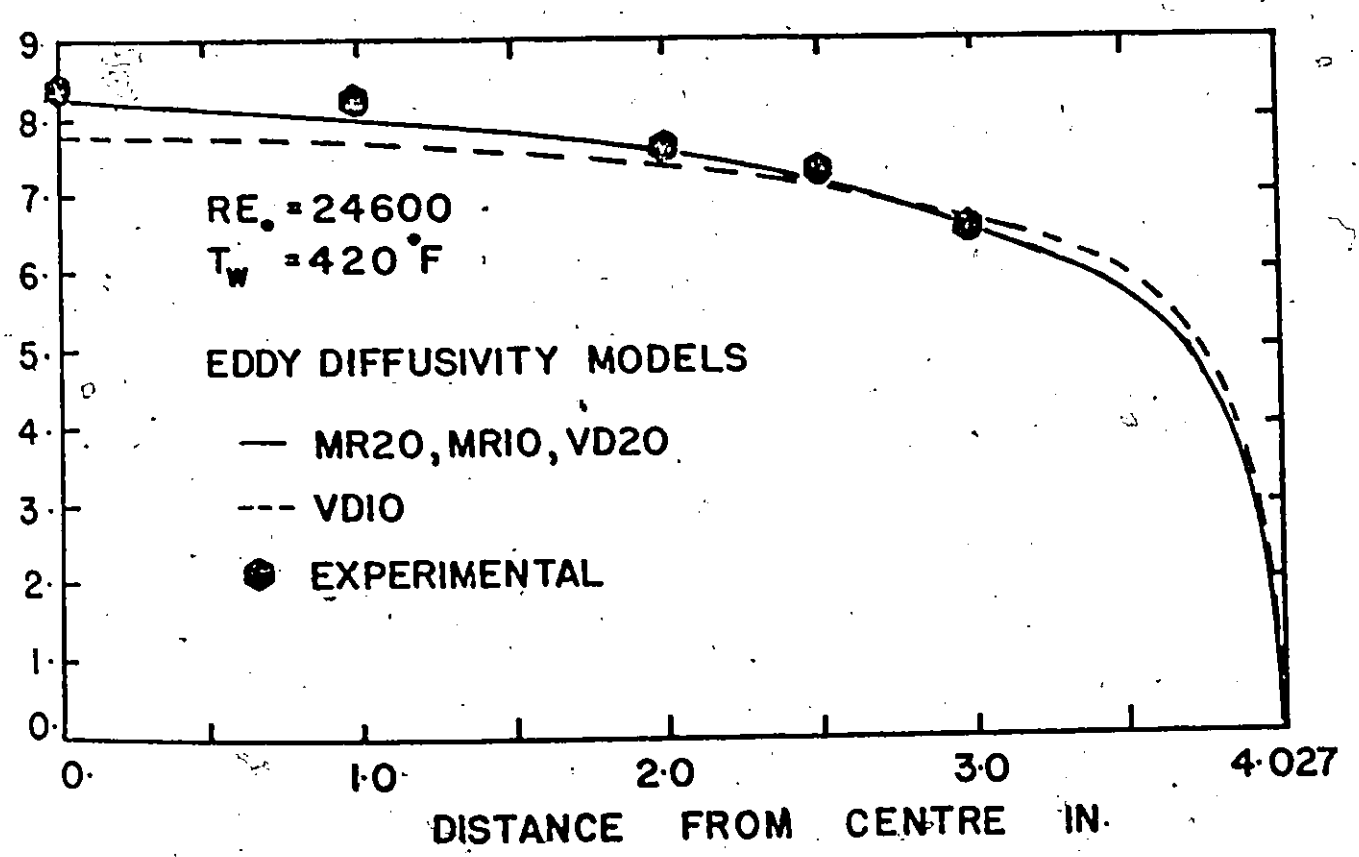

Figure 5-6. Comparison of the Observed and Predicted Velocity Profiles at 1 1/2" Upstream the Exit of the Test Section, Run No. 3.

ment of the velocity profile under isothermal conditions, model VD10 was found to give lower velocities at the centre than the other models. It was thus concluded that the model VD10 was not suitable. It is difficult to make any distinction between the rest of the models on the basis of a comparison with the measured velocity profile. A comparison of temperature profiles indicates that the two versions MR10 and MR20 of Reichardt's model are slightly better than model VD20. This, in addition to the other deficiencies in VD20, discussed in section 3.6.1, helped in eliminating this model too. Since there is not much difference between the results from models MR10 and MR20, the latter is chosen for future discussion.

5.3.2 Effect of Physical Properties

Most of the theoretical analyses of convective heat transport [P1, S1, M12] were based on the assumption of constant physical properties. This assumption certainly makes the computational problem a lot easier; however, it can be justified only when relatively small temperature differences exist. With high speed and large memory digital computers this restriction can be relaxed.

Note, for example, that by assuming a constant density fluid, unrealistic velocity profiles will be predicted, even if all other effects remain the same as in isothermal flow. In this case, the velocity profile would remain constant although, in fact, with high wall temperatures, the fluid in the region of the wall must accelerate by virtue of the expansion of the gas.

At the same time the total mass flow rate over any cross section of pipe must remain constant.

Since the parameters in the turbulent exchange models have been derived from the measurements made in isothermal or near isothermal flows, these parameter estimates may be incorrect under the present circumstances. In the absence of parameter values for the particular conditions employed here, these values must be assumed to apply.

On the other hand, the effect of physical property variation on the dependent and the independent variables in these expressions may have to be accounted for. Traditionally, physical property variation has been accounted for by evaluating all properties at some particular temperature; either at the bulk temperature (cup mixed temperature) or the film temperature (for example, the average of the centre line and wall temperatures). On the other hand, it can be argued that the turbulent characteristics are dependent on those phenomena occurring in the region of the wall and therefore, the properties should be evaluated at the wall temperature. It may also be argued that, since there is a significant variation of physical properties throughout the thermal boundary layer and since the turbulent exchange expressions are applicable to most fluids with widely varying physical properties, the physical properties evaluated at the local temperatures in the boundary layer should be used in turbulent exchange models. Goldmann [G6] adopted this idea and suggested that the turbulent properties should be

a function of the dimensionless radial distance from the wall and defined this distance as:

$$y^+ = \int_0^y \sqrt{\frac{\tau_w}{\rho}} \frac{1}{\nu} dy \qquad (5.1)$$

where properties are evaluated at the local temperatures.

Figure 5.7 provides the comparison of the observed and predicted temperature profiles for inlet Reynolds number of 24600 and $T_w = 420^oF$, using various choices of physical property evaluation for use in modified Reichardt eddy viscosity expressions, Equations (3.31 to 3.33). It is observed that none of the choices are able to match the predicted temperature profiles to the experimental values. The choice of wall temperature seems to be the worst one while use of local or film temperatures or Goldmann's equation did not give very much different results from each other. Property evaluation at bulk temperature gives somewhat closer values only near the wall. The sum of squares of temperature differences between the observed and the predicted values across the cross section, is the highest for the case when properties were evaluated at wall temperatures and the lowest when evaluated at the bulk temperature. Even though the use of local properties does not give the lowest sum of squares, it is chosen for further discussion, as being the most logical one, on the basis that it represents the actual conditions in the flow field rather than an arbitrary choice of temperature valid for the entire cross section of the pipe.

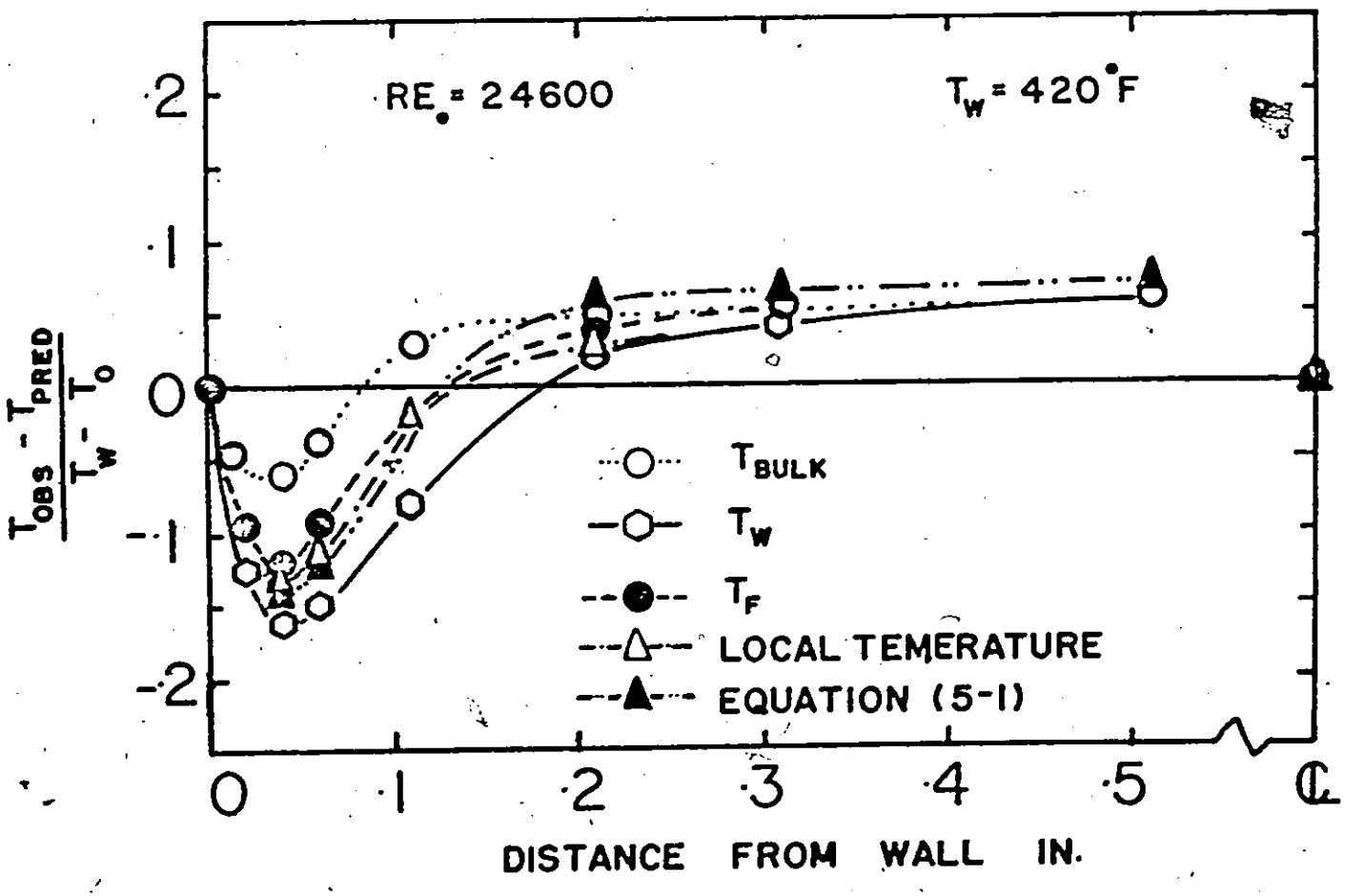

Figure 5-7. Comparison of the Observed and Predicted Temperature Profiles for the Bottom Port, Run No. 3, Evaluating Physical Properties at Various Characteristic Temperatures in Eddy Diffusivity Model.

5.3.3 Turbulent Prandtl Number

The breakdown of Reynolds analogy, i.e., equality between eddy properties of heat and mass transport has been observed by many authors. It has been found that the turbulent Prandtl number, $Pr_t = \varepsilon_m/\varepsilon_h$, is not only different from unity but is a function of radial location and Reynolds number of the flow. Quarmby and Quirk [Q1] based on their experimental data proposed an empirical expression for Pr_t as a function of radial location but independent of Reynolds number, viz.,

$$Pr_t^{-1} = \frac{\varepsilon_h}{\varepsilon_m} = 1 + (4[illegible])(R-1) \qquad (5.2)$$

This expression is simply a best fit in the experimental data and there is $\pm$ 15% scatter around it.

Use of this equation to evaluate eddy conductivity from the values of the eddy viscosity given by modified Reichardt expressions, (Equations 3.31 to 3.33), was attempted for the present situation. Figure 5.8 compares the predicted and the observed temperature profiles for Run No. 3. Also shown for comparison are the predictions using Reynolds analogy. It is observed that the use of Quarmby's equation gave some improvement over the Reynolds analogy assumption but is far from adequate in describing the phenomenon of free and forced convection interaction.

5.3.4 Effect of Buoyancy Force

It has been assumed till now that the buoyancy force makes its contribution only as a body force in the

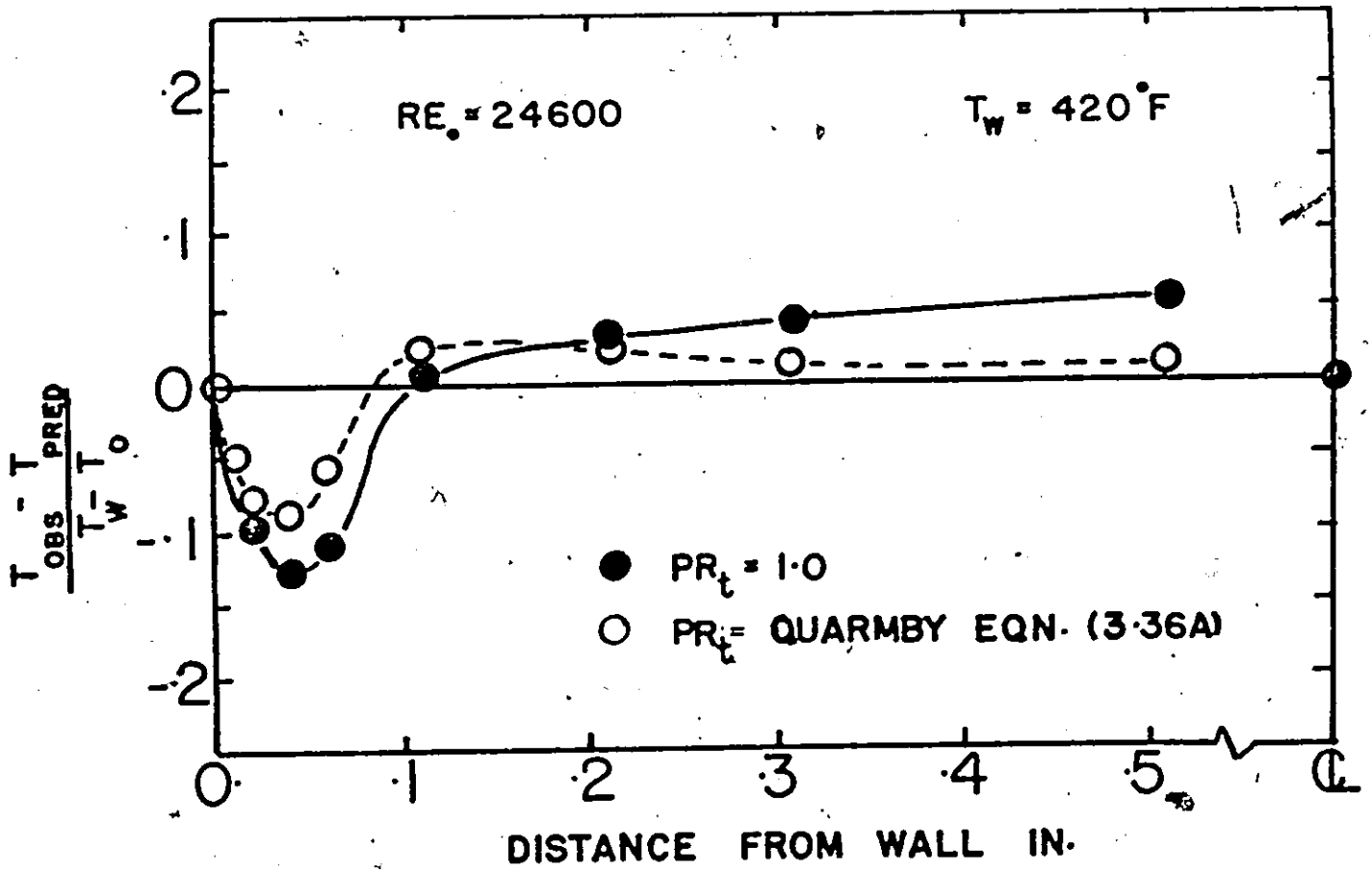

Figure 5-8. Comparison of the Observed and Predicted Temperature Profiles for the Bottom Port, Run No. 3, using Reynolds' Analogy, and Quamby's Equation for Turbulent Prandtl Number.

momentum conservation equation. The characteristics of the flow field are assumed to remain unchanged. However, upon examination of the momentum conservation equation in the integral form, it is observed that the shear stress profile is influenced by the buoyancy force if the latter is of comparable magnitude. For a fully developed isothermal turbulent flow, shear stress varies linearly from a maximum value at the wall to zero at the centre line. The maximum value is determined by the axial pressure gradient which is a function of friction factor and average velocity but is independent of radial position. However, with buoyancy force included, it is now the algebraic sum of the pressure drop and body force that determines the shear stress profile. Since the buoyancy force is dependent on the density of the fluid, its variation with radial location becomes significant especially at high wall temperatures. Thus shear stress no longer varies linearly across the cross section of the pipe. Since the buoyancy force is greatest at the wall (the greatest density difference being between the fluid at ambient temperature and that at the wall temperature), the resulting shear at the wall is greatly reduced. Shear stress was calculated by integrating the momentum conservation equation.

$$\tau = \frac{1}{r} \int_0^r \left(- \frac{dP}{dx} + g(\rho-\rho_a) - \rho\, u\frac{\partial u}{\partial x} - \rho v \frac{\partial u}{\partial r}\right) r\, dr \qquad (5.3)$$

Figure 5.9 presents the calculated shear stress profile from Equation (5.3) for the bottom port for Run No. 3. The values of the variable in the right hand side of Equation (5.3) were

obtained from the solution of the conservation equations. Also shown for comparison are, the shear stress profile when the body force term was equated to zero and the profile for isothermal flow. Without the body force term, the shear stress profile is almost linear across the cross section of the pipe except for a small rise near the wall due to physical property variations. But when buoyancy force is taken into account, its opposing direction to the main flow decreases the shear stress at the wall. The wall shear stress becomes zero and then negative as the buoyancy force increases. A negative shear stress implies flow reversal.

To support the flow in the pipe when the wall shear stress is decreasing, the shear stress somewhere over the cross section must increase. The shear stress, thus, increases from the value at the wall, reaches a maximum and then decreases to zero at the centre of the pipe. The latter constraint is imposed by the symmetry condition of the flow field.

In the turbulent exchange models, the eddy viscosity is expressed as a function of dimensionless radial distance, y^+, which in turn is a function of wall shear stress. The wall shear stress, τ_{wc}, has normally been obtained from the friction factor and Fanning's equation. Since the eddy viscosity expressions have been obtained for fully developed isothermal flow, there is a built-in assumption of linear variation in shear stress over the pipe cross section. If the shear stress at the wall is evaluated by integrating Equation (5.3) and this value, τ_{wn}, when substituted in the eddy viscosity expression will imply

a linear variation of shear stress from τ_{wn} at the wall to zero at the centre line. The decrease in wall shear stress, caused by the opposing buoyancy force, will make the eddy viscosity values appear as if a drastic reduction in the turbulence level of the flow has occurred. With the wall shear stress value approaching zero and ultimately becoming negative, the correspondence between the wall shear stress and the turbulence in the flow breaks down. The use of wall shear stress, τ_{wn}, in evaluating eddy viscosity expressions leads to unstable solution even for a moderate buoyancy force situation shown in Figure 5.9.

Patankar and Spalding [P13] suggested that the shear stress distribution in the flow field should be accounted for in the eddy viscosity expression. They proposed that the dimensionless distance, y^+, should be defined by the local shear stress instead of the value at the wall so that the complex flow pattern is represented through it in the eddy viscosity expression. Launder and Priddin [L8] examined the various other modifications suggested in the literature to account for the non linear shear stress profile. Considering under isothermal conditions, accelerating flow, blowing or suction at the wall, and low Reynolds number flow in a pipe and a channel, they suggested that y^+ may be redefined as

$$y^+ = y'^+ \, (\tau/\tau_{wall})^n = \frac{y\sqrt{(\tau_{wall}\, g_c)/\rho}}{\nu} \, (\tau/\tau_{wall})^n \tag{5.4}$$

The value of n = 0.5 reduced the above equation to that suggested in [P13]. Launder and Priddin found that n = 1.7 gave adequate

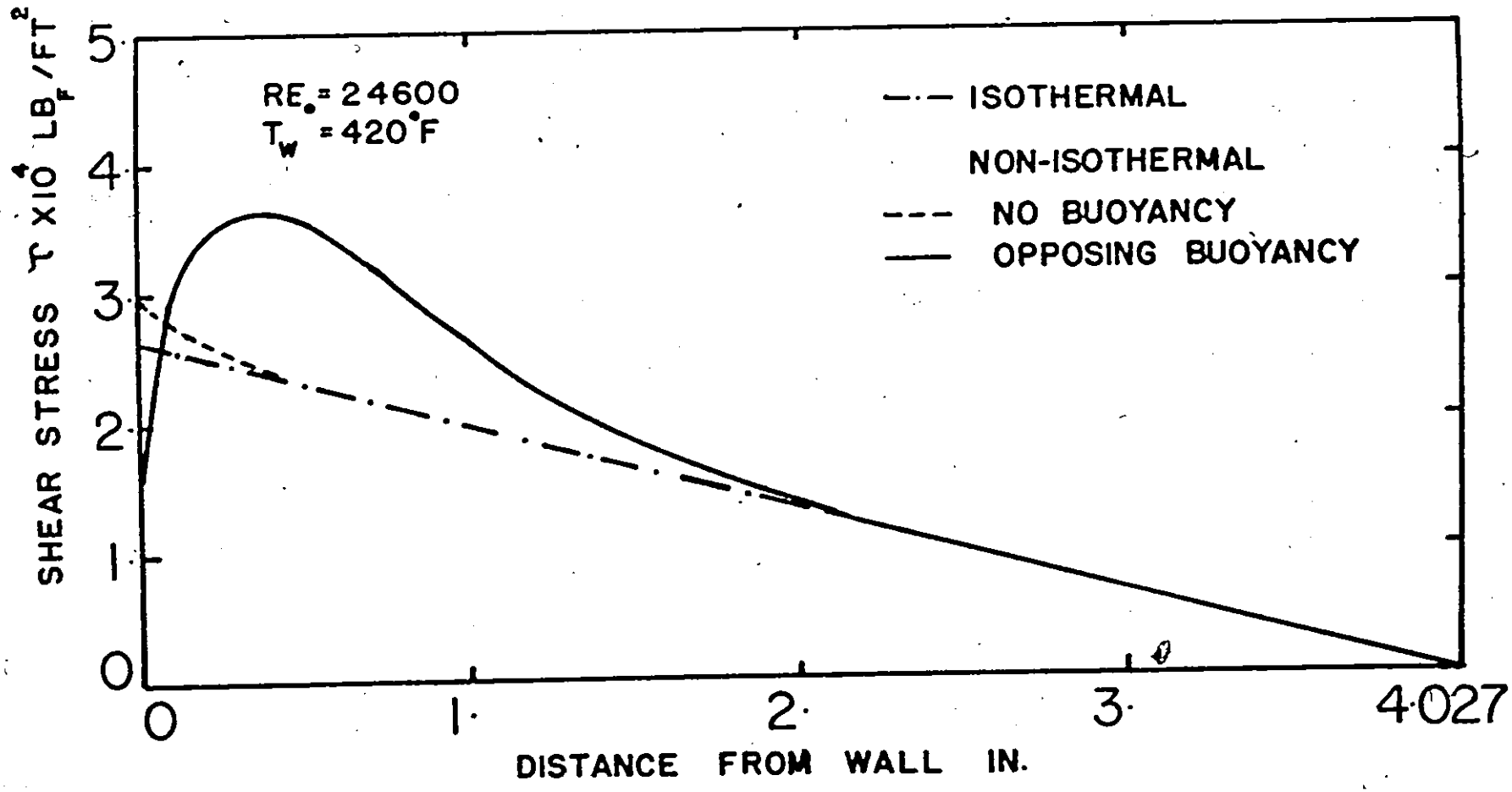

Figure 5-9. Calculated Shear Stress Profiles for the Bottom Port, Run No. 3.

agreement with the experimental values for the variety of flows considered.

This modification was applied to the present situation. The question of which wall shear stress value to be used in Equation (5.4) is unresolved. Though the most logical choice is τ_{wn}, as it is determined by the physical phenomenon, that is, interaction of forced and free convection for the present case. In the definition of y^+ in Equation (5.4), τ_{wall} appears with an exponent $(\frac{1}{2} - n)$. For $n = 1.7$, as suggested by Launder and Priddin, and τ_{wn} decreasing due to the growing buoyancy force along the length of the pipe, unrealistically high values of y^+ were obtained leading to an unstable numerical solution. Launder and Priddin suggested the modification of y^+, by shear stress ratio, only in the exponential term of Van Driest's eddy viscosity expression. Probably in the situations they considered, the shear stress profile deviated only in the wall region. In the present case, however, the effect of the buoyancy force on the shear stress profile occurred till well beyond the wall region and consequently the eddy viscosity expression must also be modified over the central core as well.

It may be argued that a peaking shear stress profile can be considered in two sections,

(i) The region between the wall and the place of maximum shear stress, $y^+_{\tau m}$.

(ii) The region between $y^+_{\tau m}$ and the centre of the pipe.

In the wall region, y^+ may be defined by local value of the shear stress while in the core region by a fictitious value at

the wall, τ_{wm}, obtained by the extrapolation of the line joining the zero value at the centre and the maximum shear stress.

Table 5-1 lists the various modifications tried. Some of the trials were unsuccessful because the solution became unstable. Some of the successful runs are shown in Figure 5.10 for the bottom port for Run No. 3. It is observed that any substantial improvement was obtained only for Van Driest's modification model VD25. Here the fictitious wall shear stress for the core region and the value of the exponent n = 1.7 was used for the wall region. Trials with n = 1.5, 1.8 and 2.0 failed to reveal any substantial improvement and instead led to instability for higher values. Moreover, the exponent n = 1.7 did not stabilize the solution for cases with higher buoyancy effects (e.g., Re = 18150 and T_w = 745°F).

It can thus be concluded that the modification of eddy property equations by taking into account the shear stress distribution, as a representation of the complex flow phenomena occurring in the present situation, had limited success.

Table 5-1 Turbulent Exchange Models

Code	Author	Equations	Range	Shear Stress in y^+	Denominator of Shear Stress Ratio in Eqn. (5.4)	n	Success
MR20	Travis et al. (Modified Reichardt 2-equation model)	(i) $\frac{\varepsilon}{\nu}=k[y^+-A\tanh(y^+/A)]$ (ii) $\frac{\varepsilon}{\nu}=\frac{k}{6}\frac{Ru^*}{\nu}[1-(Fr/R)^2][\frac{2}{3}+2(Fr/R)^2]$ Constants k, y_L^+, A, F are functions of Re	(i) $0<y^+<y_L^+$ (ii) $y_L^+<y^+<y_c^+$	τ_{wc}			Yes
MR21				τ_{wn}			No
MR22					τ_{wn}	1.7	No
MR23			(i) $0<y^+<y_{\tau_m}^+$ (ii) $y_{\tau_m}^+<y^+<y_c^+$	τ τ_{wm}			Yes
MR10	Reynolds et al. (Modified Reichardt 1-equation model)	$\frac{\varepsilon}{\nu}=\frac{k}{6}[y^+-A\tanh(y^+/A)][2-y^+/y_c^+][1+2(1-y^+/y_c^+)^2]$ k = .423, A = 11+9 exp (-.003Re)	$0<y^+<y_c^+$	τ_{wc}			Yes
MR11				τ_{wn}			No
MR12				τ_{wc}	Only in the argument of tanh τ_{wn}	1.7	No
MR13				τ_{wn}			No
VD10	Van Driest 1-equation model	$\frac{\varepsilon}{\nu}=[ky^+(1-\exp(-y^+/A)]^2\frac{du^+}{dy^+}$ k = .4 A = 26	$0<y^+<y_c^+$	τ_{wc}			Yes
VD11				τ_{wn}	τ_{wn} Only in the argument of exp	1.7	Yes

VD20	Van Driest 2-equation model	(i) $\frac{\varepsilon}{\nu} = [ky^+[1-\exp/-y^+/A)]^2 \frac{du^+}{dy^+}$ (ii) $\frac{\varepsilon}{\nu} = ky^+(1-y/R_o)-1$ $y_L^+ = 35+.247\ y_c^+$	(i) $0<y^+<y_L^+$ (ii) $y_L^+<y^+<y_c^+$	τ_{wc}			Yes
VD21					$-\tau_{wc}$	1.7	No
VD22					τ_{wc}	0.5	Yes
VD23				τ_{wn}	τ_{wn}	.5	No
VD24			(i) $0<y^+<y^+_{\tau_m}$ (ii) $y^+_{\tau_m}<y^+<y_c^+$	τ_{wm}	τ_{wn} Only in the argument of exp	.5	Yes
VD25						1.7	Yes

τ_{wc} Wall shear stress calculated from friction factor

τ_{wn} Wall shear stress calculated from the integration of Equation (5.3)

τ_{wm} Fictitious wall shear stress obtained by linear extrapolation by joining zero value at the centreline and the maximum shear stress τ_m

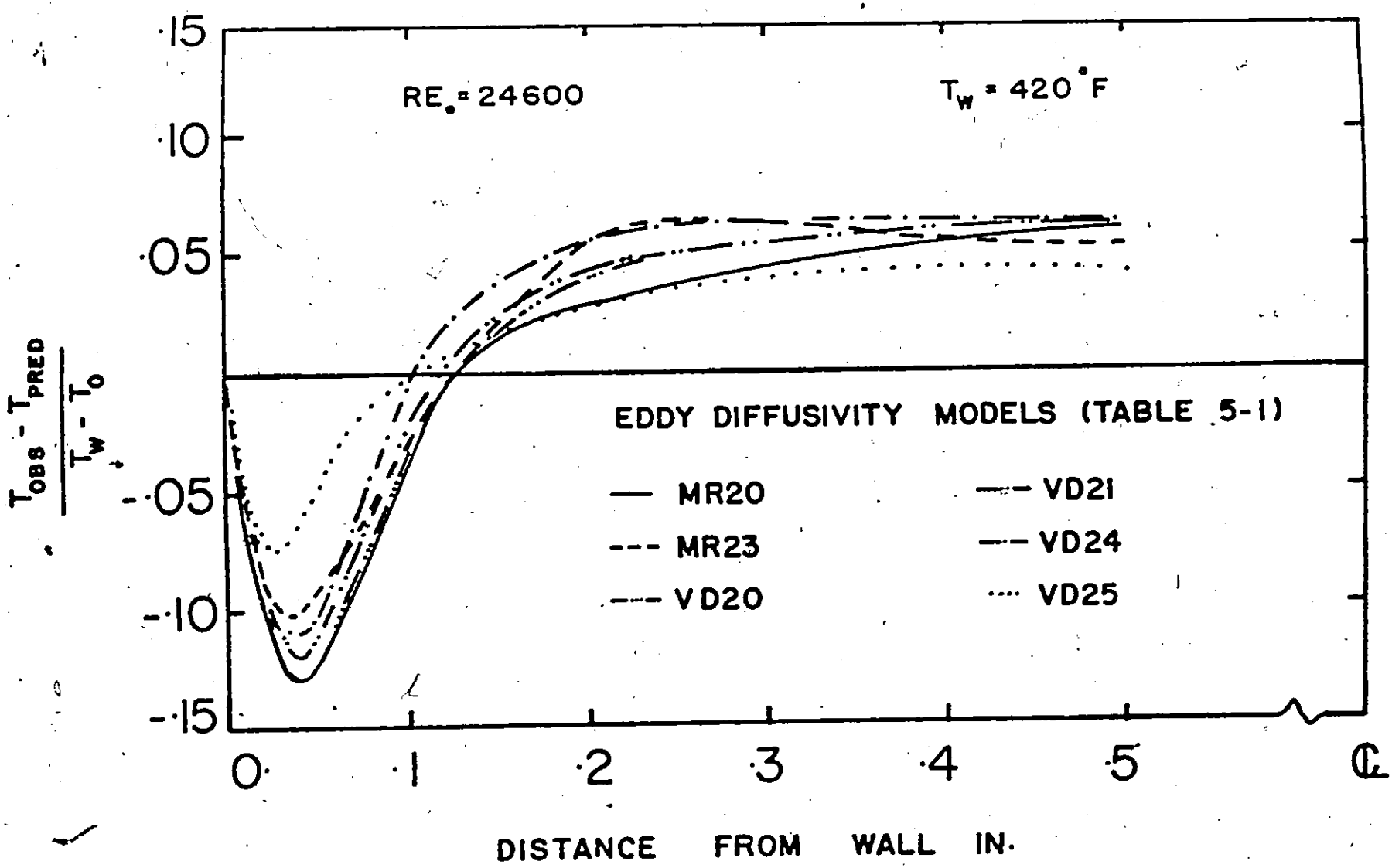

Figure 5-10. Comparison of the Observed and Predicted Temperature Profiles for the Bottom Port, Run No. 3, using Various Modifications in Eddy Diffusivity to Account for the Non-Linear Shear Stress Distribution.

5.4 Temperature Fluctuations

In the literature [B3, E1, H5, H6] it has been suggested that an increased turbulent activity results due to the interaction between the opposing free and forced convection in turbulent flow. During the course of this work, it was observed that the intensity of temperature fluctuations at a point seemed to become greater as the wall temperature was increased. Since the turbulent contribution to the heat transport is the time-average of the product of radial velocity and temperature fluctuations, that is $\overline{v'T'}$, the magnitude of the temperature fluctuations can give some semi-quantitative measure of any change in the turbulent structure of the flow field. Unfortunately, the simultaneous measurement of the radial velocity fluctuations were not possible with the available instrumentation.

Temperature fluctuations can be made dimensionless by referring them to wall-to-centre line temperature difference as has been done by previous investigators [B3, H5]. This procedure is based on the concept that the turbulent activity is a function of the property (velocity, temperature, etc.) gradient in the flow field. That is to say, if the temperature gradient is higher at any given point, the temperature fluctuations should be higher. In the present situation of developing thermal boundary layer, however, it is possible to have different temperature gradients at a given radial position, for the same wall-to-centre line temperature difference at different Reynolds numbers. For this reason, the root mean square values of the temperature fluctuations, measured at any radial point,

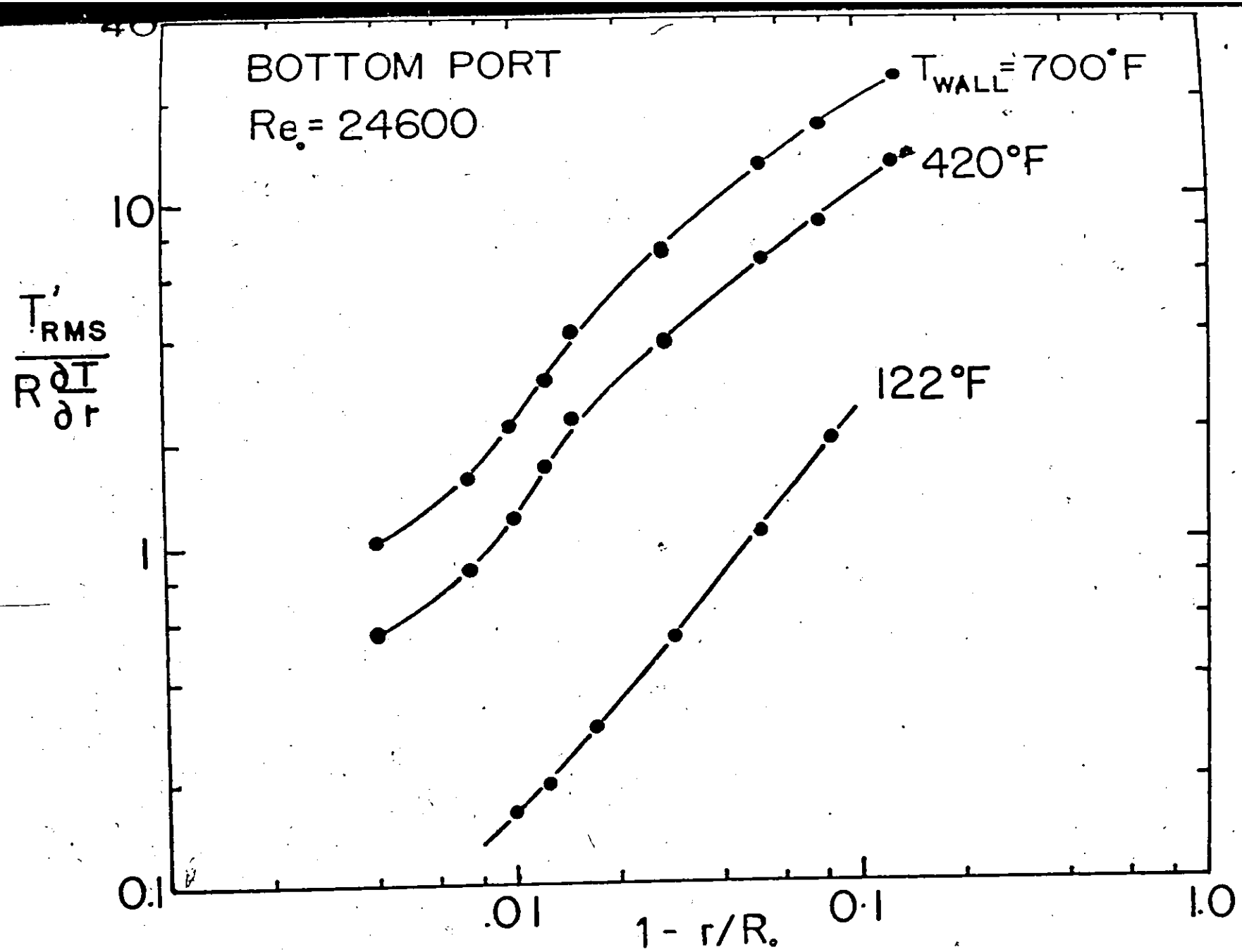

Figure 5-11. Dimensionless Temperature Fluctuation Profiles as a Function of Wall Temperature.

were normalized with respect to the temperature gradient at that point. The method of calculating temperature gradients is given in Appendix C.

Figure 5.11 indicates the dimensionless root mean square temperature fluctuations as a function of the radial position with wall temperature as a parameter. For a fixed Reynolds number, the wall temperature is an indication of the magnitude of the buoyancy force. It is observed in Figure 5.11 that the dimensionless r.m.s. temperature fluctuations increase with wall temperature and hence the buoyancy force. It was noted that the intensity of the temperature fluctuations goes through a maximum and this maximum increases and moves away from the wall as the wall temperature increases. These observations suggest that the turbulent activity (transport) increases as the buoyancy force increases. This observation is consistent with the hypothesis suggested by Eckert and Diaguila [E1]. Note also that the discrepancy between the observed and predicted temperatures increases with the buoyancy force. This provides a clue to the nature of the phenomena causing the discrepancies.

5.5 Calculation of Effective Conductivity Profiles

To understand the opposing free and forced convection interaction phenomena, in which change in the level of turbulence is a contributory factor, it was decided to calculate the effective turbulent conductivity from the experimental observations. This can be done by integrating the energy conservation equation

$$\rho u \frac{\partial T}{\partial x} + \rho v \frac{\partial T}{\partial r} = \frac{1}{r} \frac{\partial}{\partial r} \left[\frac{k}{C_p} r \left(1 + \frac{\varepsilon_h \rho C_p}{k}\right) \frac{\partial T}{\partial r}\right]$$

This equation can be written in the integrated form, viz.,

$$1 + \frac{\varepsilon_h \rho C_p}{k} = 1 + \frac{\varepsilon_h}{\alpha} = \frac{\int_o^r (\rho u(\partial T/\partial x) + \rho v(\partial T/\partial r)) r \, dr}{r(k/C_p) \quad (\partial T/\partial r)} \tag{5.5}$$

Evaluation of the effective conductivity profile from Equation (5.5) requires the knowledge of the temperature, and axial and radial velocities as functions of the radial location, r. Accurate measurement of the temperature profiles had been possible in this investigation, while axial velocity profiles could not be measured in the wall region. This problem of the axial and radial velocity profiles can be circumvented by using, as a first guess, those values predicted by the numerical solution of the conservation equations as outlined in Chapter 3; using the isothermal expressions for eddy properties. The temperature gradients are evaluated from the experimental data. Since the temperature profiles near the centre of the test section are flat, considerable error is likely to occur in evaluating its derivatives. Integrating from the centre line to the wall, these errors will build up to seriously affect the values of eddy conductivity near the wall. Since the wall values are important in studying the free and forced convection interaction phenomenon, this method of evaluating eddy conductivity is highly unsatisfactory. However, the use of boundary conditions at the wall, where there is no contribution of turbulence towards

transport properties, i.e., $\varepsilon_h = 0$, gives the following expression for effective conductivity.

$$1 + \frac{\varepsilon_h}{\alpha} = \frac{R_o\left[\frac{k}{C_p}\frac{\partial T}{\partial r}\right]_{r=R_o} - \int_{R_o}^{r}\left(\rho u \frac{\partial T}{\partial x} + \rho v \frac{\partial T}{\partial r}\right) r\, dr}{\frac{k}{C_p}\, r\, \frac{\partial T}{\partial r}} \tag{5.6}$$

Owing to the steep nature of the radial temperature gradients and the large number of experimental points, near the wall, the evaluation of derivatives will be reasonably accurate and consequently, so will be the values of eddy conductivity.

Effective conductivity profiles are evaluated from Equation (5.6) by determining the axial and radial temperature gradients and performing the integration from the wall to the radial location. Radial gradients were numerically evaluated by piecewise fitting of Equation (5.7) to the experimental data by the least square estimates of the coefficients, A_1, A_2, A_3 and A_4.

$$\frac{T_w - T}{T_w - T_o} = \text{Exp}\left[A_1 + \frac{A_2}{r} + \frac{A_3}{r^2} + \frac{A_4}{r^3}\right] \tag{5.7}$$

Axial gradients, however, had to be evaluated graphically as measurements were taken only at three axial locations and a parabola fit was found not to be adequate for all the profiles.

The integration in Equation (5.6) was done numerically using the Legendre-Gauss Quadrature. This technique requires the values of the integrand at specified intervals over the

range of the independent variable, r. This was accomplished by the use of Lagrangian Interpolation Polynomials for unequal interval data. The same method was also used in the interpolation of axial and radial velocity profiles obtained from the solution of the conservation equations. Details of all these numerical techniques are given in Appendix C.

In the evaluation of the effective conductivity from Equation (5.6), it is recognised that at the centre of the test section, as the radial temperature gradient approaches zero, the effective conductivity becomes indeterminate. In the present case of short test section, this problem is encountered well before the centre line is reached because of the developing thermal boundary layer. Change of independent variable in Equation (5.6) from r to r^2, which circumvents the indeterminate situation only at the centre line, does not alleviate the problem.

Near the edge of the thermal boundary layer where the temperature profiles start becoming flat, a large percentage of uncertainty is introduced in the calculation of the radial temperature gradients, as they approach zero. Thus, the errors in the calculation of effective conductivity profiles are amplified, since the temperature gradient term occurs in the denominator of Equation (5.6). However, the lack of accuracy in the effective conductivity profiles near and beyond the edge of the thermal boundary layer is not detrimental because of its small contribution to the total heat transport, and the interaction between the free and forced convection is essentially

a wall-phenomenon. The detailed statistical analysis of the effective conductivity profiles will be done in the next section.

Since for the present system, the values for eddy viscosity could not be calculated for the lack of accurate measurements of the velocity profiles over the cross section, they can be estimated by any of the following optional schemes.

(i) Use of the isothermal eddy viscosity expressions.

(ii) Use of eddy viscosity equal to the calculated eddy conductivity.

(iii) Use of eddy viscosity to eddy conductivity ratio, Pr_t, suggested in the literature, e.g., by Quarmby (Equation (5.2)).

The last option seems to be the most logical one, since Quarmby's analysis seems to be the most complete at the present time and the empirical equation suggested is quite convenient to use.

In the solution of Equation (5.6), to obtain eddy conductivity profiles, an initial guess of the axial and radial velocity profiles was obtained from the solution of the conservation equations. For Run Nos. 7 and 8 where the solution was unstable, an initial guess of the velocity profiles was obtained from the solution when the body force term in the momentum conservation equation was equated to zero. The eddy diffusivity profiles, thus obtained, were used to solve the conservation equations for improved predictions of velocity and temperature profiles. The numerical solution, however, requires the eddy diffusivity profiles over the whole cross section of the pipe, while the solution of Equations (5.2) and (5.6) is only valid

over the thermal boundary layer thickness. Since the core of the fluid was essentially under isothermal conditions, it was assumed that the eddy viscosity in the central region is given by the modified Reichardt expressions (3.32). The eddy viscosity and eddy conductivity values between the edge of the thermal boundary layer and the centre line were obtained by interpolation. Since the calculation of the effective conductivity was carried out at the three axial locations in the test section, the ε_m and ε_h values at intermediate axial locations were obtained by linear interpolation, starting with isothermal values at the entrance.

The improved predictions of the velocity profiles, from the solution of the conservation equations employing the newly calculated values of effective diffusivities, were used to solve Equation (5.6) again for further improvement in the estimates of eddy conductivity at each radial point. This iterative cycle can be repeated till the change in velocity, temperature and eddy diffusivity profiles is less than a given tolerance. However, because excessive computer time was required, only two iterations were performed for each run and even so, no appreciable change (less than 10%) in the effective conductivity values in the wall region was found between the first and second iterations.

5.6 Effective Conductivity Profiles

Changes in the turbulence level in the flow field due to the opposing free and forced convection can be studied

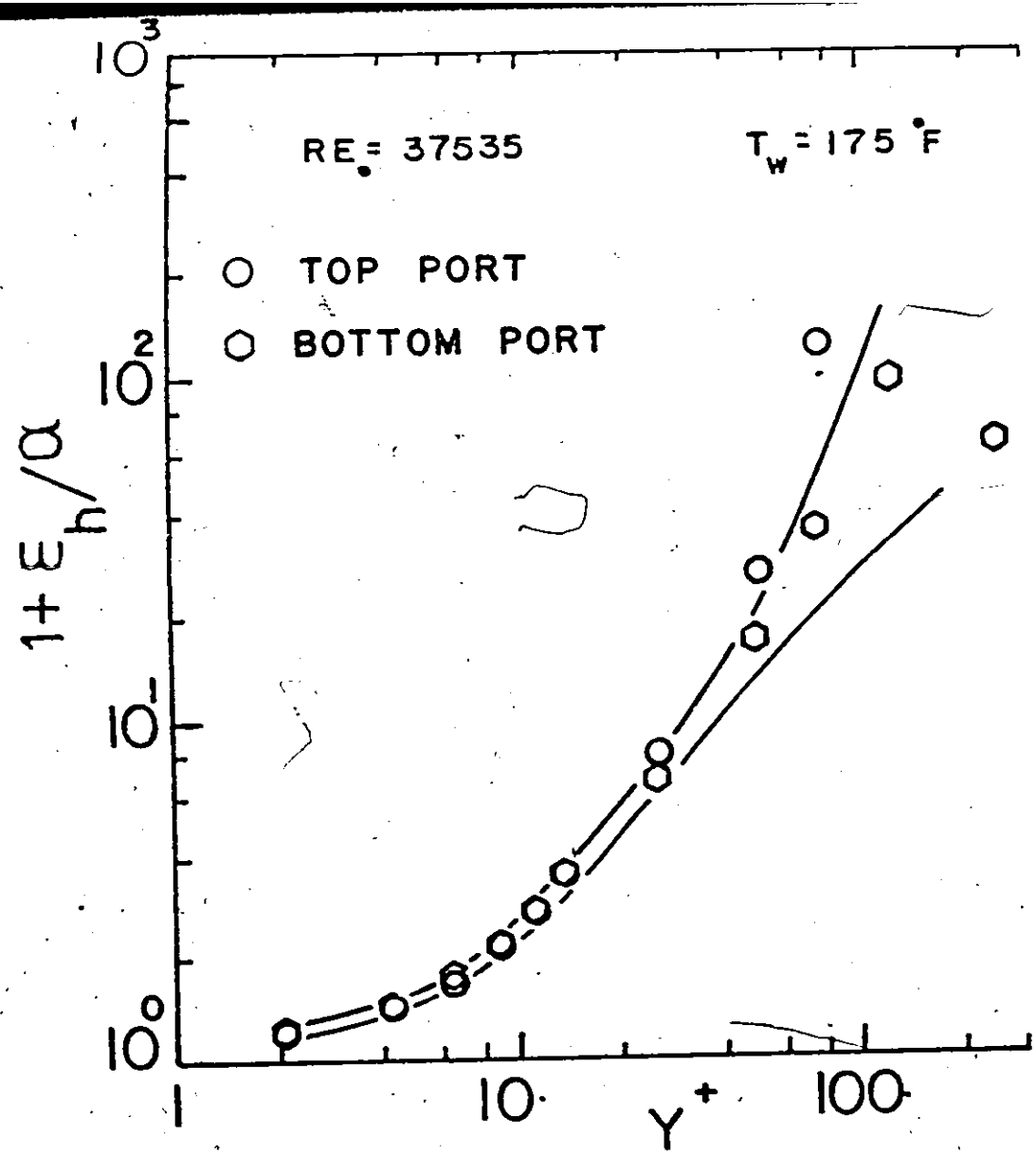

Figure 5-12A. Calculated Effective Heat Diffusivity Profiles. 95% Confidence Interval on Bottom Port —.

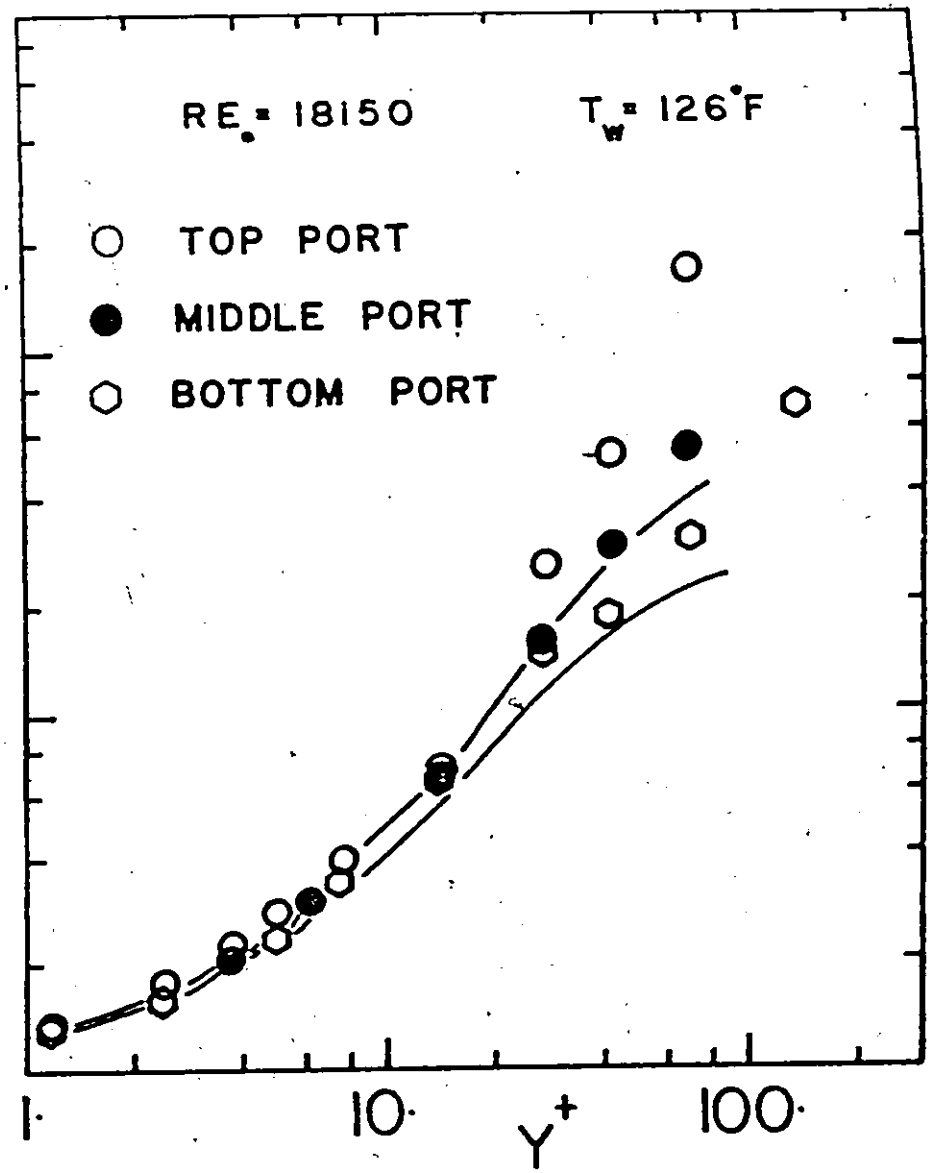

Figure 12-B. Calculated Effective Heat Diffusivity Profiles. 95% Confidence Interval on Bottom Port —.

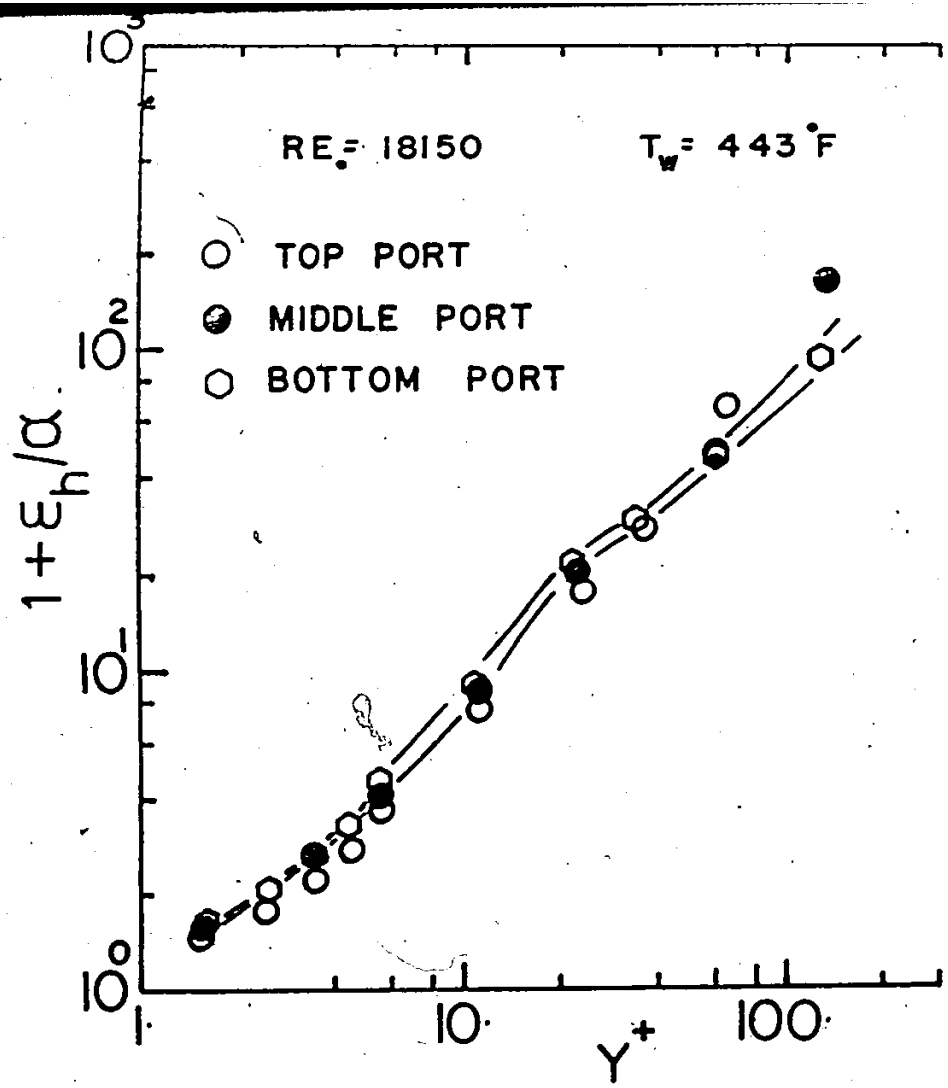

Figure 5-12C. Calculated Effective Heat Diffusivity Profiles. 95% Confidence Interval on Bottom Port —·

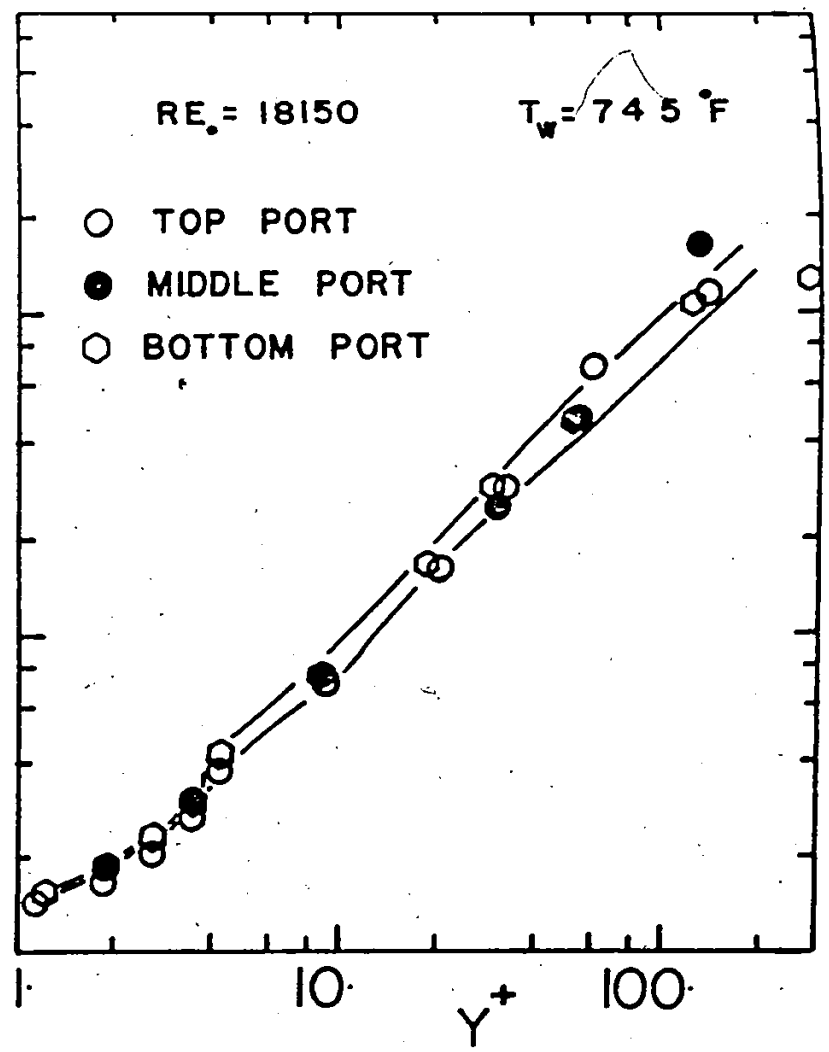

Figure 5-12D. Calculated Effective Heat Diffusivity Profiles. 95% Confidence Interval on Bottom Port —·

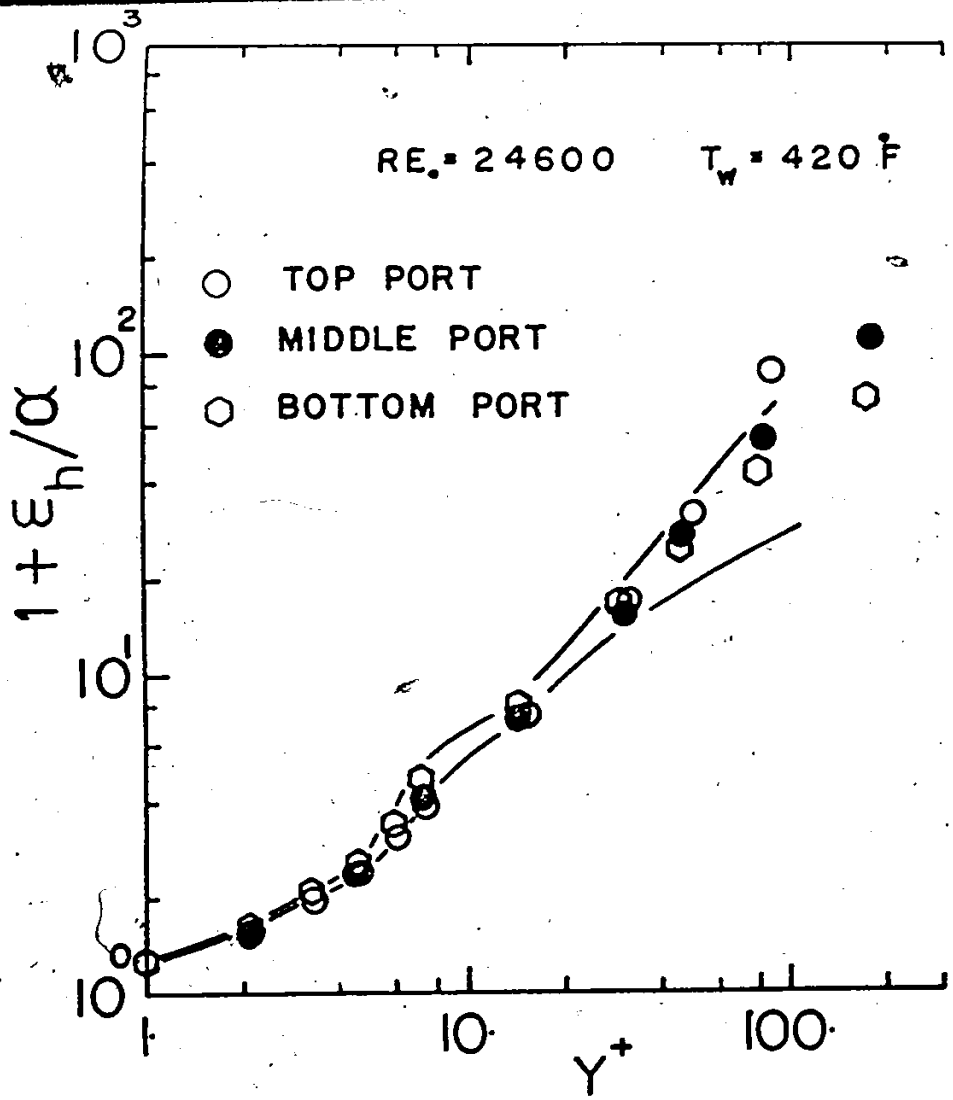

Figure 5-12E. Calculated Effective Heat Diffusivity Profiles. 95% Confidence Interval on Bottom Port —.

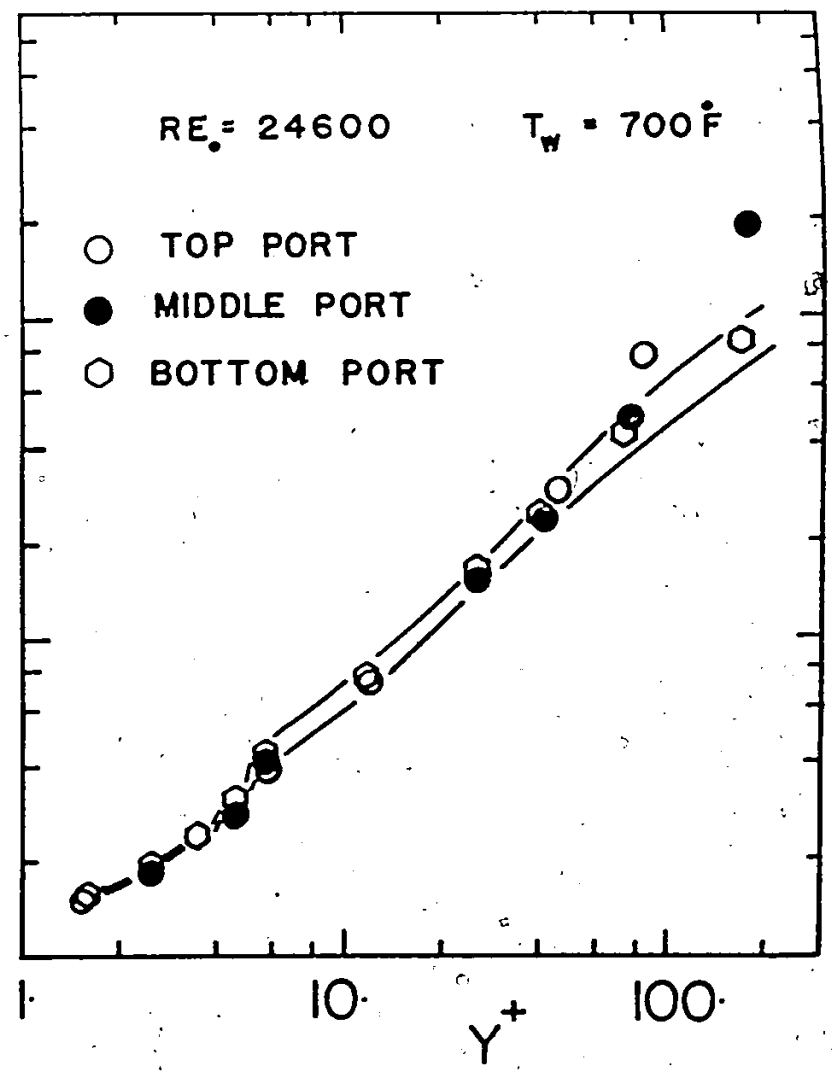

Figure 5-12F. Calculated Effective Heat Diffusivity Profiles. 95% Confidence Interval on Bottom Port —.

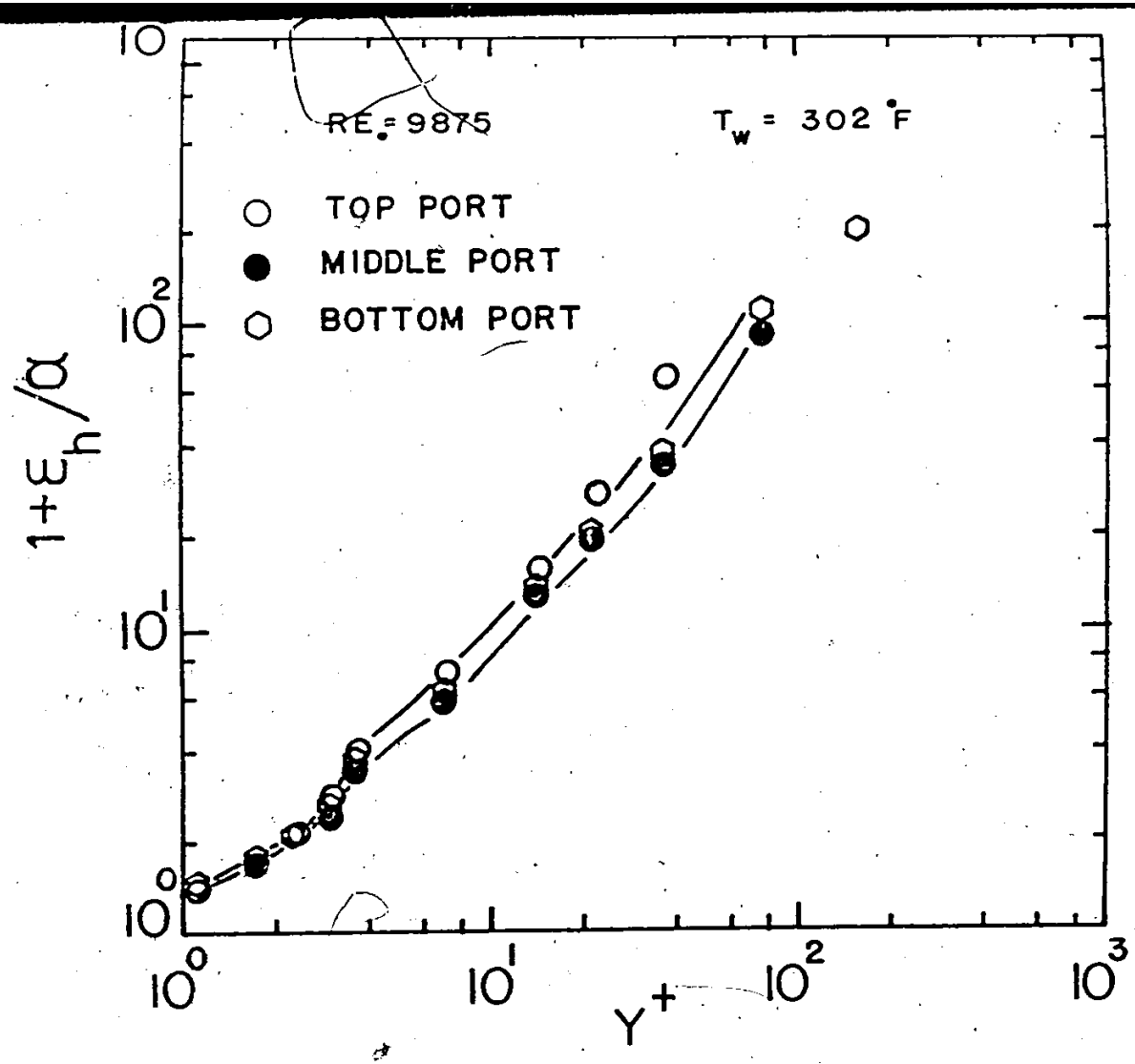

Figure 5-12G. Calculated Effective Heat Diffusivity Profiles. 95% Confidence Interval on Bottom Port —·

by considering the variations in the effective conductivity profiles. Figures 5.12A to 5.12G show the calculated effective conductivity, $1+\varepsilon_h/\alpha$, profiles as a function of the dimensionless radial distance, y^+, for various runs. The latter was based on local physical properties and wall shear stress calculated from friction factor correlation, Equation (3.34). The variance of the calculated effective conductivity profile can be approximately estimated from the variance of the temperature profile gradients estimated in Appendix C. If it is assumed that in Equation (5.6), the uncertainties in calculating the integrand are nullified by the averaging procedure of the integration then the estimation of variance of $(1+\varepsilon_h/\alpha)$ is very much simplified and can be written as:

$$\mathrm{Var}\ (1+\varepsilon_h/\alpha) = \mathrm{Var}\ \left[\frac{R_o\,[k/C_p\ \partial\theta/\partial r]_{r=R_o}}{r\ k/C_p\ \partial\theta/\partial r}\right] \tag{5.8}$$

$$\mathrm{Var}\ (1+\varepsilon_h/\alpha) = \left[\frac{R_o\,[k/C_p\,\partial\theta/\partial r]_{r=R_o}}{r\ k/C_p\ (\partial\theta/\partial r)^2}\right]^2 \mathrm{Var}\ \left(\frac{\partial\theta}{\partial r}\right) = s_1^2 \tag{5.9}$$

The 95% confidence interval for the estimate of $(1+\varepsilon_h/\alpha)$ can be calculated from the estimate of its variance from Equation (5.9) and (C-3-16). The probability that the true value of $(1+\varepsilon_h/\alpha)$ lies in the interval

$$(1+\varepsilon_h/\alpha) - t(p/2,n-m-1)\ s_1 \le (1+\varepsilon_h/\alpha) \le (1+\varepsilon_h/\alpha) + t(p/2,n-m-1)\ s_1 \tag{5.10}$$

is 1-p = 95%. In Figures 5-12A to 5-12G, this confidence envelope is also plotted for the bottom port profiles. It is observed that the uncertainty is very small in the wall region where measurements were made at close intervals. Near the edge of the thermal boundary layer, however, the uncertainty is large because measurements were made at large intervals; and since the temperature profiles were flat in this region, the estimates of temperature gradients were not accurate. However, the contribution of the region near the edge of the thermal boundary layer to the total heat transport process is small and consequently, the uncertainties in the calculation of $(1+\varepsilon_h/\alpha)$ are not detrimental. Similar confidence envelopes can be drawn around the calculated $(1+\varepsilon_h/\alpha)$ profiles for the other ports. It is surprising to note that although there is a dramatic change in the radial effective conductivity profile from the inlet, where the isothermal value must prevail, to that determined at the top port, there is only a slight change over the rest of the heating section.

Using these calculated effective conductivity profiles in the solution of conservation equations, improved estimates of temperature and velocity profiles at the three port locations were made. Figures 5-13A to 5-13K show the comparison between the predicted and observed temperature and velocity profiles. Also shown for comparison are the predictions that were obtained by using the eddy properties given by modified Reichardt expressions (3.31 to 3.33) and assuming a turbulent Prandtl number of unity. The predicted and the observed temperature

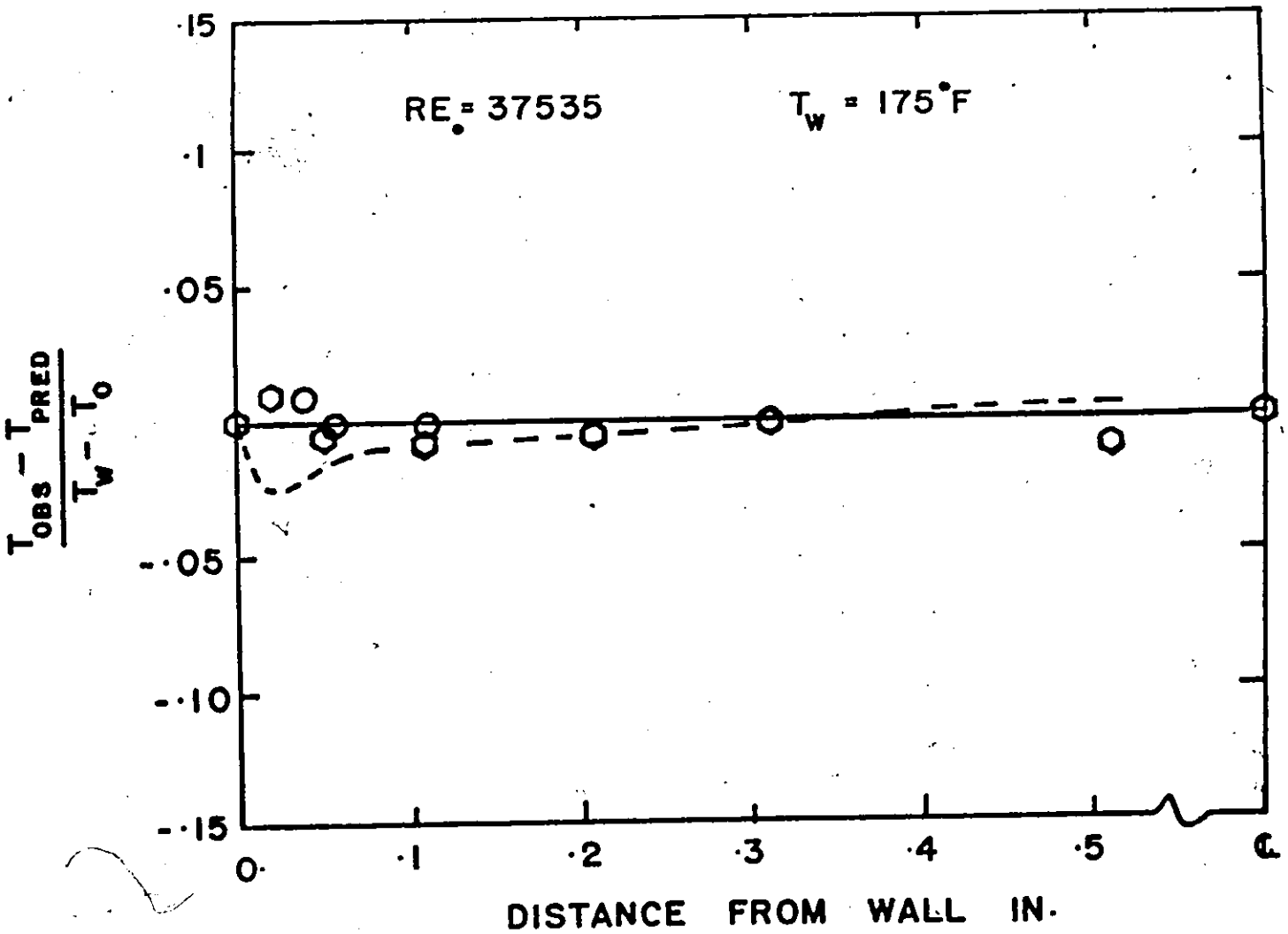

Figure 5-13A. Comparison of the Observed and Predicted (from Calculated Eddy Diffusivity Profiles for Heat, Pr_t from Quarmby Equation) Temperature Profiles. Top Port, O; Bottom Port, O; Predictions based on Modified Reichardt Model and Reynolds Analogy ---.

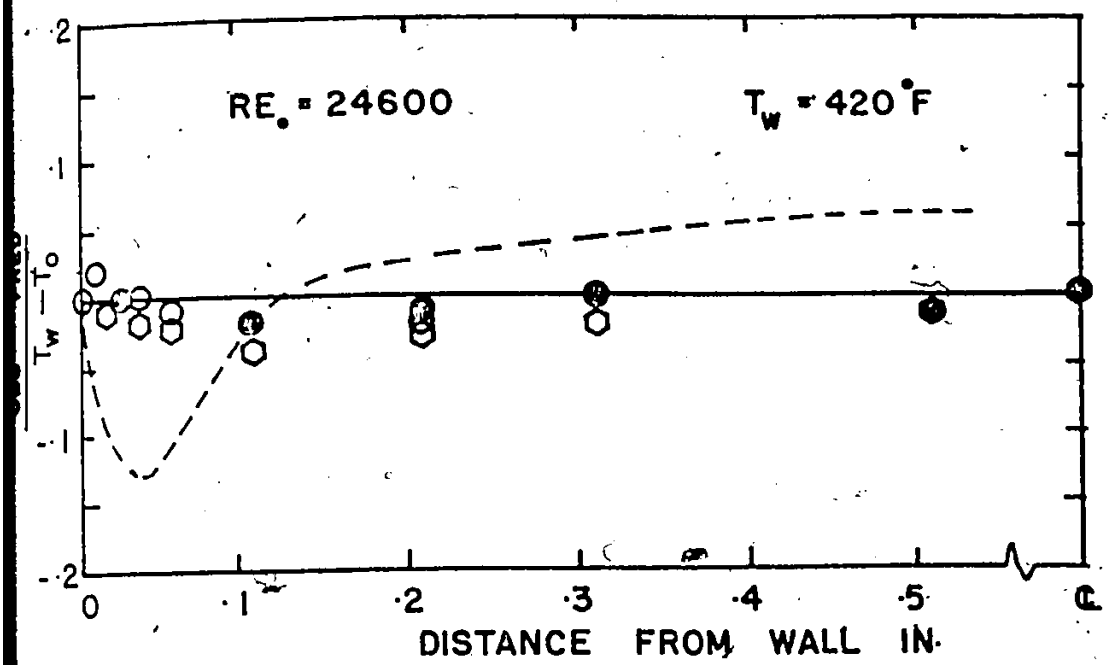

Figure 5-13B. Comparison of the Observed and Predicted (from Calculated Eddy Diffusivity Profiles for Heat, Pr_t, from Quarmby Equation) Temperature Profiles. Top Port, ○ ; Middle Port, ● ; Bottom Port, ○ ; Predictions based on Modified Reichardt Model and Reynolds Analogy --- .

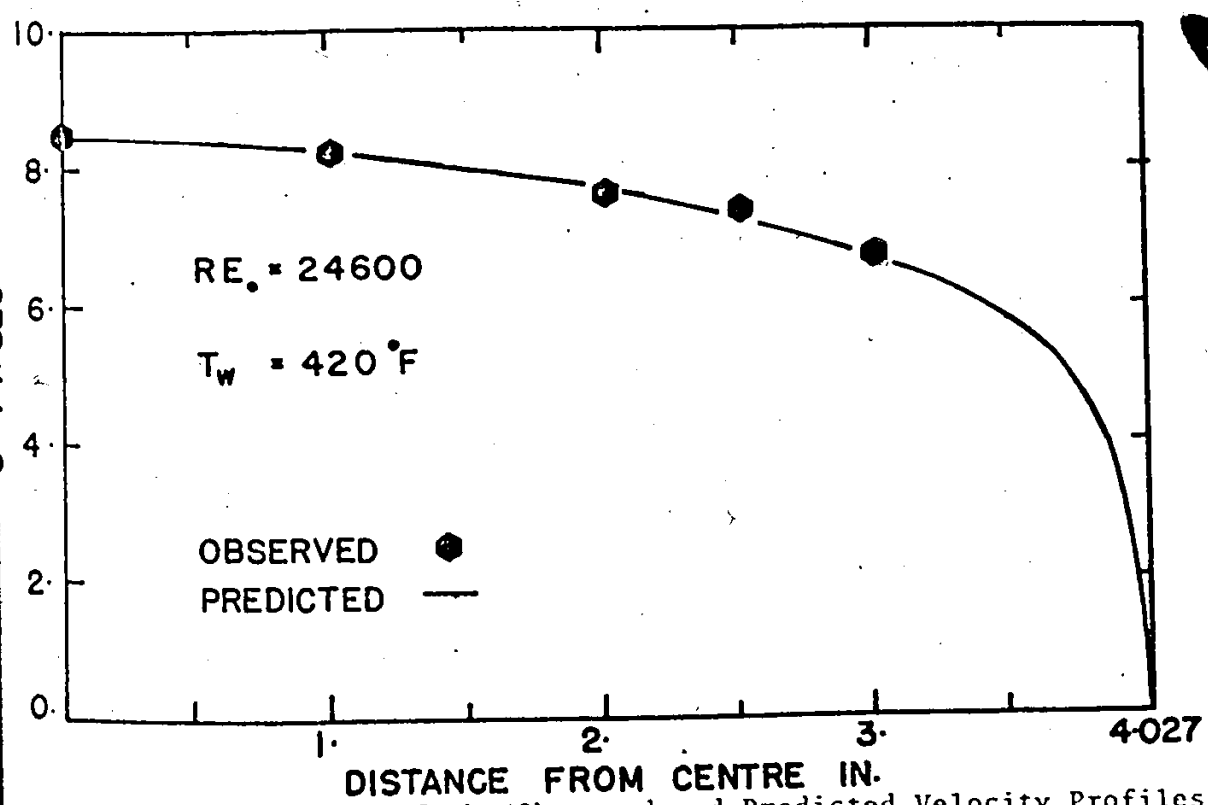

gure 5-13C. Comparison of the Observed and Predicted Velocity Profiles at 1 1/2" Upstream of the Exit of the Test Section.

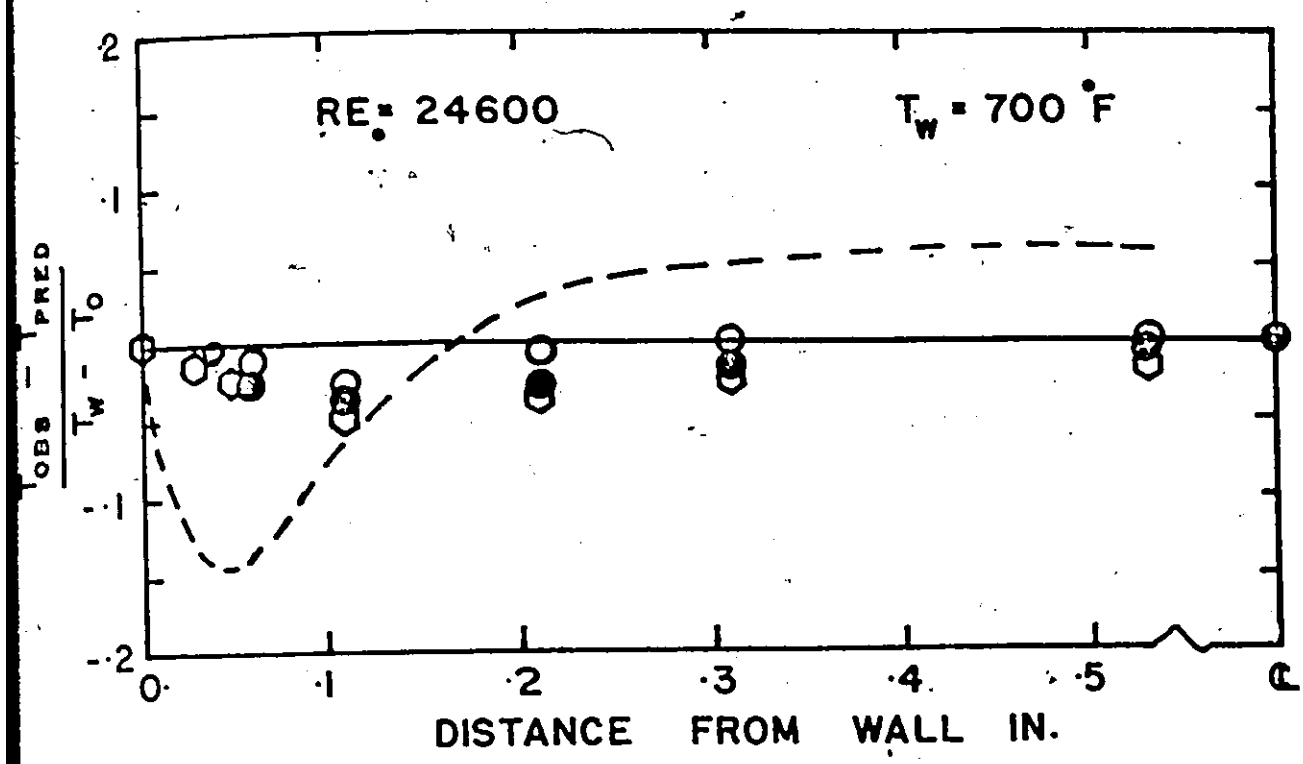

Figure 5-13D. Comparison of the Observed and Predicted (from Calculated Eddy Diffusivity Profiles for Heat, Pr_t from Quarmby Equation) Temperature Profiles. Top Port, ○ ; Middle Port, ● ; Bottom Port, ⬡ ; Predictions based on Modified Reichardt Model and Reynolds Analogy ---.

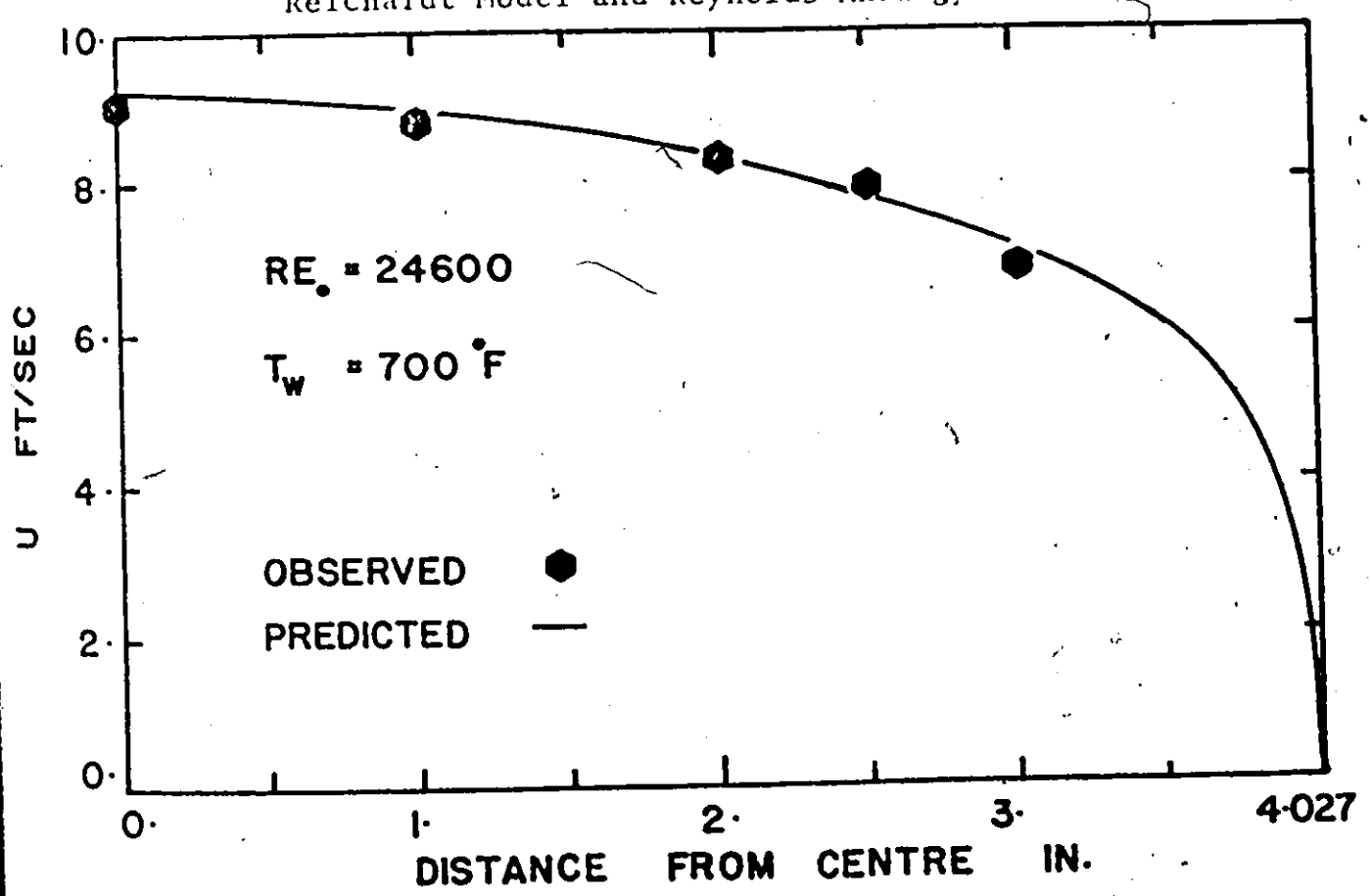

Figure 5-13E. Comparison of the Observed and Predicted Velocity Profiles at 1 1/2" Upstream of the Exit of the Test Section.

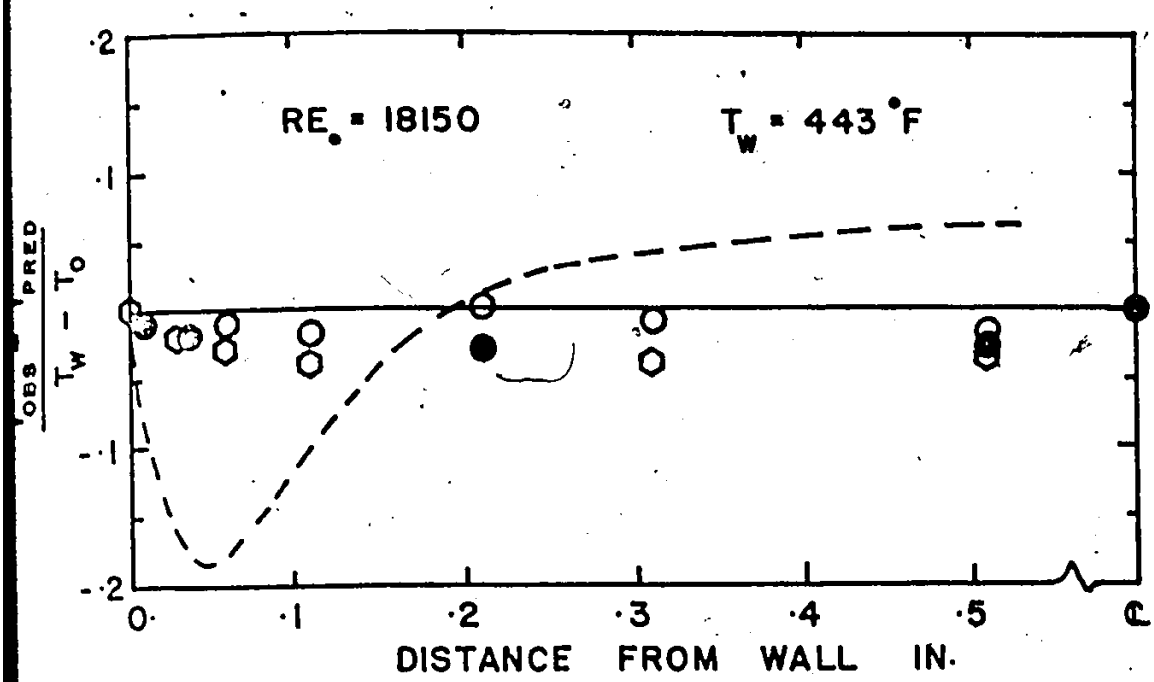

Figure 5-13F. Comparison of the Observed and Predicted (from Calculated Eddy Diffusivity Profiles for Heat, Pr_t from Quarmby Equation) Temperature Profiles. Top Port, ○; Middle Port, ● ; Bottom Port, ⬡ ; Predictions based on Modified Reichardt Model and Reynolds Analogy---.

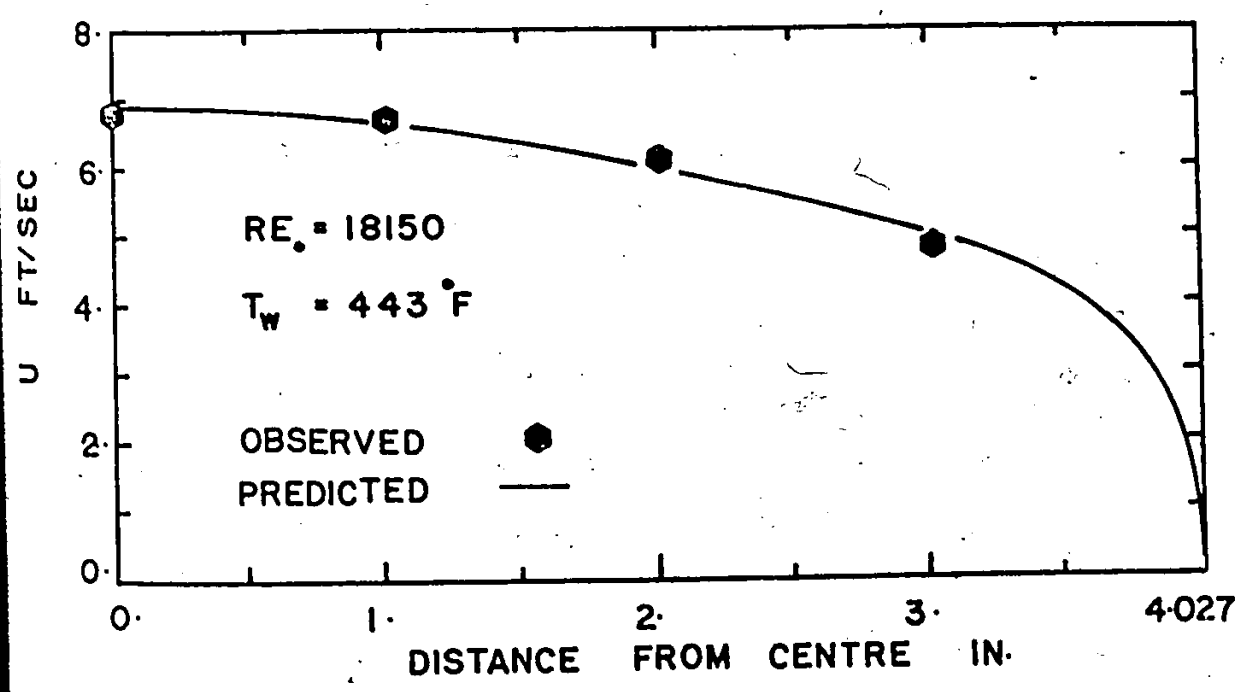

Figure 5-13G. Comparison of the Observed and Predicted Velocity Profiles at 1 1/2" Upstream of the Exit of the Test Section.

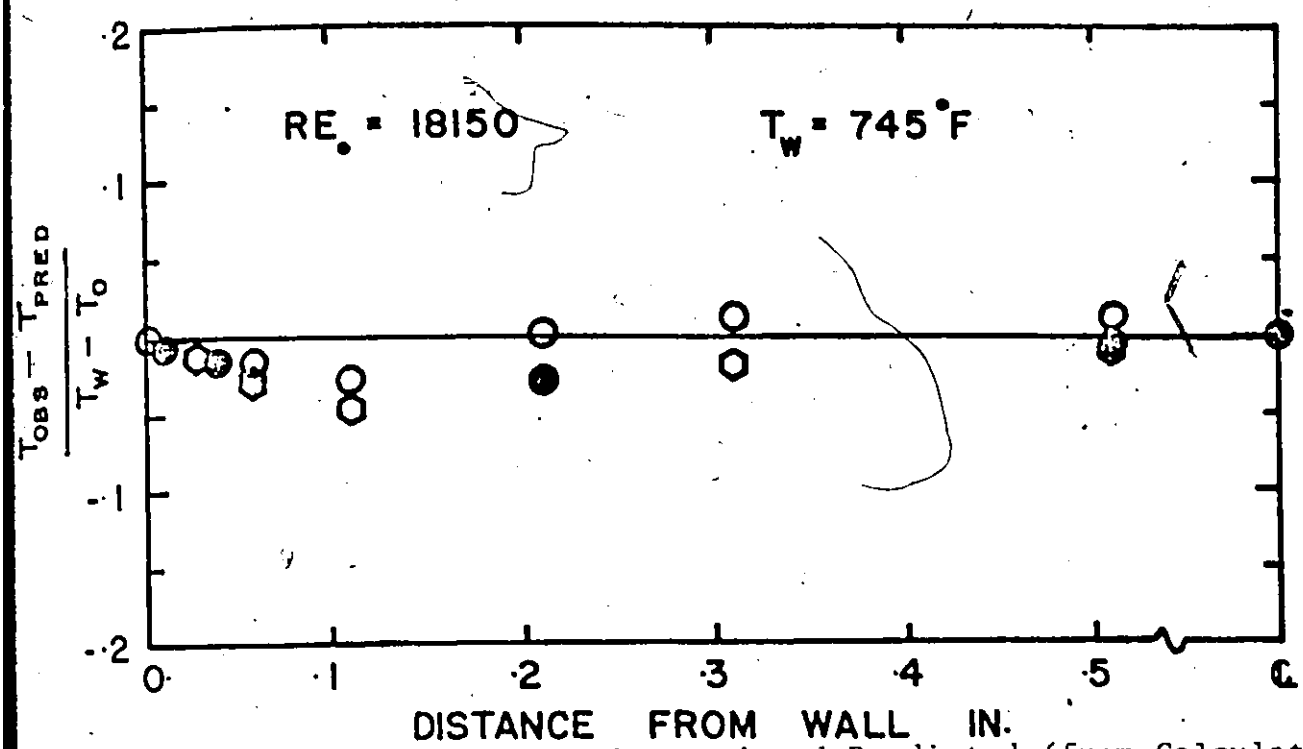

Figure 5-13H. Comparison of the Observed and Predicted (from Calculated Eddy Diffusivity Profiles for Heat, Pr_t from Quarmby Equation) Temperature Profiles. Top Port, ○ ; Middle Port, ● ; Bottom Port, ⬡ ; Predictions based on Modified Reichardt Model and Reynolds Analogy and Reynolds Analogy Solution was Unstable.

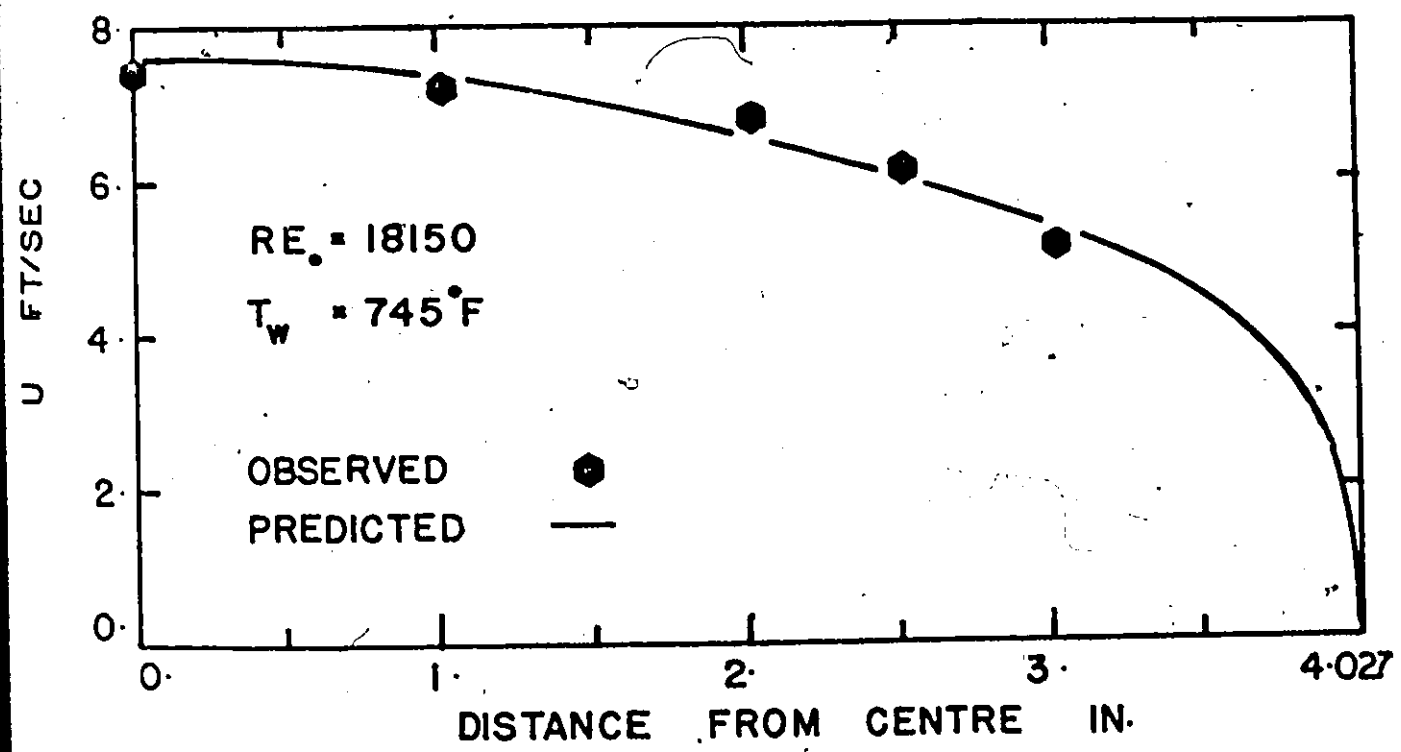

Figure 5-13I. Comparison of the Observed and Predicted Velocity Profiles at 1 1/2" Upstream of the Exit of the Test Section.

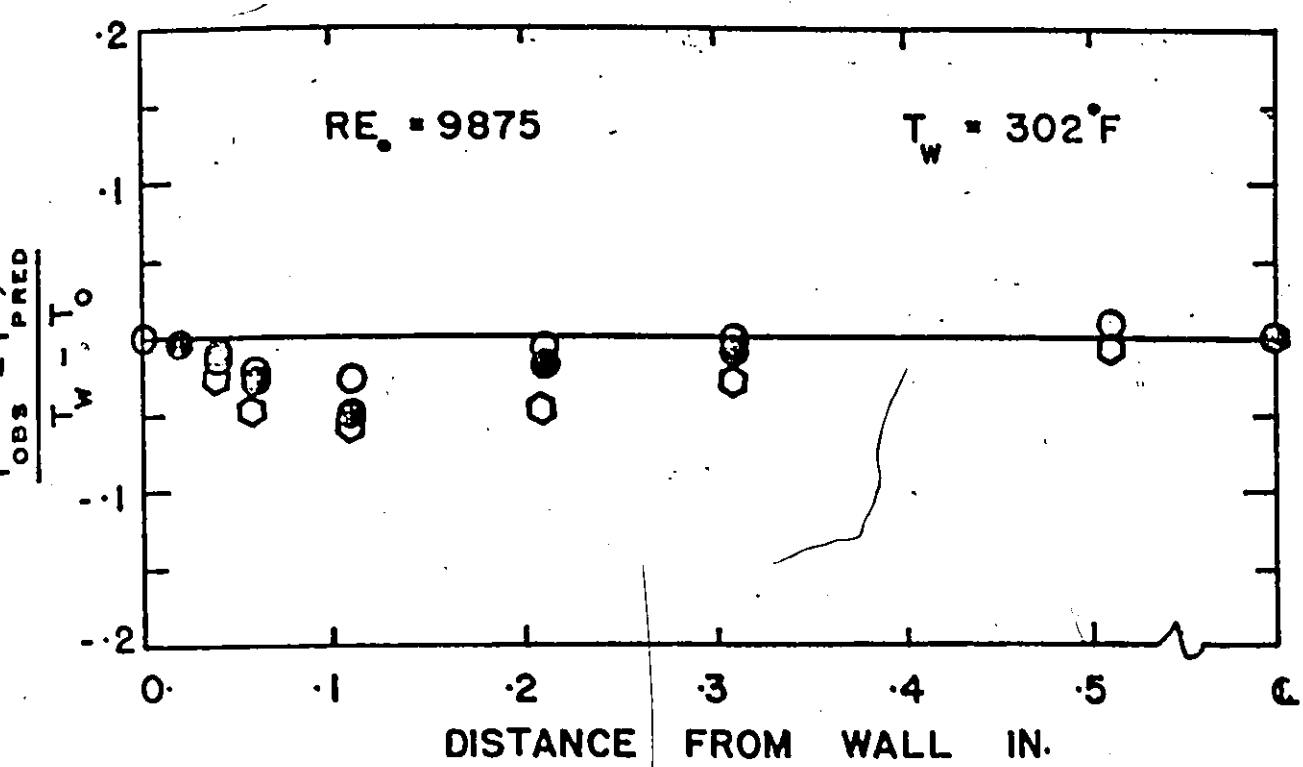

ure 5-13J. Comparison of the Observed and Predicted (from Calculated Eddy Diffusivity Profiles for Heat, Pr_t from Quarmby Equation) Temperature Profiles. Top Port, ○; Middle Port, ●; Bottom Port, ⬡; Predictions based on Modified Reichardt Model and Reynolds Analogy and Reynolds Analogy Solution was Unstable.

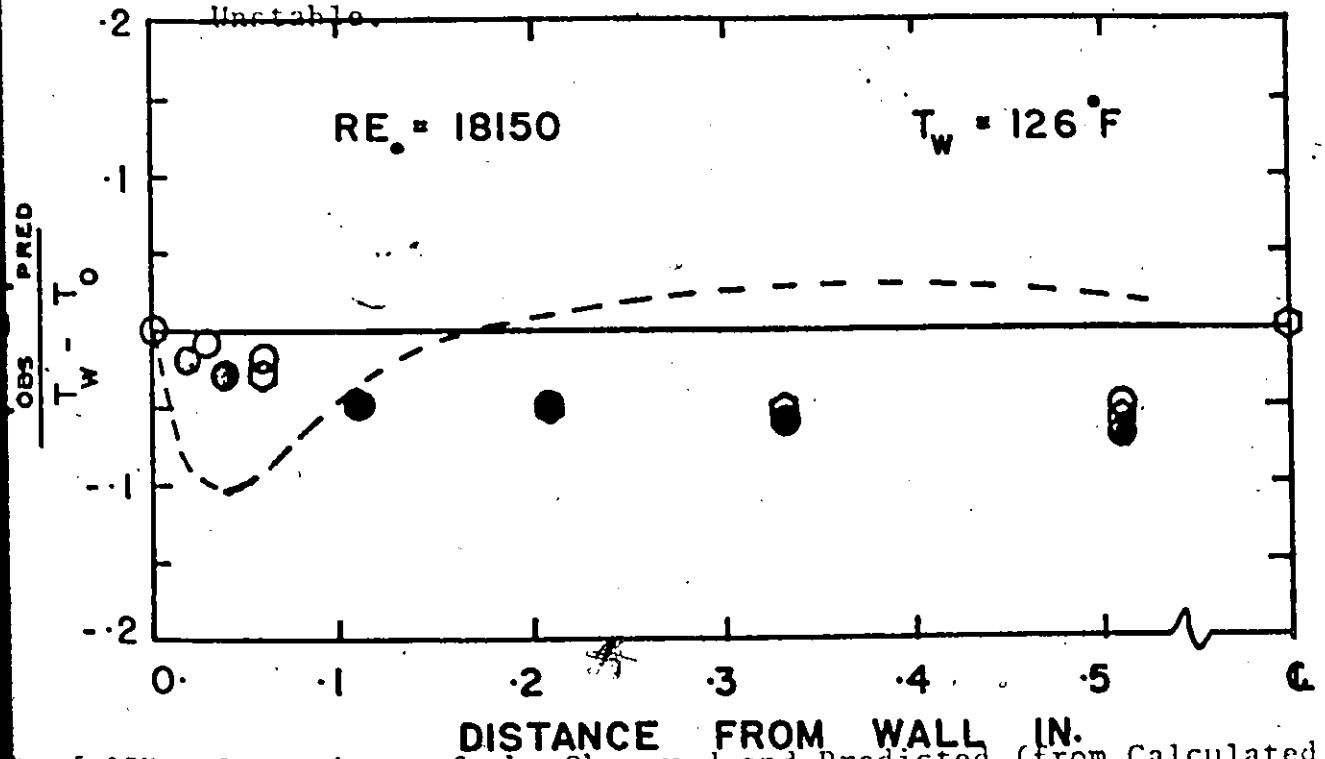

ure 5-13K. Comparison of the Observed and Predicted (from Calculated Eddy Diffusivity Profiles for Heat, Pr_t from Quarmby Equation) Temperature Profiles. Top Port, ○; Middle Port, ●; Bottom Port, ⬡; Predictions based on Modified Reichardt Model and Reynolds Analogy ---.

profiles now agree more closely although errors still appear to be correlated with the radial position. Similarly, a comparison of the measured and the predicted velocity profiles indicate good agreement in the turbulent core; unfortunately the measurements in the wall region could not be made so that the comparison in this region cannot be done.

Certainly the predicted temperature profiles could be made to agree more closely with those measured by adjusting the radial variation in turbulent Prandtl number. This would require a considerable amount of computer time. In the absence of velocity measurements in the region where the greatest difference between the measured and predicted temperatures occur, it was felt that this fitting procedure was unwarranted. On the other hand, since the eddy diffusivity values are substantially affected by the free-forced convection interaction phenomenon, there is no reason to believe that the radial variation in turbulent Prandtl number should remain the same as that for the isothermal flow.

The radial variation in turbulent Prandtl number is an important characteristic of the free and forced convection interaction phenomenon. It was one of the original objectives of this work. Unfortunately, the measurement of velocity profile in the wall region by the cross correlation technique, outlined in Appendix F, failed in the wall region. Laser anemometry [D12] is the only currently available technique which could be used in this experimental system. When the velocity measurements become available in the region of interest, then meaningful

turbulent Prandtl number variations can easily be calculated. In that case, the eddy viscosity can be determined from the integration of momentum conservation equations using measured velocity profiles. The eddy conductivity can be calculated as was done here. The variation in turbulent Prandtl number follows directly by obtaining the ratio of the two turbulent transport properties. Note also, that the laser anemometry can be used to measure turbulent properties directly so that a more direct way of evaluating free and forced convection interaction phenomenon can become available.

The ratio of buoyancy and inertia forces, Gr/Re^2, has often been taken as a measure of the relative magnitude of free and forced convection for turbulent flows. The temperature at which the physical properties in this ratio are to be evaluated is a matter of controversy. For thermally fully developed flows, a film temperature, often defined as an arithmetic mean between the wall and centre line temperature, has been recommended for physical property evaluation. The implications of this in Gr/Re^2 evaluation are that the average velocity $\bar{u} = G/\bar{\rho}$ in $Re(=DG/\mu)$ is based on the film temperature. This poses no problem for small wall-to-centre line temperature differences $(T_w - T_\ell)$, as the film temperature and bulk temperature of the fluid are not very much different. However, in the entrance region and the large wall-to-centre line temperature differences, where the film and the bulk temperatures are quite different, an average velocity based on the film temperature is substantially different from the true average velocity based on the bulk

temperature. Thus at a fixed inlet Reynolds number, e.g., 18150, $(Gr/Re^2)_f$ for wall temperatures of 443°F and 745°F Gr/Re^2 is 0.292 and 0.30 respectively, (Table 5-2) It has been noted in section 5.3 that the numerical solution of the conservation equations for Run No. 7 was unstable because of the buoyancy term in the momentum conservation equation, while a stable solution was obtained for Run No. 6. It seems unlikely that the difference of 0.008 in the value of $(Gr/Re^2)_f$ caused the instability in the numerical solution. Thus the obvious conclusion is that $(Gr/Re^2)_f$ is not a representative of the free and forced convection interaction.

If instead of calculating the ratio of Gr_f and $Re^2{}_f$, the parameter Gr/Re^2 is first simplified, it then reduces to $Dg\beta\Delta T/\bar{u}^2$. The true average velocity $\bar{u}$ can be calculated from the definitions

$$\bar{\rho}\,\bar{u} = \int_0^{R_o} 2\pi\, r\, \rho u\, dr, \qquad \bar{\rho} = \int_0^{R_o} 2\pi\, r\, \rho\, dr$$

where ρ is a function of radial distance, r, by virtue of its dependency on temperature. The term $\beta\Delta T$ also needs special mention. ΔT is the wall-to-centre line temperature difference and β is the coefficient of volumetric expansion. The product $\beta\Delta T$ represents the density difference responsible for the buoyancy force. For an ideal gas $\beta = \frac{1}{T}$ and over a range of temperatures, β is represented by the geometric mean of the temperature extremes of the range. For not so large ΔT the

geometric and arithmetic means are nearly the same and consequently, $\beta\Delta T$ can be written as $\Delta T/T_f$. Therefore the ratio of buoyancy to inertia forces can be written as:

$$Gr/Re^2 = Dg\Delta T/(\bar{u}^2 T_f) \qquad (5.11)$$

Alternatively, an expression for Gr/Re^2 can be derived from physical interpretations of the dimensionless groups.

$$\text{Reynolds number, } Re = \frac{\text{Inertia force}}{\text{Viscous force}} = \frac{\bar{\rho}\ \bar{u}^2/L}{\mu\ \bar{u}/L^2}$$

$$\text{Grashof number, } Gr = \frac{(\text{Buoyancy force})(\text{Inertia force})}{(\text{Viscous force})^2} = \frac{g(\rho_c-\rho_w)(\bar{\rho}\bar{u}^2/L)}{(\mu\ \bar{u}/L^2)^2}$$

$$Gr/Re^2 = \frac{\text{Buoyancy force}}{\text{Inertia force}} = \frac{g(\rho_c-\rho_w)}{\bar{\rho}\ \bar{u}^2/L}$$

Here L is a characteristic length, ρ_c, ρ_w and $\bar{\rho}$ are the centre line, wall and average densities and $\bar{u}$ is the average velocity. The characteristic length L is taken as the diameter of the pipe, D, though a more rigorous representation would involve the axial distance, x, and the thickness of the thermal boundary layer, δ.

$$Gr/Re^2 = Dg\ (\rho_c-\rho_w)/(\bar{\rho}\ \bar{u}^2) \qquad (5.12)$$

Brown and Gauvin [B3] suggested that to account for the changing velocity profile due to heating, wall-to-bulk rather

Table 5-2

Run No.	Re_o	T_w °F	$(Gr/Re^2)_f$	Gr/Re^2 Eq.(5-11)	Gr/Re^2 Eq.(5-13)	Nu^*_{pf}	Nu^{**}_{ε}	Percent Increase
1	37535	175	.0322	.0373	.033	107.35	147.0	37
3	24600	420	.160	.250	.2115	75.27	166.5	121
4	24600	700	.1655	.344	.274	72.8	164.93	127
5	18150	126	.076	.085	.078	62.06	124.4	100
6	18150	443	.292	.450	.3875	59.47	164.7	177
7	18150	745	.300	.6175	.4826	57.45	162.0	182
8	9875	302	.784	.9957	.897	38.03	119.5	215

* Nu_{pf} is Nusselt number at the bottom port, calculated from the solution of the conservation equations assuming zero body force term, i.e., pure forced convection.

** Nu_{ε} is Nusselt number from the use of the calculated effective conductivity profiles and taking into account the free convection interaction in the solution of conservation equations, at the bottom port.

than wall-to-centre line temperature difference should be used as a measure of buoyancy force. However, in an open system like the present one where the flow is exhausted to the atmosphere, the buoyancy force is determined by the temperature difference between the wall and the ambient conditions. Because, if the flow is shut down, the 'chimney effect' created will be proportional to the wall-to-ambient temperature difference. Therefore

$$\frac{Gr}{Re^2} = \frac{Dg(\rho_a - \rho_w)}{\bar{\rho}\ \bar{u}^2} \qquad (5.13)$$

The experimental operating conditions and the corresonding Gr/Re^2 values based on the film temperature and Equations (5.11) and (5.13) are listed in Table 5-2. Equation (5.13) is probably the best representation of the ratio of buoyancy and inertia forces.

Figure 5-14 shows the effective conductivity $(1+\frac{\epsilon_h}{\alpha})$ profiles plotted against dimensionless distance, y^+, for the bottom port of the various runs with Gr/Re^2 as the parameter. Also shown for comparison is the profile calculated by Abbrecht and Churchill [A3] for Re = 15000 and 65000; and those obtained from the modified Reichardt eddy viscosity expressions (3.31 to 3.33) when

(i) Reynolds analogy, $\epsilon_m = \epsilon_h$, is assumed,

(ii) turbulent Prandtl number recommended by Quarmby (Equation 5.2) is assumed.

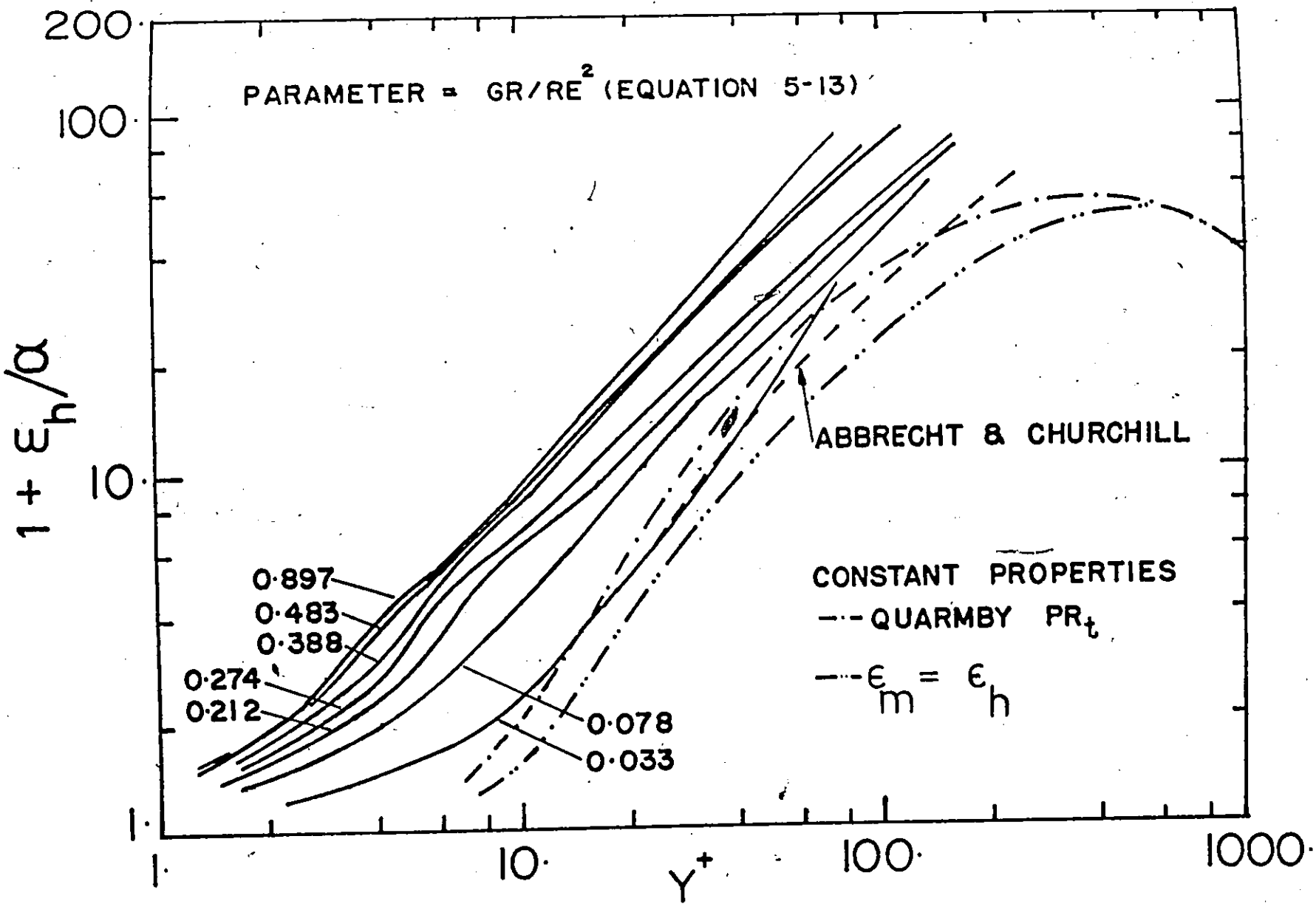

Figure 5-14. Calculated Eddy Diffusivity for Heat Profiles for the Bottom Port as a Function of $Gr/_{Re}{}^2$ (Calculated from Equation (5.13).)

It is observed that for $Gr/Re^2 = .033$ (Run No. 1), which is in the pure forced convection region in Figure 4-7, the calculated effective conductivity profile is very close to the one obtained by Abbrecht and Churchill. From Figure 11 of [A3], it was not possible to accurately determine the values for $y^+ < 20$. The excellent agreement between the two is due to the fact that in both experimental studies forced convection was accompanied by only negligible buoyancy force (the relative direction of the two convections for [A3] is not known). The departure of those profiles from the Reynolds analogy could possibly be due to the breakdown of the Reynolds analogy in this low Reynolds number range of the turbulent flow. Small deviations from the profile based on Quarmby's equation is not surprising as the latter is based on a mean curve through the experimental data of [Q1], and there is a $\pm$ 15% scatter around it. Moreover, Quarmby's measurements were done on diffusion from a point source of heat rather than a continuous one, as is the case in the present investigation and [A3]. The present investigation thus, substantiates the evidence in the literature regarding the invalidity of equality of eddy properties of heat and mass transport.

A systematic increase in the effective conductivity $(1 + \varepsilon_h/\alpha)$ profiles with Gr/Re^2 in Figure 5-14 indicates that with the increase in the interaction between free and forced convection, the contribution of the turbulent transport of heat increases and consequently so does the heat transfer rate. This substantiates the previous observation in Figure 5-11 of the increased temperature fluctuations, indicative of higher turbulent activity, with the increase in the relative magnitude of the

free convection. Table 5-2 lists the comparsion between the Nusselt numbers obtained from the pure forced convection considerations, and those by including the free convection interaction and the calculated effective conductivity profiles. It is noted that as much as 215% increase in Nusselt number is observed for Run No. 8. In Figure 4-7, Run No. 8 is indicated to be on the verge of flow reversal and has the highest Gr/Re^2 ratio with unidirectional flow. A 100% increase in Nusselt number is observed for $Gr/Re^2 = 0.078$. Herbert and Sterns [H6] obtained 54% increase for $Gr/Re^2 = 0.10$, but these results are for large downstream distances from the entrance while in the present investigation only the entrance region has been studied. Comparison with the results of Eckert and Diaguila [E1] will not be appropriate as the entering velocity profile was flat in this case while fully developed in the present investigation.

Kline [K1] in his flow visualisation study of isothermal water flow in a diverging channel observed that the turbulent eddies leaving the wall region experience a violent bursting phenomena at $y^+ \simeq 30$. Higher turbulent bursting rates were observed for a diverging channel than for a straight one. This increased turbulent activity was attributed to the adverse pressure gradient, created by the deceleration of the fluid, which when severe enough causes flow separation. It is analogous to the present case of free and forced convection interaction where the opposing buoyancy force creates the adverse pressure gradient and ultimately results in flow reversal.

It is recognised that the interaction between free and forced convection is a complicated phenomenon, and is probably not a simple function of Gr/Re^2. An empirical correlation relating the effective conductivity profile with Gr/Re^2 will be an over simplification of the phenomenon. It is felt that the increased turbulent activity observed in this investigation is the result of a breakdown of the assumption relating to the local equilibrium among the processes of turbulent energy generation, dissipation and diffusion.

The calculated effective conductivity profiles represent the net effect of two phenomena having opposing effects on the structure of the turbulent flow:

(i) Opposing free and forced convection interaction,

(ii) Relaminarisation effect in the wall region.

The relaminarisation effect is due to the increased gas viscosity arising in the wall region where high temperatures exist. This results in an increase in thickness of viscous sublayer and a consequent damping of the turbulence in the region where the turbulence is generated. Under the operating conditions of the present investigation the flow may not actually become laminar but the effect of change in viscosity is significant to affect the turbulence structure of the flow. The continuous thickening of the viscous sublayer also causes a breakdown of local equilibrium between the turbulent processes in this region. In the numerical solution, all these factors should be taken into account while defining effective viscosity and effective conductivity for the turbulent flow.

Jones and Launder [J6] suggested that in addition to the mass, momentum and energy conservation equations, equations representing conservation of turbulence kinetic energy and turbulence dissipation rate should also be solved simultaneously. For use in these equations, the effective viscosity and conductivity are related to the turbulence kinetic energy and the length scale of turbulence. The length scale parameter is changed to the dissipation rate since the former is not a well-conditioned variable. Thus the eddy properties (viscosity and conductivity) change with the turbulence structure of the flow. However, this means that the constitutive equations relating eddy properties to the characteristic turbulence quantities (kinetic energy and dissipation rate), have to be provided. The constants involved in these equations and the conservation equations have also to be provided and related to the system parameters, e.g., Gr/Re^2, viscous sublayer growth, etc. This process is still under evolution as more experimental and theoretical research needs to be directed towards the understanding of non-equilibrium turbulent flows.

5.7 Conclusions

It can be concluded that the phenomenon of free and forced convection interaction is a complex one. The occurrence of flow reversal creates complex flow patterns. Even when there is no flow reversal, there is a significant influence of the free convection on the mechanism of turbulent transport of heat. Over the limited length of the test section, the

effective conductivity has been found to be independent of the axial distance. Experiments with longer test sections should confirm or refute this observation. A systematic increase in the effective conductivity profiles has been observed with the increase in the ratio of buoyancy to inertia forces. This indicates the effect of free convection on the force convection phenomenon. It has thus provided a substantial proof of the increased turbulent activity due to free and forced convection interaction, as has been speculated in the literature to explain the observed increase in the heat transfer rates.

The use of the turbulent diffusivity concept, that is an extension of the mixing length models, in situations involving the non-equilibrium between the turbulent processes is questioned. It is suggested that a real understanding of the effects of laminarisation and free convection on the forced convective heat transfer phenomenon can only be obtained if a more fundamental approach is taken in solving the conservation equations.

CHAPTER 6

SUMMARY AND RECOMMENDATIONS

6.1 Summary

The work of the present investigation and the contribution to the knowledge can be summarised as follows:

(i) By the use of an electro-chemically generated tracer, the flow pattern at the wall, for water flow in a pipe, has been visualised under the conditions of opposing free and forced convection. The onset of flow reversal has been indicated as a function of flow parameters; such as Reynolds number, Grashof number, Prandtl number and the length to diameter ratio.

(ii) From the results of flow visualisation in water and using dynamic similarity considerations, operating conditions for the air heating experiment have been designed so that only unidirectional flow prevails for most of the experiments.

(iii) Radial measurements of the temperature and the measurement of axial velocity in the flow field have been done in a 24 in. long, 8.054 in. diameter stainless steel test section for $7500 < Re_o < 37535$ and $122 < T_w < 890^oF$, with the gas exhibiting a fully developed, turbulent velocity profile at the inlet.

(iv) Measured temperature profiles, under conditions where flow reversal is expected from dynamic similarity, revealed

unusual behaviour with axial distance as compared to the situations where flow reversal is not expected. This indirectly indicated flow reversal.

(v) Analysis of the air flow field involving considerations of mass, momentum and energy conservation was done. The numerical solution of the resulting partial differential equations was used to predict the temperatures and the velocities at various axial and radial locations.

(vi) The body force, due to the temperature and hence the density differences in the flow field, was found to have a large influence on the convection phenomena. With a large buoyancy force, instability in the numerical solution developed due to the severe retardation of the flow in the region of the wall.

(vii) Comparison of the predicted and measured temperature and velocity profiles indicated that for negligible buoyancy force, the agreement is excellent while the deviations increase with the increase in the relative magnitude of the free to forced convection.

(viii) Various modifications to the empirical correlations (based on isothermal flow measurements) for the eddy properties of the turbulent flow were tried. Use of local physical properties, departure from the Reynolds analogy of equality between the transport of energy and momentum, and modifications accounting for changing shear stress profile gave limited success.

(ix) Measurements of temperature fluctuations indicated increased turbulent activity with the buoyancy force. The non-dimensionalising parameters were modified for a developing thermal boundary layer.

(x) From the measured temperature profiles and estimated velocity profiles, the effective conductivity profiles were calculated by the integration of the energy equation. An iterative procedure involving integration of the energy equation to provide an estimate of effective conductivity and using this to obtain new predictions, from the solution of the conservation equation, of the temperature and velocity profiles was carried out. Systematic variations of the calculated effective conductivity profiles with Gr/Re^2 ratio (a measure of relative magnitudes of free and forced convection) was observed. This indicated increased turbulent activity in the flow field with the increase in interaction between the free and the forced convection. The (Gr/Re^2) ratio was modified for it to be applicable in the developing thermal boundary layer.

(xi) The predictions of temperature and velocity profiles from the calculated effective conductivity profiles and using Quarmby's recommendation for the variation in turbulent Prandtl number, were in reasonable agreement with the experimental values.

(xii) Increased heat transfer coefficients (215%), as compared to the pure forced convection predictions, have been observed with increasing Gr/Re^2 (0.9).

(xiii) The development of a new velocity measurement technique was attempted. Reliable measurements could only be made for the central core of the flow.

6.2 Recommendations for Future Work

To further understand the free and forced convection interaction phenomena, the following lines of attack are suggested for future work.

(i) In the present investigation, no significant variation of the effective conductivity profiles with the axial distance was observed. However, the calculated conductivity profiles represent a significantly different flow behaviour from the isothermal turbulent flow at the inlet of the test section. Thus it seems that at the very entrance (less than 1 diameter), a substantial change in the flow structure takes place. This phenomenon should be investigated by measurements in the immediate entrance region. Investigations should also be carried out at axial distances greater than 3 diameters (used in the present investigation) to substantiate or refute the observation of effective conductivity being independent of the axial distance.

(ii) Accurate measurements of velocity profile in the non-isothermal flow field, especially near the wall should be done, if possible, by laser anemometry or any other

suitable technique so that the effective viscosity and hence the turbulent Prandtl number could be determined.

(iii) Since the diverging channel flow is an analogous situation to the opposing free and forced convection, the measurements of mean velocity and turbulence quantities may give considerable information about the decelerating flow structure. However, a detailed study of the dynamic similarity of the two flow situations will be required to establish the validity of the analogy. Since in a diverging channel the flow is isothermal, the measurements would be easier to perform than in a non-isothermal flow field.

(iv) Oosthuizen [O1] recently tried to incorporate the effect of buoyancy force in the eddy viscosity expression and showed that the experimental data of Hall and Price [H9] for aiding free and forced convection situation could be predicted reasonably well by adjusting a constant 'J'. The extension of this analysis to the opposing convection situation though is straightforward, it is doubtful if J will be a single valued or some simple function of flow parameters. Moreover, since it is recognised that the interaction of the opposing free and forced convection is a complex phenomenon, the validity of such an approach seems limited.

(v) Jones and Launder [J6] have recommended a procedure which may be applicable to the complex flow phenomena associated with the free and forced convection interaction. This

method accounts for the local equilibrium in the turbulent boundary layer, Conservation equations of turbulent kinetic energy and dissipation rate along with those of mass, momentum and energy need to be solved simultaneously. Thus eddy properties are related to the changing turbulent flow structure. However, the parameters involved in these equations have to be provided and related to the system parameters. This approach seems quite appropriate as it is more fundamental in nature than the assumption of flow similarity in equilibrium boundary layers.

CHAPTER 7

CONCLUSIONS

The major conclusions of the present investigation are as follows:

(i) Cooling of an upward flow of water and heating of a downward flow of air are dynamically similar situations and the flow parameters, Reynolds number, Grashof number, Prandtl number and the length to diameter ratio characterise the flow field. Thus conditions of flow reversal observed in one system can be transferred into the other through these flow parameters.

(ii) The presence of the body force has a strong influence on the convection phenomena. Its presence in the momentum conservation equation causes a peaking shear stress profile whose value at the wall may decrease to zero and then become negative.

(iii) The use of the empirical correlation (based on isothermal flow) for eddy properties is unsuitable for predicting heat transfer rates by the numerical solution of the conservation equations where there is a significant interaction between the free and forced convection. Use of local physical properties, suggested turbulent Prandtl numbers and various modifications accounting for the non-linear shear stress distribution did not resolve the discrepancies observed.

(iv) The effect of opposing free and forced convection interaction is to increase the turbulent activity in the flow field as has been observed from the calculated effective conductivity profiles. This explains the increased heat transfer rates observed in the literature.

NOMENCLATURE

C_p	Heat capacity, BTU/lb-^oF
D	Diameter of pipe, ft.
f	Fanning's friction factor
g	Acceleration due to gravity, ft/sec^2
g_c	Gravitational constant, lb_m-ft/lb_f-sec^2
G	Mass flow rate, lb/hr-ft^2
Gm	Dimensionless effective momentum diffusivity defined in Equation (3.10)
Gh	Dimensionless effective thermal diffusivity defined in Equation (3.10)
h	Heat transfer coefficient, BTU/ft^2-hr-^oF
H	Constant for step size, Equation (3.18)
k	Thermal conductivity, BTU/ft-hr-^oF
ℓ	Mixing length, ft.
N	Number of radial nodes
p	pressure, lb_f/ft^2
P	Dimensionless pressure, Equation (3.10)
$\dot{q}''$	Heat flux density, BTU/hr-ft^2
r	Radial location, ft.
R_o	Radius of pipe, ft.
R	Dimensionless radial location, r/R_o
T	Temperature, ^oF
T'	Temperature fluctuations, ^oF
u	Axial velocity, ft/sec
$\bar{u}$	Average axial velocity, ft/sec

u'	Axial velocity fluctuations, ft/sec
U	Dimensionless axial velocity, $u/\bar{u}_o$
u^*	Characteristic velocity $\sqrt{\tau_w g_c/\rho}$
v	Radial velocity, ft/sec
V	Dimensionless radial velocity, $v/\bar{u}_o$
v'	Fluctuating radial velocity, ft/sec
x	Axial distance from the entrance, ft
X	Dimensionless axial distance, $x\|R_o$
y	Distance from wall, (R_o-r), ft.
y^+	Dimensionless radial distance, $y \sqrt{\frac{\tau_w g_c}{\rho}} \frac{\rho}{u}$

Dimensionless Groups

Gr	Grashof number, $D^3 g \beta (T_w-T_o)/ \nu^2$
Nu	Nusselt number, hD/k
Pr	Prandtl number, $C_p \mu/k$
Pr_t	Turbulent Prandtl number, ϵ_m/ϵ_h
Re	Reynolds number, DG/u

Greek Letters

α	Thermal diffusivity, $k/\rho C_p$, ft^2/sec
α	Weighting factor, Equation (3.24)

β	$1-\alpha$
γ	Weighting factor, Equation (3.27)
ε_m	Eddy kinematic viscosity, ft^2/sec
ε_h	Eddy thermal diffusivity, ft^2/sec
θ	Dimensionless temperature, Equation (3.10)
μ	Dynamic viscosity, lb/ft-sec
ν	Kinematic viscosity, μ/ρ, ft^2/sec
ρ	Density, lb/ft^3
τ	Shear stress, lb_f/ft^2
ϕ	Flow property, eg., temperature, velocity, etc.

Subscripts

b	Bulk
C	Centreline
f	Film
t	Turbulent
w	Wall
0	Inlet
∞	Large downstream distance

BIBLIOGRAPHY

A1 Abramowitz, M., J. Math. and Phy., 32, 184 (1953).

A2 Azer, N. Z., and Chao, B. T., Int. J. Heat Mass Transfer, Vol. 1, pp. 121-38 (1960).

A3 Abbrecht, P. H., and Churchill, S. W., AIChEJ, Vol. 6, pp. 268-73 (1960).

A4 Acrivos, A., AIChEJ, Vol. 4, No. 3, pp. 285-89 (1958).

A5 Altman, M., and Staub, F. W., Chem. Eng. Prog. Symp. Ser., No. 29, 55, pp. 121-26 (1959).

A6 Aerodynamic Measurements, Gas Turbine Laboratory, Massachussets Institute of Technology (1953).

B1 Baker, D. J., 'A technique for precise measurement of small fluid velocities', J. Fluid Mech., Vol. 26, part 3, pp. 573-5 (1966).

B2 Brown, C. K., and Gauvin, W. H., Can. J. Chem. Eng., pp. 306-12 (1965).

B3 Brown, C. K. and Gauvin, W. H., Can. J. Chem. Eng., pp. 312-18 (1965).

B3A Brown, C. K. and Gauvin, W. H., Chem. Eng. Sci., 21, pp. 961-70 (1966).

B4 Brown, W. G., VDI-Forschingsh, 26, 480 (1960).

B5 Biggs, R. C., and Stachiewicz, V. W., 'Combined free and forced convection heat transfer to gases', Paper NC 3.1, Fourth International Heat Transfer Conference, Paris (1970).

B6 Bird, R. B., Stewart, W. E., and Lightfoot, E. N., Transport Phenomena, John Wiley and Sons, Inc. (1960).

B7 Brodkey, R. S., AIChEJ, Vol. 9, No. 4, pp. 448-451 (1963).

B8 Botje, J. M., Ph.D Thesis, Purdue University (1956).

B9 Berry, Jr., V. J., Appl. Sci. Res., Section A, Vol. 4 (1953).

B10 Bankston, C. A., and McEligot, D. M., Int. J. Heat Mass Transfer, Vol. 13, pp. 319-44 (1970).

B11 Bankston, C. A., ASME-AIChE Heat Transfer Conference, Minneapolis, Minn., Aug. 3-6 (1969), paper 69-HT-54.

B12 Barnes, N. F., and Jackson, J. D., J. Mech. Eng. Science, Vol. 3, p. 303 (1961).

B13 Blom, J., Fourth Int. Heat Transfer Conference, Paris, Paper FC 2.2, (1970).

B14 Brighton, J. A., J. Basic Engineering, pp. 1079-80 (Dec. 1965).

B15 Barakat, H. Z., and Clark, J. A., J. Heat Transfer, pp. 421-27 (1966).

B16 Bentley, P. G., and Dawson, D. G., Trans. of Society of Instrument Technology, pp. 783-93 (Sept. 1966).

B17 Beck, M. S., and Plaskowski, A., Electronics Letters, Vol. 3, # 4, pp. 169-71 (1967).

B18 Boonstoppel, F., Veltman, B., and Vergouwen, F., Industrial Measurement Techniques for on-line Computers, Conference Publication No. 43 (June 1968).

C1 Colburn, A. P., and Hougen, O. A., Ind. Eng. Chem., 22, 522 (1930).

C2 Colburn, A. P., Trans. AIChE, 29, 174 (1933).

C3 Coon, C. W., and Perkins, H. C., J. Heat Transfer, pp. 506-512 (1970).

C4 Coon, C. W., Ph.D Thesis, University of Arizona (1968).

C5 Carr, A. D., Connor, M. A., Buhr, H. O., AIChE-ASME Heat Transfer Conference, Denver, Colo., U.S.A. (Aug. 1972), Paper 72-HT-19.

C6 Churchill, S. W., and Balzhiser, R. E., Chemical Engineering Progress Symposium Series, Vol. 55, # 29, pp. 127-135 (1948).

C7 Corcoran, W. H., Page, F., Schlinger, W. G., and Sage, B. H., Ind. Eng. Chem., Vol. 44, pp. 410-30 (1952).

D1 Deissler, R. G., NACA Report 1210 (1955) Also Recent Advances in Heat and Mass Transfer, McGraw Hill (1961).

D2 Deissler, R. G., NACA, TN-2242 (1950).

D3 Deissler, R. G. and Eian, C. S., NACA, TN-2629 (1952).

D4 Dittus, F. W., and Boelter, L. M. K., Univ. Calif. (Berkeley) Publs. Eng., 2, 443 (1930).

D5 Deissler, R. G., NACA, TN-2138.

D6 Deissler, R. G., Trans. ASME, pp. 73-85 (1954).

D7 Deissler, R. G., Int. Developments in Heat Transfer, Part III (1961), Int. Heat Transfer Conference, Colorado.

D8 Deissler, R. G., Trans. ASME, pp. 1221-33 (1955).

D9 Dimmock, N. A., British Chemical Engineering, June, 1957, pp. 302-307.

D10 Dutka, A. F., and Ewens, F. J., J. Quality Technology, 3, # 4, pp. 149-155 (1971).

D11 DeNevers, N., AIChEJ, 12, # 6, pp. 1110-15 (1966).

D12 DISA Information, Measurement and Analysis, No. 12, (Nov. 1971).

E1 Eckert, E. R. G., and Diaguila, A. J., Trans. ASME, pp. 497-504 (1954).

E2 Everett, M., The Chemical Engineer, CE159 (Sept. 1969).

F1 Fluid Meters, Their Theory and Application, Fifth Edition, ASME Publication (1959).

G1 Gowen, R. A. and Smith, J. W., Chemical Eng. Science, Vol. 2, pp. 1701-11 (1967).

G2 Graetz, L., Ann. Phys. U. Chem., 25, 337 (1885).

G3 Guerrieri, S. A., and Hanna, R. J., ONR Final report No. N-Onr-622(01), (1952).

G4 Gill, W. N. and Scher, M., AIChEJ, Vol. 7, No. 1, pp. 61-63 (1961).

G5 Grass, A. J., J. Fluid Mech., Vol. 50, Part 2, pp. 233-63 (1971).

G6 Goldmann, K., Chem. Eng. Prog. Symposium Series, Nuclear Eng., Part III, Vol. 50, No. 11 (1954).

G7 Graybill, F. A., Introduction to Linear Statistical Models, Vol. 1, McGraw-Hill Book Co. (1961).

G8 Goldberg, P., Upstream history and apparent stress in turbulent boundary layer, Gas Turbine Lab. Report No. 85, M.I.T., May (1966) DDC AD-636,323.

H1 Hausen, H., Z., Ver. deut. Ing., 4, 91 (1943).

H2 Hallman, T. M., Trans. ASME, 78, pp. 1831-42 (1956).

H3 Hallman, T. M., NASA Tech. Note, TN D-1104 (1961).

H4 Hinze, J. O., Turbulence, McGraw-Hill Book Co., (1959).

H5 Hall, W. B., and Price, P. H., Heat and Mass Transfer by Combined Forced and Natural Convection, Inst. of Mech. Engrs. Symposium Paper C113 (1971).

H6 Herbert, L. S., and Sterns, U. J., Private Communication, CSIRO, Astratia (1971).

H7 Hall, W. E., and Jackson, J. D. ASME-AIChE Heat Transfer Conference, Minneapolis, U.S.A., Aug. 3-6 (1969), Paper 69-HT-55.

H8 Hershey, H. C., Zakin, J. L., and Simha, R., I & EC Fundamentals, 6, # 3, pp. 413-21 (1967).

H9 Hall, W. B. and Price, P. H., Proc. Fourth Int. Heat Transfer Conference, NC 3.3 (1970).

H10 Hoffman, T. W., Gauvin, W. H., Can. J. Chem. Eng., Vol. 40, p. 110 (1962).

I1 Intaglietta, M., and Tompkins, W. R., IEEE Trans. on Bio-medical Engineering (Sept. 1971).

J1 Jackson, P. V., 'Relative viscosity in isothermal turbulent flow in a vertical tube', M.S. Thesis, George Washington University (1965).

J2 Jackson, T. W., Harrison, W. B., and Boetler, W. C., Trans. ASME, pp. 739-745 (1958).

J3 Jackson, J. D., A theoretical investigation into the effects of surface/gas temperature ratio for fully developed turbulent flow of air, He, CO_2 in smooth circular tubes, ARC 22, 784, FM 3084, Great Britain, 1961, DDC AD 269 066.

J4 Jenkins, R., Heat Transfer and Fluid Mechanics Institute Preprints, Stanford University Press, Stanford, California, pp. 147-58 (1951).

J5 Johnk, R. E., and Hanratty, T. J., Chem. Eng. Science, Vol. 17, pp 881-92 (1962).

J6 Jones, W. P. and Launder, B. E., Int. J. Heat Mass Transfer, 16, pp. 1119, (1973).

K1 Kline, S. J., Reynolds, W. C., Schraub, F. A., Runstadler, P. W., J. Fluid Mech., Vol. 30, Part 4, pp. 741-73 (1967).

K2 Kestin, J. and Richardson, P. D., 'Heat transfer across turbulent, incompressible boundary layers', Int. J. Heat Mass Transfer, Vol. 6, pp. 147-189 (1963).

K3 Kays, W. M., Trans. ASME, 77, 1265 (1955).

K4 Knudsen, J. G. and Katz, D. L., Fluid Dynamics and Heat Transfer, McGraw-Hill Book Co., Inc. (1958).

K5 Kutateladze, S. S., and Leontiev, A. I., Turbulent boundary layer in compressible gases, Academic Press, New York, N.Y. (1964).

L1 Laufer, J., The structure of turbulence in fully developed pipe flow, NACA-TR-1174 (1954).

L2 Ludwieg, H., Z. Flugwiss, Vol. 4, pp. 73-81 (1956).

L3 Lawn, C. J., Turbulent heat transfer at low Reynolds number, J. Heat Transfer, pp. 532-6 (Nov. 1969).

L3A Ibid., CEGB, RD/B/NI004 (1968).

L4 Leveque, J., Ann. mines, 13, 201, 305, 381 (1928).

L5 Langhaar, H. L., Trans. ASME, 64, A-55 (1942).

L6 Lykoudis, P. S., and Toulukin, Y. S., Trans. ASME, Vol. 80, p. 653, (1958).

L7 Lynn, Scott, AIChEJ, Vol. 5, No. 4, pp. 566-67 (1959).

L8 Launder, B. E., and Priddin, C. H., Int. J. Heat and Mass Transfer, Vol. 16, pp. 700-702, (1973).

L9 Lax, P. D., and Richtmeyer, R. D., Comm. Pure Appl. Math., 9, 267 (1956).

L10 Lapidus, L., Digital Computation for Chem. Engrs., p. 60, McGraw-Hill Book Co., Inc. (1962).

M1 Metais, B., Criteria for mixed convection, HTL, TR No. 51, Heat Transfer Laboratory, University of Minnesota, Also J. Heat Transfer, pp. 295-6 (May 1964).

M2 Martinelli, R. C., and Boelter, L.M.K., 'Analytical prediction of superposed free and forced convection in a vertical pipe', University of California publications in Engineering, Vol. 5, No. 2, pp. 23-58 (1942).

M3 Martinelli, R. C., et al., Trans. ATChE, 38, pp. 493-530 (1942).

M4 Martinelli, R. C., Trans. ASME, Vol. 69, pp. 947-59 (1947).

M5 McEligot, D. M., Magee, P. M., Leppert, G., J. Heat Transfer, pp. 67-76 (1965).

M6 Magee, P. M., Ph.D. Thesis, Stanford University (1964).

M7 McEligot, D. M., Smith, S. B., Bankston, C. A., J Heat Transfer, pp. 641-650 (1970).

M8 McEligot, D. M., Ormand. L. W., and Perkins, H. C., J. Heat Transfer, Vol. 88, pp. 239-45 (1966).

M9 McEligot, D. M., Coon, C. W., and Perkins, H. C., Int. J. Heat Mass Transfer, Vol. 13, pp. 431-33 (1970).

M10 McEligot, D. M., and Bankston, C. A., ASME-AIChE Heat Transfer Conference, Minneapolis, Minn. Aug. 3-6 (1969), Paper 69-HT-52.

M11 McEligot, D. M., Ph.D. Thesis, Stanford University (1963), TID-19446.

M12 Marner, W. J., and McMillan, H. K., J. Heat Transfer, pp. 559-61, (Aug. 1970)

M13 McEligot, D. M., and Bankston, C. A., Los Alamos Scientific Laboratory Report LA-4149 (1969).

M14 McDonald, H., Aero. Quarterly, Vol. XIX, pp. 1-19 (1968).

N1 Nikuradse, J., Proc. of 3rd Int. Cong. Appl. Mech., Vol. 1, p. 239 (1930).

N2 Nash, J. F., and MacDonald, A. G. J., Calculation method for incompressible turbulent boundary layer including effect of upstream history on shear stress, NPL Aero. Report 1234, ARC 29 088, FM 3844, May (1967), NASA N68-20516.

O1 Oosthuizen, P. H., Turbulent combined convective flow over a vertical plane surface, To be published in Proc. Int. Heat Transfer Conference (Tokyo 1974).

P1 Pollock, K. G., 'Heat transfer to sprays and flowing gases', Ph.D Thesis, McMaster University, Hamilton (1967).

P2 Pigford, R. L., AIChE Conference, St. Louis, (1953) Preprint 15.

P3 Perkins, H. C., and Worsoe-Schmidt, P., Int. J. Heat Mass Transfer, 8, pp. 1011-31 (1965).

P4 Petukhov, B. S., Kirillov, V. V., Maidanik, V. N., 3rd Int. Heat Transfer Conference, Chicago, Vol. 1, Paper 28 (1966).

P5 Petukhov, B. S., Nolde, L. D., Toploenergetika, 6, pp. 72-80 (1959).

P6 Pai, S. I., Viscous Flow Theory, II-Turbulent Flow, Van Nostrand, Princeton, N.J. (1957).

P7 Pennell, W. T., Sparrow, E. M., and Eckert, E. R. G., Int. Heat Mass Transfer, Vol. 15, pp. 1067-74 (1972).

P8 Petukhov, B. S., Advances in Heat Transfer, Vol. 6, pp. 503-64 (1970).

P9 Petukhov, B. S. and Popov, V. N., High temperature Heat Physics, Vol. 1, No. 1 (1963).

P10 Pinkel, B., Trans. ASME, Vol. 76, pp. 305-317 (1954).

P11 Patel, V. C., and Head, M. R., J. Fluid Mech., Vol. 34, Part 2, pp. 371-92 (1968).

P12 Page, F., Schlinger, W. G., Breaux, D. K., and Sage, B. H., Ind. Eng. Chem., Vol. 44, No. 2, pp. 424-430 (1952).

P13 Pantankar, S. V., and Spalding, D. B., Heat and Mass Transfer in Boundary Layers, International Textbook Co., London (1970).

Q1 Quarmby, A., and Quirk, R., Int. J. Heat and Mass Transfer, Vol. 15, pp. 2309-27 (1972).

R1 Rosen, E. M., Ph.D. Thesis, University of Illinois, U.S.A. (1959).

R2 Reichardt, H., Complete representation of turbulent velocity distribution in smooth pipes', Z. Angew. Math. Mech., 31, 208 (1951). Also in Recent Advances in Heat and Mass Transfer, Ed., J. P. Hartnett, McGraw Hill Book Co. Inc. (1961).

R3 Reynolds, H. C., Davenport, M. E., and McEligot, D. M., ASME Paper No. 68-WA/FE-34 (1968).

R4 Reynolds, H. C., Swearingen, T. B., and McEligot, D. M., J. Basic Engineering, pp. 87-94 (1969).

R5 Richardson, E. G., J. of the Aeronautical Sciences, Vol. 23, pp. 970-1 (1956).

R6 Repile, Ye. U., and Ponomareva, V. S., Heat Transfer, Soviet Research, Vol. 2, No. 4, pp. 43-49, July 1970.

S1 Sparrow, E. M., Hallman, T. M., Siegel, R., 'Turbulent heat transfer in the thermal entrance region of a pipe with uniform heat flux', App. Sci. Res. Sec. A, Vol. 7, pp. 37-52 (1958).

S2 Sellers, J. R., Tribus, M., and Klein, J. S., Trans. ASME, 78, 441 (1956).

S3 Schenk, J., and Dumore, J. M., Applied Sci. Research, 4A, 39 (1953).

S4 Sieder, E. N., and Tate, G. E., Ind. Eng. Chem., 28, 1429 (1936).

S5 Stokes, G. G., Trans. Cambridge Philos. Soc. Vol. 9 (1851).

S6 Spalding, D. B., J. Appl. Mech. 28E, 455 (1961).

S7 Sherwood, T. K., Smith, K. A. and Fowles, P.E., Chem. Eng. Science, Vol. 23, pp. 1225-36 (1968).

S8 Sleicher, C. A., Tribus, M., Recent Advances in Heat and Mass Transfer, Ed. J. P. Harnell, McGraw Hill Book Co., Inc. (1961).

S9 Seban, R. A., and Shimazaki, T. T., Trans. ASME, Vol. 73, pp. 803-9 (1951).

S10 Summerfield, M., Heat Transfer Symposium, Eng. Res. Inst. Univ. Mich., pp. 155-71 (1953).

S11 Siegel, R., and Sparrow, E. M., J. Heat Transfer, pp. 152-3 (1960).

S12 Senecal, V. E., Sc.D. Thesis, Carnegie Institute of Technology, Pittsburgh, Pa., 1951.

S13 Seban, R. A., and Shimazaki, T. T., Inst. Mech. Eng., London, pp. 122-26 (1951).

S14 Sleicher, C. A., Trans. ASME, pp. 693-704 (1958).

S15 Siegel, R., and Sparrow, E. M., J. Heat Transfer, pp. 280-90 (1959).

S16 Scheele, G. F., Rosen, E. M., and Hanratty, T. J., Can. J. Chem. Eng., Vol. 38, pp. 67-73 (1960).

S17 Scheele, G. F., and Hanratty, T. J., AIChEJ., 9, pp. 183-85 (1963).

S18 Steiner, A., J. Fluid Mech., 47, # 3, pp. 503-12 (1971).

S19 Seban, R. A., and Shimazaki, T. T., Trans. ASME, 73, 803 (1951).

S20 Spalding, D. B., Applied Mechanics Reviews, 20, # 8, 735-40 (1967).

T1 Travis, J. R., Buhr, H. O. and Sesonske, A., A model for velocity and eddy diffusivity distribution in fully turbulent pipe flow, Can. J. Chem. Eng., Vol. 49, No. 1, (1971).

T2 Taylor, M. F., Int. J. Heat Mass Transfer, Vol. 10, pp. 1123-28 (1967).

T3 Townsend, A. A., The structure of turbulent shear flow, Cambridge University Press, New York (1956).

T4 Taylor, M. F., NASA TN D 4332 (1968).

V1 Van Driest, E. R., On turbulent flow near a wall, J Aeronautical Science, pp. 1007-11 (1956).

V2 Von Karman, Trans. ASME, Vol. 61, pp. 705-710 (1939).

V3 Venezian, E., and Sage, B. H., AIChEJ., 7, pp. 688-92 (1961).

W1 Wright, C., and Walters, H., WADC Tech. Report 59-423, August (1959).

W2 Wolf, H., and McCarthy, J., Abstract 100, Presented at annual meeting, Washington, D.C., Dec. 4-7 (1960).

W3 Wolf, H., J. Heat Transfer, pp. 267-79 (1959).

W4 Wills, J. A. B., J. Fluid Mech., Vol. 12, Part 3, pp. 388-96 (1962).

W5 Worrsoe-Schmidt, P. M., and Leppert, G., Int. J. Heat Mass Transfer, Vol. 8, pp. 1281-1301 (1965).

Z1 Zellnik, H. E., and Churchill, S. W. AIChEJ., Vol. 4, No. 1, pp. 37-42 (1958).

APPENDIX A

PHYSICAL PROPERTIES OF AIR AT ATMOSPHERIC PRESSURE

The correlations for heat capacity, viscosity and thermal conductivity cover the range 450 to 1980°F. The correlation for density covers the range 540 to 1800°R. The polynomial forms have been obtained by regressing the tabulated values presented in National Bureau of Standards Circular 564. Temperature, T, is in degree Rankin.

(i) Density, lb./cu.ft.

$$\rho = 0.20738 - 0.41492 \times 10^{-3}T + 0.39657 \times 10^{-6}T^2$$
$$-0.18148 \times 10^{-9}T^3 + 0.31925 \times 10^{-13}T^4$$

S^2 (y) = 0.97789×10^{-7} on 11 degrees of freedom

(ii) Heat capacity, B.T.U./lb. °R

$$Cp = 0.24688 - 0.35554 \times 10^{-4}T + 0.49476 \times 10^{-7}T^2$$
$$-0.12047 \times 10^{-10}T^3$$

S^2 (y) = 0.13419×10^{-6} on 14 degrees of freedom

(iii) Thermal Conductivity, B.T.U./hr.-ft.-°F

$$k = 0.28670 \times 10^{-3} + 0.32778 \times 10^{-4}T - 0.84398 \times 10^{-8}T^2$$
$$+ 0.13190 \times 10^{-11}T^3$$

S^2 (y) = 0.51112×10^{-9} on 14 degrees of freedom

(iv) Viscosity, lb./ft.-sec.)

$$\mu = 0.28967 \times 10^{-6} + 0.28330 \times 10^{-7}T - 0.13157 \times 10^{-10}T^2$$
$$+0.44536 \times 10^{-14}T^3 - 0.63962 \times 10^{-18}T^4$$

S^2 (y) = 0.21966×10^{-15} on 13 degrees of freedom

APPENDIX B

CALIBRATION

Various measuring instruments, e.g., rotameter, sonic nozzle, thermocouples, averaging voltmeter, true random signal voltmeter, hot-wire anemometer and Pitot tube have been used in the course of this investigation. These instruments need to be calibrated for their response against a known input or a standard instrument. In this section, calibration procedures and curves for various instruments will be presented.

B-1 Rotameter

In the flow visualisation experiments, the flow rate of hot water in the circulation loop is measured by a Brooks R-12M-25-4-Br 1 1/2-17G10 rotameter with 12RV 221 stainless steel float. The calibration is done with cold water circulating in the loop and weighing the amount of water collected in a known time interval from the return leg of the loop. The calibration was determined over the full operating range employed in the study.

According to 'Recommended Practices in Calibrating Rotameters No. RP-16-6' (a publication of Instrument Society of America) for the shape of the float used, the calibration is immune to viscosity variations if $\mu \sqrt{\frac{\rho}{\rho_{ref.}}}$ is less than 10, where the viscosity is in centistokes and $\rho_{ref.}$ is

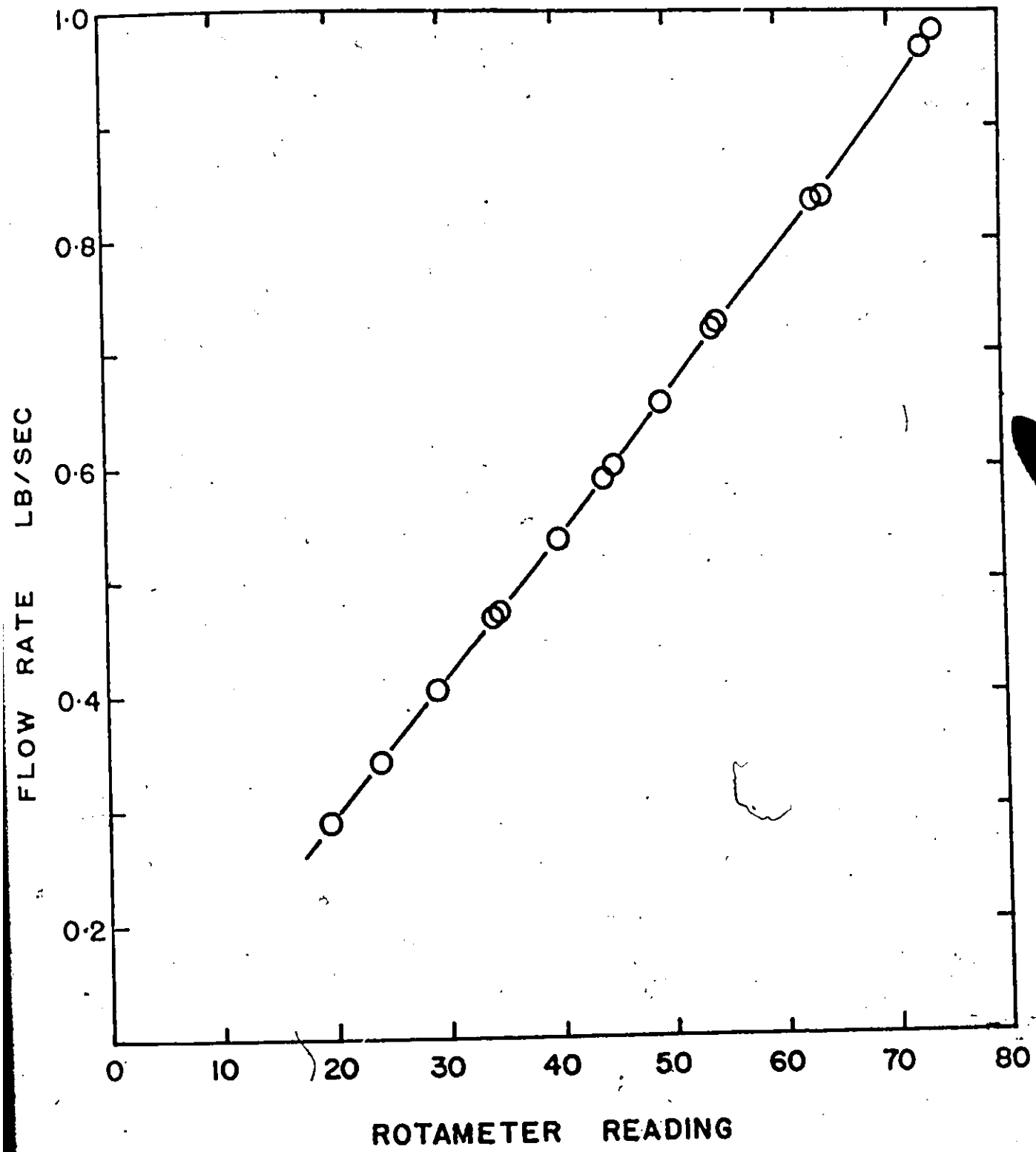

Figure B-1. Calibration of the Rotameter.

the density of the calibrating fluid. In the present case calibration was done at 57°F while the maximum operating temperature was 171°F. Thus $\mu \sqrt{\frac{\rho}{\rho_{ref.}}}$ was between 0.3 and 1.2 and no correction for viscosity was needed. The correction for density variations was approximated by

$$F\ (\text{lb/sec}) = F_{ref.}\ (\text{lb/sec}) \sqrt{\frac{\rho}{\rho_{ref.}}}$$

as recommended in the above reference. Figure B-1 shows the calibration curve thus obtained.

B-2 Sonic Nozzle

The air supply to the air heating experimental equipment is from the building compressed air supply line. The compressors supplying the air are equipped with an off-on pressure controller. When a large volume (200 scfm) of air was required to obtain Reynolds numbers of the order of 37000, large changes in the supply line pressure occurred. Thus it was found necessary to have a flow control device to ensure a constant flow rate of air. In a sonic nozzle, with air flowing, the ratio of the downstream-to-upstream pressures across the nozzle throat must be less than 0.53. If this condition is met, the flow through the nozzle will correspond to the sonic velocity at the temperature and pressure at the throat. In this case, the mass flow rate of air is proportional to upstream pressure and is independent of downstream pressure. Thus, to

obtain a constant flow rate of air it is only necessary to control the upstream pressure. A 5/16 in. diameter nozzle was designed according to the ASME specifications [F1]. Careful machining and polishing of the nozzle contour was done in an attempt to obtain a discharge coefficient close to 1 over the whole range. The upstream pressure of the sonic nozzle was controlled by a pneumatic pressure control system. The flow through the nozzle can be calculated from the real gas law and for air the simplified equation is

$$F = 0.533\ C_v\ (\tfrac{\pi}{4}\ d^2)\ \frac{P_1}{\sqrt{T}}\ .\ 3600 \qquad \text{(B-1)}$$

where F is the flow rate of air in lbs/hr, C_v is the discharge coefficient of the sonic nozzle, d is its diameter of the throat in inches, P_1 is the upstream pressure in psia and T is the temperature of air in ^oR. The discharge coefficient of the nozzle can be obtained by measuring the flow of air through the nozzle by some standard method. For low volumetric flow rate, a wet gas test meter is an adequate standard. For large flow rates, calibrated flow nozzles (Type 210) supplied by Cox Instrument Division were used.

The Cox nozzle was mounted on the centre line and exterior of the end plate of a 24 in. diameter, 36 in. long aluminum drum. The air after passing through the sonic nozzle was fed into the drum at an entrance opposite to the Cox nozzle. The drum was equipped with packing and screens to ensure a uniform flow over the cross section of the drum. By

measuring the pressure in the drum just upstream of the Cox nozzle by an inclined manometer, the air flow rate was determined from the calibration curves supplied by the manufacturer.

To calibrate the sonic nozzle its upstream pressure and temperature were measured along with those for the flow nozzle. From the available calibration curves for the flow nozzle, the mass flow rate of air corresponding to the observed pressure drop was calculated and the discharge coefficient for the sonic nozzle was obtained from Equation (B-1). By varying the upstream pressure of the sonic nozzle, a wide range of flow rates was obtained. The highest upstream pressure was restricted by the pressure in the compressed air supply. To obtain higher or lower flow rates, sonic nozzles of different diameters 3/16 in. and 1/2 in. were used. Table B-1 shows the discharge coefficients calculated by this calibration procedure.

TABLE B-1

P_1 p.s.i.a.	ΔH in.H_2O	F (from calibration curves lbs/hr.	C_v
Cox Flow Nozzle 6A			
34.75	2.19	224	1.011
44.75	3.64	287	1.006
52.35	5.02	336	1.010
59.35	6.366	380	1.005

Cox Flow Nozzle 7A

44.75	.615	289.5	1.013
65.15	1.327	423	1.017
85.35	2.285	555	1.021
95.65	2.875	622	1.020

B-3 Thermocouples

The radial temperature measurement probe and the inside wall surface temperature probe were calibrated against a standard thermocouple in a muffle furnace. Since the geometric configuration of the radial temperature probe was such that it could not be inserted in the hole at the top of the muffle furnace, another thermocouple made from the same batch of materials was used for calibration.

An aluminum block, 2.5 in. diameter and 8 in. long was drilled to make a 5/8 in. diameter and 7 in. long cavity in its centre. It was placed in the heated muffle furnace and the thermocouples were suspended in the cavity through the hole at the top of the furnace. The aluminum block provided a large heat capacity and thus shielded the thermocouples from the temperature fluctuations in the furnace. The output of the thermocouples, with reference junction immersed in an ice water mixture, was recorded at various levels of temperature in the furnace. Deviations of less than 1.5°F were observed for furnace temperatures up to 960°F. Since in the measurement of radial temperature profiles highly fluctuating

temperatures (fluctuations of the order of 10 to 50°F) were encountered, it was decided that no significant loss in the accuracy would occur if the standard temperature vs. e.m.f. tables were used instead of the calibration curve. This was done for ease and accuracy in the interpolation of the temperature from the measured thermocouple output.

B-4 Voltmeters

A true random signal voltmeter (Flow Corporation model 12A1) was used to measure the temperature fluctuations. An averaging digital voltmeter system (a combination of Hewlett-Packard voltage to frequency converter model 2212B and a frequency counter model 5321B) was used to measure the radial temperatures averaged over a span of 100 sec. The calibration of the averaging digital voltmeter was done by internal voltage source whose accuracy was checked from time to time by a potentiometer. The calibration of the true random signal voltmeter was done by supplying a 60 cycles/sec voltage from the Hewlett-Packard 6920B meter calibrator. The output from the calibration meter was checked by the averaging digital voltmeter system.

5.5 Hot-Wire Anemometer

A Flow Corporation model 700 series constant temperature hot-wire anemometer was used to measure the velocity profile in air flow. The anemometer had built-in linearising and temperature compensation circuits. The temperature

compensation was done by having two sensors in the flow field, one of which acted as velocity sensor and the other as temperature sensor. The former carried four times the current than the latter and thus they were named as hot and cold wires respectively. These two wires form two legs of the Wheatstone bridge and thus the changes in the temperature of the flow stream are compensated for in the response of the anemometer to the flow velocity.

The calibration of the hot-wire anemometer was attempted by a calibration flow nozzle DISA model 55D90 which provides a jet of air with a flat velocity profile. A constant flow rate of air was obtained by the use of 0.020" diameter sonic orifice and passed through the calibration flow nozzle. Hot wire sensors were placed one nozzle diameter downstream from the nozzle exit and perpendicular to the flow. The anemometer output voltage was correlated to the air velocity based on the volumetric flow rate and the flow nozzle diameter. It was, however, found that with this calibration the centre line velocity in the 8.054 in. diameter test section was observed to be about 12% lower than the theoretical predictions from the modified Reichardt expressions for eddy viscosity. On the other hand, measurement by the Pitot tube agreed with the theoretical predictions. It was concluded that either the assumption of flat velocity profile in the jet at the exit of the flow nozzle is incorrect or the hot wire response in a laminar jet is different from that in turbulent flow at the pipe centre. Since the manufacturer of the flow nozzle claims

the existence of a flat velocity across the jet, it must be the response of the anemometer which has different behaviour in the laminar and turbulent flow field. The underlying reason for this behaviour is difficult to understand. Thus it was concluded that the flow nozzle cannot be used as a primary standard in the calibration of a hot-wire anemometer.

Observing that the Pitot tube measurements of velocity profile at the centre of the test section were in agreement with the theoretical predictions, it was decided to use the Pitot tube as a primary standard. The Reynolds number based on Pitot tube diameter (1/8") was greater than 100 for the whole measureable velocity range and hence the coefficient of the Pitot tube was assumed to be unity in accordance with the recommendations in [A6].

The calibration of the hot-wire anemometer was done by measuring, at the centre line of the test section, pressure differences produced by the Pitot tube and then the response of the hot-wire anemometer for various flow rates. Assuming a Pitot tube coefficient of 1, the centre line velocity was calculated from

$$u = \sqrt{2g\ \Delta H}$$

where ΔH is the Pitot tube pressure differential in ft. of air. In Figure B-2, the centre line velocity as measured by the Pitot tube is plotted against the total mass flow rate in the test section. Also the response of the hot-wire anemometer is plotted as a function of total mass flow rate. Combining

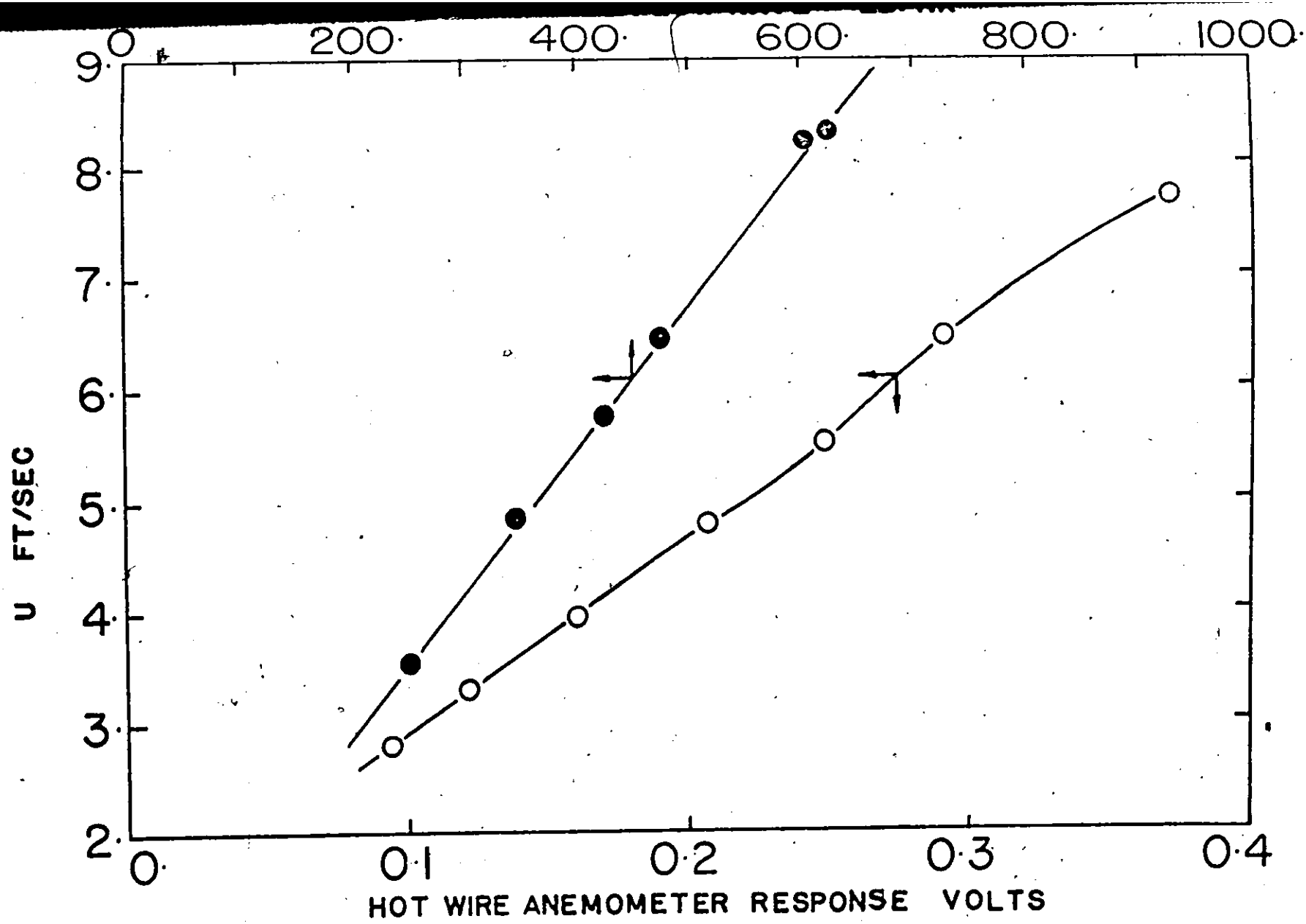

Figure B-2. Calibration of Hot-Wire Anemometer. Measurements by Pitot Tube, ; Hot-wire Anemometer, ; at the Centre of the Test Section.

the two, the hot-wire anemometer response is given as a function of velocity. It is assumed that this calibration curve obtained at the centre line of the test section will be valid when the hot-wire probe traverses the entire cross section.

APPENDIX C

MATHEMATICAL TECHNIQUES

Three numerical techniques used in the integration of the energy equation are described in detail in this section. These are interpolation, integration and differentiation. Since the experimental measurements of temperature are unevenly spaced across the cross section of the test section, special methods were used in the interpolation and integration techniques.

C.1 Numerical Interpolation

For the unequal interval data, the Lagrangian interpolation polynomial was used. For $y = f(x)$, with data points at x_o, x_1, $x_2, \ldots, x_n$, having corresponding values y_o, y_1, $y_2, \ldots, y_n$, an interpolation polynomial can be written as

$$\phi_n(x) = \sum_{j=0}^{n} a_j \prod_{\substack{i=0 \\ i \neq j}}^{n} (x - x_i) \qquad \text{(C-1-1)}$$

where a_j are the coefficients which can be eliminated to give the form

$$\phi_n(x) = \sum_{j=0}^{n} y_j \prod_{\substack{i=0 \\ i \neq j}}^{n} \frac{x - x_i}{x_j - x_i} \qquad \text{(C-1-2)}$$

The interpolation polynomial is exactly equal to f(X) if f(x) is a polynomial of degree n, otherwise $\phi_n(x) = f(x)$ only

at the data points. Thus the degree of the polynomial has to be known beforehand. A couple of values of n were tried to see if the interpolated values are consistant. In Equation (C-1-2) x is the value where the function is to be interpolated and the calculation of the right hand side of (C-1-2) gives the corresponding interpolated value. The advantages of this mehtod, apart from being applicable to unequal interval data, are the simplicity in programming and low storage requirements.

C.2 Numerical Integration

The use of Gaussian Quadrature for numerical integration of the unevenly spaced data has been preferred owing to its higher accuracy for a given number of ordinates. For n ordinates this method is exact for any polynomial of the degree 2n-1; this property makes it superior to those formulae based on equally-spaced ordinates, since the latter are exact for a (n-1) degree polynomial. This special feature arises from the fact that the function to be integrated, $y=f(x)$, is expressed as a sum of Lagrangian polynomials of the degree n-1 and another polynomial of the degree 2n-1. The integration over the latter polynomial can be made zero by the use of Legendre orthogonal polynomials. Thus integration over the function $f(x)$ is equal to integration over the Lagrangian polynomial if the points used in the summation are the roots of Legendre orthogonal polynomial, λ.

$$\therefore \int_a^b f(x)\,dx = \frac{b-a}{2}\int_{-1}^{+1} f(\lambda)\,d\lambda = \frac{b-a}{2}[H_1 y(\lambda_1)+H_2 y(\lambda_2)+\ldots+H_n\, Y(\lambda)]$$

(C-2-1)

where the transformation for the change of interval is given by $x = a + b + (b-a)\frac{\lambda}{2}$ and H is given from the Lagrangian polynomial. For various values of n the appropriate values of λ and H are tabulated [L10].

Thus from the tabulated data of $y=f(x)$ values of $y=f(\lambda)$ are obtained by interpolation through the use of the Lagrangian polynomial, as described in Section C.1 and then substitution in Equation (C-2-1). This procedure provides the required integration of $f(x)$ over the interval (a,b).

The integration in Equation (5.6) is done over the interval R_0 to r, where the second limit of the integration is a variable. For integration between the wall and the first few data points away from the wall, the trapezoidal rule was employed. As sufficient data points become available for interpolation of the y at λ, the Gaussian Quarature method was used.

C.3 Numerical Differentiation

Obtaining differentials from the tabulated data is a difficult mathematical operation to perform numerically. Approximating the differential with differences is highly unsatisfactory as errors in the data are very much amplified when very small numbers appear in the denominator. In the

graphical method, the experimental data are plotted and a free hand smooth curve is drawn through them. The derivatives are obtained by drawing tangents to the curve by optical means. Though this method is free of the large errors which can occur in the difference method, the results are highly subjective, that is, susceptibe to operator error. Two persons may draw two different curves through a set of data points or even one may draw two different curves at two different times. The same is true of the drawing of the tangents.

Fitting a polynomial by a least square fit through a set of data points though quite satisfactory for integration purposes is as unsatisfactory for differentiation as the difference method. However, a piecewise polynomial fit can be quite suitable, According to this method, a polynomial is fit into a sub-set of consecutive data points and the gradients are evaulated by differentiating the fitted polynomial. The calculated gradient at the middle point of the sub-set is taken as the best estimate. Different sub-sets of the data points are formed so that every point is at the mid-point of some sub-set. Thus fitting different polynomials, the gradient at every point in the data can be evaluated. Since the points at the ends of the data set cannot be made the mid-points of any sub-set, some degree of uncertainty is likely in gradient evaluation at these points.

The use of orthogonal polynomials is particularly suitable for higher degree polynomials [D10]. As for such a

case the matrix to be inverted in the least square technique is quite often ill conditioned. However, when the degree of polynomial of the expected fit is not high and when the data are not evenly spaced the use of orthogonal polynomials is not worth the increased effort in programming and effecting subsequent changes in terms of the degree of polynomial and the number of data points in the sub-set [H8].

DeNevers [D11] suggested a method of plotting the gradient from the difference table against the independent variable. This is followed by the smoothing of the curve and again constructing the difference table. The procedure is repeated till the derivatives form a smooth sequence. The real advantage of this method lies in obtaining the second and higher order derivatives. Moreover, this is a multistep method and thus is more laborious than the other methods.

It may be concluded at this stage that the piecewise polynomial fit by the least square method is the most suitable technique for the present case of evaluating radial temperature gradients from the unevenly spaced measured data. The radial temperature profile data in the dimensionless form has a value of 1 at the wall and asymptotically decays to zero towards the centre of the pipe. Since the boundary layer is still developing, the dimensionless temperature becomes zero well before the centre line. The function that will be the most suitable for the piecewise polynomial fit should conform to these boundary conditions and should have the above mentioned behaviour.

A simple polynomial of the following form was tried.

$$\frac{T-T_o}{T_w-T_o} = A_1 + A_2 r + A_3 r^2 + A_1 r^3 + \ldots \qquad \text{(C-3-1)}$$

The coefficient of the polynomial were obtained by linear least square method. Ill conditioned matrices were obtained for a cubic polynomial using sub-sets of 7 data points, especially near the wall. Reducing the degree of polynomial to 2, alleviated this problem but a large residual sums of squares was obtained for the data points away from the wall where the temperature profile starts flattening out.

As an alternative the following exponential decay model was used

$$\theta = \frac{T-T_o}{T_w-T_o} = \text{Exp}\ [(A_1 + \frac{A_2}{r} + \frac{A_3}{r^2} + \frac{A_4}{r^3} + \ldots)] \qquad \text{(C-3-2)}$$

It can be linearised by taking logarithms

$$\ln \theta = [A_1 + \frac{A_2}{r} + \frac{A_3}{r^2} + \frac{A_4}{r^3} + \ldots] \qquad \text{(C-3-3)}$$

$$d\theta/dr = -\theta'[\frac{A_2}{r^2} + \frac{2A_3}{r^3} + \frac{3A_4}{r^4} + \ldots] \qquad \text{(C-3-4)}$$

It is realised that using this model, computational problems arise in evaluating logarithms when $\theta = 0$ which in the present case of developing thermal boundary layer occurs also for values of r other than zero. One way to circumvent this problem is to delete the data points where $\theta \to 0$ before taking logarithms. For cases where the influence

of heating has reached the centre line, a slightly different form of the above model may be used to ensure zero temperature gradient at the centre line

$$\ln (1-\theta) = [A_1 + A_2/(R_o-r) + A_3/(R_o-r)^2 + A_4/(R_o-r)^3] \tag{C-3-5}$$

Since this equation creates singularity at the wall, $r = R_o$, a combination of the two may quite successfully be used.

C.3.1 Linear Least Square Formulation

The proposed model (Equation (C-3-3)) can be written as

$$Y_i = \ln (\theta_i) = \sum_{j=0}^{m} A_j/(r_i^{j-1}) + \varepsilon_i \tag{C-3-6}$$

or

$$\underline{Y} = \underline{X}\ \underline{A} + \underline{\varepsilon} \tag{C-3-7}$$

where $\underline{Y}$ is the vector of observed values of $\ln\theta$, $\underline{A}$ is the coefficient vector, matrix $\underline{X}$ is formed from the radial locations corresponding to the observation and $\underline{\varepsilon}$ is the vector of random, normally distributed errors with mean zero and variance σ^2. From the linear, least square theory the best estimates of $\underline{A}$ are given by

$$\hat{A} = [X'X]^{-1}\ X'\ Y \tag{C-3-8}$$

$$\hat{Y} = X\ \hat{A} \tag{C-3-9}$$

$$\mathrm{Var}\ (\hat{Y}) = \sigma^2 = \frac{(Y'Y) - \hat{A}'\ (X'Y)}{n-m-1} \tag{C-3-10}$$

where n is the number of data points in the sub-set and m is the degree of the polynomial. Since $\hat{Y} = \ln \hat{\theta}$, the variance of $\hat{\theta}$ can be written as

$$\mathrm{Var}\,(\hat{\theta}) = \hat{\theta}^2\ \mathrm{Var}\,(Y) = \hat{\theta}^2\ \sigma^2 \qquad \text{(C-3-11)}$$

Using these estimates of the coefficients A_1, A_2, A_3, A_4, etc. the local gradients of the radial temperature profile were calculated. It was found that a third degree polynomial gave a better fit away from the wall than a second degree one, using sub-sets of seven data points. Use of five data point sub-sets would drastically decrease the degree of freedom of the polynomial and thus increasing the possibility of the fitted functions becoming nonsmooth. To guard against this, the values of the function and the gradients were calculated at intermediate locations between the data points to see if there is any sign of the gradient profile becoming irregular.

Differentiating Equation (C-3-9)

$$\frac{d\hat{Y}_i}{dr} = \sum_{j=0}^{m} - (j-1)\ r_i^{-j}\ \hat{A}_j \qquad \text{(C-3-12)}$$

The estimation of the variance of the slope $d\hat{Y}/dr$ at any data point is a special case of finding the confidence interval of any linear combination of A_j and has been treated for the general case by Graybill [G7]. If a vector G(X) is defined such that it represents $d\hat{Y}/dr$

$$G'(X) = (0, {}^{-1}/_{r^2}, {}^{-2}/_{r^3}, {}^{-3}/_{r^4}, \ldots, -(m-1)/r^m) \qquad \text{(C-3-13)}$$

the variance of the slope dY/dr is given by

$$\mathrm{Var}\left(\frac{d\hat{Y}}{dr}\right) = s^2 = G'(X)\,[X'X]^{-1}\,G(X)\,\sigma^2 \qquad \text{(C-3-14)}$$

Since $\hat{Y} = \ln \hat{\theta}$; $\frac{d\hat{\theta}}{dr} = \hat{\theta}\,\frac{d\hat{Y}}{dr}$,

$$\mathrm{Var}\left(\frac{d\hat{\theta}}{dr}\right) = \hat{\theta}^2\,\mathrm{Var}\left(\frac{d\hat{Y}}{dr}\right) + \left(\frac{d\hat{Y}}{dr}\right)^2 \mathrm{Var}\,(\hat{\theta}) \qquad \text{(C-3-15)}$$

$$\mathrm{Var}\left(\frac{d\hat{\theta}}{dr}\right) = \hat{\theta}^2\,s^2 + \left(\frac{d\hat{\theta}}{dr}\right)^2 \sigma^2 \qquad \text{(C-3-16)}$$

Equation (C-3-16) gives the variance of the calculated temperature gradient in terms of variance of $\hat{Y} = \ln \hat{\theta}$, i.e., σ^2

APPENDIX D

D.1 Finite Difference Approximation

The continuity, momentum and energy equations in the dimensionless variables can be transformed from partial differential equations to a set of algebraic equations by means of finite differences. A function $\phi(Z)$ can be expanded in a Taylor series about a point $Z' = Z$ for an increment h

$$\phi(Z+h) = \phi(Z) + \frac{h}{1!}\phi'(Z) + \frac{h^2}{2!}\phi''(Z) + \frac{h^3}{3!}\phi'''(Z) + \frac{h^4}{4!}\phi''''(Z) + \ldots \tag{D.1}$$

where the number of primes on ϕ represent the order of differential of ϕ with respect to Z at Z = Z.

If the increment h is small so that powers of h higher than one are small enough to be neglected, then Equation (D.1) reduces to

$$\phi(Z+h) = \phi(Z) + h\frac{d\phi}{dZ} + 0(h^2)$$

or

$$\frac{d\phi}{dZ} = \underset{h\to\infty}{Lt}\frac{\phi(Z+h)-\phi(Z)}{h} + 0(h) \tag{D.1A}$$

If ϕ is a function of more than one variable then keeping the other variables constant, total differentials are equivalent to partial differentials.

$$\left(\frac{\partial\phi}{\partial Z}\right)_y = \underset{h\to\infty}{Lt}\frac{\phi(y,Z+h)-\phi(y,Z)}{h}$$

Thus under suitable conditions partial or total derivatives can be replaced by differences. This method thus offers the possibility of effecting a numerical solution of equations whose analytical solution is impossible or difficult.

In a variable step-size situation, such as employed here, the finite difference approximation takes on a somewhat more complicated form than in the constant step size situation. Rewriting Equation (D.1) such that powers of h greater than three are negligible.

$$\phi(Z+h_1) = \phi(Z) + h_1\,\phi'(Z) + \frac{h_1^2}{2!}\,\phi''(Z) + \frac{h_1^3}{3!}\,\phi'''(Z) + 0(h_1^4) \tag{D.2}$$

similarly writing for $(Z-h_2)$

$$\phi(Z-h_2) = \phi(Z) - h_2\,\phi'(Z) + \frac{h_2^2}{2!}\,\phi''(Z) - \frac{h_2^3}{3!}\,\phi'''(Z) + 0\,(h_2^4) \tag{D.3}$$

Representing location Z with i, $Z+h_1$ with i+1 and $Z-h_2$ with i-1

$$\phi_{i+1} = \phi_i + h_1\,\phi'_i + \frac{h_1^2}{2!}\,\phi''_i + \frac{h_1^3}{3!}\,\phi'''_i + 0(h_1^4) \tag{D.4}$$

$$\phi_{i-1} = \phi_i - h_2\,\phi'_i + \frac{h_2^2}{2!}\,\phi''_i - \frac{h_2^3}{3!}\,\phi'''_i + 0(h_2^4) \tag{D.5}$$

Equations (D.4) and (D.5) yield respectively,

$$\phi''_i = \frac{2}{h_1^2}\,\phi_{i+1} - \frac{2}{h_1^2}\,\phi_i - \frac{2}{h_1}\,\phi'_i - \frac{2}{3!}\,h_1\,\phi'''_i - 0(h_1^2) \tag{D.6}$$

$$\phi''_i = \frac{2}{h_2^2}\,\phi_{i-1} - \frac{2}{h_2^2}\,\phi_i - \frac{2}{h_2}\,\phi'_i + \frac{2}{3!}\,h_2\,\phi'''_i - O(h_2^2) \tag{D.7}$$

Equating Equations (D.6) and (D.7) and simplifying

$$\phi'_i = \frac{d\phi_i}{dZ} = \frac{1}{(h_1+h_2)}\left[\frac{h_2}{h_1}\,\phi_{i+1} - \frac{h_1}{h_2}\,\phi_{i-1} + \frac{h_1^2-h_2^2}{h_1h_2}\,\phi_i\right] \tag{D.8}$$

A simplified representation of $\frac{d\phi}{dZ}$ is given by

$$\phi'_i = \frac{d\phi_i}{dZ} = \frac{\phi_{i+1} - \phi_{i-1}}{h_1+h_2} \tag{D.9}$$

Substituting Equation (D.8) into (D.6)

$$\phi''_i = \frac{d^2\phi}{dZ^2} = \frac{2\phi_{i+1}}{h_1(h_1+h_2)} - \frac{2\phi_i}{h_1h_2} + \frac{2\phi_{i-1}}{h_2(h_1+h_2)} \tag{D.10}$$

The order of magnitude of errors in (D.8 to D.10) is $O(h^2)$ if $h_1 \simeq h_2$.

D.2 Momentum Equation

The momentum equation in dimensionless form can be written as

$$(RO)\,U\,\frac{\partial U}{\partial X} + (RO)V\,\frac{\partial U}{\partial R} = -\frac{dP}{dX} + \frac{1}{Re_o}\left[Gm\,\frac{\partial^2 U}{\partial R^2} + \frac{\partial Gm}{\partial R}\,\frac{\partial U}{\partial R} + \frac{Gm}{R}\,\frac{\partial U}{\partial R}\right]$$

$$+ \frac{R_o g_c}{\rho_o \bar{u}_o^2}\,(\rho-\rho_a) \tag{D.11}$$

U, which is a function of X and R, can be represented by $U_{i,j}$; the axial location is indicated by j and the radial position by i. The flow field grid is shown in Figure 3-2.

Equation (D.11) is a parabolic partial differential equation with a second derivative in R and a first derivative in X. An implicit finite difference approximation and a marching solution in the axial direction is proposed. From stability considerations for the solution, the modified Crank-Nicholson approximation for derivatives in the radial direction is employed. According to this scheme some average between gradients at j^{th}, the present state; and $j+1^{th}$, state to be predicted; is used. The averaging is done by choosing a suitable value of the weighting factor α such that $0 \leq \alpha \leq 1$, $\beta = 1-\alpha$. The axial and radial derivatives can be written as

$$\frac{\partial \phi_{i,j}}{dx} = (\phi_{i,j+1} - \phi_{i,j})/\Delta x$$

$$\frac{\partial \phi_{i,j+\alpha}}{\partial r} = \alpha\phi'_{i,j+1} + \beta\phi'_{i,j}$$

$$\frac{\partial^2 \phi_{i,j+\alpha}}{\partial r^2} = \alpha\phi''_{i,j+1} + \beta\phi''_{i,j}$$

Various gradients for use in (D.11) have been approximated by finite differences in the following way:

$$\partial U/\partial X = (U_{i,j+1} - U_{i,j})/DX$$

$$\partial U/\partial R = [\alpha(U_{i+1,j+1} - U_{i-1,j+1}) + \beta(U_{i+1,j} - U_{i-1,j})]/DR1$$

$$\frac{\partial^2 U}{\partial R^2} = 2\left[\frac{\alpha U_{i+1,j+1} + \beta U_{i+1,j}}{DR1 \cdot DR2} - \frac{\alpha U_{i,j+1} + \beta U_{i,j}}{DR2 \cdot DR3} + \frac{\alpha U_{i-1,j+1} + \beta U_{i-1,j}}{DR1 \cdot DR3}\right] \tag{D.11A}$$

where

$DX = (X_{j+1} - X_j)$, $DR1 = (R_{i+1} - R_{i-1})$, $DR2 = (R_{i+1} - R_i)$,

$DR3 = (R_i - R_{i-1})$

Also defined are:

$F1 = (RO\ U)_{i,j}/DX$, $F2 = 2/(DR1 \cdot DR2)$, $F3 = 2/(DR2 \cdot DR3)$,

$F4 = 2/(DR1 \cdot DR3)$, $F5 = 1/DR1$ (D.12A)

Since sometimes small discontinuities occur in the effective viscosity profile, $\partial Gm/\partial R = FGm/DR1$, is approximated by Equation (D.8), by defining:

$$FGm = (Gm_{i+1,j+\alpha})\ DR3/DR2 - (Gm_{i-1,j+\alpha})\ DR2/DR3 + (Gm_{i,j+\alpha})$$

$$(DR2^2 - DR3^2)(F3)/2 \tag{D.12B}$$

Substituting these equations in Equation (D.11) and simplifying, we get

$$(\alpha\ A1_i/C1_i)\ U_{i+1,j+1} - U_{i,j+1} + (\alpha\ B1_i/C1_i)\ U_{i-1,j+1} =$$

$$- [(\beta\ A1_i)\ U_{i+1,j} + D1_i\ U_{i,j} + (\beta B1_i)\ U_{i-1,j} + DPDX+GRR_i]/C1_i \qquad (D.12)$$

where

$$A1_i = -RO.V.F5 + \{F2.Gm_{i,j+\alpha} + FGm(F5)^2 + Gm_{i,j+\alpha}\ (F5)/R_i\}/Re_o$$

$$B1_i = RO.V.F5 + \{F4.Gm_{i,j+\alpha} - FGm\ (F5)^2 - Gm_{i,j+\alpha}\ (F5)/R_i\}\ /Re_o$$

$$C1_i = F1 + \alpha(F3)\ Gm_{i,j+\alpha}\ /Re_o;\ D1 = F1 - \beta(F3)\ Gm_{i,j+\alpha}\ /Re_o$$

$$DPDX = (-dP/dX),\quad GRR_i = R_o g_c(\rho-\rho_a)/(\rho_o \bar{u}_o^2)$$

D.3 Energy Equation

The energy conservation equation in dimensionless form can be written as

$$(RO)\,U\,\frac{\partial\theta}{\partial X} + (RO)\ V\,\frac{\partial\theta}{\partial R} = \frac{1}{Re_o}\ [Gh\ \frac{\partial^2\theta}{\partial R^2} + \frac{\partial Gh}{\partial R} + \frac{Gh}{R}\ \frac{\partial\theta}{\partial R}] \qquad (D.13)$$

The associated simplifying assumptions have previously been mentioned in the text. The momentum Equation (D.11) is coupled to this equation by the dependent variables U, V and θ. The energy equation is also a parabolic partial differential equation with second derivative in R and first derivative in X. A prescribed heat flux or temperature profile at the wall

and axial symmetry at the centre line are the two boundary conditions to be satisfied.

The finite-difference approximation of the axial and radial gradients is done in a manner similar to that employed for the momentum equation

$$\frac{\partial\theta}{\partial X} = (\phi_{i,j+1} - \phi_{i,j})/DX$$

$$\frac{\partial\theta}{\partial R} = [\ \alpha(\phi_{i+1,j+1} - \phi_{i-1,j+1}) + \beta(\phi_{i+1,j} - \phi_{i-1,j})]/DR1$$

$$\frac{\partial^2\phi}{\partial R^2} = 2[\frac{\alpha\phi_{i+1,j+1} + \beta\phi_{i+1,j}}{DR1\ \ DR2} - \frac{\alpha\phi_{i,j+1} + \beta\phi_{i,j}}{DR2\ \ DR3} + \frac{\alpha\phi_{i-1,j+1} + \beta\phi_{i-1,j}}{DR1\ \ DR3}] \qquad \text{(D.13A)}$$

where DX, DR1, DR2 and DR3 were defined in Equation (D.11A). Also defining F1, F2, F3, F4 and F5 as in Equation (D.12A) and FGh in the same form as Equation (D.12B), the energy Equation (D.13) can be written in finite difference form as:

$$(\alpha\ A2_i/C2_i)\ \theta_{i+1,j+1} - \theta_{i,j+1} + (\alpha\ B2_i/C2_i)\ \theta_{i-1,j+1} = - [(\beta\ A2_i)\ \theta_{i+1,j} + D2_i\ \theta_{i,j} + (\beta B2_i)\ \theta_{i-1,j}]/C2_i \qquad \text{(D.14)}$$

where

$$A2_i = -RO.V.F5 + [F2\ Gh_{i,j+\alpha} + FGh\ (F5)^2 + Gh_{i,j+\alpha}\ (F5)R_i]/Re_o$$

$$B2_i = RO.V.F5 + [F4\ Gh_{i,j+\alpha} - FGh\ (F5)^2 - Gh_{i,j+\alpha}\ (F5)/R_i]/Re_o$$

$$C2_i = F1 + \alpha(F3)\ Gh_{i,j+\alpha}/Re_o; \quad D2_i = F1 - \beta(F3)\ Gh_{i,j+\alpha}/Re_o$$

D.4 Continuity Equation

The mass conservation equation is a first order elliptic equation and thus can be explicitly solved to give the radial component of velocity, V.

$$\frac{\partial}{\partial X}((RO)U) + \frac{1}{R}\frac{\partial}{\partial R}((RO)R.V) = 0$$

$$(RO.V) = \frac{1}{R}\int_0^R R\,\frac{\partial}{\partial X}(RO.U)\,dR \qquad (D.15)$$

Instead of representing Equation (D.15) by a finite difference approximation and integrating, a control volume mass balance is applied in the evaluation of V.

In a control volume, Figure D-1, surrounded by R_{i+1}, R_i and X_{j+1}, X_j, axial flow velocities may be assumed to be the arithmetic average between the point velocities at R_{i+1} and R_i.

$\therefore$ Inflow to the control volume $= \pi\,(R^2_{i+1} - R^2_i)\dfrac{(RO.U)_{i+1,j} + (RO.U)_{i,j}}{2}$

$$+ 2\pi\, R_i\,(X_{j+1} - X_j)\,(RO.V)_{i,j+\alpha}$$

Outflow from the control Volume $= \pi(R^2_{i+1} - R^2_i)\dfrac{(RO.U)_{i+1,j+1} + (RO.U)_{i,j+1}}{2}$

$$+ 2\pi\, R_{i+1}\,(X_{j+1} - X_j)(RO.V)_{i+1,j+\alpha}$$

Under steady state conditions, Inflow = Outflow

$$\therefore (RO.V)_{i+1,j+\alpha} = (RO.V)_{i,j+\alpha}\,\frac{R_i}{R_{i+1}} + \frac{(R^2_{i+1} - R^2_i)}{4R_{i+1}(X_{j+1} - X_j)}$$

$$[(RO.U)_{i+1,j} + (RO.U)_{i,j} - (RO.U)_{i+1,j+1} - (RO.U)_{i,j+1}]$$

(D.16)

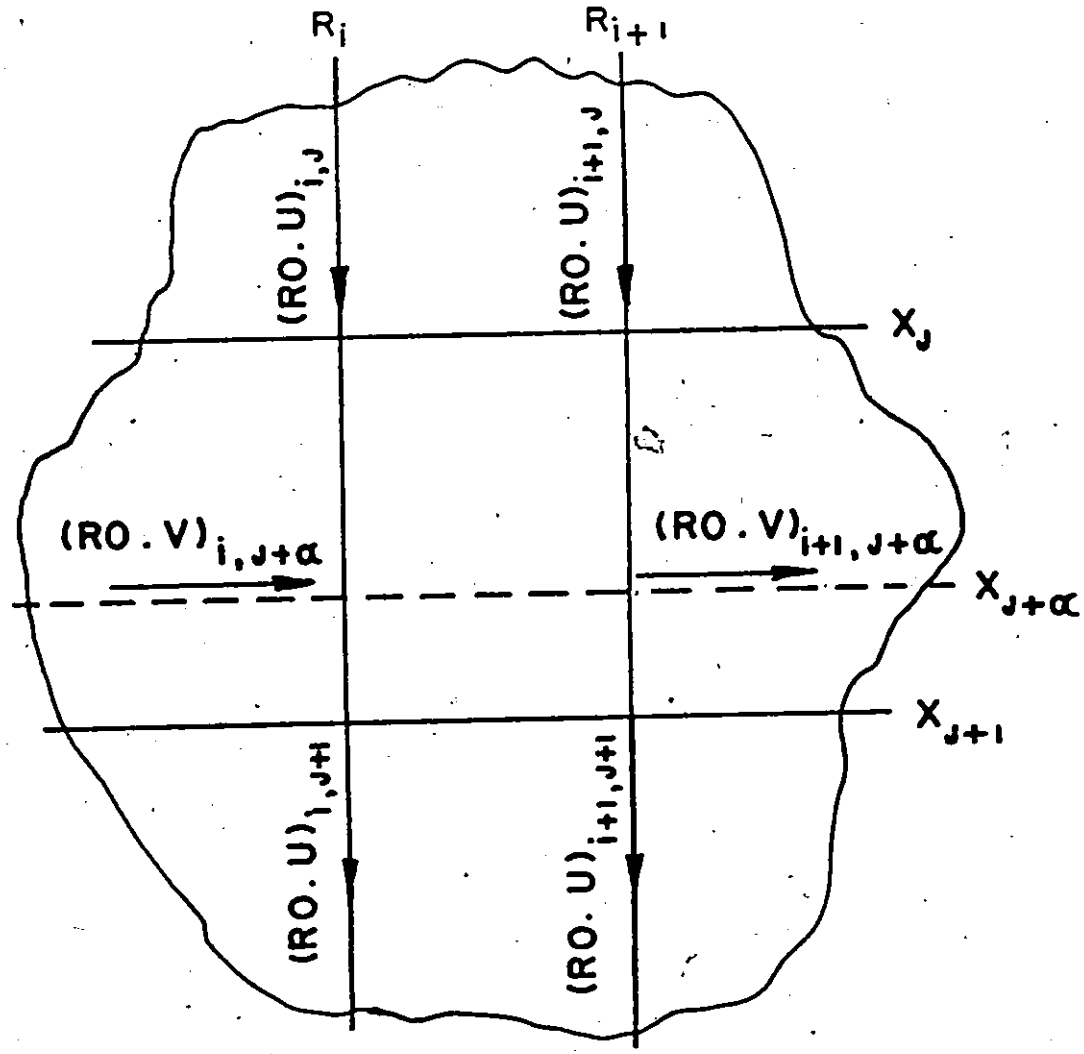

Figure D-1 Control Volume Mass Balance.

D.4.1 Overall Mass Balance

The pressure difference term DPDX in the momentum Equation (D.12) has to be specified. Since pressure has been assumed to be a function of the axial direction only, an overall mass balance at any pipe cross section can be used to determine the pressure drop.

A simplified version of Equation (D.12) is obtained by defining

$$U1_i = \alpha U_{i,j+1} + \beta U_{i,j} \quad \text{and} \quad C11_i = (F3)\, Gm_{i,j+\alpha} / Re_o$$

so that Equation (D.12) can be written as

$$U_{i,j+1} = U_{i,j} + [DPDX + GRR_i + A1_i\, U1_{i+1,j} + B1_i\, U1_{i-1,j} - C11_i\, U1_{i,j}]/F1 \tag{D.17}$$

Integrating (D.17) over the cross section of pipe after multiplying by $(RO)_{i,j+1}\, R_i$

$$\int_0^1 R_i (ROU)_{i,j+1}\, dR = \int_0^1 R_i (RO)_{i,j+1} [DPDX/F1 + U_{i,j} + (GRR_i + A1_i\, U1_{i+1} + B1_i\, U1_{i-1} - C11_i\, U1_i)/F1]\, dR = \frac{\text{Total Flow}}{2\pi R_o^2\, \rho_o u_o} = Q$$

$$DPDX = \frac{Q - \int_0^1 R_i (RO)_{i,j+1} [U_{i,j} + (A1_i U1_{i+1} + B1_i U1_{i-1} - C11_i U1_i + GRR_i)/F1]\, dR}{\int_0^1 (R_i (RO)_{i,j+1})/F1\, dR} \tag{D.18}$$

Equation (D.18) gives the value of the pressure drop to ensure that the velocity profile at any cross section integrates out to the total mass flow in the pipe. The integrations in Equation (D.18) are carried out by Trapezoidal rule.

D.5 Boundary Conditions

D.5.1 Centre line Conditions

A. Momentum Equation

Since the flow symmetry about the centre line (i=1) has been assumed, the velocities at points equidistance from i=1 on either side are equal and the velocity gradient at the centre line is zero.

For i=1, $U_{i+1} = U_{i-1}$ and F2 = F4, it can be shown by using Equation (3.17) that $A1_1 = B1_1 = 2(F2)(Gm_{1,j+\alpha})/Re_o$. Redefining $A1_1$, $D1_1$ and $C1_1$ as,

$$A1_1 = 4(F2)(Gm_{1,j+\alpha})/Re_o;\ D1_1 = F1 - 2\beta(F3)Gm_{1,j+\alpha}/Re_o$$

$$C1_1 = F_1 + 2\,\alpha(F3)\,Gm_{1,j+\alpha}/Re_o \qquad \text{(D.19A)}$$

we can write

$$U_{1,j+1} = [\alpha A1_1\, U_{2,j+1} + \beta A1_1\, U_{2,j} + D1_1\, U_{1,j} + DPDX + GRR_1]/C1_1 \qquad \text{(D.19)}$$

Substituting the value of $U_{1,j+1}$ from Equation (D.19) into Equation (D.12) and rearranging we can write for i=2

$$[-1+\frac{\alpha^2 A1_1 B1_2}{C1_1 C1_2}]\ U_{2,j+1} + \frac{\alpha A1_2}{C1_2} \cdot U_{3,j+1} = -\frac{1}{C1_2}\ [\beta A1_2 U_{3,j} + D1_2 U_{2,j}$$

$$+ \beta B1_2 U_{1,j} + DPDX+GRR_2] - \frac{\alpha B1_2}{C1_1 C1_2}\ [\beta A1_1\ U_{2,j} + D1_1\ U_{1,j} + DPDX+GRR_1]$$

(D.20)

B. Energy Equation

Along with flow symmetry, thermal symmetry is also assumed, i.e., the radial temperature profile has zero gradient at the centre line. Using Equation (3.11A) it can be shown that $A2_1 = B2_1 = 2\ (F2)(Gh_{1,j+\alpha})/Re_o$. Redefining $A2_1$, $D2_1$, $C2_1$ as,

$$A2_1 = 4(F2)(Gh_{1,j+\alpha})/Re_o;\ D2_1 = F1 - 2\beta\ (F3)\ Gh_{1,j+\alpha}/Re_o,$$

$$C2_1 = F1 + 2\alpha\ (F3)\ Gh_{1,j+\alpha}\ /Re_o$$

we can write

$$\theta_{1,j+1} = [\alpha\ A2_1\ \theta_{2,j+1} + \beta A2_1\ \theta_{2,j} + D2_1\ \theta_{i,j}]/C2_1 \qquad (D.21)$$

For i=2 substituting Equation (D.21) into Equation (D.14) and rearranging we get

$$[-1+\frac{\alpha^2 A2_1 B2_2}{C2_1 C2_2}\ \theta_{2,j+1} + \frac{\alpha A2_2}{C2_2}\ \theta_{3,j+1} = -\frac{1}{C2_2}[\beta A2_2 \theta_{3,j} + D2_2\ \theta_{2,j}$$

$$+ \beta B2_2\ \theta_{1,j}] - \frac{\alpha B2_2}{C2_2 C2_1}\ [\beta A2_1\ \theta_{2,j} + D2_1\ \theta_{1,j}] \qquad (D.22)$$

C. Continuity Equation

A symmetric flow around the centre line imposes no net transverse flow condition at the centre line. So at i=1

$$V = 0 \qquad (D.23)$$

D. Overall Mass Balance

Definitions fo Equations (D.19A) and (D.23) were used in the evaluation of Equation (D.18).

D.5.2 Wall Conditions

A. Momentum Equation

At the pipe wall there is no slip between the fluid and the solid wall surface, i=N, i.e., the fluid at the wall is stationary.

$$\therefore \quad U_{N,j} = 0 \qquad (D.24)$$

For i=N-1 Equation (D.12) reduces to

$$-U_{N-1,j+1} + (\alpha Bl_{N-1}/Cl_{N-1})\, U_{N-2,j+1} = -[Dl_{N-1}\, U_{N-1,j} + \beta Bl_{N-1}\, U_{N-2,j} + DPDX + GRR_{N-1}]/Cl_{N-1} \qquad (D.25)$$

B. Energy Equation

The rate of heat transfer between the pipe wall and the fluid flowing in it is influenced by the thermal conditions of the wall. It Is assumed that the wall temperature is a known function of distance along the length of the test section.

Though in the present investigation the wall temperature is assumed to be uniform, provision is made in the computer program for it to be a tabulated function of axial distance. Since the value of θ_N is known for all axial distances,

$\therefore$ For $i=N-1$, Equation (D.14) reduces to

$$-\theta_{N-1,j+1} + (\alpha B2_{N-1}/C2_{N-1})\theta_{N-2,j+1} = -[\alpha A2_{N-1}\ \theta_{N,j+1} + \beta A2_{N-1}\ \theta_{N,j}$$

$$+ D2_{N-1}\ \theta_{N-1,j} + \beta B2_{N-1}\ \theta_{N-2,j}]/C2_{N-1} \qquad (D.26)$$

C. <u>Continuity Equation</u>

The fact that the pipe wall is impervious to flow implies that

$$V_N = 0 \text{ for all axial distances} \qquad (D.27)$$

APPENDIX E

DEVELOPMENT OF VELOCITY PROFILE

As an initial boundary condition in the theoretical solution, the flow entering the heating section is assumed to be fully developed turbulent flow. This condition has been chosen so that the laws of turbulent transport, available in the literature can be used. To fully develop the flow, i.e., when there is no acceleration or decleration in the flow, an unobstructed straight length of 40 to 80 diameters is required. The development length depends upon the Reynolds number and can be calculated from the following empirical relation given in [H4].

$$x/D = 0.693\ Re^{0.25}$$

For practical purposes a minimum of 40 diameters is recommended.

In the present case with 8.054" diameter pipe in vertical orientation, laboratory space available does not permit more than 40 diameters of development length. So the development of the flow has to be hastened by artificial means. Thus special attention has to be paid to the design of the entrance section. Due to the vertical orientation of the air heating experimental equipment and the limited available height of the building, the 2" diameter compressed air supply line was joined to an 8" diameter column by a short right angle bend. Going around the bend, the centrifugal forces on the flow tend to maldistribute it. Immediately downstream of the bend there

is the junction between the 2" and the 8" diameter pipes and the high velocity jet emerging from the former makes the distribution even worse.

In the initial designs of the entrance section 2" downstream of the junction between the pipes, a perforated plate was used to break the high velocity jet and was followed by a set of ten 100-mesh screens to further distribute the flow. To hasten the growth of boundary layer, a combination of trip wires and sand paper was used. The design of Brighton [B14] suggesting five concentric rings of 1/16" steel wire supported in the pipe cross-section was used. The spacing between the rings, chosen empirically, was such that the wakes from these rings merge with each other and the boundary layer at some distance downstream and thus help in momentum transfer. A 16" length of 40 grit floor sanding paper was glued to the pipe wall to provide surface roughness for growth of the boundary layer.

Figure E-1 shows a typical velocity profile under isothermal conditions, 40 diameters downstream of the entrance at the three port locations. Since the three ports are in planes containing the column axis and 60° apart from each other, the approximate velocity contours drawn across the column cross-section are also shown. The contours indicating an area of high velocity and hence high mass flow rate was situated opposite to the direction in which the 2" supply line was connected to the column by a right angle elbow. Upon dismantling the entrance section, it was found that on the

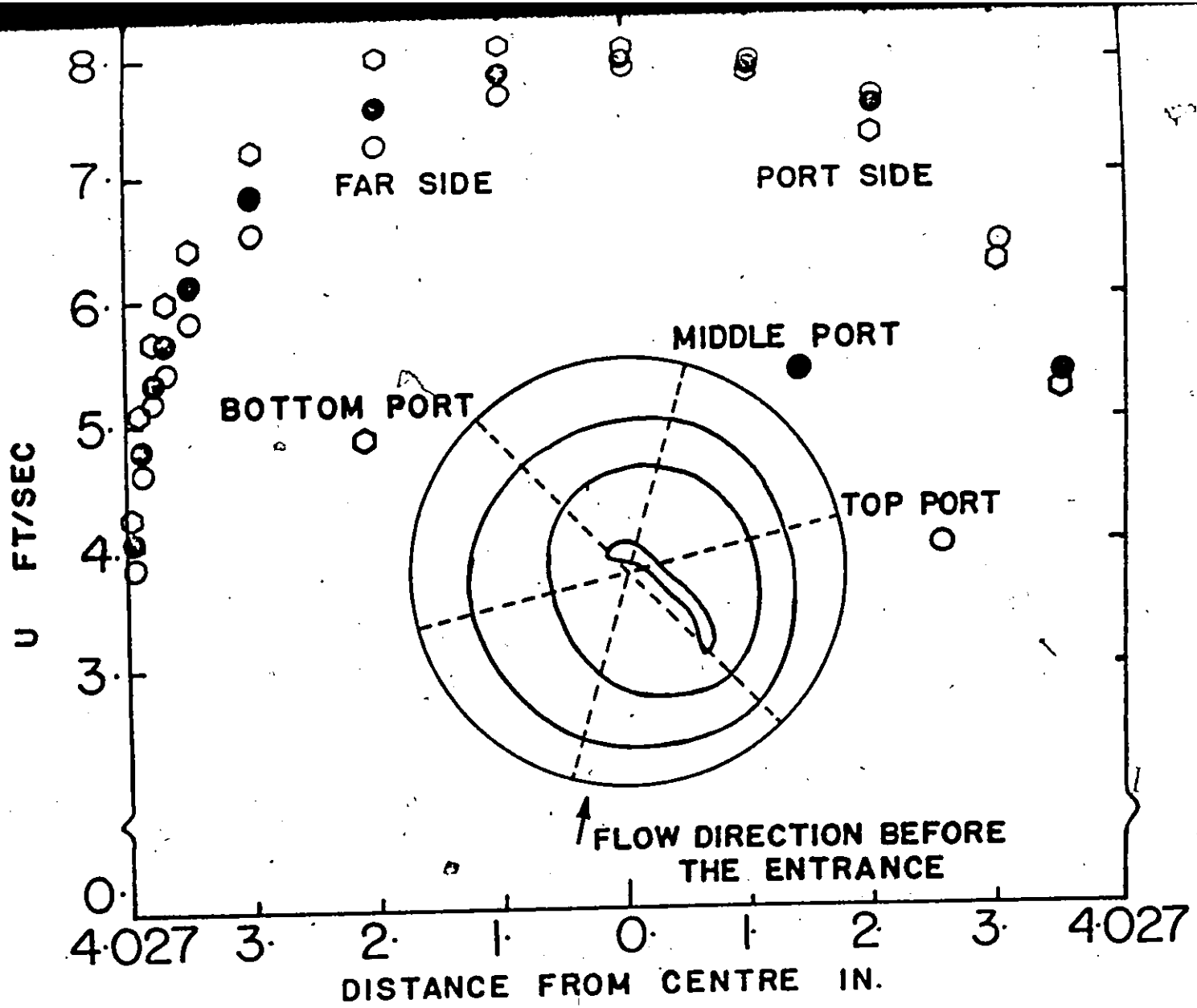

Figure E-1. Asymmetric Velocity Profile and the Velocity Contours for Isothermal Turbulent Flow.

100-mesh screens, the rust particles in the air made marks corresponding to the perforations on the plate above. Intense marks on certain areas on the screens provided a visual proof of flow maldistribution because of centrifugal forces. The rust particles in the air were due to a leak in the air filter which was, however, corrected upon detection.

From the evidence of velocity profile measurements and rust marks on the screen set, the following two observations can be made,

(i) Asymmetry in velocity profile is caused at the entrance of the column by the elbow connecting the supply line to the column.

(ii) Shear stresses in the flow are not able to take care of the asymmetry over the length of 40 diameters.

Since the building height limits the length of pipe available for flow development, the design of the entrance section was modified. Following is the list of series of modifications made in the design of the top section of 8" pipe to solve the problem of maldistribution of flow.

(i) A 1/8" thick porous stainless steel plate placed between the perforated plate and the set of screens was used to create resistance to the flow but no substantial improvement was observed. As a further attempt, a 1/2" thick layer of 150-micron glass beads supported on the porous plate, although created pressure drops of the order of 8 to 10 psi yet, the flow distribution was not uniform because of agglomeration of glass beads due to the moisture in the air.

(ii) It was decided that the air jet from the 2" pipe expanding into the 8" column should have more space to expand so that its kinetic energy is completely dissipated. The air from the 2" line was allowed to expand into a 23" diameter, 30" long drum. A cylindrical baffle in the drum twice reversed the flow direction. From the drum, a 23" long cone accelerated the flow from 23" to 10" diameter cross-section. The cone exit opened into a 10" diameter right angled bend containing flow straightening vanes. The design of the vanes was according to the empirical equations given by Dimmock [D9]. The aerofoil shaped vanes were spaced on a variable pitch according to arithmetic progression so that the pressure distribution downstream from the bend is more or less uniform across the pipe cross-section. A 5" long cone connected the 10" diameter bend exit to the 8" diameter column. In the column porous plate was followed by two 8" long packs of plastic straws. The straws, 7/32" I.D. and .007" wall thickness, were glued together to fill the cross-section of the column and were intended to take the swirl out of the flow and make it unidirectional. Wire rings and sand paper followed the straw packs. The velocity-profile obtained was still asymmetric.

(iii) Five pieces of 8" diameter steel pipe joined together made the 27 ft. height of the column. It was felt that

part of the trouble could be arising from the fact that all of the pieces of pipe are not exactly the same diameter. It was decided to hone the pipes so that every one had the same inside diameter as that of heating section with a tolerance of $\pm$ .005". A wooden plug of the same diameter as the pipes, was used to assure that the pipes were properly aligned while assembling. Thus a perfectly straight 40 diameters length of the column was obtained.

(iv) As a last attempt it was decided to place the expansion drum and the accompanying cones directly on top of the column and thus dispense away with the bend containing straightening vanes. Now the 2" air supply line has the right angled bend but the twice change of direction, deceleration in the expansion drum, acceleration in the cones and direct entrance to the column should make the flow distribution reasonably uniform. A set of 36, 100-mesh bronze screens were placed between the straw packs and wire rings to create additional pressure drop and more uniform distribution of flow.

A large number of minor design changes were carried out in every category of the major changes mentioned above. Figure E-2 shows typical velocity profiles through various modifications. With the final design the velocity profile was reasonably symmetrical for Reynolds numbers of 25000 or less. But for Re = 48000 the profile obtained was asymmetric.

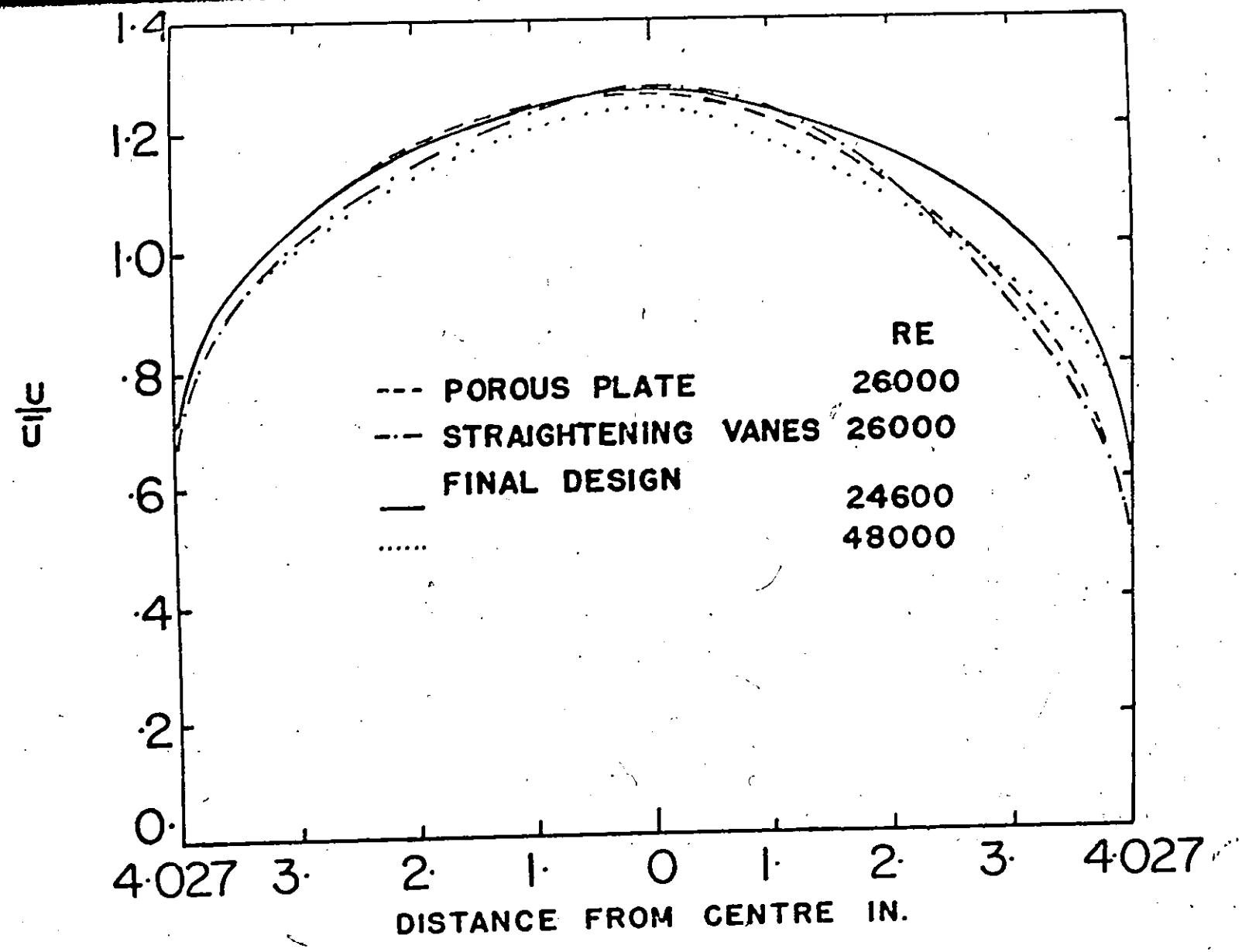

Figure E-2. Development of an Isothermal Symmetric Velocity Profile with Various Designs of the Entrance Section.

As noted earlier, there are two factors affecting the velocity profile, (i) entering flow distribution, (ii) development length available. Given enough development length any flow distribution at the entrance will develop to a symmetric fully developed condition. From the experimental observations, it may be concluded that the entrance flow distribution in the final design is such that for Re ≈ 24000 shear stresses are able to make the flow symmetric over 40 diameters, while for Re ≈ 48000 larger development lengths are required. This is consistent with the literature that development length increases with Reynolds number.

APPENDIX F

VELOCITY MEASUREMENT BY CROSS-CORRELATION

F.1 Introduction

Recently a powerful tool for measuring the velocity of a fluid in a system, utilising the unconventional technique of signal cross-correlation, has become more attractive with the advent of on-line mini-computers. The major advantage of this technique is its applicability to inaccessible places or operation under extreme conditions of high solid contents, high temperature, pressure and radiation fields where conventional velocity measurement techniques fail. In principle, the method of signal cross-correlation makes use of the fact that a disturbance in a flow system takes a finite amount of time to lose its identity completely and that this disturbance faithfully follows the flow in the system. If signals representing the disturbance at two points along the direction of the flow are observed, then these signals will be similar to each other as they represent the same disturbance. If the disturbance retains its form completely, then the two signals will be identical but displaced with respect to each other by the time it took the disturbance to travel between the two measuring stations. However, the disturbance is expected to change its shape, i.e., get distorted and may even become beyond visual recognition. But it is possible to detect similarities (if they exist) between the two signals by evaluating the

correlation coefficient between them. An exact match between the signals gives the correlation coefficient of 1 while complete dissimilarity makes it zero.

There are not many restrictions imposed on the type of disturbance or the signals representing the disturbance. In many flow situations there are already some disturbances present, e.g., velocity fluctuations in a turbulent flow. However, when the disturbances are not present, they can be artificially introduced in the system. The level of disturbance required for measurement by cross-correlation is normally low enough so that the system is not unduly disturbed. Fluctuations in velocity, temperature, concentration and conductivity have been common forms of disturbances used in such measurements.

F-2 Theory

If signals (usually in the form of voltage) $x(t)$ and $y(t)$ are generated by the sensors in the flow stream at the two measuring stations, ℓ ft. apart, the maximum correlation between the signals occurs when one is delayed with respect to the other. The required delay time, τ_m, is equal to the time taken by the fluid to travel ℓ ft. Thus the velocity, u, of the fluid can directly be calculated

$$u = \ell/\tau_m$$

Let us assume that the signal from the downstream station is delayed by time τ, then the maximum similarity between $x(t)$ and

$y(t-\tau)$ is obtained by minimising the function $\overline{[x(t)-y(t-\tau)]^2}$ which is equivalent to

$$\phi(\tau) = \text{Max} \quad \overline{x(t)\ y(t-\tau)} \qquad \text{(F-1)}$$

It is here assumed that the signals are stochastic in nature such that $\overline{x(t)^2}$ and $\overline{y(t)^2}$ are constants, i.e., the signals are steady and there is no drift. The function $\phi(t)$ is called an estimate of the cross-correlation function; averaging over an infinitely long time gives the exact correlation function.

The cross correlation function is for convenience normally expressed in the normalised form

$$\phi(\tau) = \frac{\overline{x(t)\ y(t-\tau)}}{\sqrt{\overline{x(t)^2}}\ \sqrt{\overline{y(t)^2}}} \qquad \text{(F-2)}$$

If the cross correlation function $\phi(\tau)$ is calculated for various values of delay time then the value of $\tau = \tau_m$ for which $\phi(\tau)$ is maximum is the time of travel of the flow.

The function $\phi(\tau)$ can be written as

$$R_{xy}(\tau) = \lim_{T\to\infty} \frac{1}{T} \int_0^T x(t)\ y(t-\tau)\ dt \qquad \text{(F-3)}$$

If an appropriate sampling procedure is used, $R_{xy}(\tau)$ can be approximated by

$$R_{xy}(\tau) = \frac{1}{N} \sum_{k=1}^{N} x(k\Delta t)\ y(k\Delta t-\tau) \qquad \text{(F-4)}$$

where N is the number of samples taken at Δt intervals. The sampling rate should be such that it is at least twice the highest useful frequency in the signals x and y. For calculating $R_{xy}(\tau)$ for various values of τ, the above expression can be written as

$$R_{xy}(m\Delta\tau) = \frac{1}{N} \sum_{k=m}^{N+m-1} x(k\Delta\tau)\, y(k\Delta\tau - m\Delta\tau) \qquad \text{(F-5)}$$

where $m = 0, 1, 2, 3, \ldots, m'$; $m' = 99$ (say)

Here, it is expected that the maximum value of the cross correlation function occurs between $0 < \tau_m < m'\Delta\tau$; and $N\Delta\tau$ is sufficiently large so that summation is equivalent to integration and is representative of the process.

F-3 Applications of the Method

The systems where naturally occurring disturbances do not exist or are not suitable, artificial excitation is used. Two types of disturbances are normally used, (i) Single frequency disturbance, e.g., sinusoidal wave, (ii) Random disturbance.

Bentley and Dawson [B16] used an electric heater to create a temperature disturbance in the flow of water in a pipe. The input to the heater was controlled by a signal from a signal generator. Thus the variation in heat input produced temperature variations in the flow of the same form as the signal from the signal generator. Downstream from the heater, the temperature of the fluid was measured by two

thermocouples whose output was analysed for both the single frequency disturbance and the random disturbance. The signals were passed through band filters and squared to find the zero crossing. The interval between the same sense zero crossing of the two signals was a measure of transit time. Excellent agreement was obtained between the velocity values from the correlation method and those observed gravimetrically. It was shown that this method is good for various geometrical configurations of the pipe as long as the assumption that the disturbances follow the flow is valid. In a short expansion chamber where stagnation of the flow in the corners occurs, higher velocities were calculated. Application to measurements in a high pressure water loop and molten sodium flow was demonstrated to give less than 5% error.

Beck and Plaskowaski [B17] argued that the method of [B16] using band-pass filters does not make use of all of the information in the signals. The phase lag of the thermocouples could not be separated from the lag due to the transit time of the flow, due to filtering all but a narrow range of frequency. This required very accurately matched thermocouples. The cross correlation method using random disturbances (without any filtering of the signals) is free from the phase lags of the sensors and the distributed parameter system. An 8% perturbation, in a pseudorandom binary sequence, to the heat input to a stirred tank having continuous inflow and outflow of water, was used to measure the outlet flow rate by cross correlation. Excellent agreement with the gravimetrically

measured flow rates was obtained.

Boonstoppel et al. [B18] suggested that the accuracy of delay time measurement can be increased by obtaining a sharp peak in the cross correlation function. This can be achieved by creating a high degree of correlation between the two signals. It was reported that results in the measurement of the speed of a steel plate in a steel mill were due to the low frequency of the signal as compared to the frequency of measurements necessary for control purposes. Measurement at two areas rather than two points was suggested to increase the signal frequency. The use of only the fluctuating component of the signals for cross correlation allows amplifiers to be a.c. coupled so that their sensitivity and the non-linearity of the sensors are not of primary importance.

The measurement of a velocity profile in a solid suspension flow by the cross correlation method was reported by Intaglietta and Tompkins [I1]. Measurements of blood flow of 0.01 to 5 cm/sec range in 0.01 cm diameter tubes were done by using optical signals from the flow of blood cells. Departure of the measured profile from the parabolic behaviour confirmed the non-Newtonian behaviour of the blood flow.

E-4 Velocity Profile Measurements

The application of the cross correlation technique to the measurement of velocity profile in an air stream in a 8.054 in. diameter pipe, for the present investigation, was found particularly attractive. The use of conventional methods

of velocity measurements such as Pitot tube or hot-wire anemometer are particularly unsuitable for near the wall measurements where high temperature gradients exist. The Pitot tube cannot give low velocity measurements near the wall because of its size and the very low pressure differentials generated. A hot-wire anemometer, on the other hand, cannot distinguish between the signals from the velocity and the temperature fields. Thus a very extensive and laborious calibration procedure has to be adopted so that the anemometer output voltage can be expressed as a function of flow velocity and temperature. Additional complications are created by very large temperature gradients in the wall region.

The cross correlation technique has the advantage that no distinction need be made in the hot-wire signals; the signals may be generated by both temperature and velocity. Furthermore, since an absolute measurement of time delay is done, no calibration curve is needed. This is contrasted with the tedious and difficult calibration of hot-wire anemometers at velocities less than 5 ft./sec., even under isothermal conditions. The natural fluctuations of velocity in turbulent flow were found adequate disturbances for cross correlation purposes.

A two-wire probe was made by soldering 0.0005 in. diameter platinum wires onto stainless steel supported prongs. The wires were oriented perpendicular to the main flow and were parallel to each other and separated by a distance of 0.52 in. Figure F-1 shows the hot-wire circuitry and the

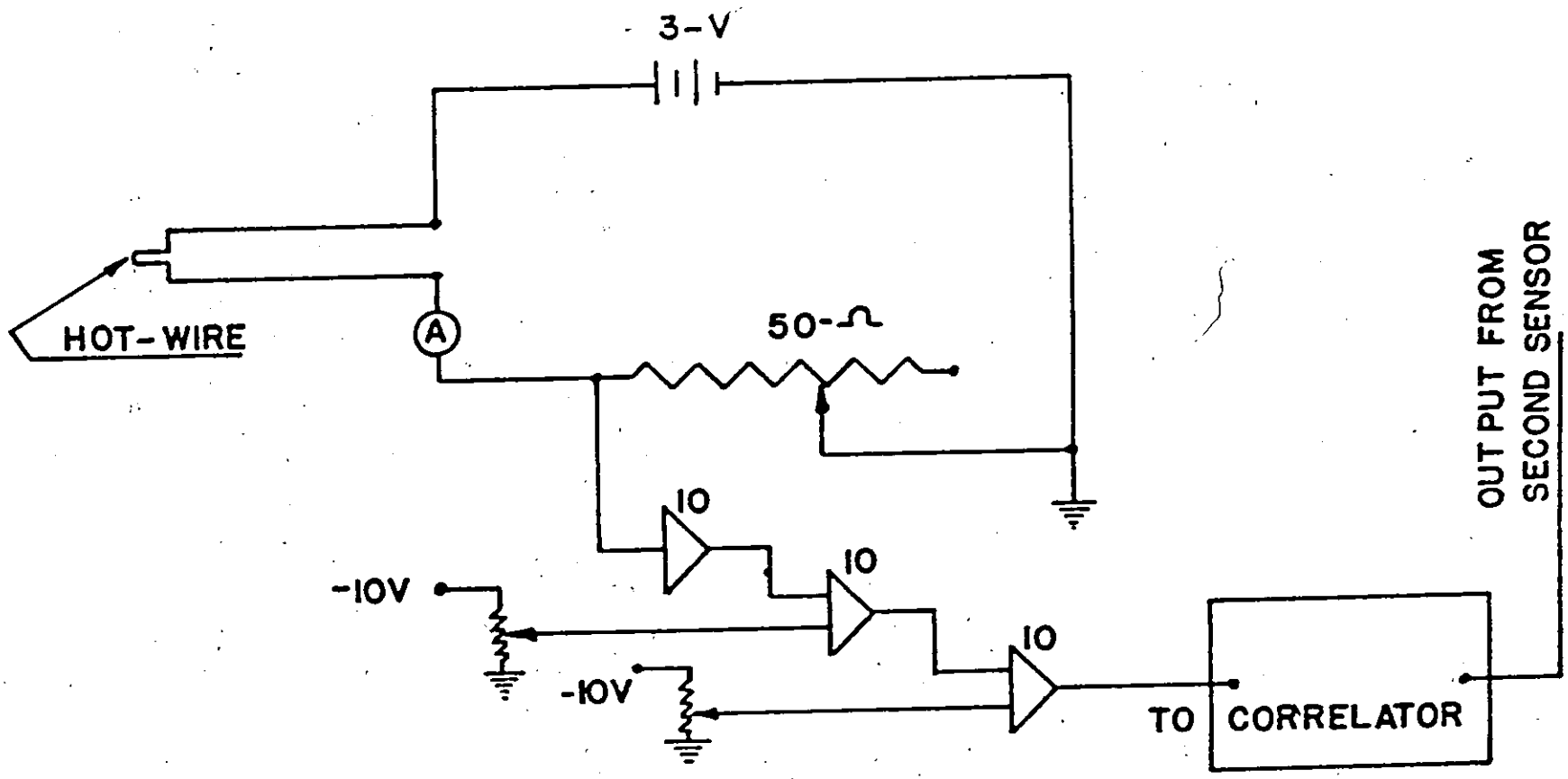

Figure F-1. Hot-Wire Circuitry for Velocity Measurement by Cross-Correlation.

following signal processing. A constant voltage was supplied from a series of mercury cells, to the hot-wires and their associated external resistances. The current in the wires was kept between 70-120 mA. The cooling of the wires due to the flow of air changed the resistance of the circuit and hence the current in it. This current change was represented in the output voltage signal, tapped from the variable resistor whose resistance is not affected by the flow. The voltage signals from the hot-wire circuits were separately fed to a series of D.C. amplifiers in an analogue computer. At various stages of amplification controlled negative voltages were added to subtract the D.C. component in the signals and only allow the amplification of the fluctuating component. Thus high amplications of the signal were obtained without overloading the amplifiers. The amplified signals were fed to the Hewlett-Packard 3721-A correlator set on A.C. coupling. The signals were also fed to a dual beam oscilloscope for visual display and examination. On the correlator, the two signals were first individually examined to determine if the signal was at a reasonable level. The randomness of the signals, representing the velocity fluctuations, was confirmed by examining their probability density function; this was very close to being a Gaussian distribution. With suitable settings of time scale ($\Delta\tau$), number of samples, N, the averaging mode, and delaying one signal with respect to the other, the cross correlation between the two signals was obtained and displayed on the CRT

screen of the correlator. The peak in the correlation function was observed and the corresponding delay time, τ_m, was noted from the visual display. This delay time was assumed to be the average time for the air to flow between the two sensors. The velocity of the air at the radial location of the probe in the test section was obtained by dividing the separation between the sensors by this transit time. These measurements were repeated at various radial locations to determine the velocity profile at any axial location. Figure F-2 shows typical velocity profiles thus obtained under isothermal conditions. The observed profiles are compared with the theoretical results obtained by substituting the modified Reichardt eddy viscosity expressions (3.31, 3.32) into Equation (3.37).

It is observed that the agreement between the two is reasonably good in the central region. But near the wall where the theoretical velocity decreases sharply, it is found that the observed velocity remains almost constant as the wall is approached. Various trials with different settings on the correlator, viz., time interval, number of samples and amplifications of the signals and various changes in the hot-wire circuitry failed to resolve the discrepancy. The separation between the sensors was decreased to increase the correlation between the signals but this also did not show any improvement. Use of two DISA hot-wire anemometers instead of the present circuitry and the use of thermocouples as sensors in a

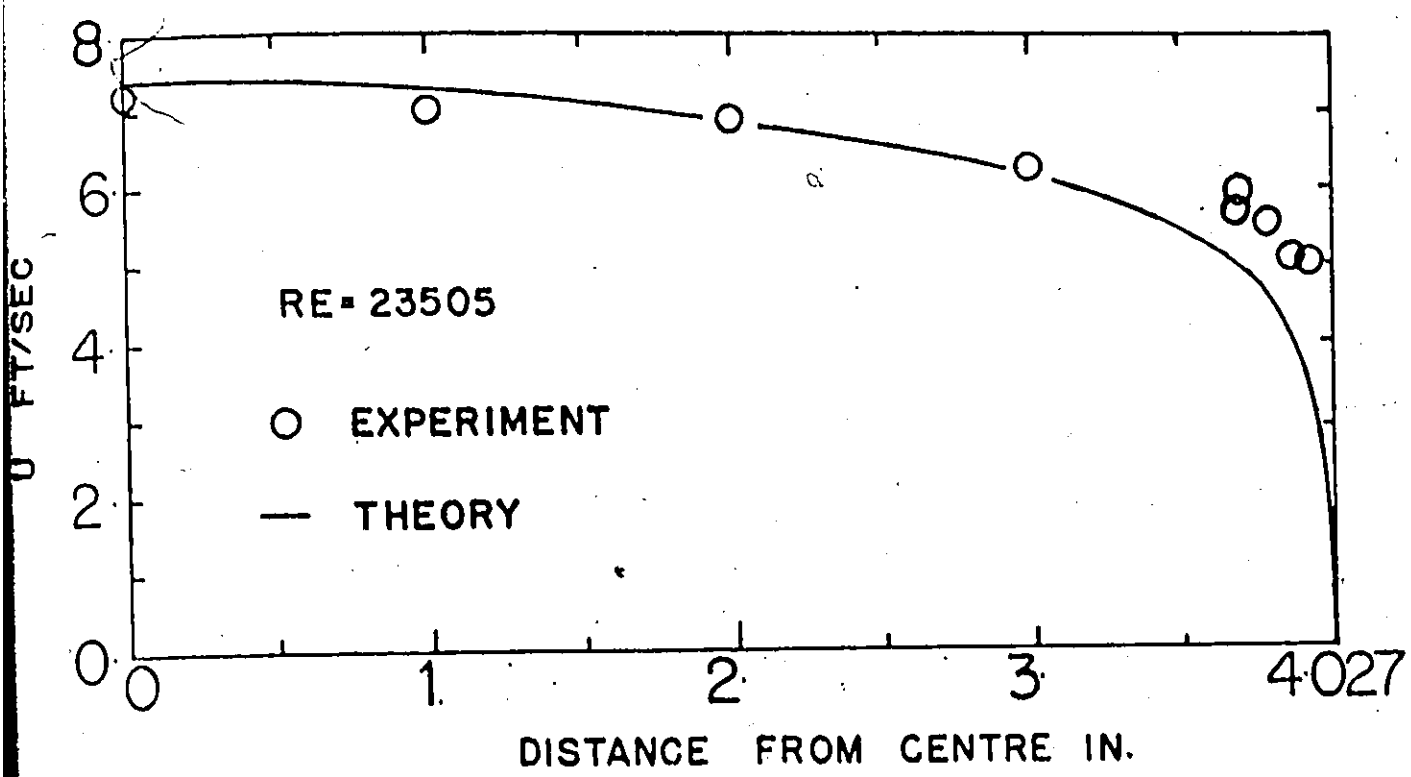

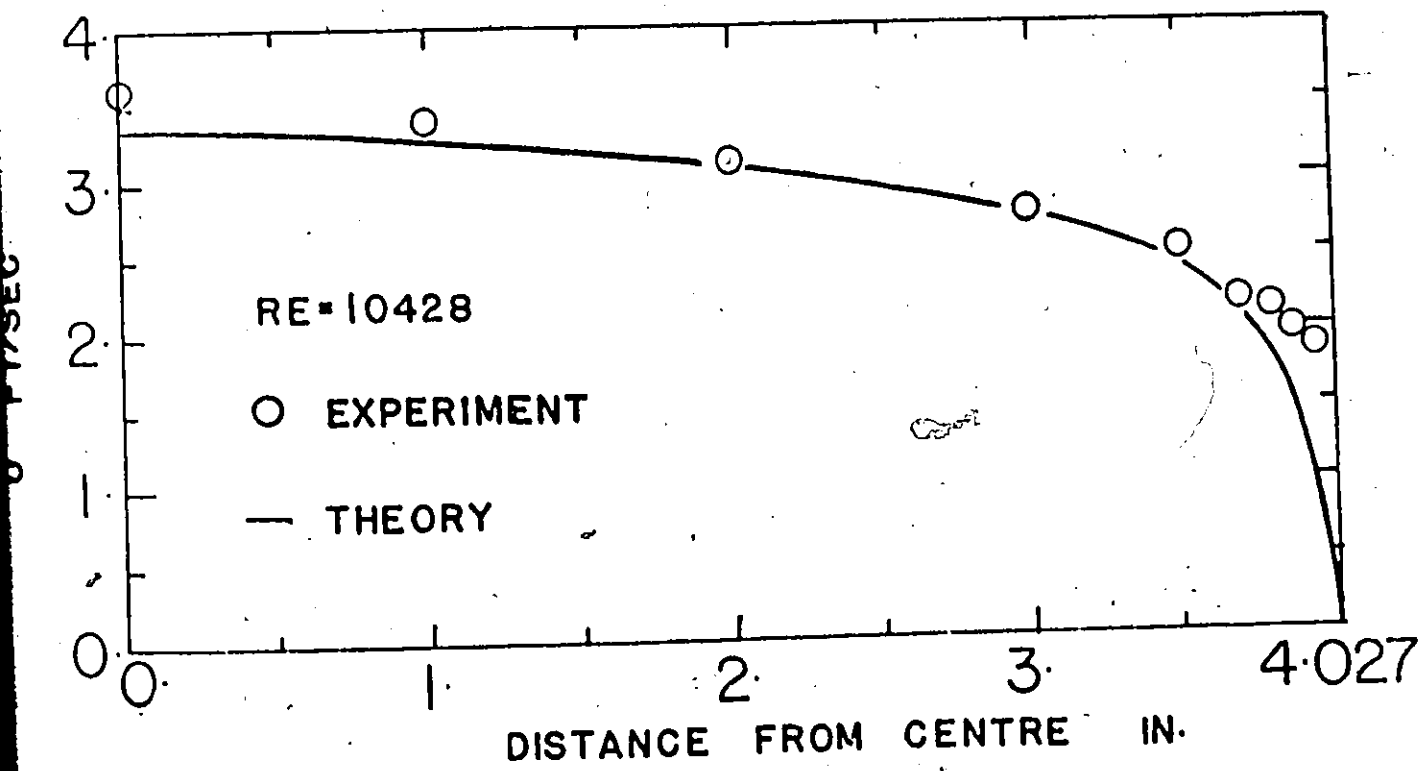

Figure F-2. Velocity Measurement by Cross-Correlation Technique for Isothermal Turbulent Flow.

non-isothermal flow field did not indicate a different profile.

It was decided to re-examine the assumptions involved in the use of the correlation technique. One of the basic assumptions is that the disturbance in the flow field travel with the average velocity of the flow. Thus for a turbulent flow in a pipe, for the above assumption to be valid, the fluctuation in velocity must be about the mean velocity at the point. Moreover, the magnitude of the fluctuations should be small as compared to the mean velocity. This is true for pipe flow over most of the cross section. However, near the wall an altogether different turbulence structure prevails. The flow visualisation experiments of Kline et.al. [K1] showed that the mechanism of production of turbulent kinetic energy is the violent ejection of low speed fluid from the wall region. This is followed by an inrush of fluid from the high velocity region to fill the voids. Grass [G5] gave a similar sort of picture of the wall turbulance from his flow visualisation studies.

The inrush of fluid eddies from the high velocity regions produces high velocity fluctuations in the wall region. These velocities are more characteristic of the flow at a further distance from the wall than they are of the velocity in the wall region. The bursting phenomena and the ensuing inrush of the fluid create high fluctuating velocities and it seems that these fluctuations do not travel longitudinally with the local mean velocity. These fluctuating velocities, due to their high relative magnitude, give rise to the high

velocity observed by the correlation method. In the laminar sublayer region where the wall effects damp the turbulent eddies, the velocity measurements are difficult because the low level of fluctuations requires very high amplification.

Thus it can be concluded that though the method of cross correlation is very attractive from the standpoint of its use in a highly non-isothermal flow field, measurements in the wall region are quite inaccurate because the assumptions behind the measurement are not valid in this region.

APPENDIX G

IN THIS APPENDIX EXPERIMENTAL AND CALCULATED DATA ARE PRESENTED

NOMENCLATURE

θ/DR	RADIAL TEMPERATURE GRADIENT F/(F-IN.)
θ/DX	AXIAL TEMPERATURE GRADIENT F/(F-IN.)
EPSLN	CALCULATED EDDY CONDUCTIVITY, $\epsilon_H \rho/\mu_0$
TOBS	OBSERVED TEMPERATURE F
TPRD	PREDICTED TEMPERATURE USING EPSLN F
UOBS	OBSERVED AXIAL VELOCITY FT/SEC
UPRD	PREDICTED AXIAL VELOCITY USING EPSLN FT/SEC
Y	DISTANCE FROM THE WALL IN.

Poor Quality Original

RUN NO: 1

FLOW RATE 885 LB/HR TWALL 175 F TIN 81.5 F TAMB 81.5 F

Y	T OBS	DΘ/DR	DΘ/DX	EPSLN	T PRD	UL PRD
TOP PORT						
0.000	175.00	.1650E+02	0.	0.	175.00	0.00
.010	160.39	.1400E+02	.2660E-02	.3214E+00	160.39	1.14
.020	148.71	.1202E+02	.4775E-02	.6878E+00	147.98	2.16
.030	138.48	.1030E+02	.4775E-02	.1096E+01	137.21	3.06
.040	130.22	.8300E+01	.6800E-02	.1763E+01	128.40	3.83
.050	121.42	.6718E+01	.8333E-02	.2556E+01	121.37	4.46
.060	115.50	.5176E+01	.9000E-02	.3774E+01	115.88	4.97
.110	100.01	.2200E+01	.1567E-01	.9993E+01	100.31	6.51
.210	89.20	.5650E+00	.1130E-01	.3700E+02	90.01	7.68
.310	86.36	.1039E+00	.1050E-01	.6500E+02	86.41	8.21
.410	81.50	0.	.8300E-02	.1300E+03	83.58	8.77
1.010	81.50	0.	0.	.8000E+02	81.73	9.61
2.010	81.50	0.	0.	.6900E+02	81.50	10.83
3.010	81.50	0.	0.	.6000E+02	81.50	11.51
4.027	81.50	0.	0.	.5400E+02	81.50	11.78
BOTTOM PORT						
0.000	175.00	.1415E+02	0.	0.	175.00	0.00
.010	162.37	.1100E+02	.2660E-02	.3452E+00	162.02	1.13
.020	154.07	.1004E+02	.4775E-02	.7372E+00	152.76	2.12
.030	143.83	.8637E+01	.4775E-02	.1144E+01	144.11	2.99
.040	136.85	.7114E+01	.6800E-02	.1743E+01	136.84	3.75
.050	130.77	.5680E+01	.8333E-02	.2583E+01	130.07	4.37
.060	125.60	.4307E+01	.9000E-02	.3892E+01	126.38	4.87
.110	111.27	.2314E+01	.6800E-02	.9274E+01	112.30	6.44
.210	99.70	.9240E+00	.3100E-02	.2231E+02	99.34	7.87
.310	94.06	.4307E+00	.3000E-02	.4800E+02	94.18	8.44
.410	88.04	.1405E+00	.4500E-02	.1350E+03	90.32	8.90
1.010	85.89	.1372E+00	.4500E-02	.8000E+02	85.88	9.54
2.010	81.50	0.	0.	.6900E+02	81.65	10.02
3.010	81.50	0.	0.	.6000E+02	81.50	11.61
4.027	81.50	0.	0.	.5400E+02	81.50	11.88

RUN NO. 2

LOW RATE .575 LB/HR TWALL 122 F TIN 81.6 F TAMB 81.6 F

BOTTOM PORT

Y	T 025	DT/DR	T'(RMS)
0.	122.	16.302	
0.010	116.3	12.484	
0.020	112.0	9.572	
0.030	108.8	7.284	
0.040	105.9	6.743	4.2
0.050	104.	5.376	4.3
0.060	102.2	4.755	5.0
0.110	96.3	2.250	4.7
0.210	90.3	0.916	4.2
0.310	89.2	0.527	4.2
0.510	85.2	0.276	
1.010	82.5	0.0569	
2.010	81.6	0.	
3.010	81.6	0.	
4.027	81.6	0.	

RUN NO. 3

LOW RATE 576 LB/HR TWALL 420 F TIN 77 F TAMB 77 F

Y	T OBS	DΘ/DR	DΘ/DX	FPSLN	T+	PMS T PRD	U PRD
OP PORT							
0.000	420.00	.1506E+02	0.	0.		420.00	0.00
.010	380.59	.1243E+02	0.	.5311E+00		374.83	.60
.020	338.47	.1029E+02	.5600E-02	.1157E+01	17.5	337.38	1.15
.030	303.83	.8764E+01	.1030E-01	.1781E+01	22.5	305.98	1.63
.040	278.07	.7252E+01	.9830E-02	.2615E+01	28.0	279.64	2.06
.050	254.98	.5705E+01	.1323E-01	.3889E+01	29.8	258.43	2.42
.060	238.14	.4678E+01	.1730E-01	.5181E+01	31.4	241.31	2.72
.110	180.52	.2500E+01	.1616E-01	.1119E+02	30.7	185.77	3.77
.210	126.53	.1076E+01	.2030E-01	.2680E+02	24.1	132.61	4.86
.310	107.71	.5190E+00	.1730E-01	.5145E+02	16.7	108.96	5.41
.510	85.23	.1468E+00	.1100E-01	.1500E+03		92.19	5.86
.710	77.79	.5400E-02	.1000E-02	.1580E+03		80.71	6.36
.910	77.00	0.	0.	.5200E+02		77.02	7.14
.910	77.00	0.	0.	.4300E+02		77.00	7.58
.927	77.00	0.	0.	.3700E+02		77.00	7.73
DDLE PORT							
.000	420.00	.1309E+02	0.	0.		420.00	0.00
.010	380.56	.1086E+02	0.	.5177E+00		379.98	.61
.020	345.60	.8931E+01	.1150E-02	.1114E+01	18.5	346.77	1.16
.030	319.64	.7574E+01	.1830E-02	.1775E+01	24.0	319.06	1.65
.040	293.19	.6340E+01	.4450E-02	.2558E+01	27.0	295.87	2.07
.050	272.36	.5053E+01	.4670E-02	.3758E+01	30.	277.09	2.43
.060	258.02	.3871E+01	.5230E-02	.5520E+01	31.8	262.37	2.72
.110	207.34	.2268E+01	.8500E-02	.1087E+02	33.0	215.28	3.71
.210	150.73	.1080E+01	.1220E-01	.2410E+02	26.5	164.34	4.84
.310	137.06	.6016E+00	.1093E-01	.4233E+02	22.	138.98	5.41
.510	117.76	.2702E+00	.1100E-01	.8400E+02	14.0	115.34	5.95
.910	81.00	.8420E-01	.2640E-02	.1500E+03		93.84	6.50
.910	77.00	0.	.2000E-03	.5200E+02		78.61	7.26
.917	77.00	0.	0.	.4300E+02		77.00	7.81
.927	77.00	0.	0.	.3700E+02		77.00	7.96
TTOM PORT							
.000	420.00	.1323E+02	0.	0.		420.00	0.00
.010	379.97	.1071E+02	0.	.5834E+00		381.20	.65
.020	345.88	.8678E+01	.1500E-02	.1276E+01	19.5	340.79	1.22
.030	321.42	.7010E+01	.6700E-03	.2116E+01	24.0	324.34	1.71
.040	296.76	.5838E+01	.1000E-02	.2996E+01	26.2	303.52	2.13
.050	279.68	.4466E+01	.3000E-02	.4557E+01	30.0	287.12	2.47
.060	267.02	.3274E+01	.2670E-02	.6040E+01	30.6	274.74	2.74
.110	222.64	.2029E+01	.5930E-02	.1257E+02	31.0	225.60	3.62
.210	179.00	.1000E+01	.8100E-02	.2714E+02	26.5	180.86	4.67
.310	156.44	.6856E+00	.8600E-02	.3941E+02	23.2	165.62	5.27
.510	131.09	.3677E+00	.1100E-01	.6850E+02	18.7	136.80	5.94
.710	93.26	.1047E+00	.1110E-01	.1100E+03		106.50	6.64
.910	78.03	.1440E-01	.5000E-03	.5200E+02		82.59	7.44
.910	77.00	0.	0.	.4300E+02		77.10	8.07
.927	77.00	0.	0.	.3700E+02		77.00	8.23

RUN NO. 4
[illegible] 580 LB/HR TWALL 700 F TIN 77 F TAMB 77 F

X	T PRS	DΘ/DR	DΘ/DX	EPSLN	TIRMS	T PRD	U PRD
[illegible] PORT							
[illegible]	700.00	.1274E+02	0.		0.	700.00	0.00
[illegible]	650.01	.1282E+02	.1900E-02		.5509E+00	628.63	.50
[illegible]	567.90	.9220E+01	.5600E-02		.1186E+01	567.69	.97
[illegible]	513.10	.7956E+01	.5250E-02		.1843E+01	515.36	1.40
[illegible]	465.13	.6698E+01	.6750E-02		.2701E+01	470.69	1.79
[illegible]	420.40	.5458E+01	.7030E-02		.3878E+01	433.81	2.12
[illegible]	385.61	.4121E+01	.8430E-02		.5891E+01	404.76	2.41
[illegible]	[illegible]	.2425E+01	.1107E-01		.1145E+02	312.14	3.37
[illegible]	201.53	.1181E+01	.1480E-01		.2425E+02	209.61	4.57
[illegible]	117.13	.6515E+00	.1573E-01		.4092E+02	157.48	5.24
[illegible]	115.53	.2176E+00	.1470E-01		.9146E+02	112.79	5.91
[illegible]	91.24	.1860E-01	.1900E-02		.1280E+03	83.00	6.61
[illegible]	78.42	.0200E-02	0.		.5000E+02	77.02	7.40
[illegible]	77.00	0.	0.		.4350E+02	77.00	7.90
[illegible]	77.00	0.	0.		.3700E+02	77.00	8.08
[illegible] PORT							
[illegible]	700.00	.1176E+02	0.		0.	700.00	0.00
[illegible]	637.79	.9051E+01	.1170E-02		.5610E+00	636.13	.52
[illegible]	583.01	.8439E+01	.1500E-02		.1109E+01	582.08	1.00
[illegible]	530.36	.7274E+01	.2000E-02		.1864E+01	536.01	1.44
[illegible]	486.87	.6125E+01	.4150E-02		.2724E+01	496.81	1.83
[illegible]	452.49	.4909E+01	.4250E-02		.4037E+01	464.88	2.17
[illegible]	424.14	.3583E+01	.6000E-02		.6389E+01	440.38	2.44
[illegible]	334.08	.2109E+01	.7670E-02		.1190E+02	362.74	3.36
[illegible]	254.80	.1091E+01	.1027E-01		.2567E+02	272.63	4.52
[illegible]	[illegible]	.7309E+00	.1113E-01		.3760E+02	220.88	5.23
[illegible]	153.19	.3361E+00	.1055E-01		.7316E+02	164.37	6.02
[illegible]	92.05	.6870E-01	.5400E-02		.1280E+03	110.87	6.93
[illegible]	78.68	.0200E-02	.1900E-02		.5000E+02	79.28	7.71
[illegible]	77.00	0.	0.		.4350E+02	77.01	8.29
[illegible]	77.00	0.	0.		.3700E+02	77.00	8.46
[illegible] PORT							
[illegible]	[illegible]	.1178E+02	0.		0.	700.00	0.00
[illegible]	638.22	.9764E+01	0.		.6251E+00	638.28	.57
[illegible]	590.07	.8100E+01	0.		.1359E+01	33.5	587.36	1.07
[illegible]	534.53	.6771E+01	.1330E-02		.2177E+01	43.0	544.05	1.52
[illegible]	494.22	.5704E+01	.1600E-02		.3096E+01	50.5	509.42	1.91
[illegible]	463.26	.4468E+01	.2250E-02		.4646E+01	53.5	480.85	2.25
[illegible]	439.34	.3258E+01	.3330E-02		.7252E+01	54.0	459.13	2.51
[illegible]	354.48	.2021E+01	.4430E-02		.1324E+02	57.0	390.27	3.40
[illegible]	225.34	.1011E+01	.6530E-02		.2865E+02	50.5	309.63	4.52
[illegible]	143.15	.6943E+00	.7950E-02		.4196E+02	45.5	262.48	5.20
[illegible]	102.83	.2806E+00	.9450E-02		.7096E+02	34.0	204.89	6.04
[illegible]	117.45	.1520E+00	.9330E-02		.1280E+03		139.78	7.01
[illegible]	79.54	.1100E-01	.3830E-02		.5000E+02		87.30	8.02
[illegible]	77.31	.0000E-03	0.		.4350E+02		77.13	8.70
[illegible]	77.00	0.	0.		.3700E+02		77.00	8.97

RUN NO: 5

[illegible] RATE 422.LB/HR TWALL 126 F TIN 78.5 F TAMB 78.5 F

Y	T DRS	DΘ/DR	DΘ/DX	EPSLN	T PRD	U PRD
[illegible] POST						
[illegible]	126.00	.1830E+02	0.	0.	126.00	0.00
[illegible]	119.69	.1410E+02	.3250E-02	.5000E+00	118.63	.56
[illegible]	112.46	.1086E+02	.6330E-02	.1132E+01	112.95	1.02
[illegible]	107.95	.8566E+01	.9000E-02	.1865E+01	108.51	1.39
[illegible]	104.53	.6991E+01	.7170E-02	.2643E+01	104.93	1.71
[illegible]	101.54	.5820E+01	.9100E-02	.3427E+01	101.97	1.97
[illegible]	98.78	.4916E+01	.1175E-01	.4421E+01	99.48	2.20
[illegible]	96.30	.3701E+01	.1467E-01	.9100E+01	91.14	3.01
[illegible]	93.47	.6760E+00	.1800E-01	.3800E+02	85.02	3.65
[illegible]	90.63	.3037E+00	.9500E-02	.7500E+02	83.02	3.89
[illegible]	79.71	.9120E-01	.4400E-02	.1050E+03	81.08	4.17
[illegible]	78.50	0.	0.	.1000E+03	79.04	4.63
[illegible]	78.50	0.	0.	.4100E+02	78.50	5.26
[illegible]	78.50	0.	0.	.3400E+02	78.50	5.64
[illegible]	78.50	0.	0.	.2850E+02	78.50	5.79
[illegible] PRE POST						
[illegible]	126.00	.1508E+02	0.	0.	126.00	0.00
[illegible]	119.63	.1212E+02	.3250E-02	.4041E+00	119.08	.54
[illegible]	114.37	.9769E+01	.6330E-02	.8931E+00	115.13	.99
[illegible]	110.22	.7848E+01	.7500E-02	.1504E+01	111.24	1.37
[illegible]	106.91	.6303E+01	.8600E-02	.2261E+01	108.12	1.69
[illegible]	104.20	.5337E+01	.9100E-02	.2954E+01	105.55	1.95
[illegible]	102.01	.4342E+01	.1050E-01	.3985E+01	103.42	2.18
[illegible]	99.37	.2406E+01	.1267E-01	.8287E+01	96.43	2.93
[illegible]	97.33	.9776E+00	.1560E-01	.2110E+02	89.80	3.64
[illegible]	95.80	.4800E+00	.1257E-01	.4051E+02	86.07	3.94
[illegible]	92.95	.2286E+00	.9250E-02	.7500E+02	84.28	4.23
[illegible]	78.50	0.	.1800E-02	.1000E+03	81.16	4.63
[illegible]	78.50	0.	0.	.4100E+02	78.70	5.27
[illegible]	78.50	0.	0.	.3400E+02	78.50	5.71
[illegible]	78.50	0.	0.	.2850E+02	78.50	5.84
[illegible] TION POST						
[illegible]	126.00	.1209E+02	0.	0.	126.00	0.00
[illegible]	120.50	.1051E+02	.3250E-02	.3874E+00	120.86	.49
[illegible]	116.00	.8516E+01	.6330E-02	.8596E+00	116.71	.91
[illegible]	112.35	.7060E+01	.6750E-02	.1369E+01	113.31	1.27
[illegible]	109.40	.5856E+01	.9670E-02	.1976E+01	110.50	1.57
[illegible]	106.70	.4941E+01	.9100E-02	.2631E+01	108.15	1.83
[illegible]	104.62	.3878E+01	.8670E-02	.3642E+01	106.21	2.05
[illegible]	97.70	.2207E+01	.1117E-01	.7707E+01	99.86	2.78
[illegible]	91.25	.9851E+00	.1240E-01	.1956E+02	93.76	3.48
[illegible]	88.00	.6262E+00	.1600E-01	.2589E+02	90.50	3.85
[illegible]	83.70	.2935E+00	.1000E-01	.4300E+02	86.59	4.26
[illegible]	78.50	.1156E+00	.3500E-02	.1000E+03	82.66	4.70
[illegible]	78.50	0.	0.	.4100E+02	79.34	5.27
[illegible]	78.50	0.	0.	.3400E+02	78.52	5.77
[illegible]	78.50	0.	0.	.2850E+02	78.50	5.91

RUN NO. 6

RATE 427.18/HR TWALL 443 F TIN 80 F TAMB 80 F

X OBS	DΘ/DX	DΘ/DX	FPSLN	T PRD	U PRD
PORT					
443.00	.1324E+02	0.	0.	443.00	0.00
407.81	.1122E+02	.6000E-03	.4561E+00	399.72	.36
372.94	.9706E+01	.6700E-03	.9498E+00	362.45	.69
336.94	.8325E+01	.6700E-03	.1555E+01	330.55	1.01
300.71	.6833E+01	.7750E-03	.2330E+01	303.73	1.30
275.73	.5676E+01	.6330E-03	.3274E+01	281.56	1.55
250.06	.4345E+01	.6930E-03	.4820E+01	263.94	1.76
222.73	.3206E+01	.9100E-03	.1130E+02	209.58	2.49
156.18	.0770E+00	.1305E-01	.2650E+02	158.13	3.28
127.00	.6280E+00	.1467E-01	.3925E+02	131.47	3.74
97.07	.3384E+00	.1333E-01	.7000E+02	104.06	4.28
82.00	.1050E-01	.3100E-02	.1400E+03	84.53	4.85
80.00	0.	.4500E-03	.3800E+02	80.04	5.42
80.00	0.	0.	.3250E+02	80.00	5.93
80.00	0.	0.	.2850E+02	80.00	5.96
PIPE PORT					
443.00	.1365E+02	0.	0.	443.00	0.00
397.62	.1119E+02	.1100E-02	.5643E+00	400.74	.43
363.34	.9194E+01	.1300E-02	.1211E+01	365.96	.81
330.34	.7394E+01	.2330E-02	.2073E+01	337.69	1.15
306.51	.5879E+01	.4330E-02	.3171E+01	315.11	1.44
288.02	.4706E+01	.6750E-02	.4496E+01	297.12	1.68
272.48	.3804E+01	.6000E-02	.6036E+01	282.62	1.88
233.62	.1969E+01	.9000E-02	.1358E+02	236.50	2.58
182.64	.9624E+00	.9170E-03	.3300E+02	192.72	3.30
154.14	.5794E+00	.1200E-01	.4876E+02	169.08	3.72
126.57	.3496E+00	.1163E-01	.7000E+02	139.02	4.27
90.28	.0020E-01	.5930E-02	.1400E+03	105.03	4.94
80.08	0.	.5300E-03	.3800E+02	82.93	5.59
80.00	0.	.3000E-03	.3250E+02	80.01	6.11
80.00	0.	0.	.2850E+02	80.00	6.23
TOP PORT					
443.00	.1305E+02	0.	0.	443.00	0.00
400.17	.1049E+02	.1300E-02	.6153E+00	403.36	.45
366.41	.8415E+01	.1660E-02	.1351E+01	371.59	.85
338.78	.6851E+01	.6150E-02	.2185E+01	345.93	1.19
316.03	.5570E+01	.5000E-02	.3196E+01	325.07	1.49
297.01	.4566E+01	.4250E-02	.4334E+01	308.08	1.74
282.64	.3350E+01	.3330E-02	.6670E+01	294.02	1.94
240.77	.1790E+01	.7670E-02	.1448E+02	255.47	2.50
200.49	.7739E+00	.7900E-02	.3544E+02	216.74	3.28
170.82	.5672E+00	.9670E-02	.4852E+02	194.79	3.69
149.83	.3567E+00	.9100E-02	.7000E+02	164.53	4.27
127.62	.1571E+00	.9180E-02	.1400E+03	126.69	4.99
93.29	.1760E-01	.5000E-03	.3800E+02	91.48	5.78
81.31	0.	.6000E-03	.3250E+02	80.17	6.44
80.00	0.	0.	.2850E+02	80.00	6.57

RUN NO. 7

[illegible] 423 LB/HR TWALL 745 F TIN 77.7 F TAMB 77.7 F

[illegible]	[illegible]	DΘ/DR	DΘ/DX	EPSLN	T PRD	U PRD
[illegible] PORT						
[illegible]	745.00	.1102E+02	0.	0.	745.00	0.00
[illegible]	671.60	.1037E+02	.6000E-03	.4956E+00	672.50	.29
[illegible]	610.51	.9043E+01	.9100E-03	.1026E+01	609.28	.59
[illegible]	553.80	.8007E+01	.3600E-02	.1580E+01	553.60	.87
[illegible]	503.17	.6680E+01	.6670E-02	.2429E+01	505.57	1.14
[illegible]	456.00	.5455E+01	.9430E-02	.3576E+01	466.07	1.38
[illegible]	421.00	.3933E+01	.1030E-01	.5871E+01	435.72	1.67
[illegible]	332.00	.2237E+01	.1460E-01	.1202E+02	342.71	2.26
[illegible]	240.32	.1053E+01	.1300E-01	.2657E+02	240.29	2.17
[illegible]	187.21	.5974E+00	.1483E-01	.4569E+02	187.71	3.71
[illegible]	139.46	.2410E+00	.1430E-01	.8000E+02	134.14	4.33
[illegible]	[illegible]	.1047E+00	.7630E-02	.1730E+03	90.77	4.97
[illegible]	79.70	.0000E-02	0.	.4500E+02	77.92	5.57
[illegible]	77.70	0.	0.	.3250E+02	77.70	5.98
[illegible]	77.70	0.	0.	.2850E+02	77.70	6.12
[illegible] PORT						
[illegible]	745.00	.1169E+02	0.	0.	745.00	0.00
[illegible]	671.00	.9772E+01	.5200E-03	.6197E+00	677.25	.35
[illegible]	614.40	.8180E+01	.1550E-02	.1326E+01	620.59	.68
[illegible]	564.50	.6840E+01	.3100E-02	.2144E+01	573.16	.98
[illegible]	522.50	.5787E+01	.3930E-02	.3051E+01	533.31	1.25
[illegible]	485.00	.4624E+01	.4300E-02	.4473E+01	500.88	1.49
[illegible]	458.50	.3400E+01	.6130E-02	.6958E+01	475.04	1.68
[illegible]	347.00	.2062E+01	.8000E-02	.1314E+02	307.12	2.34
[illegible]	288.30	.1017E+01	.9100E-02	.2905E+02	307.32	3.21
[illegible]	240.30	.6930E+00	.1030E-01	.4338E+02	255.80	3.75
[illegible]	180.61	.3704E+00	.1145E-01	.8000E+02	195.85	4.43
[illegible]	115.30	.9520E-01	.6900E-02	.1730E+03	135.09	5.15
[illegible]	79.50	.2780E-01	.1700E-03	.4500E+02	87.66	5.80
[illegible]	77.70	0.	0.	.3250E+02	77.75	6.46
[illegible]	77.70	0.	0.	.2850E+02	77.70	6.60
[illegible] PORT						
[illegible]	745.00	.1117E+02	0.	0.	745.00	0.00
[illegible]	675.00	.9329E+01	[illegible]500E-03	.6173E+00	681.07	.39
[illegible]	621.28	.7800E+01	[illegible]800E-02	.1322E+01	627.66	.75
[illegible]	574.07	.6514E+01	.2370E-02	.2147E+01	583.03	1.08
[illegible]	531.44	.5486E+01	.1500E-02	.3075E+01	545.66	1.37
[illegible]	496.63	.4324E+01	.1800E-02	.4597E+01	515.59	1.61
[illegible]	473.68	.3062E+01	.2800E-02	.7484E+01	493.04	1.81
[illegible]	392.73	.1990E+01	.4700E-02	.1375E+02	422.97	2.47
[illegible]	320.06	.9310E+00	.6530E-02	.3026E+02	340.11	3.24
[illegible]	291.23	.5500E+00	.6300E-02	.5234E+02	295.54	3.84
[illegible]	232.08	.3600E+00	.9600E-02	.8000E+02	241.93	4.48
[illegible]	152.50	.1323E+00	.9000E-02	.1730E+03	176.52	5.27
[illegible]	84.93	.8300E-01	.5200E-02	.4500E+02	109.45	6.19
[illegible]	77.70	0.	0.	.3250E+02	78.48	6.97
[illegible]	77.70	0.	0.	.2850E+02	77.71	7.13

RUN NO. 8

LIQ RATE 334 LB/HR TWALL 302 F TIN 85 F TAMB 85 F

Y	T OBS	D /DR	P /DX	EPSLN	T PRD	U PRD
OS PORT						
0.000	302.00	.1327E+02	0.	0.	302.00	0.00
.010	276.01	.1127E+02	.1850E-02	.3916E+00	276.73	.15
.020	255.02	.9609E+01	.9300E-02	.8291E+00	255.17	.31
.030	238.03	.8432E+01	.1170E-01	.1237E+01	236.49	.46
.040	216.02	.6860E+01	.3510E-01	.1971E+01	220.66	.60
.050	201.00	.5331E+01	.3560E-01	.3050E+01	208.11	.73
.060	194.02	.3723E+01	.3500E-01	.5099E+01	198.79	.83
.110	163.07	.2069E+01	.1720E-01	.1036E+02	170.85	1.19
.210	138.23	.9558E+00	.2320E-01	.2335E+02	140.17	1.67
.310	125.42	.5216E+00	.2000E-01	.4087E+02	124.55	1.95
.510	100.56	.2400E+00	.1780E-01	.7000E+02	108.12	2.29
.710	90.12	.1877E+00	.9900E-02	.1400E+03	92.52	2.68
.910	85.00	0.	.6000E-03	.3800E+02	85.35	3.05
.910	85.00	0.	0.	.2450E+02	85.00	3.11
.927	85.00	0.	0.	.1700E+02	85.00	3.[illegible]
DDLE PORT						
0.000	302.00	.1021E+02	0.	0.	302.00	0.00
.010	278.00	.8828E+01	.8300E-03	.3493E+00	282.02	.14
.020	262.48	.7650E+01	.8300E-03	.7285E+00	264.71	.27
.030	246.80	.6560E+01	.2750E-02	.1108E+01	249.79	.41
.040	232.00	.5622E+01	.3400E-02	.1736E+01	237.02	.54
.050	222.31	.4710E+01	.3530E-02	.2454E+01	226.32	.66
.060	211.21	.3363E+01	.4730E-02	.4184E+01	218.08	.76
.110	182.00	.2050E+01	.8700E-02	.8152E+01	192.55	1.11
.210	158.00	.9763E+00	.8500E-02	.1950E+02	163.03	1.60
.310	145.50	.4600E+00	.1097E-01	.3011E+02	148.11	1.90
.510	129.01	.3665E+00	.1116E-01	.5530E+02	129.52	2.28
.710	113.00	.1300E+00	.9900E-02	.1400E+03	110.58	2.69
.910	86.30	.4430E-01	.1750E-02	.3800E+02	92.75	3.14
.910	85.00	0.	0.	.2450E+02	85.13	3.57
.927	85.00	0.	0.	.1700E+02	85.00	3.66
TTOM PORT						
0.000	302.00	.1029E+02	0.	0.	302.00	0.00
.010	279.19	.8752E+01	.1600E-03	.3862E+00	283.03	.14
.020	261.83	.7450E+01	.2500E-03	.8212E+00	266.80	.28
.030	249.51	.6239E+01	.7500E-03	.1371E+01	253.25	.42
.040	236.01	.5303E+01	.1150E-02	.1966E+01	241.74	.55
.050	224.01	.4270E+01	.7700E-03	.2909E+01	232.31	.66
.060	214.98	.3089E+01	.2170E-02	.4729E+01	225.10	.75
.110	189.01	.1878E+01	.3900E-02	.9030E+01	202.51	1.09
.210	167.00	.8036E+00	.5150E-02	.2087E+02	176.83	1.55
.310	156.50	.6143E+00	.6830E-02	.3165E+02	162.16	1.85
.510	140.01	.3427E+00	.7250E-02	.5682E+02	144.29	2.24
.710	116.01	.1158E+00	.9900E-02	.1400E+03	125.26	2.68
.910	88.00	.5790E-01	.4330E-02	.3800E+02	103.77	3.21
.910	85.00	0.	0.	.2450E+02	86.21	3.86
.927	85.00	0.	0.	.1700E+02	85.05	3.98

RUN NO. 9

FLOW RATE 225 LB/HR TWALL 744 F TIN 82.7 F TAMB 82.7 F

Y	TOP PORT T OBS	MIDDLE PORT T OBS	BOTTOM PORT T OBS
0.0	744.	744.	744.
0.010	695.	687.5	699.5
0.020	673.0	652.0	667.5
0.030	632.5	617.0	630.
0.040	602.0	585.0	597.5
0.050	562.0	555.0	564.
0.060	524.0	519.0	545.
0.110	400.5	419.0	440.
0.210	310.	342.0	361.5
0.310	267.0	309.0	329.
0.510	218.0	268.0	292.0
1.010	149.0	199.5	231.0
2.010	87.8	117.0	151.0
3.010	83.1	87.2	98.05
4.027	82.7	84.5	86.

RUN NO. 10

FLOW RATE 180 LB/HR TWALL 889 F TIN 68 F TAMB 68 F

Y	TOP PORT T OBS	MIDDLE PORT T OBS	BOTTOM PORT T OBS
0.0	889.	889.	889.
0.010	817.5	809.5	803.5
0.020	773.5	777.5	763.
0.030	731.0	737.	728.0
0.040	691.5	697.0	695.0
0.050	668.0	666.5	658.0
0.060	632.0	637.5	630.0
0.110	501.5	526.5	538.
0.210	396.5	437.5	436.0
0.310	351.5	386.0	395.
0.510	299.0	342.0	358.
1.010	212.5	271.0	296.0
2.010	125.5	184.0	219.
3.010	91.0	123.0	158.4
4.027	81.0	99.0	123.

VELOCITY PROFILE AT 1.5 IN. UPSTREAM THE EXIT OF THE TEST SECTION

RUN NO. 3

Y	U OBS	U PRD
1.0	6.66	6.70
1.5	7.31	7.25
2.0	7.57	7.70
3.0	8.19	8.25
4.03	8.33	8.47

RUN NO. 4

Y	U OBS	U PRD
1.0	6.85	7.1
1.5	7.90	7.77
2.0	8.3	8.3
3.0	8.8	8.97
4.03	9.05	9.25

RUN NO. 6

Y	U OBS	U PRD
1.0	4.92	5.0
2.0	6.05	5.92
3.0	6.2	6.15
4.03	6.8	6.92

RUN NO. 7

Y	U OBS	U PRD
1.0	5.2	5.32
1.5	6.1	6.0
2.0	6.7	6.55
3.0	7.25	7.35
4.03	7.45	7.6

FLOW VISUALISATION

	A	B	C
T WAT F	118.	138.2	171.
T WALL F	108.5	123.6	152.7
GRASHOF NUMBER	3.475E+07	8.310E+07	2.062E+08
PRANDTL NUMBER	3.88	3.16 5	2.38
REYNOLDS NUMBER			
UPPER LIMIT *	7900	9420	11800
LOWER LIMIT **	6800	8500	10500

ALL PHYSICAL PROPERTIES WERE EVALUATED AT FILM TEMPERATURE

* UPPER LIMIT OF FLOW REVERSAL OCCURENCE, THAT IS, ABOVE THIS REYNOLDS NUMBER FLOW REVERSAL WAS OBSERVED INTERMITTANTLY AND ONLY AT SOME OF THE ELECTRODES

** LOWER LIMIT OF THE FLOW REVERSAL BAND, THAT IS, BELOW THIS REYNOLDS NUMBER FLOW REVERSAL WAS DEFINITELY OCCURRING ALL ALONG THE LENGTH OF THE PIPE

APPENDIX Z

Computer programs written in Fortran IV for a CDC 6400 computer are listed in this section. Extensive use of 'comment cards' permits the flow of information in the calculation procedure to be followed easily. Solution of the conservation equations, evaluation of radial temperature gradients and the integration of the energy equation, with the associated subroutines are documented here.

```
*****************************************************************
* FINITE DIFF. SOLUTION OF MOMENTUM-ENERGY EQNS.
*****************************************************************

NON-DIMENSIONALISING PARAMETERS ARE   INLET AVERAGE VELOCITY AND
DENSITY AT INLET AVERAGE TEMPERATURE

COMMON/BLK1/ VISCCT,VISCA,VISCB,VISCC,VISCD,VISCE,
1TCONCT,TCONA,TCONB,TCONC,        CPCT,CPA,CPB,CPC,CPD,
2 DENSCT,DENSA,DENSB,DENSC,DENSD,
3 H,OPPOS,      RWTF,WTF,XLIM,DPDXX,WALLF,AMBF,PULKF,WFLOW,
4   MM,JPRIN1,IAF,IND,IAE,LM,LLM,IAB,IAA,IAG,INN,IAH,
5 X(5),GAS(8),XL(25),WALLT(25),RL(25),UL(25),RT(25,3),TR(25,3),
6 LMM(3),XL1,XL2,M1,M2,M3,H1

COMMON/BLK3/ RADIUS,KKK,N,IAD
COMMON/BLK4/ UX(50)
COMMON/ELEVEN/ EDDYM(50)
COMMON/TWEN/ EDDY(50,2)
IAA   1 FOR  AN OBSERVED RADIAL TEMP. PROFILE GIVEN
IAB   0 IF NO OBSERVATION WAS MADE
IAB   DESIGNATES THE LAST PORT OBSERVATION WAS MADE
IAC   0
IAD   0
IAE   0
IAG   LOCATION AT WHICH FIRST OBS. WAS TAKEN
IAH   1 FOR GIVEN EDDY DIFFISIVITY
INN   IS 0 IF ONLY ENERGY EQN. TO BE SOLVED

READ(5,1) IAA,IAB,IAC,IAD,IAE,IAG,IAH,INN


CONSTANTS FOR PROPERTY CORRELATIONS
READ(5,3) VISCCT,VISCA,VISCB,VISCC,VISCD,VISCE
READ(5,3) TCONCT,TCONA,TCONB,TCONC
READ(5,3) CPCT,CPA,CPB,CPC,CPD
READ(5,3) DENSCT,DENSA,DENSB,DENSC,DENSD


GEOMETRY OF THE SYSTEM
RADIUS OF  PIPE,N  NO.OF RADIAL MESH POINTS,H DETERMINES RADIAL
SPACING
IF BUOYANCY FORCE IS OPPOSING THE MAIN FLOW THEN OPPOS=1, AND
-1 FOR AIDING FLOW SITUATION
WTF   WEIGHTING FUNCTION FOR CRANK-NICHOLSON TYPE REPRESENTATION
WEIGHTING FACTOR  FOR STABALISING THE SOLUTION
MM   STARTING AXIAL LOCATION
JPRIN1   CONTROLS PRINTING EVERY JPRIN1 AXIAL STEPS

READ(5,1) N,MM
READ(5,1) JPRIN1
READ(5,4) X(1)
READ(5,4) RADIUS,OPPOS,WTF,RWTF

H   DETERMINES THE RADIAL STEP SIZE
H1   DETERMINES THE AXIAL STEP SIZE
XL1  NO. OF RADII TO BE TRAVERSED          ISOTHERMAL SOLUTION
```

```
XL2  NO. OF RADII TO BE TRAVERSED.  NON ISOTHERMAL SOLUTION
H1   NO. OF AXIAL STEPS ISOTHERMAL SOLUTION .
H    NO. OF STEPS IN AXIAL DIRECTION   NON ISOTHERMAL SOLUTION
M3   NO. OF AXIAL STEPS NON ISOTHERMAL SOLUTION IS TO BE TERMINATED

READ(5,4) H, H1
READ(5,4) XL1,XL2
READ(5,1) M1,M2,M3

KKK  1 FOR ISOTHERMAL AND NON ISOTHERMAL SOLUTIONS
KKK  2 FOR NON ISOTHERMAL SOLUTION ONLY
IND  0 FOR FLAT, 1 FOR OBSERVED, 2 FOR A GIVEN PROFILE
IAF  0 FOR UNIFORM WALL TEMP.

READ(5,1) KKK,IND,IAF

FLOW AND TEMP. CONDITIONS OF THE SYSTEM IN LB/HR  AND DEGREE F
CONSTANT WALL TEMP.  TWALLF AND AMBIENT TEMP. TAMBF
GAS NTITLE OF THE RUN .

READ(5,4)   WALLF, AMBF, BULKF,WFLOW
READ(5,2) (GAS(I),I=1,9)

IF(IAF.EQ.0) GO TO 18

LM   NO. OF AXIAL OBSERVATION LOCATIONS
XL AND WALLT ARE AXIAL LOCATION(IN.) AND CORRESPONDING WALL TEMP.F

READ(5,1) LM
READ(5,9)(XL(I),WALLT(I),I=1,LM)
18 CONTINUE
IF(IND.NE.1) GO TO 19

LLM   NO. OF RADIAL OBSERVATION OF VELOCITY
RL AND UL ARE RADIAL LOCATION (IN.) AND CORRESPONDING AXIAL
VELOCITY (FT/SEC.)

READ(5,1) LLM
READ(5,9) (RL(I),UL(I),I=1,LLM)
19 CONTINUE
IF(IAB.NE.1) GO TO 20
IF(IAB.EQ.0) GO TO 20
DO 21  J=1,IAB
IF(J.LT.IAB) GO TO 21

LMM   NO. OF RADIAL OBSERVATION OF TEMPERATURE
RT   OBSERVATION RADIAL LOCATION  INCH
TR   OBSERVATION DIMENSIONLESS TEMP. AT RT

READ(5,1) LMM(J)
LX=LMM(J)
READ(5,4) (          RT(I,J),I=1,LX)
READ(5,4) (          TR(I,J),I=1,LX)
21 CONTINUE
20 CONTINUE
IF(IAH.NE.1) GO TO 24
DO 22 J=1,IAB

EDDY    HEAT DIFFUSIVITY *DENSITY/  INLET  VISCOSITY,  CALCULATED
```

```
      READ(5,4) (EDDY(I,J),I=1,N)
22    CONTINUE
C
C     EDDYM  IS EDDY FOR MOMENTUM TRANSPORT FORM ISOTHERMAL CORRELATION
C
      READ(5,4) (EDDYM(I),I=1,N)
24    CONTINUE
      IF(IND.NE.2) GO TO 26
C
C     UX  DIMENSIONLESS VELOCITY WRT MEAN VELOCITY AT N GRID POINTS
C
      READ(5,4) (UX(I),I=1,N)
26    CONTINUE
C
      CALL OBJECT
C
    1 FORMAT(10I5)
    2 FORMAT(9A8)
    3 FORMAT(6F13.6)
    4 FORMAT(6F12.6)
    5 FORMAT(6F12.4)
    6 FORMAT(1X,5F15.7)
    9 FORMAT(2F12.6)
   99 FORMAT(//10X,*NORMALISING VALUES OF PARAMETERS*,6F12.4)
      STOP
      END
```

```
SUBROUTINE  OBJECT

DIMENSION EEE(5)
DIMENSION S(50),          A1(50),A2(50),B1(50),B2(50),C1(50),C2(50),
1 D1(50),D2(50),Y(50),YPLUS(50),YTHOU(50),DUMB(50),RHS1(50),
2 RHS2(50)
DIMENSION U(50,2),U1(50,2),THETA(50,2),THET(50,2),TIME(50),
1 TR11(2,50),TR12(2,50),DEN(50,2),TT(50),VEL(50),UV(50,2)
DIMENSION TAU(50),USTARL(50),THETA1(50)
DIMENSION VISCT(50)
DIMENSION ROHV(50)
DIMENSION RADVEL(50)
DIMENSION DUDX(50),DTDX(50)
DIMENSION AA(50), BB(50)
DIMENSION GRR(50)
DIMENSION UU1(50)
DIMENSION TT1(50)
DIMENSION DEN1(50)
DIMENSION C11(50),C1(50)
DIMENSION  DUR(50),RRR(50)
DIMENSION          TCONT(50),CPT(50)
DIMENSION TNUSS(200),X1(200),DXX(200),TWA(200)
DIMENSION BOUVEL(50)
DIMENSION RRT(50)

COMMON/BLK1/ VISCCT,VISCA,VISCB,VISCC,VISCD,VISCE,
1TCONCT,TCONA,TCONB,TCONC,          CPCT,CPA,CPB,CPC,CPD,
2 DENSCT,DENSA,DENSB,DENSC,DENSD,
3 U,DRDOS,      RWTE,WTE,XLTM,DPDXX,WALLE,AMBE,BULKE,WELOW,
4   MM,JPRIN1,IAE,IND,IAF,LM,LLM,IAB,IAA,IAG,INN,IAH,
5 X(5), GAS(2),XL(25),WALLT(25),PL(25),UL(25),RT(25,2),TR(25,2),
6 LMM(2),XL1,XL2,M1,M2,M3,H1
COMMON/BLK3/ RADIUS,KKK,N,IAD
COMMON/BLK4/ UX(50)

COMMON/ONE/ G1(50),G2(50)
COMMON/THREE/U1,YPLUS,RR,REW,USTAR,VISCT,Y,U,UV,DEN1,TCONT,CPT
COMMON/FOUR/P,SHEARW,DEN,DENSTA,TAU
COMMON/FIVE/DENSTW
COMMON/SIX/ JKK
COMMON/SEVEN/DX,DPDX,ROHV
COMMON/EIGHT/REE,EEE
COMMON/NINE/UAVER,AMU,AMUS,PRAV
COMMON/TEN/ GRR
COMMON/ELEVEN/ EDDYM(50)
COMMON/TWEN/ EDDY(50,3)

DATA GRYGC,GC/1.0,32.17/
DATA PI,SECHR/3.14159,3600./

ARITHMATIC FUNCTION STATEMENTS FOR PHYSICAL PROPERTIES CALCULATION

VISC(Z) = VISCCT + Z*(VISCA + Z*(VISCB + Z*(VISCC + Z*(VISCD +
1  Z*VISCE))))
TCON(Z) = TCONCT + Z*(TCONA + Z*(TCONB + Z*TCONC))
CP(Z) = CPCT + Z*(CPA + Z*(CPB + Z*(CPC + Z*CPD)))
DENS(Z) = DENSCT + Z*(DENSA + Z*(DENSB + Z*(DENSC + Z*DENSD)))

ZERO OUT MATRICES
```

```
      DO 10 I=1,50
      A1(I)=0.
      A2(I)=0.
      B1(I)=0.
      B2(I)=0.
      C1(I)=0.
      C2(I)=0.
      D1(I)=0.
      D2(I)=0.
      R(I)=0.
      Y(I)=0.
      YPLUS(I)=0.
      YTWOU(I)=0.
      DUM2(I)=0.
      TINF(I)=0.
      RHS1(I)=0.
      RHS2(I)=0.
      DUDX(I)=0.
      DTDX(I)=0.
      THETA1(I)=0.
      DEN1(I)=1.
      TT(I)=0.
      VISCT(I)=0.
      C11(I)=0.
      C1(I)=0.
      ROHV(I)=0.
      RADVEL(I)=0.
      UUU(I)=0.
      GRP(I)=0.
      DO 10 J=1,2
      U(I,J)=0.
      U1(I,J)=0.
      DEN(I,J)=0.
      THETA(I,J)=0.
      THET(I,J)=0.
      UV(I,J)=0.
10    CONTINUE
      DO 11 I=1,3
      DO 11 J=1,50
      TRI1(I,J)=0.
11    TRI2(I,J)=0.
      DO 15 I=1,100
      DXX(I)=0.
15    CONTINUE

      TWALLF=WALLF
      TAMBF=AMBF
      TBULKF=BULKF
      FTIN=TBULKF
      TEMPNF=TWALLF
      TEMPN=TEMPNF+460.
      TWALL =TWALLF+460.
      TAMB=TAMBF+460.
      TBULK=TBULKF+460.
      TIN=FTIN+460.
      DENSTA=DENS(TIN)

      INLET PARAMETERS
```

```
TNORM=TEMPN-TIN
AREA=PI*RADIUS*RADIUS/144.
GFLOW=WFLOW/AREA
UAVER =GFLOW/(DENS(TIN  )*SECHR)
UAVERG=UAVER
RE=(2.*RADIUS/12.)*GFLOW/(SECHR*VISC(TIN))
CALL FFAC(RE,FFAC)
SHEARW=FFAC*DENS(TIN  )*UAVER *UAVER /(2.*GC)
TAU(N)=SHEARW
USTAR =SQRT(2HEARW*GC/DENS(TIN))
FFAX=FFAC
AMU=VISC(TIN)
AMUB=VISC(TBULK)
RWTF1=RWTF

CALCULATION OF RADIAL MESH SIZE

DRNOT=1.E-06
NMINUS=N-1
SUM=0.
SUMX=0.
DO 20  I=1,NMINUS
DUMR(I)=DRNOT*(H**I-1.)/(H-1.)
SUM=SUM+DUMR(I)
20 CONTINUE
NORMALIZING
DO 30 I=1,NMINUS
DUMR(I)=DUMR(I)/SUM
SUMX=SUMX+DUMR(I)
30 CONTINUE
CALCULATION OF RADIAL MESH LOCATION
R(1)=0.
Y(1)=1.
YTHOU(1)=RADIUS*1000.
DO 40 I=2,N
NX=N-(I-1)
R(I)=R(I-1)+DUMR(NX)
Y(I)=1.-R(I)
YTHOU(I)=Y(I)*RADIUS*1000.
40 CONTINUE

INLET TEMP. PROFILE

DO 45 I=1,N
TINF(I)=FTIN
TT(I)=FTIN
THETA(I,1)=(TINF(I)-FTIN)/TNORM
DEN(I,1)=1./(1.+TNORM*THETA(I,1)/TIN)
45 CONTINUE


DO 50 I=1,N
YPLUS(I)=Y(I)*(RADIUS/12.)*USTAR*DENS(TIN  )/VISC( TIN )
50 CONTINUE


LINEAR SHEAR STRESS DISTRIBUTION     INITIAL PROFILE
```

```
   DO 17 I=1,N
   TAU(I)=SHEARW*R(I)
17 CONTINUE

   INLET VELOCITY PROFILE

   IF(IAD.EQ.1) GO TO 31
   IF(IND-1)31,32,33

31 DO 49 I=1,N
   U(I,1)=1.
   UX(I)=U(I,1)
49 CONTINUE
   GO TO 47

32 CONTINUE
   DO 46 I=1,N
   RINCH=R(I)*RADIUS
   CALL INTERP(LLM,RL,UL,RINCH,UR)
   U(I,1)=UR/UAVER
   UX(I)=U(I,1)
46 CONTINUE
   GO TO 47

33 CONTINUE
44 DO 43 I=1,N
   U(I,1)=UX(I)
43 CONTINUE

47 CONTINUE

   INTEGRATION OF INLET VELOCITY PROFILE
   CALCULATION OF INLET HEAT CONTENTS

   VR=0.
   TVRH1=0.
   DO 38 I=1,NMINUS
   VR1= 0.5*(R(I+1)-R(I))*(U(I,1)*DEN(I,1)*R(I) + U(I+1,1)*DEN(I+1,1)
  1 *R(I+1))
   VR=VR+VR1
   T11=TT(I)+460.
   T12=TT(I+1)+460.
   TVRH1=TVRH1+0.5*(R(I+1)-R(I))*(U(I,1)*DEN(I,1)*R(I)*T11*CP(T11) +
  1 U(I+1,1)*DEN(I+1,1)*R(I+1)*T12*CP(T12))
38 CONTINUE
   GFLOW=2.*VR*UAVER*DENSTA*SECHR

   TVRH1 = 0.5 * INLET ENTHALPY PER UNIT CROSS SECTION
   TVRH1=TVRH1*UAVER*DENSTA

   OUT PUT OF RUN CONDITIONS

   WRITE(6,999)
   WRITE(6,998) (GAS(I),I=1,9)
   WRITE(6,998) TAMBE,TWALLE,WFLOW,GFLOW,UAVER ,RE,FFAC,SHEARW,USTAR
  1 ,CPROS,WTF,RWTF
   WRITE(6,997)  RADIUS,N,H
   WRITE(6,995) SUMX
   WRITE(6,992) (TINF(I),I=1,N)
```

```
      IF(IAB.EQ.0) GO TO 39
      WRITE(6,891)
      WRITE(6,890) (XL(I),I=1,LM)
      WRITE(6,890) (WALLT(I),I=1,LM)
39    CONTINUE
      IF(IAA.NE.1)  GO TO 37
      WRITE(6,897)
      DO 36 IXX=1,IAB
      IF(IXX.LT.IAG) GO TO 36
      LX=LMM(IXX)
      WRITE(6,890) (RT(I,IXX),I=1,LX)
      WRITE(6,890) (TR(I,IXX),I=1,LX)
36    CONTINUE
37    CONTINUE
      WRITE(6,894)
      WRITE(6,893) (I,R(I),Y(I),YPLUS(I),U(I,1),YTHOU(I),I=1,N)

      CALCULATE AXIAL POSITION AND MARCH IN AXIAL DIRECTION

92    CONTINUE
      IJK=0
      J=1

      IF(KKK.NE.1) GO TO 92
      M=M1
      XLL=XL1
      GO TO 93
92    M=M2
      XLL=XL2
93    CONTINUE
      CALL DELTAX(DXX,XLL,M,H1)
      IF(KKK.NE.1) M=M2

      TURBULENT PR   FROM EQN. BY  QUARMBY
      DO 80 I=1,N
      PRT(I)=1./(1. +.400.**(R(I)-1.))
80    CONTINUE

      WRITE(6,897) (PRT(I),I=1,N)
      WRITE(6,897) (EDDYM(I),I=1,N)

      START OF THE MARCHING SOLUTION

      DO 100 JKK=MM,M
      JJ=JKK+1
      DX=DXX(JKK)

      ADJUSTMENTS IN AXIAL LOCATIONS

      IF(IAB.EQ.0) GO TO 97
      IF(JKK.EQ.29)  DX=0.1
      IF(JKK.EQ.39)  DX=0.16685
      IF(JKK.EQ.44)  DX=0.203
      IF(JKK.EQ.49) DX=.191
97    CONTINUE

      X(J+1)=X(J)+DX
```

```
      XINCH=X(J+1)*RADIUS
      IF(KKK.NE.2) GO TO 54

      WALL TEMPERATURE PROFILE

      IF(IAF.EQ.0) GO TO 63
      IF(NCOUNT.NE.1) GO TO 64
      CALL INTERP(IM,XL,WALLT,XINCH,TWAA)
      TWA(JKK)=TWAA
64    CONTINUE
      TWALLF=TWA(JKK)
      GO TO 56
63    CONTINUE
      TWALLF=WALLF
      IF(JKK.EQ.1) TWALLF=(WALLF+FTIN)/2.
56    CONTINUE
      TWALL=TWALLF+460.
      THETA(N,J+1)=(TWALL-TIN)/TNORM
      DEN(N,J+1)=1./(1.+TNORM*THETA(N,J+1)/TIN)
      GO TO 59
54    TWALL=TIN
      DEN(N,J+1)=DEN(N,J)
59    CONTINUE
      TT(N)=TWALL-460.
      DENSTW=DEN(N,J+1)*DENSTA

      BOUNDARY CONDITIONS AT THE WALL
      U(N,J+1) = 0.


      KK   COUNTER FOR THE NO. OF ITERATIONS IN ANY AXIAL STEP
      K    COUNTER TO STORE TWO CONSECUTIVE ITERATIONS FOR COMPARISON

      K=1
      KK=0

55    KK=KK+1

      INITIAL ESTIMATES OF THE VALUES AT THE NEXT STEP

      IF(KK.GT.1) GO TO 51
      DO 52 I=1,N
      UV(I,1) = U(I,J) +DUDX(I)*DX
      U1(I,J)=U(I,J)    +DUDX(I)*DX*WTF
      DD1= THETA(I,J)+DTDX(I)*DX
      DEN(I,J+1) =1./(1.+TNORM*DD1/TIN)
      THETA1(I)=THETA(I,J)+DTDX(I)*DX*WTF
      TT1(I)=FTIN+TNORM*THETA1(I)
52    CONTINUE
51    CONTINUE

      CALCULATION OF THE FLOW PARAMETERS

      TFILM=TBULK
      UAVER1=UAVERG
      GFLOW=WFLOW/AREA
      UAVERG=GFLOW/(DENS(TBULK)*SECHR)
      REF=(2.*RADIUS/12.)*UAVERG*DENS(TFILM)/VISC(TFILM)
      RES=REF*VISC(TBULK)*TBULK/(VISC(TWALL)*TWALL)
```

```
FFAC=0.0014 + 0.125/(RES**0.32)
FFAC=FFAC*((TBULK/TWALL)**0.5)
IF(KKK.EQ.1) CALL FREAC(REF,FFAC)
SHEARW=FFAC*DENS(TBULK)*UAVERG*UAVERG/(2.*GC)

REW=RE/2.
PR=CP(TWALL)*VISC(TWALL)*SECHR/TCON(TWALL)
PRAV=CP(TBULK)*VISC(TBULK)*SECHR/TCON(TBULK)
DPDOSE = DPDOS
IF(KKK.NE.2) DPDOSE = 0.

DO 80 I=1,N
T=TT1(I)+460.

CALCULATION OF THE BODY FORCE TERM IN THE MOMENTUM EQUATION

GBR(I)=DPDOSE*GC*(RADIUS/12.)*(DENS(T)-DENS(TAMB))/(DENSTA*UAVER
1 *UAVER)

LOCAL PROPERTIES FOR EDDY DIFFUSIVITY EVALUATION

DEN1(I)=DENS(T)/DENSTA
VISCT(I)=VISC(T)
TCONT(I)=TCON(T)
CPT(I)=CP(T)
80 CONTINUE

CALCULATION OF THE EDDY DIFFUSIVITY

IF(IAH.EQ.1) GO TO 85
IF(KKK.EQ.1.AND.JKK.GT.1 ) GO TO 82
IF(KK.GT.1) GO TO 82
CALL G
82 CONTINUE
GO TO 87

85 CONTINUE
IF(KKK.EQ.1.AND.JKK.GT.1 ) GO TO 87
IF(KK.GT.1) GO TO 87
DO 86 I=1,N
IF(XINCH.LE.6.) GO TO 83
IF(XINCH.LE.12.) GO TO 84
IXX=2
SAVE=12.
GO TO 81
83 IXX=1
SAVE=0.
GO TO 81
84 IXX=2
SAVE=6.
81 CONTINUE

LINEAR INTERPOLATION OF THE EDDY DIFFUSIVITY PROFILE

DUMMY1 =EDDYM(I)/PRT(I)
IF(IXX.GT.1) DUMMY1 =EDDY(I,IXX-1)
DUMMY= DUMMY1 +(EDDY(I,IXX)- DUMMY1 )*(XINCH-SAVE)/6.
```

```
      G1(I)=VISCT(I)/AMU + DUMMY * PRT(I)
      G2(I)= TCONT(I)/ (CPT(I)*3600.*AMU) +  DUMMY
96    CONTINUE
97    CONTINUE

      IF(KKK.NE.2) GO TO 350

      SOLUTION OF ENERGY EQUATION

      COEFFICIENTS FOR I EQ 1
      I=1
      DR1=R(2)-R(1)
      DR2=2.*DR1
      F1=DEN(I,J)*U(I,J)/DX
      F2=2./(DR1*DR2)
      F3=2./(DR1*DR1)
      A2(1)=4.*G2(1)*F2/REW
      C2(1)= F1+2.*WTF*G2(1)*F3/REW
      B2(1)=F1-2.*(1.-WTF)*G2(1)*F3/REW

      COEFFICIENTS FOR I GT 1
      DO 200 I=2,NMINUS
      DR1=R(I+1)-R(I-1)
      DR2=R(I+1)-R(I)
      DR3=R(I)-R(I-1)
      F1=DEN(I,J)*U(I,J)/DX
      F2=2./(DR1*DR2)
      F3=2./( DR2*DR3)
      F4=2./(DR1*DR3)
      F5=1./DR1
      FG2=G2(I+1)*DR3/DR2 -G2(I-1)*DR2/DR3 +G2(I)*(DR2*DR2-DR3*DR3)
     1 /F3/2.
      A2B2= FG2*F5*F5+G2(I)*F5/R(I)
      A2(I)=(G2(I)*F2+A2B2)/REW -ROHV(I)*F5
      B2(I)=(G2(I)*F4-A2B2)/REW +ROHV(I)*F5
      C2(I)=F1+G2(I)*(F3*WTF     )/REW
      D2(I)=F1-G2(I)*(F3*(1.-WTF)     )/REW
200   CONTINUE

      TRIDIAGONAL MATRIX INVERSION FOR ENERGY EQUATION

      DO 300 I=2,NMINUS
      TRI2(2,I-1)=-1.
      IF(I.EQ.2) TRI2(2,1) = TRI2(2,1)+A2(1)*B2(2)*WTF*WTF/(C2(1)*C2(2))
      IF(I.EQ.2) GO TO 301
      TRI2(1,I-1)=WTF*B2(I)/C2(I)
      IF(I.EQ.NMINUS) GO TO 302
301   TRI2(3,I-1)=WTF*A2(I)/C2(I)
302   RHS2(I-1)=-((1.-WTF)*(A2(I)*THETA(I+1,J)+B2(I)*THETA(I-1,J))
     1 +D2(I)*THETA(I,J)        )/C2(I)
      IF(I.EQ.2) RHS2(1)=RHS2(1)-(B2(2)*WTF/(C2(1)*C2(2)))*((1.-WTF)*
     1 A2(1)*THETA(2,J)+D2(1)*THETA(1,J)        )
      IF(I.EQ.NMINUS) RHS2(I-1)=RHS2(I-1)-A2(I)*WTF*THETA(I+1,J+1)/C2(I)
300   CONTINUE
      NN=NMINUS-1

      CALL RNDSOL (TRI2,RHS2,3,1,NN)

      DO 400 I=2,NMINUS
```

```
      THETA(I,J+1)=RHS2(I-1)
   20 CONTINUE
      THET(1,J+1)=(WTF*A2(1)*THETA(2,J+1)+(1.-WTF)*A2(1)*THETA(2,J)
     1 +B2(1)*THETA(1,J))/C2(1)
      DO 422 I=1,N
      THET(I,K)=THETA(I,J+1)
   22 CONTINUE
      IF(K.EQ.1) GO TO 402
      DO 421 I=1,N
      THETA(I,J+1)=THET(I,K-1) + RWTF*(THET(I,K)-THET(I,K-1))
   21 CONTINUE
   42 CONTINUE

      CALCULATION OF TEMP.     AT J+ALPHA

      DO 430 I=1,N
      DTDX(I)=(THETA(I,J+1)-THETA(I,J))/DX
      THETA1(I)=WTF*THETA(I,J+1) + (1.-WTF)*THETA(I,J)
      TT1(I)=TTIN+TNORM*THETA1(I)
      DEN1(I)    =1./(1.+(TNORM*THETA1(I))/TIN)
      DEN(I,J+1)=1./(1.+(TNORM*THETA(I,J+1)))/TIN)
   30 CONTINUE
      IF(KKK.EQ.2) GO TO 380

      IF THE ENERGY EQUATION IS TO BE BY-PASSED

   50 DO 370 I=1,N
      DEN(I,J)=1.
      DEN(I,J+1)=1.
      DEN1(I)=1.
      THETA(I,J)=0.
      THETA(I,J+1)=0.
      THET(I,K)=0.
      THETA1(I)=0.
   70 CONTINUE
   80 CONTINUE
      IF(INN.NE.0) GO TO 395

      IF ONLY ENERGY EQUATION IS TO BE SOLVED

      DO 397 I=1,N
      U(I,J+1)=U(I,J)*UAVERG/UAVER1
      UV(I,1)=U(I,J+1)
      UV(I,2)=UV(I,1)
      THET(I,2)=THET(I,1)
   97 CONTINUE
      K=2
      GO TO 535
  395 CONTINUE

      SOLUTION OF INTEGRAL MASS CONSERVATION EQUATION

      IF(K.EQ.1) GO TO 500
      DO 432 I=1,NMINUS
      F1=DEN(I,J)*U(I,J)/DX
      IF(I.EQ.1)  GO TO 429
      Q1(I)=(                    (A1(I)*U1(I+1,J)+B1(I)*U1(I-1,J))-C11(I)*
     1 U1(I,J)          +GRR(I)                                    )/F1
      IF(I.EQ.NMINUS) Q2=F1*Q1(I)
```

```
GO TO 432
U(I)=(                    A1(I)*U1(I+1,J)                    -C11(I)*U1(I,J)
     +GR2(I)                                    )/F1
CONTINUE

Q=FLOW/(2.*DENSTA*UAVER*SECHR)
UR1=0.
UR2=0.
UR3=0.

DO 431 I=1,NMINUS
F1=DEN(I,J)*U(I,J)/DX
F11=DEN(I+1,J)*U(I+1,J)/DX
UR2=UR2+(R(I+1)-R(I))*(DEN(I,J+1)*R(I)*U(I,J)+DEN(I+1,J+1)*R(I+1)
1 *U(I+1,J))/2.
IF(I.EQ.NMINUS) GO TO 432
UR1=UR1+(R(I+1)-R(I))*(DEN(I,J+1)*Q1(I)*R(I)+DEN(I+1,J+1)*
1 Q1(I+1)*R(I+1))/2.
UR3=UR3+(R(I+1)-R(I))*(DEN(I,J+1)*R(I)/F1 + DEN(I+1,J+1)*R(I+1)
1 /F11)/(2.*DX)
GO TO 431
CONTINUE

UR1=UR1+(R(I+1)-R(I))*DEN(I,J+1)*R(I)*Q2*2./F1
UR3=UR3+(R(I+1)-R(I))* DEN(I,J+1)*R(I)*2./(DX*F1)
CONTINUE

DP=(Q-UR1-UR3)/UR2
DPDX1=DP/DX
DPDX = DPDX1
CONTINUE

SOLUTION OF MOMENTUM EQUATION

COEFFICIENTS FOR I EQ 1
I=1
DR1=R(2)-R(1)
DR2=2.*DR1
F1=DEN(1,J)*U(I,J)/DX
F2=2./(DR1*DR2)
F3=2./(DR1*DR1)
A1(1)=4.*G1(1)*F2/REW
C11(1) =2.*G1(1)*F3/REW
C1(1) =F1 + WTF*C11(1)
B1(1) = F1-(1.-WTF)*C11(1)

CALL RADV(R,DEN,U,UV,N,DX,ROHV)

COEFFICIENTS FOR I GT 1
DO 520 I=2,NMINUS
DR1=R(I+1)-R(I-1)
DR2=R(I+1)-R(I)
DR3=R(I)-R(I-1)
F1=DEN(I,J)*U(I,J)/DX
F2=2./(DR1*DR2)
F3=2./( DR2*DR3)
F4=2./(DR1*DR3)
F5=1./DR1
FG1=G1(I+1)*DR3/DR2 -G1(I-1)*DR2/DR3 +G1(I)*(DR2*DR2-DR3*DR3)
```

```
1 *F3/2.
  A1B1=FG1*F5*F5+ G1(I)*F5/R(I)
  A1(I)=(G1(I)*F2+A1B1)/REW -ROHV(I)*F5
  B1(I)=(G1(I)*F4-A1B1)/REW +ROHV(I)*F5
  C1D1=G1(I)*F3/REW
  C1(I)=C1D1
  C1(I) = F1 + WTF*C1D1
  D1(I) = F1-(1.-WTF)*C1D1
0 CONTINUE

  TRIDIAGONAL MATRIX INVERSION FOR MOMENTUM EQUATION

  DO 530 I=2,NMINUS
  TRI1(2,I-1)=-1.
  IF(I.EQ.2) TRI1(2,1) = TRI1(2,1)+A1(1)*B1(2)*WTF*WTF/(C1(1)*C1(2))
  IF(I.EQ.2) GO TO 521
  TRI1(1,I-1)=WTF*B1(I)/C1(I)
  IF(I.EQ.NMINUS) GO TO 522
1 TRI1(3,I-1)=WTF*A1(I)/C1(I)
2 RHS1(I-1)=-((1.-WTF)*(A1(I)*U(I+1,J)+B1(I)*U(I-1,J))+D1(I)*U(I,J)
1 +DPDX          +GRR(I)                                  )/C1(I)
  IF(I.EQ.2) RHS1(1)=RHS1(1)-(B1(2)*WTF/(C1(1)*C1(2)))*( (1.-WTF)*
1 A1(1)*U(2,J)+D1(1)*U(1,J)+DPDX          +GRR(1)                    )
  IF(I.EQ.NMINUS) RHS1(I-1)=RHS1(I-1)-A1(I)*U(I+1,J+1)*WTF/C1(I)
0 CONTINUE

  NN=N-2
  CALL BNDSOL(TRI1,RHS1,3,1,NN)

  DO 540 I=2,NMINUS
  U(I,J+1)=RHS1(I-1)
0 CONTINUE
  U(1,J+1)=(WTF*A1(1)*U(2,J+1)+(1.-WTF)*A1(1)*U(2,J)+D1(1)*U(1,J)
1 +DPDX          +GRR(1)                                  )/C1(1)
  DO 425 I=1,N
  UV(I,K)=U(I,J+1)
5 CONTINUE
5 CONTINUE
  IF(K.EQ.1) GO TO 542
  DO 541 I=1,N
  U(I,J+1)=UV(I,K-1) + RWTF*(UV(I,K)-UV(I,K-1))
1 CONTINUE
2 CONTINUE
5 CONTINUE

  CALL RADV(R,DEN,U,UV,N,DX,ROHV)
  DO 601 I=1,N
  DUDX(I)= (U(I,J+1)-U(I,J))/DX
  TT(I)=FTIN+TNORM*THETA(I,J+1)
  VEL(I)=UAVER*U(I,J+1)
  UUU(I)=VEL(I)/USTAR
  RADVEL(I)=ROHV(I)/DEN1(I)

  ROHVEL - RADIAL VEL. AND DENSITY PRODUCT  LB/(FT FT SEC)
  ROHVEL(I)=ROHV(I)*DENSTA*UAVER
1 CONTINUE

  CALCULATION OF THE BULK TEMPERATURE
```

```
      TVR=0.
      VR=0.
      DO 610 I=1,NMINUS
      T=TT(I)+460.
      T1=TT(I+1)+460.
      TVR=TVR+(R(I+1)-R(I))*(VEL(I)*DENS(T)*R(I)*T+VEL(I+1)*DENS(T1)
     1 *R(I+1)*T1)/2.
      VR = VR+(R(I+1)-R(I))*(VEL(I)*DENS(T)*R(I)+VEL(I+1)*DENS(T1)*
     1 R(I+1))/2.
610   CONTINUE

      TBULK=TVR/VR
      TBULK=TBULK-460.
      AMUR=VISC(TBULK)
411   CONTINUE

      IF(K.NE.1) GO TO 410
      GO TO 455
410   JPP=0
      IF(KKK.NE.2) GO TO 415

      TEST OF CONVERGENCE

      DO 450 I=1,NMINUS
      IF(ABS((THET(I,K)-THET(I,K-1))/THET(I,K)).GT.1.E-04) JPP=1
450   CONTINUE
415   CONTINUE
      DO 460 I=1,NMINUS
      IF(ABS((UV(I,K)-UV(I,K-1))/UV(I,K)).GT.1.E-04) JPP=1
460   CONTINUE
      IF(KK.GE.100) JPP=0
      IF(JPP.LT.1) GO TO 600

      CALCULATION OF VELOCITY AT J+ALPHA

55    DO 550 I=1,N
      VS=(1.-WTF)*U(I,J)
      U1(I,J) = WTF*U(I,J+1) + VS
550   CONTINUE
      IF(K.NE.1) GO TO 560
      K=2
      GO TO 55
560   DO 570 I=1,N
      THET(I,K-1)=THETA(I,J+1)
      UV(I,K-1)=U(I,J+1)
570   CONTINUE
      GO TO 55

600   CONTINUE

      CALL SHEAR

      CALCULATION OF NUSSELT,STANTON NUMBERS,HEAT FLUX AND AVERAGE
      PROPERTIES

      TNUSSL=0.
      FLUX=0.
      TVRH=0.
```

```
      IF(KKK.EQ.1) GO TO 640
      DO 630 I=1,NMINUS
      T=TT(I)+460.
      T1=TT(I+1)+460.
      TVRH=TVRH+(R(I+1)-R(I))*(VEL(I)*DENS(T)*CP(T)*T*R(I) +
     1 VEL(I+1)*DENS(T1)*CP(T1)*T1*R(I+1))/2.
630   CONTINUE
      IF(JKK.EQ.1) HTVR=0.
      HTVR  TOTAL ENTHALPY TRANSFERED  UPTO THIS AXIAL LOCATION PER UNIT
      CROSS SECTION
      HTVR=HTVR + 2.*(TVRH-TVRH1)
      FLUX =(TVRH-TVRH1)/DX
      FLUX  HEAT TRANSFER PER UNIT CIRCUMFERENCIAL AREA
      TNUSSL=FLUX*(2.*RADIUS/12.)/((TWALL-TBULK)*TCON(TBULK)/SECHR)
      TNUSS(JJ)=TNUSSL
      CALL NUSS(R,TT,N,GRADW)
      GNUSSL=2.*GRADW*TCON(TWALL)/(TCON(TBULK)*(TWALL-TBULK))
640   CONTINUE
      TVRH1=TVRH
      FLOW=AREA*(2.*VO)*SECHR
      VISCAV=VISC(TBULK)
      DENSAV=DENS(TBULK)
      ST=TNUSSL/(REE*PRAV)

      AXIAL LOCATION IN DIAMETERS
      XX=X(J+1)/2.
      X1(JJ)=XX


      PRINTING OF THE OUT PUT

      IF(JKK.EQ.1.OR.JKK.EQ.M) GO TO 614
      IF(KKK.EQ.1.AND.JKK.LT. M) GO TO 619
      IF(IAF.EQ.1) GO TO 619
      IF(JKK.EQ.29.OR.JKK.EQ.38.OR.JKK.EQ.44) GO TO 614
616   CONTINUE
      IJK=IJK+1
      IF(IJK.NE.JPRIN1) GO TO 619
      IJK=0
614   CONTINUE

      WRITE(6,899) JJ,XX,XJNCH,KK,DX
      WRITE(6,898)  SHEARW,USTAR,TNUSSL,FLOW,TBULK,DPDX,PRAV,UAVERG,
     1 REE,ST,HTVR,EFAC,GNUSSL,RES
      WRITE(6,896)
      WRITE(6,897) (TT(I),I=1,N)
      WRITE(6,892)
      WRITE(6,897) (VEL(I),I=1,N)
      WRITE(6,894)
      WRITE(6,897) (TAM(I),I=1,N)
      WRITE(6,869)
      WRITE(6,897) (YPLUS(I),I=1,N)
      WRITE(6,871)
      WRITE(6,897)(G1(I),I=1,N)
      WRITE(6,863)
      WRITE(6,897) (G2(I),I=1,N)

      WRITE(6,897) (RADVEL(I),I=1,N)
```

```
      IF(KKK.NE.1) GO TO 617
      WRITE(6,870)
      WRITE(6,897) (UUU(I),I=1,N)
      WRITE(7,864) (U(I,J+1),I=1,N)
617   CONTINUE
      IF(JKK.EQ.29.OR.JKK.EQ.38.OR.JKK.EQ.44) GO TO 612
      GO TO 619
612   CONTINUE
      WRITE(7,864) TRULKE,TT(N)
      WRITE(7,864) (U(I,J+1),I=1,N)
      WRITE(7,864) (RADVEL(I),I=1,N)
      WRITE(7,864) (TT(I),I=1,N)

      COMPARISON OF THE OBSERVED AND THE PREDICTED TEMPERATURE PROFILES

      SUM1=0.
      IF(IAA.NE.1) GO TO 613
      IF(KKK.NE.2) GO TO 613
      IF(JKK.EQ.29) IX=0
      IX=IX+1
      IF(IX.LT.IAG) GO TO 613
      LX=LMM(IX)
      DO 618 I=1,LX
      RTR=RT(I,IX)/RADIUS
      CALL INTERP(N,R,TT,RTR,TR1)
      RESIDUALS ARE DIFFERENCE BETWEEN OBSERVED AND PREDICTED
      TRE=TTIN+ TNORM*TR(I,IX)
      RESD=(TRE-TR1)/TNORM
      SUM1=SUM1 + RESD*RESD/LX
      CALL PLOTPT(RTR,RESD,10)
618   CONTINUE
      CALL SCALE(.8,1.,-.25,.25)
      CALL OUTPLT
      WRITE(6,865) SUM1
      WRITE(6,862)
613   CONTINUE
619   CONTINUE

      MOVING TO NEXT STEP

      DO 620 I=1,N
      U(I,J)=U(I,J+1)
      DEN(I,J)=DEN(I,J+1)
      THETA(I,J)=THETA(I,J+1)

      X(J)=X(J+1)
620   CONTINUE

      IF(IAD.EQ.1) RETURN
      IF(KKK.NE.2) GO TO 110
      RETURN

110   KKK=2
      X(1)=0.
      DO 111 I=1,N
      UX(I)=U(I,J+1)
111   CONTINUE
      GO TO 90
```

```
1 FORMAT(5I5)
2 FORMAT(9A8)
4 FORMAT(6F12.8)
5 FORMAT(8F9.5)
6 FORMAT(1X,5E15.7)
7 FORMAT(F1[illegible].5,2I5)
8 FORMAT(8F9.6)
9 FORMAT(2F12.5)
10 FORMAT(1H0/50X,18(1H*)/50X,18H* RUN CONDITIONS *,/50X,18(1H*)///)
[illegible] FORMAT(          5X,14HAMBIENT TEMP.=,F6.2,2H F,10X,11HWALL TEMP.=
 2 F6.1,2H F,10X,10HFLOW RATE=,F6.1,6H LB/HR,10X,10HMASS VEL.=,
 3 F1[illegible].5,13H LB/(SQFT-HR)//5X,13HAVERAGE VEL.=,F10.5,7H FT/SEC,2X,
 4 13HREYNOLDS NO.=,F10.2,5X,16HFRICTION FACTOR=,F10.6,6X,11HWALL SH
 5EAR=,F10.7,8H LB/SQFT,//5X,6HUSTAR=,F10.6,5X,*BUOYANCY=*,F6.2,
 6 5X,*CRANK-NICHOLSON WTF=*,F5.2,5X,*RELAXATION WTF=*,F5.2,/)
[illegible] FORMAT(5X,*RADIUS=*,F6.2,5X,*RADIAL MESH POINTS=*,I5,5X,*H=*,F6.2,
 1/)
[illegible] FORMAT(5X,43HSUMX= TOTAL OF NORMALIZED RADIAL POSITIONS=,F10.2)
[illegible] FORMAT(1H1,///,30X,1HI,6X,1HR,13X,1HY,11X,2HY+,12X,2HU+,10X,
 1 12HY(INCH*E-03)//)
[illegible] FORMAT(20X,I11,F12.8,F13.7,2F14.4,F15.2)
[illegible] FORMAT(//50X,26HRADIAL TEMPERATURE PROFILE,//,5(20X,10F8.2,/))
[illegible] FORMAT(//50X,26H AXIAL TEMPERATURE PROFILE,/)
[illegible] FORMAT(/,10X,15F7.2,5X,5HXINCH)
[illegible] FORMAT(/,10X,15F7.2, 5X,8HDEGREE F)
[illegible] FORMAT(//,40X,9A8,//)
[illegible] FORMAT(//50X,*PORT RADIAL TEMP. PROFILE*,/)
[illegible] FORMAT(1H1,5X,11HAXIAL POS*N,I5,5X,3HX/D,F11.4,5X,8HX (INCH),F11.4
 1,5X,17HNO OF ITERATIONS=,I5,5X,16HAXIAL STEP SIZE=,E11.3,
 2 7H*RADIUS,/)
[illegible] FORMAT(5X,*SHEARW =*,F11.4,5X,*USTAR =*,F7.4,5X,*NUSS NO. =*,F10.5
 1,5X,*MASS FLOW =*,F10.5,*LB/HR*,5X,*BULK TEMP.=*,F8.2,* F*,
 2//5X,*DDDX =*,F8.6,5X,*PRAV =*,F8.2,5X,*AVERAGE VELOCITY =*,F8.3,*
 3 FT/SEC*,  5X,*REYNOLDS NO.=*,E10.4,5X,*STANTON NO.=*,F10.4,//5X,
 4 * ENTHALPY =*,F10.5,*BTU/(SQFT-SEC)*,5X,*FRICTION FACTOR=*,
 5 F10.6,5X,* GNUSS NO.*,F10.4,5X,*MOD. REY. NO.*,F10.4)
[illegible] FORMAT(10X,10F11.6)
[illegible] FORMAT(1H0, 50X,24HTEMPERATURES IN DEGREE F,/                )
[illegible] FORMAT(1H0,  50X,26HDIMENSIONLESS TEMPERATURES,/              )
[illegible] FORMAT(1H0,50X, *SHEAR STRESS*,/)
[illegible] FORMAT(1H0,50X,20HVELOCITIES IN FT/SEC,/                      )
[illegible] FORMAT(/,60X,2HG1,/)
[illegible] FORMAT(/,60X, *UPLUS*,/)
[illegible] FORMAT(/,57X,5HYPLUS,/)
[illegible] FORMAT(1H1,//,5X,1HI,7X,3HX/D,12X,9HNUSSL NO.,//)
[illegible] FORMAT(4X,I3,4X,F10.4,10X,F10.4)
[illegible] FORMAT( /,50X,12HSHEAR STRESS,/)
[illegible] FORMAT( 10X,*OBJECTIVE FUNCTION=*,E15.8)
[illegible] FORMAT(6F12.6)
[illegible] FORMAT(/,60X,*G2*/)
[illegible] FORMAT(10X,*CO ORDINATES   Y  DIFF. OF OBS. AND PREDICTED NORMALIS
 1ED BY WALL AND INLET TEMP. DIFF.   X  R/RADIUS*)
  END
```

```
      SUBROUTINE FRFAC(RF,FFAC)

      EVALUATE ADIABATIC K-N FRICTION FACTOR

      DATA FRS, FTRY / 0.00003, 0.007 /
      IF(RF.LE.2100.) GO TO 3000
      FLHS = 1.0/SQRT(FTRY)
1000  FRHS = 4.0*ALOG10(RF/FLHS) - 0.40
      IF(ABS((FRHS - FLHS)/FRHS).LT.FRS) GO TO 1000
      FLHS = FRHS
      GO TO 2000
2000  FFAC = 1.0/(FRHS*FRHS)
      GO TO 4000
3000  FFAC=16./RF
4000  CONTINUE
      RETURN
      END
```

```
SUBROUTINE  DELTAX(DUMR,XL,NMINUS,H)

THIS SUBROUTINE DETERMINES THE AXIAL STEP SIZE

XL IS AXIAL LENGTH IN RADII  NMINUS IS NO. OF AXIAL STEPS
H IS A CONSTANT    DR IS ANY SMALL NUMBER

DIMENSION DUMR(1)
DR= 1.0E-06
SUM=0.
DO 20 I=1,NMINUS
DUMR(I)= DR*(H**I-1.)/(H-1.)
SUM= SUM + DUMR(I)
20 CONTINUE
DO 30 I=1,NMINUS
DUMR(I)= DUMR(I) * XL / SUM
30 CONTINUE
RETURN
END
```

```
SUBROUTINE INTG(JK,X,Y,A,B,SUM)

THE VALUE OF THE INTEGRAL BY GAUSS LEGENDRE METHOD IS GIVEN BY
 (B-A)/2.*SUMMATION OF (H(I)*YLAMDA(I))
IT REQUIRES  INTERP FOR INTERPOLATION

DIMENSION H(20),ALAMDA(20)
DIMENSION X(1),Y(1)

DATA ALAMDA/-.9739066,-.8650634,-.6794096,-.4333954,-.14887434,
1 .14887434,.4333954,.6794096,.8650634,.9739066,0.,0.,0.,0.,0.,0.,
2 0.,0.,0.,0./
DATA H/.06667134,.14945134,.2190864,.2692668,.2955242,.2955242,
1 .2692668,.2190864,.14945134,.06667134,0.,0.,0.,0.,0.,0.,0.,0.,
2 0.,0./
NN=10

CALCULATION OF THE INDEPENDENT VARIABLE AT THE SPECIFIED
 VALUES OF ALAMDA

  SUM1=0.0
50 DO 51 I=1,NN
     X1=.5*((B-A)*ALAMDA(I)+A+B)
  CALL INTERP(JK,X,Y,X1,YLAMDA)

  SUM1=SUM1+H(I)*YLAMDA
51 CONTINUE
  SUM=(B-A)/2.*SUM1
  RETURN
  END
```

```
SUBROUTINE INTERP(JK,X,Y,XA,YA)

THIS SUBROUTINE INTERPOLATES A GIVEN SET OF DATA USING LAGRANGIAN
INTERPOLATION POLYNOMIALS.

THE DATA SHOULD BE ARRANGED IN THE ASCENDING ORDER OF THE INDEPEND
ENT VARIABLE,X.  A SET OF SIX DATA POINTS AROUND THE POINT TO BE
INTERPOLATED IS USED FOR INTERPOLATION

DIMENSION X(1),Y(1)
*

      IF(XA.LE.X(1)) GO TO 813
      IF(XA.GE.X(JK)) GO TO 811
      YA=0.0
      IF((X(1)-X(2)).GT.0.0) GO TO 804
      DO 805 II=1,JK
      IF((XA-X(II)).LE.0.0) GO TO 806
    5 CONTINUE
    4 DO 809 II=1,JK
      IF((X(II)-XA).LE.0.0) GO TO 806
    9 CONTINUE
    6 IF(II.LE.3) GO TO 807
      IF(II.GE.(JK-2)) GO TO 808
      MM=II-3
      MMM=II+2
      GO TO 810
    7 MM=1
      MMM=6
      GO TO 810
    8 MM=JK-5
      MMM=JK
   10 DO 801 I=MM,MMM
      PROD=Y(I)
      DO 800 J=MM,MMM
      IF(J.EQ.I) GO TO 800
      PROD=PROD*(XA-X(J))/(X(I)-X(J))
    0 CONTINUE
    1 YA=YA+PROD
      GO TO 812
   13 YA=Y(1)
      GO TO 812
   11 YA = Y(JK)
   12 RETURN
      END
```

```
SUBROUTINE NUSS(XX,YY,NN,GRADW)

THIS ROUTINE EVALUATES THE TEMPERATURE GRADIENT AT THE WALL BY
PERFORMING A LINEAR LEAST SQUARES FIT OVER THE MESH POINTS WHICH
ARE ADJACENT TO THE WALL.......THE NUMBER OF POINTS TAKEN DEPENDS
UPON THE NO. OF RADIAL MESH POINTS USED .

DIMENSION X(35),Y(35)
DIMENSION XX(1),YY(1)
N=12
N=5
DO 50 I=1,N
L = NN + 1 - I
Y(I) = YY(L)
50 X(I)=XX(L)
SUMX = 0.0
SUMY = 0.0
SUMX2 = 0.0
SUMY2 = 0.0
SUMXY = 0.0
DO 100 I=1,N
SUMX = SUMX + X(I)
SUMY = SUMY + Y(I)
SUMX2 = SUMX2 + X(I)*X(I)
SUMY2 = SUMY2 + Y(I)*Y(I)
100 SUMXY = SUMXY + X(I)*Y(I)
DATA = N
XP2 = SUMX2 - SUMX*SUMX/DATA
YP2 = SUMY2 - SUMY*SUMY/DATA
XYP = SUMXY - SUMX*SUMY/DATA
XAV = SUMX/DATA
YAV = SUMY/DATA
SLOPE = XYP/XP2
GRADW = SLOPE
RETURN
END
```

```
      SUBROUTINE RADV (R,DEN,U,UV,N,DX,ROHV)

      SUBROUTINE FOR THE CALN. OF RADIAL MASS VELOCITY
      BY MASS BALANCE OVER A CONTROL VOLUME.
      THE PRODUCT (DEN)*(U)  IS AVERAGED OVER THE RADIAL STEP I AND I+1

      DIMENSION U(50,2),UV(50,2),DEN(50,2), ROHV(50),R(50)
      J=1
      NMINUS=N-1
      PAI=3.14159
      DO 10 I=1,50
      ROHV(I)=0.
   10 CONTINUE
      DO 30 IJ=2,NMINUS
      I=N-(IJ-1)
      AREA1=2.*PAI*DX*R(I)
      AREA2=2.*PAI*DX*R(I+1)
      AREA3=PAI*(R(I+1)**2-R(I)**2)
      ROHV(I)=-AREA3*(U(I,J)*DEN(I,J)+U(I+1,J)*DEN(I+1,J)
     1 -UV(I,1)*DEN(I,J+1)-UV(I+1,1)*DEN(I+1,J+1))/(2.*AREA1)
     2 +AREA2*ROHV(I+1)/AREA1
   30 CONTINUE
      RETURN
      END
```

```
SUBROUTINE SHEAR

EVALUATES THE RADIAL PROFILE OF THE SHEAR STRESS.
INTEGRATION OF MOMENTUM CONSERVATION EQUATION IS PERFORMED.

DIMENSION R(50),DEN(50,2),ROHR(50),TAU(50)
DIMENSION Q(50),ROHV(50)
DIMENSION U1(50,2),YPLUS(50),VISCT(50),Y(50),U(50,2),UV(50,2)
DIMENSION DEN1(50),TCONT(50),CPT(50)
DIMENSION GRR(50)
COMMON/THREE/U1,YPLUS,PR,REW,USTAR,VISCT,Y,U,UV,DEN1,TCONT,CPT
COMMON/FOUR/R,SHEARW,DEN,DENSTA,TAU
COMMON/FIVE/DENSTW
COMMON/SIX/ JKK
COMMON/SEVEN/DX,DPDX,ROHV
COMMON/NINE/UAVER,AMU,AMUB,PRAV
COMMON/TEN/ GRR
COMMON/BLK2/ RADIUS,KKK,N,IAD
NMINUS=N-1
TAU(1)=0.
ROHR(1)=0.
Q(1)=0.
DO 50 I=2,N
A=DEN1(I)*U1(I,1)*(UV(I,1)-U(I,1))/DX
IF(I.NE.N) GO TO 20
B=ROHV(I)*(U1(N,1)-U1(N-1,1))/(R(N)-R(N-1))
GO TO 30
20 CONTINUE
B=ROHV(I)*(U1(I+1,1)-U1(I-1,1))/(R(I+1)-R(I-1))
30 CONTINUE
Q(I)=R(I)*(-A-B+GRR(I))
ROHR(I)=ROHR(I-1)+(R(I)-R(I-1))*(Q(I)+Q(I-1))/2.
50 CONTINUE
DO 100 I=2,N
ROHR(I)=ROHR(I)+DPDX*R(I)*R(I)/2.
TAU(I)=ROHR(I)*DENSTA*UAVER*UAVER/(32.17*R(I))
100 CONTINUE
RETURN
END
```

```
SUBROUTINE G

EDDY DIFFUSIVITY CORELATION  OF REICHARDT MODIFIED BY TRAVIS,BUHR
AND SESONKE
LOCAL PROPERTIES ARE USED
A SUBROUTINE FNCTN IS REQUIRED FOR EVALUATION OF VARIOUS CONSTANTS
THE OUT PUT OF THIS SUBROUTINE ARE G1 AND G2 CORRESPOND TO  GM AND
GH IN EQUATION  3-10 IN CHAPTER 3

DIMENSION U1(50,2),YPLUS(50),Y(50),VISCT(50)
DIMENSION DEN1(50),TCONT(50),CPT(50)
DIMENSION U(50,2),UV(50,2)
DIMENSION R(50), DEN(50,2),TAU(50)
DIMENSION FFF(5).
DIMENSION EDDYX(50)
COMMON/ONE/ G1(50),G2(50)
COMMON/THREE/U1,YPLUS,PR,REW,USTAR,VISCT,Y,U,UV,DEN1,TCONT,CPT
COMMON/FOUR/R,SHEARW,DEN,DENSTA,TAU
COMMON/FIVE/DENSTW
COMMON/EIGHT/REF,FFF
COMMON/NINE/UAVER,AMU,AMUB,PRAV
COMMON/BLK3/ RADIUS,KKK,N,IAD
NMINUS=N-1
TPR=1.
REFFT=RADIUS/12.
CALL FNCTN(REF,FFF)
YLIM=FFF(1)
YL  =FFF(2)
F   =FFF(3)
A   =FFF(4)
CK  =FFF(5)
C =CK/100.
DO 50 I=1,N
YPLUS(I)=Y(I)*REFFT          *SQRT(ABS(SHEARW)*32.17*DEN1(I)*DENSTA)/
1 VISCT(I)
50 CONTINUE
DO 100 I=1,N
IF(YPLUS(I).LE.YL) GO TO 60
FR=F*R(I)
RESTAR=(2.*RADIUS/12.)*SQRT(SHEARW*32.17*DEN1(I)*DENSTA)/VISCT(I)
EPSLN2=     C*(RESTAR/2.)*(1.-FR*FR)*(2./3.+2.*FR*FR)/6.
EDDYX(I)=EPSLN2*VISCT(I)/AMU
GO TO 80
60 CONTINUE
EPSLN1=C*(YPLUS(I)-A*TANH(YPLUS(I)/A))
EDDYX(I)=EPSLN1*VISCT(I)/AMU
80 CONTINUE
G1(I)=VISCT(I)/AMU + EDDYX(I)
G2(I)= TCONT(I)/(CPT(I)*3600.*AMU) + EDDYX(I)/TPR
100 CONTINUE
RETURN
END
```

```
      SUBROUTINE FNCTN(RE,FUNCTN)

      THIS SUBROUTINE EVALUATES CONSTANTS REQUIRED BY SUBROUTINE G FOR
      CALCULATION OF MOMENTUM EDDY DIFFUSIVITY BY REICHARDT AND MODIFIED
      BY TRAVIS ET AL.

      DIMENSION ALPHA(5,4),AA(5,4),A(5,4,3)
      DIMENSION FUNCTN(1)
      DATA ALPHA/ 3.35,3.602,3.602,3.602,3.602,3.677,3.888,3.931,3.35,
     1 4.643,4.334,5.805,4.421,4.787,4.767,6.7,6.7,5.122,5.384,6.7/
      DATA AA/ .619,24.91,1.123,19.77,52.34,.7473,22.68,1.040,15.52,49.,
     1 .8009,25.6,1.015,12.84,49.14,.8009,25.6,1.004,14.87,49.140/
      DATA A/ 1.46,-12.58,-.2755,-19.19, -7.276,.1106,-4.791,-.123,
     1 -7.533,.728,.0495,5.546,-.0334,-.046,1.472,.0495,5.546,-.0066,
     2 3.031,1.472,-5.878,22.78,.6173,26.91,4.034,-.0766,4.489,.1501,
     3 4.565,3.652,-.004,.903,.0329,2.387,2.375,-.004,.903,.0049,.417,
     4 2.375,9.537,-21.35,-.4733,-10.47,-.123,.0319,-.6235,-.0798,-1.655,
     5,-3.447,-.0008,-1.851,-.0132,-.508,-.045,-.0008,-1.851,-.0013,
     6 -1.116,-.6450/
      RFL=ALOG10(RE)
      IF(RFL.GT.6.7) GO TO 80
      DO 50 I=1,5
      IJ=0
      DO 10 J=1,4
      IF(IJ.EQ.1) GO TO 10
      IF(RFL.LE.ALPHA(I,J)) GO TO 5
      IF(J.EQ.4) JJ=4
      GO TO 10
    5 IJ=1
      JJ=J-1
   10 CONTINUE
      SUM=0.
      DO 20 K=1,3
      SUM=SUM+ A(I,JJ,K)*(RFL-ALPHA(I,JJ))**K
   20 CONTINUE
      FUNCTN(I)=AA(I,JJ) + SUM
   50 CONTINUE
      RETURN
   80 WRITE(6,90)
   90 FORMAT(//10X,*REYNOLDS NUMBER ABOVE THE RANGE OF FCN.*)
      STOP
      END
```

```
1    4    0    0    0    1    1    1
.884770E-04  .283300E-07 -.131570E-10  .445360E-14 -.639620E-18 0.
.884770E-03  .327780E-04 -.843080E-08  .131900E-11
.246890E 00 -.355540E-04  .494760E-07 -.120470E-10
.272890E 00 -.414020E-03  .396570E-06 -.181480E-09  .319250E-13
60    1
6

4.027     0.          0.75        0.75
1.05      1.05
100.      100.
99    99    48
3.    2     0
420.      77.         77.         576.
  APRIL 28 1973       576 LB/HR   420 F 77 F
15
4.027     4.017       4.007       3.997       3.987       3.977
3.967     3.917       3.817       3.717       3.517       3.017
2.017     1.017       0.
1.        .8851       .7623       .6613       .5862       .5189
.4698     .3019       .1444       .08952      .024        .0023
0.        0.          0.
16
4.027     4.017       4.007       3.997       3.987       3.977
3.967     3.917       3.817       3.717       3.517       3.017
2.017     1.017       0.
1.        .885        .7831       .7074       .6303       .5694
.5204     .33         .2412       .1751       .08967      .01165
0.        0.          0.
15
4.027     4.017       4.007       3.997       3.987       3.977
3.967     3.917       3.817       3.717       3.517       3.017
2.017     1.017       0.
1.        .8833       .7839       .7126       .6407       .5909
.554      .4246       .3          .2316       .1577       .0445
.203      0.          0.
37.000000   43.466226   45.627293   45.271024   43.760238   42.112259
41.265010   41.132536   42.650517   45.814075   50.709184   64.817977
81.369372   97.333873  112.092063  125.229793  136.496308  145.764326
53.324494  159.033517  173.622660  182.820902  186.558435  185.005470
28.632594  167.509471  152.557490  125.959125   99.933649   77.571204
53.241056   45.987656   36.696676   29.459416   23.740253   19.156714
15.435933   12.368072    9.878223    7.754768    5.826306    4.045064
2.530125    1.713340    1.173584     .730840     .404915     .187414
.053652     0.000000
37.000000   43.016313   45.104055   44.896669   43.630052   42.260256
41.433958   41.629135   43.151886   46.179747   50.790586   67.332665
86.467861  104.052017  119.294453  131.695716  140.987987  147.077884
50.096650  149.643590  147.828341  134.720717  125.685442  116.022833
38.990365   95.762252   85.531919   74.574826   64.209305   54.740421
46.227325   28.635338   31.983825   26.299624   21.631967   17.815792
14.615551   11.916619   10.010308    8.315766    6.307585    3.949194
2.479987    1.696899    1.131125     .705787     .398487     .189183
.020579     0.000000
37.000000   40.766745   42.487861   43.024895   43.033122   43.000245
43.878605   44.112129   45.658733   48.008108   51.197595   61.320137
92.874066   83.420534   92.498438   99.819664  105.233517  108.692646
93.229266  109.803950  105.932667  101.124138   95.591728   89.518964
82.064032   76.363676   69.532887   61.908098   54.660865   48.062301
```

[illegible]	37.194602	32.901426	28.852724	24.678394	20.571623
[illegible]	13.781120	11.934129	10.326376	7.964821	4.814066
[illegible]	2.311748	1.256204	.797066	.449242	.214320
[illegible]	0.000000				
[illegible]	37.423353	38.227036	39.415080	40.852524	42.414467
[illegible]	45.479512	46.807790	47.911581	48.745531	49.279153
[illegible]	47.387587	48.960233	48.224555	47.198547	45.904492
[illegible]	42.618320	40.683830	38.594790	36.381063	34.071463
[illegible]	29.374423	26.937726	24.406430	22.001129	19.640315
[illegible]	15.116277	12.979922	10.942497	9.012717	7.197715
[illegible]	3.248306	2.654265	1.667005	.967074	.511573
[illegible]	.101535	.036072	.010316	.002133	.000254
[illegible]	0.000000				
[illegible]	1.243105	1.237853	1.229962	1.220083	1.208770
1.198462	1.183500	1.170119	1.156493	1.142736	1.128923
[illegible]	1.101282	1.087480	1.073690	1.059895	1.046077
[illegible]	1.018263	1.004204	.989993	.975590	.960946
[illegible]	.930715	.914998	.898775	.881951	.864407
[illegible]	.826548	.805814	.783487	.759127	.732093
[illegible]	.665422	.621981	.568837	.504407	.429127
[illegible]	.264666	.180144	.124075	.073041	.036401
[illegible]	0.000000				

```
*****************************************************************
*  EVALUATION OF RADIAL TEMP. GRADIENTS BY POLYNOMIAL FIT       *
*  THROUGH A SMALL SET OF DATA POINTS USING LINEAR REGRESSION.  *
*  95-PERCENT CONFIDENCE INTERVAL IS CALCULATED FOR EFFECTIVE   *
*  CONDUCTIVITY                                                 *
*****************************************************************


THE GRADIENT AT THE MID POINT IS TAKEN AS THE MOST ACCURATE

      DIMENSION  R(25),T(25),Y(25),X(25,15),XPRIM(15,25),TT(25),
     1 XPRIMT(15),THETA(15),TA(25),        TITLE(9),RR(25),TP(25)
      DIMENSION XPRIMX(15,15),LX(15)
      DIMENSION GRAD(25)
      DIMENSION YINTRP(25),TINTRP(25),GRINTR(25)
      DIMENSION RESULT(15),FUN(15)
      COMMON/ONE/ M,MM
      COMMON / TWO/ XPRIMX,RESULT

      ARITHMATIC FUNCTION STATEMENTS FOR PHYSICAL PROPERTIES CALCULATION

      VISC(Z) = VISCCT + Z*(VISCA + Z*(VISCB + Z*(VISCC + Z*(VISCD +
     1  Z*VISCE))))
      TCON(Z) = TCONCT + Z*(TCONA + Z*(TCONB + Z*TCONC))
      CP(Z) = CPCT + Z*(CPA + Z*(CPB + Z*(CPC + Z*CPD)))
      DENS(Z) = DENSCT + Z*(DENSA + Z*(DENSB + Z*(DENSC + Z*DENSD)))

      CONSTANTS FOR PROPERTY CORRELATIONS
      READ(5,6) VISCCT,VISCA,VISCB,VISCC,VISCD,VISCE
      READ(5,6) TCONCT,TCONA,TCONB,TCONC
      READ(5,6) CPCT,CPA,CPB,CPC,CPD
      READ(5,6) DENSCT,DENSA,DENSB,DENSC,DENSD

      NR  NUMBER OF RUNS
      N    NO. OF PORTS
      M    NO. OF POINTS TO BE USED IN POLYNOMIAL
      MM - 1  DEGREE OF POLYNOMIAL

      READ(5,1) NR
      READ(5,1) N
      READ(5,1) M
      READ(5,1) MM
      M1=M
      MMM=MM
      DO 300 IX=1,NR

      FTIN  INLET TEMP.  F        FWALL  WALL TEMP.  F
      READ(5,3) FTIN,FWALL

      READ(5,4) (TITLE(I),I=1,9)
      DO 100 JKK=1,N
      WRITE(6,999) (TITLE(I),I=1,9)
      M=M1

      MM1  NO. OF DATA POINTS READ
      R    RADIAL LOCATION IN IN.
      TT   DIMENSIONLESS TEMP. CORRESPONDING TO R
```

```
      READ(5,1)  MM1
      READ(5,3)  (R(I),I=1,MM1)
      READ(5,3)(TT(I),I=1,MM1)

      IJKL=0
      TWALL=FWALL + 460.
      TNORM= FWALL - FTIN
      FA=R(1)*TCON( TWALL)/CP(TWALL)

      SELECTING A SUBSET OF M DATA  POINTS
      STARTING WITH R(1) FIRST M POINTS FORM A SUBSET
      AND THEN THE FIRST POINT OF THE SUBSET MOVES FROM R(1) TO R(2),
      R(3) .. AND SO ON  TILL THE LAST POINT OF THE SUBSET IS R(MM1)

      LL1=MM1-MM
      DO 200 LL=1,LL1
      MMM=MM
      IF(LL.LE.4)  MM= MMM-1
      LLM=LL+M-1
      DO 15 I=LL,LLM
      ILL=I-LL+1
      TA(ILL)=TT(I)
      Y(ILL)=R(I)
   15 CONTINUE
      CALL  YMODL1(X,Y,TA,T)
      IF(M.LE.MM ) GO TO 200

      CALCULATING THE COEFFICIENT BY LINEAR LEAST SQUARE FIT

      DO 10 I=1,M
      DO 20 J=1,MM
      XPRIM(J,I)=X(I,J)
   20 CONTINUE
   10 CONTINUE
      DO 40 J=1,MM
      SUM=0.
      DO 30 I=1,M
      A=          XPRIM(J,I)*T(I)
      SUM=SUM+ A
   30 CONTINUE
      XPRIMT(J)=SUM
   40 CONTINUE
      DO  60 J=1,MM
      DO 55 K=1,MM
      SUM=0.
      DO 50 I=1,M
      A=          XPRIM(J,I)*X(I,K)
      SUM=SUM+ A
   50 CONTINUE
      XPRIMX(J,K)=SUM
   55 CONTINUE
   60 CONTINUE
      CALL  INVMAT(XPRIMX,15,MM,1.E-12,IERR,LX)
      DO 80 J=1,MM
      SUM=0.
      DO 70 K=1,MM
      A=          XPRIMX(J,K)*XPRIMT(K)
      SUM=SUM+ A
```

```
90 CONTINUE
   THETA(J)=SUM
80 CONTINUE

   WRITING    THE COEFFICIENT  OF THE POLYNOMIAL
   CALCULATION OF THE GRADIENT

   WRITE(6,997) (THETA(J),J=1,MM)
   CALL CPREP(  M,MM,THETA,Y,GRAD,TP)

   CALCULATION OF THE FIT AT MID-POINT OF THE DATA TO CHECK IF THE
   FITTED FUNCTION IS SMOOTH

   IM=M-1
   DO 17 I=2,M
   II=I-1
   YINTRP(II)=(Y(I)+Y(II))/2.
17 CONTINUE
   CALL CPREP( IM,MM,THETA,YINTRP,GRINTR, TINTRP)

   CALCULATION OF THE RESIDUALS

   SUM=0.
   SUM1=0.
   SUM2=0.
   DO 80 I=1,M
   SUM=SUM + (ALOG(TP(I)) - ALOG(TA(I)))**2
   SUM1= SUM1 + ALOG(TA(I)) * ALOG(TA(I))
   SUM2= SUM2 + ALOG(TA(I)) * ALOG(TP(I))
80 CONTINUE

   CALCULATION OF THE VARIANCE
   IDF   DEGREE OF FREEDOM
   VARY   VARIANCE OF THE MODEL IN THE POLYNOMIAL FORM FITTED BY
   THE LEAST SQUARE METHOD

   IDF= M-MM
   VARY= (SUM1 - SUM2)/ IDF

   FOR 95 PERCENT CONFIDENCE TFACTR  AS FOLLOWS

   IF(IDF.EQ.2) TFACTR = 4.303
   IF(IDF.EQ.3) TFACTR = 3.182
   IF(IDF.EQ.4) TFACTR = 2.776

   STORING THE GRADIENT AT THE WALL
   IF(IJKL.NE.0) GO TO 92
   GRAD1=GRAD(1)
   IJKL=1
92 CONTINUE

   DO 95 I=1,M
   TEMP=FTIN+460.+TNORM*TA(I)
   FAC=FA*GRAD1*CP(TEMP)/(Y(I)*TCON(TEMP))

   VARDTR  VARIANCE OF THE  GRADIENT
   FACT  VARIANCE OF THE EFFECTIVE CONDUCTIVITY
   FUN   95 PERCENT CONFIDENCE INTERVAL
```

```
      VARDTR=(RESULT(I)                + GRAD(I)*GRAD(I)) * VARY
      FACT=FAC*FAC*VARDTR/(GRAD(I)**4)
      FUN(I)=TFACTR*SQRT(ABS(FACT))
   95 CONTINUE
      WRITE(6,996) SUM,SUM1,SUM2,VARY
      WRITE(6,998)
      WRITE(6,995) (Y(I),TA(I),TP(I),GRAD(I),FUN(I),I=1,M)
      WRITE(6,994) (YINTRP(I),TINTRP(I),GRINTR(I),I=1,IM)
  100 CONTINUE
  100 CONTINUE
  200 CONTINUE
    1 FORMAT(I5)
    2 FORMAT(2F12.6)
    3 FORMAT(6F12.6)
    4 FORMAT(9A8)
    5 FORMAT(15I5)
    6 FORMAT(6F13.6)
  994 FORMAT(10X,F20.4,20X,2F20.4)
  995 FORMAT(10X,4F20.4,F20.6)
  996 FORMAT(/10X,*RESD. SQS  *,F15.5,5X,*TOTAL SQS  *,F15.5,5X,*MODELSQ
     1S  *,F15.5,10X,*VARIANCE*,F15.5,/)
  997 FORMAT(//20X,*COEFFICIENTS OF POLYNOMIAL ARE*,//2(5E20.6/)//)
  998 FORMAT(27X,*Y*,17X,*T*,15X,*TPRID*,15X,*GRAD*,/)
  999 FORMAT(1H1,//,20X,9A8//)
      STOP
      END
```

```
      SUBROUTINE YMODL1(X,Y,TA,T)

      EXPONENTIAL MODEL

      DIMENSION TA(25),T(25),Y(25),X(25,15)
      COMMON/ONE/ M,MM

      IJ=0
      DO 10 I=1,M
      IF(TA(I).LE. .000001) GO TO 15
      T(I)= ALOG(TA(I))
      X(I,1)=1.
      DO 20 J=2,MM
      JJ=J-1
      X(I,J)=1./(Y(I)**JJ)
   20 CONTINUE
      GO TO 10
   15 CONTINUE
      IJ=IJ+1
   10 CONTINUE
      M=M-IJ
      RETURN
      END
```

```
      SUBROUTINE CPRED( M,MM,THETA,Y,GRAD,TP)

      CALCULATION OF THE GRADIENTS, PREDICTED VALUES AND THE FACTOR FOR
      THE ESTIMATION OF THE CONFIDENCE FACTOR

      DIMENSION THETA(1),Y(1),GRAD(1),TP(1)
      DIMENSION  XPRIMX(15,15) ,G(15),RESULT(15)
      COMMON / TWO/ XPRIMX,RESULT

      DO 20 I=1,M
      SUM =0.
      SUM1=0.
      DO 10 J=1,MM
      IF(J.EQ.1) GO TO 5
      JJ=J-1
      SUM=SUM+ THETA(J)/(Y(I)**JJ)

      VECTOR G  IS DEFINED BY  EQUATION C-3-13

      G(J)= JJ/(Y(I)**J)
      SUM1=SUM1 - G(J)*THETA(J)
      GO TO 10
    5 CONTINUE
      G(1)=0.
      SUM=THETA(1)
   10 CONTINUE

      TP  IS THE PREDICTED VALUE
      GRAD  IS THE FIRST DERIVATIVE OF THE GIVEN DATA

      TP(I)=EXP(SUM)
      GRAD(I)=TP(I)* SUM1
      RSUM=0.
      DO 100 NI=1,MM
      ASUM=0.
      DO 110 NJ=1,MM
      ASUM=ASUM + G(NJ)*XPRIMX(NJ,NI)
  110 CONTINUE
      RSUM=RSUM + ASUM * G(NI)
  100 CONTINUE

      RESULT  IS A FACTOR IN EQUATION C-3-14

      RESULT(I)=RSUM*TP(I)*TP(I)
   20 CONTINUE
      RETURN
      END
```

```
*****************************************************************
*  INTEGRATION OF ENERGY EQN. TO EVALUATE EFFECTIVE CONDUCTIVITY *
*****************************************************************

DIMENSION RT(25,3),TR(25,3),U(50,3),V(50,3),T(50,3)
DIMENSION DTDXX(25,3),DTDRX(25,3)
DIMENSION R(50),UU(50),VV(50)
DIMENSION RR(50),AINTG(50)
DIMENSION TT(25),DTDX(25),DTDR(25),U1(25),V1(25)
DIMENSION TITLE(9)
DIMENSION G21(25),G22(25),XINTG2(25),XINTG1(25)
DIMENSION DEN(25),CONT(25),CPT(25),VISCT(25)
DIMENSION EPSLN(50),EPSLNU(25),EPSLNW(25)
DIMENSION  YPLUS(25),EPS1HA(25),TAUN(3)

ARITHMATICAL STATEMENT FUNCTION FOR PHYSICAL PROPERTIES

VISC(Z) = VISCCT + Z*(VISCA + Z*(VISCB + Z*(VISCC + Z*(VISCD +
1  Z*VISCE))))
TCON(Z) = TCONCT + Z*(TCONA + Z*(TCONB + Z*TCONC))
CP(Z) = CPCT + Z*(CPA + Z*(CPB + Z*(CPC + Z*CPD)))
DENS(Z) = DENSCT + Z*(DENSA + Z*(DENSB + Z*(DENSC + Z*DENSD)))

READ(5,5) VISCCT,VISCA,VISCB,VISCC,VISCD,VISCE
READ(5,5) TCONCT,TCONA,TCONB,TCONC
READ(5,5) CPCT,CPA,CPB,CPC,CPD
READ(5,5) DENSCT,DENSA,DENSB,DENSC,DENSD

N  NO. OF RADIAL MESH
MM  NO. OF PORTS
R  DIMENSIONLESS RADIAL LOCATION
KJ  NO OF RUNS

READ(5,1) MM,N
READ(5,2)  (R(I),I=1,N)
READ(5,1) KJ

FTN  INLET TEMP.
RE  REYNOLDS NUMBER
G  GH AT THE WALL FROM EQN. 3-10 OF CHAPTER 3
TAUN  WALL SHEAR STRESS CALCULATED FROM FRICTION FACTOR AT EACH PORT

DO 2000 JKK=1,KJ
READ(5,2) RADIUS,FTIN,RE,G
READ(5,2)(TAUN(J),J=1,MM)
TIN=FTIN + 460.
DENSTA=DENS(TIN)
VISCTA=VISC(TIN)

READ(5,3)  (TITLE(I),I=1,9)
WRITE(6,96)
WRITE(6,97)  (TITLE(I),I=1,9)

RT  RADIAL LOCATION ,IN. AT WHICH OBSERVATIONS WERE MADE
TR  OBSERVED DIMENSIONLESS TEMP. PROFILE CORRESPONDING TO RT
```

```
      DO 10 J=1,MM
      READ(5,1) M
      READ(5,2) (RT(I,J),I=1,M)
      READ(5,2) (TR(I,J),I=1,M)
   10 CONTINUE

      DTDXX  AXIAL TEMP. GRADIENT  F/(F-IN.)
      DTDRX  RADIAL TEMP. GRADIENT   F/(F-IN.)

      DO 20 J=1,MM
      READ(5,2) (DTDXX(I,J),I=1,M)
   20 CONTINUE
      DO 25 J=1,MM
      READ(5,2) (DTDRX(I,J),I=1,M)
   25 CONTINUE

      TBULKF AND TWALLF  BULK AND WALL TEMP.  DEGREE F
      U  V  T   VELOCITY AND TEMP. PROFILES CALCULATED FROM CONSERVATION
      EQUATIONS

      DO 30 J=1,MM
      READ(5,2) TBULKF,TWALLF
      READ(5,2)   (U(I,J),I=1,N)
      READ(5,2)   (V(I,J),I=1,N)
      READ(5,2)   (T(I,J),I=1,N)
   30 CONTINUE

      CALCULATION AT EACH PORT

      DO 1000    J=1,MM
      DO 40  I=1,N
      UU(I)=U(I,J)
      VV(I)=V(I,J)
   40 CONTINUE

      DO 100  I=1,M
      II=M-I+1
      RR(II)=RT(I,J)/RADIUS
      TT(II)=TR(I,J)
      DTDX(II)=DTDXX(I,J)*RADIUS
      DTDR(II)=DTDRX(I,J)*RADIUS
      AINTG(I)=0.
      XINTG1(I)=0.
      XINTG2(I)=0.
      U1(I)=0.
      V1(I)=0.
  100 CONTINUE

      CALCULATION OF PHYSICAL PROPERTIES AND Y+

      DO 180  I=1,M
      TA= TIN+TT(I)*(TWALLF-FTIN)
      VISCT(I)=VISC(TA)
      DEN(I)=DENS(TA)
      CONT(I)=TCON(TA)
      CPT(I)=CP(TA)
      YPLUS(I)=((1.-RR(I))*RADIUS/12.)*SQRT(TAUN(J)*32.17*DEN (I))
     1 /VISCT(I)
```

```
160 CONTINUE

    INTERPOLATION OF U AND V CORRESPONDING TO RADIAL LOCATION OF THE
    OBSERVATION

    DO 200 I=1,M
    RA=RR(I)
    CALLINTERP(N,R,UU,RA,UA)
    CALLINTERP(N,R,VV,RA,VA)
    U1(I)=UA
    V1(I)= VA

    CALCULATION OF THE INTEGRAND

    AINTG(I)=(RE/2.)*RA*     (UA*DTDX(I) + VA*DTDR(I))*DEN(I)/DENSTA
200 CONTINUE

    G21(M)=G
    XINTG1(M)=G21(M )*RR(M)*DTDR(M)
    XINTG2(M)=XINTG1(M)


    INTEGRATION
    FIRST FIVE POINTS FROM THE WALL BY TRAPEZOIDAL RULE, NEXT SEVEN
    POINTS BY GUASSIAN QUADERATURE AND THE LAST THREE POINTS BY
    TRAPEZOIDAL RULE

    DO 130 I=2,M
    II=M-I+1
    XINTG1(II)=XINTG1(II+1) - .5*(RR(II+1)-RR(II))*(AINTG(II+1)
   1 +AINTG(II))
    IF(II.GE.(M-5).OR.II.LE.3) GO TO 110
    RA=RR(II)
    CALL INTG(M,RR,AINTG,RA,1.,SUM)
    XINTG2(II)=XINTG2(M) - SUM
    GO TO 130
110 CONTINUE
    XINTG2(II)=XINTG1(II)
130 CONTINUE

    CALCULATION OF EFFECTIVE HEAT DIFFUSIVITY
    ALPHA  IS THERMAL DIFFUSIVITY

    DO 300 I=2,M
    IF(DTDR(I).GT.0.000001) GO TO 150
    GO TO 170
150 CONTINUE
    G21(I )=XINTG1(I )/(RR(I )*DTDR(I ))
    G22(I )=XINTG2(I )/(RR(I )*DTDR(I ))
    EPSLNU(I)= G22(I) - CONT(I)/(CPT(I)*VISCTA*2600.)

    EPSHA   IS  1. + EPSH / ALPHA

    EPSHA(I)= G22(I)/( CONT(I)/(CPT(I)*VISCTA*2600.))
170 CONTINUE
300 CONTINUE


    WRITE(6,94)
```

```
      WRITE(6,98) (RR(I),U1(I),V1(I),AINTG(I),      G22(I),EPSLNU(I),
     1 EPS1HA(I),YPLUS(I),I=1,N)
      WRITE(6,96)
  200 CONTINUE
  300 CONTINUE

    1 FORMAT(10I5)
    2 FORMAT(6F12.6)
    3 FORMAT(9A8)
    5 FORMAT(6E13.6)
   94 FORMAT(/,16X,*R*,14X,*U*,14X,*V*,10X,*AINTG*,12X,*G22*,10X,
     1 *EPSLNU*,10X,*EPS1HA*,10X,*YPLUS*,//)
   96 FORMAT(1H1)
   97 FORMAT(//15X,9A8,///)
   98 FORMAT( 5X,8F15.6,//)
      STOP
      END
```